Theoretical and Numerical Aspects of Modelling Geological Carbon Storage with Application to Muographic Monitoring

Darren L. Lincoln

This thesis is submitted for partial consideration towards the degree
of Doctor of Philosophy at the

The Department of Civil and Structural Engineering
at the University of Sheffield

December 2015

No flow system is an island.

A. Bejan

Abstract

The storage of waste carbon dioxide (CO_2) from fossil fuel combustion in deep geological formations is a strategy component for mitigating harmfully increasing atmospheric concentrations to within safe limits. This is to help prolong the security of fossil fuel based energy systems while cleaner and more sustainable technologies are developed. The work of this thesis is carried out as part of a multi-disciplinary project advancing knowledge on the modelling and monitoring of geological carbon storage/sequestration (GCS).

The underlying principles for mathematically describing the multi-physics of multiphase multi-component behaviour in porous media are reviewed with particular interest on their application to modelling GCS. A fully coupled non-isothermal multiphase Biot-type double-porosity formulation is derived, where emphasis during derivation is on capturing the coupled hydro-thermo-mechanical (HTM) processes for the purposes of study.

The formulated system of governing field equations is discretised in space by considering the standard Galerkin finite element procedure and its spatial refinement in the context of capturing coupled HTM processes within a GCS system. This presents a coupled set of nonlinear first-order ordinary differential equations in time. The system is discretised temporally and solved using an embedded finite difference method which is schemed with control theoretical techniques and an accelerated fixed-point-type procedure.

The developed numerical model is employed to solve a sequence of benchmark problems of increasing complexity in order to comprehensively study and highlight important coupled processes within potential GCS systems. This includes fracture/matrix fluid displacement, formation deformation and Joule-Thomson cooling effects. The computational framework is also extended to allow for the simulation of cosmic-ray muon radiography (muography) in order to assess the extent to which detected changes in subsurface muon flux due to CO_2 storage can be used to monitor GCS. This study demonstrates promise for muography as a novel passive-continuous monitoring aid for GCS.

Acknowledgements

I thank the University of Sheffield for granting resource to support my development to carry out this work. I would especially like to thank Harm Askes, Colin Smith, Terry Bennett, John Cripps and Vitaly Kudryavtsev for their vision, inspiration and guidance during my studies. I would like to further express my gratitude for the technical and often philosophical discussions which have coincided and entwined with the work of this thesis. This goes to everyone who has known me from my vantage at the Department of Civil and Structural Engineering and the Department of Physics and Astronomy at the University of Sheffield, to whom I am indebted. Finally, I thank my friends and family, and not least, Petra, my parents and my brother, for whom I will continue to achieve the best I can.

Darren Lincoln
December 2015

Contents

Abstract **i**

Acknowledgements **iii**

List of Figures **xi**

List of Tables **xiii**

Nomenclature **xv**

1 Introduction **1**

1.1 Energy 1

1.2 Fossil fuels and climate change 1

1.3 Carbon capture and storage 3

1.3.1 Principles of GCS 3

1.4 Thesis aims, objectives and layout 5

2 Literature Review & Fundamentals **9**

2.1 Porous media theory 9

2.1.1 Porosity 10

2.1.2 Distribution functions and volume fractions 10

2.1.3 Averaging functions/operators 12

2.2 Kinematics 13

2.3 Identities 14

2.4 General microscopic balance equations 14

2.5 General mean macroscopic balance equations 16

2.6 Equations of state and constitutive relations 18

2.6.1 Helmholtz free energy 18

2.6.2 Entropy inequality 19

2.6.3 Porous media stress partition . . . 19
2.6.4 Effective stress and strain/deformation . . . 21
2.6.5 Fick's law . . . 22
2.6.6 Darcy's law . . . 23
2.6.7 Fourier's law . . . 23
2.6.8 Fluid thermodynamic properties . . . 24
    2.6.8.1 Density: CO_2-brine mixture p-v-T-x relationship . . . 25
    2.6.8.2 Heat capacity . . . 27
    2.6.8.3 Joule-Thomson coefficient and cooling . . . 28
2.6.9 Fluid transport properties . . . 29
    2.6.9.1 Dynamic viscosity . . . 29
    2.6.9.2 Thermal conductivity . . . 30
    2.6.9.3 Surface tension and energy . . . 30
2.6.10 Compressibility & thermal expansion coefficients . . . 31
    2.6.10.1 Fluid density . . . 31
    2.6.10.2 Solid density . . . 32
2.7 Capillarity . . . 32
2.7.1 Capillary pressure-saturation relationship . . . 33
2.7.2 Relative permeability-saturation relationship . . . 34
2.7.3 Interface stability and phase mobility contrast . . . 35
2.8 Further HTMC Processes . . . 36
2.8.1 Dissolution (solubility and ionic) mechanisms . . . 36
2.8.2 Mineral mechanisms . . . 37
2.8.3 Adsorption mechanisms . . . 37
2.8.4 Density convection mixing . . . 38
2.8.5 Porosity and permeability changes . . . 38
2.9 Upscaling . . . 38
2.10 Double-porosity transfer function . . . 39
2.11 Monitoring . . . 40
2.11.1 Electrokinetic monitoring . . . 41
2.11.2 Cosmic-ray muon tomographic monitoring . . . 42
    2.11.2.1 Muon scattering tomography imaging . . . 43
    2.11.2.2 Muon transmission imaging . . . 43

2.11.2.3 Particle transport simulation 44

2.12 Modelling 44

2.12.1 Modular Class: Sequential coupling of a flow simulator with other software 45

2.12.2 Fully Coupled Class: Fully coupled (simultaneous) behaviour 45

2.13 Review on fractures/fracturing—initiation and propagation 46

2.14 Summary of key research needs 47

3 Model Formulations **49**

3.1 Model description 49

3.2 Mass balance 51

3.2.1 Primary/state variables 51

3.2.2 Solid mass balance for a porous continuum 52

3.2.3 Generic biphasic fluid and solid phase mass balance in a porous continuum 52

3.2.4 Wetting and nonwetting phase mass balance in the porous continuum . . 53

3.2.5 Wetting and nonwetting phase mass balance in the fracture continuum . . 55

3.2.6 Illustration: 1D axisymmetric mass balance solutions 57

3.3 Momentum balance 64

3.4 Energy/enthalpy balance 65

3.5 Summary of governing field equations 70

4 Spatial Discretisation **73**

4.1 Method of weighted residuals (Galerkin procedure) 74

4.1.1 Momentum balance initial and boundary conditions 75

4.1.2 Momentum balance discretisation 76

4.1.3 Mass balance initial and boundary conditions 76

4.1.4 Mass balance discretisation 77

4.1.5 Energy balance initial and boundary conditions 78

4.1.6 Energy balance discretisation 78

4.2 The spatially discretised system of equations 79

4.3 Shape functions & isoparametric finite elements 81

4.3.1 2D Jacobian matrix and determinant 84

4.3.2 Gauss-Legendre quadrature for axisymmetric numerical integration 85

4.4 General Finite Element Formulations 86

4.4.1 Tangential stiffness element matrix 86

4.4.2 Laplace element matrix 87
4.4.3 Mass element matrix 88
4.4.4 Advection element matrix 89
4.4.5 Displacement and pressure coupling element matrices 89
4.4.6 Body force/source element vectors 89
4.4.7 Surface force/flux element vectors 90
4.5 Global matrix assembly and programming aspects 91
4.6 Meshing and mesh refinement 92

5 Temporal Integration & Solution Control 93

5.1 Method 1: The $\boldsymbol{\theta}$-method 95
5.2 Method 2: The Thomas-Gladwell method 96
5.3 Embedded backward-Euler/Thomas-Gladwell pair 97
5.4 Nonlinear solver 98
5.4.1 Solver 99
5.4.2 Anderson acceleration and mixing 99
5.4.3 Tolerance 101
5.5 Control theory: Adaptive time-step size control 101
5.5.1 Optimal error control for the integration procedure 101
5.5.2 Optimal convergence control for an accelerated fixed-point iteration method 103
5.5.3 Management of truncation error and convergence control 104
5.6 Initial variable values and time-step size 104
5.6.1 Initial derivative 104
5.6.2 Initial time-step size 104
5.6.3 Initial estimate for the nonlinear solver 105
5.7 Conditioning spatial and temporal discretisation 105
5.8 Time discretisation algorithm 106
5.9 Potential matrix partitioning and solution staggering 108

6 Model Results & Performance 111

6.1 Physical parameter base set 111
6.2 Numerical parameter base set 114
6.3 Mesh design 115
6.4 Full saturation to partial saturation flow transition 116

6.5 Stress recovery 116
6.6 Visualisation and data management 117
6.7 Model verification 117
    6.7.1 One fluid phase Hydro-Mechanical behaviour: (1H)M 118
    6.7.2 Two fluid phase Hydraulic behaviour: (2H) 121
    6.7.3 Two phase Hydro-Mechanical behaviour: (2H)M 126
    6.7.4 Two phase double-porosity (fractured) Hydro-Mechancial behaviour: (4H)M 131
        6.7.4.1 Double-porosity effects on trapping mechanisms 134
    6.7.5 Two phase Hydro-Thermal behaviour: (2H)T 137
    6.7.6 Two phase single and double-porosity Hydro-Thermo-Mechanical behaviour: (2/4H)TM 140
6.8 Algorithm performance 143

7 Muographic Modelling Applications 145
7.1 Modelling muon radiography for monitoring a GCS site 146
    7.1.1 Modelling methodology 146
        7.1.1.1 Boulby GCS test model 147
        7.1.1.2 Model integration 148
    7.1.2 Simulation results and discussion 149
7.2 Site screening of muon radiography for a real-world scenario 153
    7.2.1 Real-world CO_2 geo-storage model 154
    7.2.2 Model screening results and discussion 156
7.3 Evaluation 158

8 Conclusions & Further Work 161
8.1 Conclusions 161
8.2 Further work 165

List of Figures

2.1 Microscopic to macroscopic averaging volume and the variation of an averaged field variable 11

2.2 Illustration of porosity, saturation and volume fraction relations 12

2.3 Illustration of macroscopic overlapping continua 12

2.4 Axisymmetric elementary volume depicting stress components 22

2.5 CO_2 and brine p-v-T-x relationships over applicable ranges 27

2.6 CO_2 and brine viscosities as a function of pressure and temperature 30

2.7 van Genuchten and relative permeability correlations 35

2.8 Illustration of the double-porosity concept 39

2.9 Double-porosity system compaction and dilation illustrated with respect to matrix and fracture pressures 40

2.10 Schematic illustrating muon transmission imaging 44

3.1 Schematic of a one-dimensional axisymmetric system illustrating a typical stable CO_2-Brine interface profile 57

3.2 Simplified problem axisymmetric control volume 57

3.3 Analytical and FD solutions for fluid interface and vertically averaged bulk density profiles for varying permeability 63

3.4 Analytical and FD solutions for fluid interface and vertically averaged bulk density profiles for varying rock compressibility 63

4.1 Visualisation of domain and boundary for an arbitrary problem 74

4.2 Finite elements in global and natural coordinate systems 82

5.1 Illustration of primary variable approximations in the time domain for the θ-method of time integration 95

6.1 Model boundary conditions for a hydro-mechanical consolidation problem 119

6.2 Fourier/Laplace transform and finite element/finite difference consolidation problem solutions . . . 121

6.3 Final deformed shape and vertical effective stress profile after consolidation . . . 121

6.4 Model boundary condition schematic for multiphase hydraulic behaviour . . . 122

6.5 Example finite element mesh . . . 122

6.6 Shallow depth: cool and warm formation corresponding saturation and averaged fluid pressure distributions . . . 125

6.7 Deep depth: cool and warm formation corresponding saturation and averaged fluid pressure distributions . . . 125

6.8 Model boundary condition schematic for hydro-mechanical behaviour . . . 128

6.9 Shallow depth: cool and warm formation corresponding average fluid pressure distributions and caprock uplift . . . 129

6.10 Deep depth: cool and warm formation corresponding average fluid pressure distributions and caprock uplift . . . 129

6.11 Model boundary condition schematic for double-porosity hydro-mechanical behaviour . . . 131

6.12 Shallow depth cool fractured (double-porosity) formation corresponding saturations, averaged fluid pressure distributions and caprock uplift . . . 133

6.13 Fluid saturation profiles within a double-porosity storage system . . . 135

6.14 Model boundary condition schematic for hydro-thermal behaviour . . . 137

6.15 Low pressure (depleted) reservoir scenario highlighting Joule-Thomson cooling . 140

6.16 Model boundary condition schematic for the (fractured) hydro-thermo-mechanical behaviour . . . 141

6.17 Low pressure (depleted) reservoir scenario highlighting Joule-Thomson cooling with coupled mechanical behaviour . . . 142

6.18 Algorithm performance . . . 143

7.1 Schematic of classes developed to embed the numerical code with the Geant4 framework . . . 149

7.2 Quarter symmetric illustration of the bulk density of the storage system . . . 149

7.3 Change in column bulk mass density with the corresponding significance over muon zenith and time . . . 151

7.4 Local significance of change in muon flux . . . 152

7.5 Local geological model of the Utsira formation top layer involved in the Sleipner project . . . 155

7.6 Vertical plume thickness and extent with relative change in muon flux . . . 157

List of Tables

1.1 World greenhouse gas emission data 2

1.2 Potential trapping mechanisms enabling CO_2 sequestration in geological formations. 4

2.1 Porosity, saturation and volume fraction relationships 12

2.2 Nomenclature for the general microscopic balance equation 15

2.3 Physical microscopic balance equation variables 15

2.4 Description of physical microscopic balance equation variables 15

2.5 Nomenclature for the general mean macroscopic balance equation 17

2.6 Physical macroscopic balance equation variables 17

2.7 Description of the physical mean macroscopic balance equation variables 17

2.8 Potential GCS monitoring techniques 41

2.9 Numerical simulators developed/employed for modelling GCS scenarios 46

3.1 Storage formation parameter sets for extreme brine aquifer scenarios 62

4.1 1D 2 node quadrilateral finite element shape functions and derivatives 83

4.2 1D 3 node quadrilateral finite element shape functions and derivatives 83

4.3 2D 4 node quadrilateral finite element shape functions and derivatives 83

4.4 2D 9 node quadrilateral finite element shape functions and derivatives 83

5.1 Accelerated solution control algorithm 106

6.1 Storage formation HTM parameter sets for extreme brine aquifer scenarios . . . 113

6.2 Numerical control parameters 114

6.3 Numerical acceleration parameters 114

6.4 Summary of the coupled multi-physics problems assessed 118

6.5 Consolidation problem numerical control parameters 120

6.6 Lower pressure (depleted) reservoir parameter set for Joule-Thomson cooling scenarios 138

7.1 Boulby test site storage formation parameter set 147

7.2 Muon ray-tracing statistics 158

Nomenclature

The following is a generalised and non-exhaustive list of the symbols employed in this text, incorporating those in particular which appear in multiple contexts. All symbols employed are defined and described further throughout. The symbols are also additionally indexed where employed to further indicate to which phase/component and/or sub-domain the property is related.

Symbol	**Units**	**Description**
a	m^2	area
$\mathbf{a}$	$\mathrm{m/s}^2$	acceleration vector
A	J	Helmholtz free energy
A_m	m^2	surface pixel area for path m
b	-	Biot coefficient
$\hat{b}$	m^{-1}	Forchheimer coefficient
$\hat{b}_\mathrm{r}$	-	relative Forchheimer coefficient
c	m^2/s	compressibility coefficient
c_p	$\mathrm{J/(kg\,K)}$	specific isobaric heat capacity
c_v	Pa^{-1}	coefficient of consolidation
Cr	-	Courant number
$\boldsymbol{\mathcal{C}}$	-	capacity matrix
$\boldsymbol{D}^{\pi,\kappa}$	m^2/s	effective dispersion tensor
$\mathbf{D}_\mathrm{T}$	-	tangential stress/strain matrix
E	Pa	Young's modulus
E_μ	GeV	muon energy
f_min	-	minimum control factor
f_max	-	maximum control factor
$\boldsymbol{\mathcal{F}}$	-	force/supply vector
g_μ	$-/(\mathrm{m}^2\,\mathrm{s}\,\mathrm{sr}\,\mathrm{GeV})$	differential muon intensity
g	$\mathrm{m/s}^2$	gravitational acceleration
$\mathbf{g}$	$\mathrm{m/s}^2$	external body force/supply of momentum
G_μ	$-/(\mathrm{m}^2\,\mathrm{s}\,\mathrm{sr})$	energy integrated muon flux
h	J/kg	specific enthalpy
	m	fluid interface height
H	J	enthalpy
	m	formation thickness/height
$\boldsymbol{I}$	-	unit tensor
J_m	$-/(\mathrm{m}^2\,\mathrm{s}\,\mathrm{sr})$	detector muon flux arriving from path m
$\mathbf{J}^{\pi,\kappa}$	$\mathrm{kg/(m^2\,s)}$	diffusive-dispersive mass flux vector
$\mathbf{J}$	-	Jacobian matrix

k	m^2	permeability
k_r	-	relative permeability
k_r0	-	phase end-point relative permeability
k_I	-	integral gain control factor
k_P	-	proportional gain control factor
$\mathbf{k}$	m^2	permeability tensor
K	Pa	bulk modulus
$\boldsymbol{\mathcal{K}}$	-	conductivity matrix
l_c	m	characteristic length
$\bar{l}$	m	characteristic fracture spacing
$\boldsymbol{L}$	-	displacement/strain differential operator
m_k	-	wetting phase relative permeability exponent
m_v	Pa^{-1}	coefficient of volume compressibility
m_max	-	maximum consecutive iterations to accelerate
$\mathrm{m_v}$	-	van Genuchten parameter
$\mathbf{m}$	-	unit vector
M	-	mobility contrast
M_n	kg/s	nonwetting mass rate of injection
n	-	porosity
$\bar{n}$	-	number of orthogonal fracture sets
n_k	-	nonwetting phase relative permeability exponent
$\mathrm{n_v}$	-	van Genuchten parameter
$\mathbf{n}$	-	unit normal vector
$\hat{N}$	mol	number of moles
$\mathbf{N}$	-	shape function array
p	Pa	pressure
	-	order of integration method
p^c	Pa	capillary pressure
p_v	Pa	van Genuchten reference pressure
$\bar{\mathbf{p}}$	Pa	discrete pressure
q	$\mathrm{kg/(m^2\,s)}$	imposed boundary mass flux
q_trans	s^{-1}	double-porosity transfer function
q	m/s	fluid flux
$\boldsymbol{q}$	m/s	Darcy flux vector
$\mathbf{q}$	$\mathrm{J/(m^2\,s)}$	flux vector of heat
Q	J	heat
r	m	wellbore radius
	-	growth rate
R	m	radius of curvature
R	$\mathrm{J/(kg\,K)}$	specific gas constant
$\mathbf{R}$	-	residual error vector
s	-	safety factor
s	$\mathrm{J/(kg\,K)}$	specific entropy
	m	settlement
s_max	-	maximum number of iterations
s_startA	-	acceleration starting iteration
S	-	fluid phase saturation
	-	statistical significance

S	J/K	entropy
t	s	time
$\bar{\mathbf{t}}$	$\mathrm{N/m^2}$	traction boundary condition for stress
T	K	absolute temperature
$\bar{\mathbf{T}}$	K	discrete temperature
u	J/kg	specific internal energy
$\mathbf{u}$	m	displacement vector
$\bar{\mathbf{u}}$	m	discrete displacements
U	J	internal energy
$\mathcal{U}$	$\mathrm{J/m^3}$	interface energy per unit porous volume
v, V	$\mathrm{m^3}$	volume
$\mathbf{v}$	m/s	velocity vector
v	$\mathrm{m^3/kg}$	specific volume
w	J	weight function
W	J	work
$\mathbf{x}$	m	spatial position vector
x	m	(radial) spatial dimension
	-	composition
$\mathbf{x}$	-	arbitrary variable vector of unknowns
$\bar{\mathbf{x}}$	-	discrete arbitrary variable vector of unknowns
$\mathbf{X}$	-	Multiple variable solution vector
z	m	path distance
$\tilde{z}$	m	effective path distance
Z	-	compressibility factor
$\bar{\alpha}$	$\mathrm{m^{-2}}$	double-porosity fracture shape factor
β	$\mathrm{K^{-1}}$	thermal expansion coefficient
$\upbeta$	-	mixing/damping parameter
γ	-	phase distribution function
	-	algorithmic weighting argument
$\boldsymbol{\gamma}$	-	algorithmic weighting argument vector
γ_{ab}	-	interface energy between phases a and b
ε	-	truncation error
$\boldsymbol{\varepsilon}$		strain tensor
ζ	$\star$	averaged field variable or function
η	-	phase volume fraction
θ	$^\circ$	zenith angle
	-	numerical integration parameter
μ	Pa s	dynamic viscosity
μ_{JT}	K/Pa	Joule-Thomson coefficient
$\hat{\mu}$	J/mol	molar chemical potential
ν	-	Poisson's ratio
Ξ	-	muon survival probability function
ρ	$\mathrm{kg/m^3}$	bulk density
ρ^{π}	$\mathrm{kg/m^3}$	intrinsic phase volume average density
σ	$\mathrm{N/m^2}$	stress component
	$\mathrm{kg/m^2}$	column mass density
$\boldsymbol{\sigma}$	$\mathrm{N/m^2}$	stress tensor

τ_{R}	-	residual error tolerance
τ_{T}	-	truncation error tolerance
χ	W/(m K)	thermal conductivity
$\boldsymbol{\chi}$	W/(m K)	thermal conductivity tensor
ϕ	-	Lagrangian porosity
Φ_m	-/(m^2 s)	muon flux arriving from path m with surface pixel area A_m
$\varphi_{1,2,3}$	-	numerical integration parameters
ψ	$\star$	generic conserved thermodynamic property

Indices	**Type**	**Description**
i	sub-domain	generic sub-domain index
n	phase	nonwetting phase
n	numerical	time-step
s	phase	solid phase
s	numerical	iteration-step
w	phase	wetting phase
κ	component	generic component/species
π	phase	generic phase index
1	sub-domain	primary matrix porosity
2	sub-domain	secondary fracture network porosity

Chapter 1

Introduction

1.1 Energy

The United Nations Sustainable Development Goals (SDGs) agenda brings together its member states and organisations in agreement to achieve criteria promoting sustainable socio-economic development—that of a greater quality of life on Earth. Energy is fundamental to socio-economic development, and it is centrally recognised by the UN High-level Political Forum (HLPF) on Sustainable Development [134]. To holistically achieve these SDGs, energy must be universally accessible, affordable, and clean.

Energy is a benefit which presently comes at a significant cost to our resources and environment, its use must therefore be governed intelligently. The link, delivering an energy service compatible with both our natural environment and developmental needs, is technology. Energy resource extraction, conversion, transmission and waste management, as well as the infrastructure, production processes and appliances which necessitate energy are all technologically based systems. At all stages and levels these technologies can be addressed in order to bring about greater efficiencies. However, in developing technologies and in choosing which to employ—ethical stances, laws and regulations reflecting national capabilities, and social interests must also be respected. This is particularly the case where waste management and storage is of concern [192].

1.2 Fossil fuels and climate change

Producing energy generates harmful by-products and waste, more so than any other industrial process. For a global energy service, the main environmental challenge is preventing adverse anthropogenic interference with the climate system. This interference is predominantly a result of fossil fuel combustion, on which global primary energy demand is over 80% reliant [93, 192]. Greener technologies and end-use efficiencies require development and time to be phased into existing infrastructure due to practicality and expense. Furthermore, given the current global availability of fossil fuels they will continue to dominate as an energy source within the foreseeable future. The world demand for energy cannot be supplied by any feasible growth in the existing greener technologies alone; fossil fuels will continue to be used at a substantial rate.

Solar radiation, primarily of the ultraviolet, visible and infrared regions of the electromagnetic spectrum, is absorbed and re-emitted by the Earth's atmosphere and surface. Absorbed radiation heats up the Earth, and by way of being converted into heat energy is partly radiated as lower-energy longer-wave thermal infrared and near-infrared radiation back into the atmosphere and space. It is this radiation that certain 'greenhouse' gas molecules within the atmosphere are able to absorb and re-emit in all directions, thereby causing a greenhouse effect. This interaction is due to the intramolecular vibrational properties of the greenhouse gases which correspond with various frequencies in the infrared region of the electromagnetic radiation spectrum. This input and output of radiation is an important process that controls the climate of the Earth. The most influential greenhouse gases encountered in the Earth's atmosphere are water vapour (H_2O), carbon dioxide (CO_2), methane (CH_4), nitrous oxide (N_2O) and ozone (O_3).

The main greenhouse gas agents for which there is significant observed trends in concentrations with clear potential for future emission are listed in Table 1.1. Radiative forcing is a measure of the influence a greenhouse gas has on the energy balance of incoming and outgoing radiation in the Earth-atmosphere system, determined as the rate of energy change per unit area across the outer atmosphere. The positive increases in radiative forcing in Table 1.1 are taken relative to the standard pre-industrial 1750 values. Note that water vapour is not considered a forcing agent because its concentrations are highly variable and short-lived due to the hydrological cycle, but instead responds to the local climate, acting as an amplifier giving feedback to warming.

Table 1.1: World greenhouse gas emissions and atmospheric concentration changes, lifetime and increased radiative forcing.

	World Emissions	Tropospheric Concentrations		Atmospheric Lifetime	Radiative Forcing Increase
Species	2012 [$MtCO_2eq$]	Pre-1750	2013	[years]	2013 [Wm^{-2}]
CO_2	36,422	280 ppm	395 ppm	~100–300	1.88
CH_4	7,299	722 ppb	1893 ppb	12	0.49
N_2O	3,105	270 ppb	326 ppb	121	0.17

Sources: CDIAC [30], IPCC [97]

Anthropogenic world emissions of greenhouse gas agents have increased substantially since industrialisation due to economic and population growth. This has caused an offset in the respective greenhouse gas cycles, whereby a net accumulation in the concentration of these agents is occurring in the atmosphere and oceans. Compounded with other anthropogenic effects, this is considered the dominant cause of the observed trend in global warming, the declines in snow and ice, and the rise in sea levels [97]. Strong correlation between increased greenhouse gas concentrations and temperature are highlighted throughout the literature, both with respect to recent observation and over geological time periods via the interpretation of ice core data.

A globally averaged combined surface land and ocean temperate rise of 0.85 [0.65–1.06] °C correlating with greenhouse gas emissions since industrialisation is reported [97]. Parties to the United Nations Framework Convention on Climate Change (UNFCCC) currently limit future warming to below 2.0 °C, with the pursuit of efforts to limit warming to 1.5 °C [193], as the threshold for dangerous interference. Maintaining temperatures below these levels is likely if atmospheric CO_2-eq concentrations are stabilised below 450 ppm by 2100. The International Panel on Climate Change (IPCC) outlines multiple strategic scenarios [97] for mitigating greenhouse gas emissions to within acceptable limits while meeting global energy demands and while phasing out the use of fossil fuels. These scenarios present major challenges involving a spectrum of socio-economic-technological trajectories in order to stabilize atmospheric concentrations. Favourable scenarios leading to 2100, predict an improved energy efficiency in technology in terms of generation and end-use, and predict energy supply from nuclear, renewables, and fossil fuels with carbon dioxide capture and storage (CCS), and/or bioenergy with CCS (BECCS).

1.3 Carbon capture and storage

Carbon capture and storage/sequestration (CCS) is the process of capturing and sequestering excessive anthropogenically produced carbon dioxide from point sources, as an alternative to atmospheric disposal. It is an enabling technology that may allow for the continued safe use of fossil fuels well into this century. The ambition is that the security and stability of the world's energy systems is maintained in the short- to medium-term while adverse climate change due to the use of fossil fuels is mitigated. A key end-chain aspect to this initiative is the injection and storage of the waste carbon dioxide, in a compressed state, in deep geological formations, thereby returning the waste carbon to the subsurface. This is known as geological carbon storage/sequestration (GCS). The primary subsets of geological storage settings are deep non-potable saline sedimentary formations, depleted/declining hydrocarbon reservoirs, and unminable coal seams/beds. The contribution of CCS emission reduction within this century is estimated to be in the region of 20%, see [21, 96, 97], wherein global CO_2 storage estimates are discussed. Basic estimates of global storage capacity for the subsets are given respectively at 1,000–10,000 Gt, 675–900 Gt, and 3–200 Gt of CO_2, with individual projects/sites proposed to have capacity up to 10s of Gt. However, precise potential storage capacities, injection rates, leakage pathways, and environment and ecological impacts of a CO_2 containment breach appear to be unknown. CCS projects are taking place on increasingly unprecedented scales, following previous successful operations, and project information is being made widely available, see [22, 175] for important pilot case studies. Furthermore, due to the lack of maturity of the technologies involved, it is currently an energy intensive process in itself. To ensure the economic viability, cost competitiveness and effectiveness of CCS, substantial research on development and deployment is still required across the whole CCS chain [192], that is in general the capture, transport, storage and monitoring of the carbon dioxide.

1.3.1 Principles of GCS

Foremost, a suitable geological storage scenario is at a depth greater than 800 m [21]. It is beyond this approximate threshold that a CO_2 phase will be in a supercritical state due to the conditions of pressure and temperature, which generally increase along steady gradients with depth. The CO_2 density becomes high enough to efficiently utilise the pore space within

Table 1.2: Potential trapping mechanisms enabling CO_2 sequestration in geological formations.

Trapping Mechanism		Description
Physical	Structural	Fluid movement is impeded by low-permeability stratigraphic traps (caprocks) formed by geological depositional/diagenetic changes. These traps are large and abundant, potentially covering horizontal areas of 100s of square kilometres over more permeable trapped regions of 10s to 100s of metres in depth, and which naturally retain buoyancy driven hydrocarbons if present.
	Residual	If a CO_2 plume moves in the pore space in such a way that water is able re-invade regions where it had been drained by CO_2, then the CO_2 can become disconnected and immobilised at a residual saturation within the pore space. This is due to capillary hysteresis phenomena between the phases (Section 2.7). In the wake of a CO_2 plume large traced volumes of storage can be achieved without the need for structural trapping.
	Hydrodynamic	Trapping occurs due to the slow ($\sim$mm–cm/y) migration of the fluids within the storage formation over large regional distances such that the CO_2 would remain subsurface for geological periods, even without a structural trap, whereby the combination of residual, dissolution and mineral trapping mechanisms are able to take place [14, 22].
Chemical	Dissolution	Depending on the state variable mutual solubility and ionic behaviour of the phases (Section 2.8.1), CO_2 partially dissolves becoming trapped within the water phase and thereby loses its free-phase behaviour. As such the affected water phase becomes denser and moves down from the fluid interface regions causing further dissolution with the replacing water. This is a long-term effect, occurring over large time-scales of up to 100s of years, and also presents substantial trapping potential [192].
	Mineral	A weak carbonic acid is formed by CO_2 dissolution, this may react with the host rock matrix rich in Fe, Mg and Ca minerals and precipitate as carbonates (Section 2.8.1). The contribution of this tapping mechanism occurs substantially long-term over 100s of years to geological periods of time.
	Adsorption	CO_2 injected through fractures in coalbeds and shales diffuses into the small pore spaces where it is adsorbed onto the organic material.

the formation, and with respect to saline/brine formations, the buoyancy contrast becomes low enough between the CO_2 and in situ saline water (or brine) such that upwards CO_2 migration can potentially be managed. Note that under these conditions the CO_2 and saline water are largely immiscible. Maximum potential storage depths are dictated by geological and economic considerations, noting that once the desired high density state is met the CO_2 density does not increase significantly with further depth.

Injection is achieved by pressurising the CO_2 into a well, the section of the well injecting within the storage region is either perforated or covered with a permeable screen to enable the CO_2 to enter the formation, generally of permeable sandstone or limestone. Injection rises the pressure within the formation particularly near the well and the CO_2 enters the pore space initially occupied by the in situ fluids. Once the injection of CO_2 has taken place in a geological formation, undergoing various transport processes (Chapter 2), it displaces, dissolves, reacts and/or mixes with the already present formation fluid(s) and rock.

At the appropriate depths, physical and chemical trapping mechanisms also occur preventing the

CO_2 from migrating to the surface, these are itemised and described in Table 1.2 for reference. In general, the main contribution to trapping at the early (injection) stages of storage comes from the primary structural and/or hydrodynamic mechanisms. Over 10s of years the contribution to trapping becomes shared with the secondary residual CO_2 saturation and phase dissolution mechanisms which take place progressively over time. Over 100s to 1000s of years the secondary mechanisms contribute predominantly to trapping as the plume idles in movement after the end of its injection. Further, over geological periods of time, mineralisation is anticipated to contribute predominantly to storage. In effect, the security of the geological storage system generally increases as the mechanisms contributing to trapping progress over time [21, 192].

The integrity of the storage site depends on its geological arrangement and physical properties. For instance, at a sealing interface, the caprock should ideally be uniform in lithology, regionally extensive and thick. Key storage site issues are existing faults/fractures, exiting/abandoned wellbores and changes in site integrity and performance due to potential coupled hydro-thermo-mechanical-chemical (HTMC) system behaviours, which are discussed further throughout Chapter 2. For instance, a particular geomechanical focus is the maximum permissible ranges of injection pressures sustainable for effective storage without the coupled fracturing and/or re-opening of fractures within the storage and sealing rock, and any ensuing well damage and/or seismic behaviour. A particular geothermal factor is the expansive cooling of the CO_2 which may inhibit the successful injection of CO_2. Lastly, a particular geochemical factor is any potential acidic CO_2-rich water which may react with the rock and borehole cements and seals, causing mineral dissolution breakdown and/or mineral precipitation pore blockage, depending on the local system state, which may affect the performance of the storage system.

1.4 Thesis aims, objectives and layout

This work is part of a collaborative multi-disciplinary research project on advancing knowledge on the modelling and monitoring of GCS in particular. The contribution of this thesis is on the development of a computational framework for modelling the various multi-physics which are relevant for predicting various important physical aspects of GCS. The emphasis of the framework is on capturing the coupled HTM and muon radiographic processes of the storage system for research purposes. This framework is to allow for the investigation and development of both the physics modelled and the numerical procedures for discretising and solving the resulting systems of equations. This is to cover the following two broad and interrelated research aims.

- Firstly, large scale GCS is a relatively new concept, and given the potentially complex multi-physical nature of the problem, predictive models generally simplify the behaviour and/or concentrate on certain relevant physical aspects. The aim of this thesis is to develop an extended fully coupled non-isothermal multiphase Biot-type double-porosity modelling approach, and then to apply this to realistic GCS scenarios for the first time. This is aimed at the research need to further understand the system couplings and their co-action in terms of storage system performance. Additionally, such models are computationally expensive, in view of the model application, research needs are also attended to whereby alternative methods are developed and implemented in order to complement existing numerical discretisation and solution procedures for coupled systems of governing equations.

- Secondly, an existing CCS problem is how to cost-effectively/efficiently monitor the inaccessible geo-stored CO_2, ideally in a passive and continuous manner. A novel and unconventional potential solution to this problem is the application of cosmic-ray muon radiography. This has been successfully applied to other monitoring problems, though its application for monitoring realistic GCS scenarios is unresearched. A key aim of this work is to combine the modelling of GCS with the modelling of muon radiography for the first time. The aforementioned computational framework is therefore an multi-disciplinary one as it is to coordinate with the simulation of muon radiography in order to assess and effect the development of such a monitoring system within this context.

These broad aims are also discussed and detailed further throughout the chapters of this thesis, which are itemised below along with their key objectives.

- Chapter 2: The first objective is to give an in depth review of the underlying principles, governing balance laws and constitutive relationships for building physics applications for modelling multiphase multicomponent phenomena in heterogeneous porous media. The second objective is to review the relevant subsurface modelling and monitoring technologies and strategies. These reviews are carried out in the context of modelling and monitoring GCS in particular, such that incentives are also highlighted for further research.
- Chapter 3: The work of Chapter 2 is adopted, linked and extended in order to develop a system of fully coupled partial differential governing field equations for modelling multiphase fluid flow in fractured porous media. The research objective is to cover the key hydro-thermal-mechanical coupled physical bases for the investigative modelling of GCS, with particular emphasis on deriving a fully coupled double-porosity model formulation in order to assess the HTM processes in a fractured storage formation.
- Chapter 4: The objective is to discretise the system of governing field equations in space. Considerations on the standard Galerkin finite element procedure utilised, its spatial refinement and computational implementation are made and discussed given the derived system of coupled equations and their application. The spatial discretisation process leads to a coupled set of highly nonlinear first-order ordinary differential equations in time.
- Chapter 5: Given the complexity of the spatially discretised system of equations and the computational expense required in order to bring about their solution using standard procedures, the research objective is to devise an improved alternate solution strategy. To achieve this objective, an embedded finite difference method is schemed with advantageous control theoretical techniques and an accelerated fixed-point-type procedure.
- Chapter 6: A sequence of model verification and validation benchmark scenarios of increasing complexity are carried out and discussed in detail. The objective is to assess and discuss the performance of the numerical model against known simplified analytical

solutions to key problems and to highlight various coupled GCS phenomena in particular, which result given the model formulation. The emphasis is on assessing and highlighting coupled HTM processes in an isolated (or sealed) storage formation/system, thereby neglecting the modelling of CO_2 leakage from any sealing units (overburden) for later study.

- Chapter 7: The research objective is to integrate the modelling of geology, subsurface fluid flow phenomena and muon radiography in order to assess and develop the application of muon radiography for monitoring GCS. To achieve this objective, computational strategies are developed and implemented collaboratively. Presented and discussed are the first realistic simulations of the application of muon radiography for detecting a migrating body of CO_2 in the subsurface.

- Chapter 8: Finally, conclusions are drawn from the work of this thesis along with recommendations for future work.

The following conference and peer-reviewed work has also been carried out parallel to the work of this thesis.

Conferences

GeoRepNet Technology Transfer, BGS Keyworth, UK, 2014.

8th Numerical Methods in Geotechnical Engineering, Delft, Netherlands, Oral presentation, 2014.

International Conference on Computational Mechanics, Durham, UK, 2013, Prize session oral presentation for best paper (runner-up), 2013.

UKCCSC workshops, Nottingham & Liverpool, UK, Poster presentation, 2012.

Select publications & conference proceedings

Benton, C.J., Mitchell, C.N., Coleman, M., Paling, S.M., Lincoln, D.L., Thompson, L., Klinger, J., Telfer, S.J., Clark, S.J., Gluyas, J.G. (2015) Optimizing geophysical muon radiography using information theory. *Geophysical Journal International.* In final preparation.

Klinger, J., Clarke, S.J., Coleman, M., Gluyas, J.G., Kudryavtsev, V.A., Lincoln, D.L., Pal, S., Paling, S.M, Spooner, N.J.C, Telfer, S., Thompson, L.F., Woodward, D. (2015) Simulation of muon radiography for monitoring CO_2 stored in a geological reservoir. *International Journal. of Greenhouse Gas Control*, 42:644–654.

Lincoln, D.L., Askes, H., Smith, C.C., Cripps, J.C., Bennett, T. (2014) Coupled two-component flow in deformable fractured porous media with application to modelling geological carbon storage. *Numerical Methods in Geotechnical Engineering*, Hicks, Brinkgreve & Rohe (Eds) © 2014 Taylor & Francis Group, London, 978-1-138-00146-6.

Chapter 2

Literature Review & Fundamentals

The principal engineering challenges for the geological disposal of carbon dioxide and radioactive waste are set out in a broader enviro-socio-economic context in [72, 185, 192]. Therein the disposal space defined is deep redundant geological void spaces, the essential characteristics of which are capacity for storage and transmissibility, which are to demonstrate the necessary structural/stratigraphic, residual, solubility and mineral trapping mechanisms for safe storage. In this chapter a fundamental framework of the principles underlying these mechanisms is developed providing a basis from which to build appropriate applications to assess geological carbon storage (GCS) in particular. This fundamental perspective also gives an effective vantage from which to review the literature in the context of this emerging technology. It is envisioned that this framework will also encompass principles necessary for research on other emerging technologies, for instance, on efficient building materials, enhanced environmental (bio)remediation, geothermal energies, compressed air energy storage (CAES), and hydro-fracturing.

2.1 Porous media theory

The geological regions of interest for CO_2 storage are essentially porous media, that is solid phase materials containing an internal structure of open and closed pores forming interconnected porous networks, potentially occupied by multiple miscible and immiscible fluid phases of multiple components. Therefore, interacting multiphase multicomponent media are of interest, which present different hydro-thermo-mechanical-chemical (HTMC) behaviour than would their individual constituents alone. Such media are fundamental to many important processes in nature and in engineering, and are widely encountered [48].

Naturally formed porous structures have discontinuous and complex geometry, which makes descriptions at the microscopic scale difficult. Therefore, a representative macroscopic scale model is ordinarily assumed for engineering purposes whereby the constituents occupy, in an interpenetrable homogenised (or smeared) sense, portions of a control space via some volume fractioning. Continuum mechanics may then be applied to the substitute continua. To date, relevant descriptions of such systems are accomplished via this method broadly through the following theories. Firstly, *phenomenological theories* are based mainly on Terzaghi's work [189] on the mechanics of soils, and further developed by Biot [26, 27]. Richards equation [158] and the elaborations thereof form another important phenomenological set, and further thermodynamic developments in this context are also made by Coussy [47, 48]. Secondly, modern thermodynamic *mixture theories*, originating from classical gas mixture theory, utilise the constituent chemical potentials extended with the use of volume fractioning. In this context incompressible and compressible media are considered by Bowen [32, 33], with further consideration by de Boer [54, 55]. Lastly, *averaging theories* employ the technique of local volume averaging, whereby classical continuum balance laws governing the system at the microscopic scale are averaged over a representative volume giving macroscopic equations and thermodynamic properties. A thorough development in this context is given by Hassanizadeh & Gray [80, 81, 82, 83, 84].

The three theoretical approaches demonstrate equivalence under certain assumptions as demonstrated in [48, 53, 120], from which similar macroscopic governing field equations may be derived. This highlights their general accuracy and gives good scope for modelling strategies. During the development of various numerical models, for instance [120, 131], a crossover of these theories takes place when this is deemed appropriate during implementation. The modelling strategy in this work is similar in that the averaging theories are introduced initially because they offer the most in-depth and adaptive basis for advancement when considering a given application; it is then to this basis that elements of the other macro-theories are applied depending on the application and understanding required.

2.1.1 Porosity

Two types of porosity are distinguished because they exhibit distinct HTMC properties: *primary* (matrix) porosity, referring to the collective void spaces due to sedimentation, and *secondary* porosity, referring to fissures/fractures, vugs or other discontinuities due mainly to past cooling and tectonic activities. Most sedimentary formations have both these porosities [192]. Geological strata are widely characterised with continuous fracture networks through the porous rock mass. The implication of fractures during injection/extraction processes affects reservoir performance significantly, and models which conceptualise such strata as homogeneous can lead to conflicting and/or inadequate results [120]. Furthermore, the change in bulk properties of the reservoir, which are affected by the presence of multiple porosities, are key for statistically monitoring reservoir performance [114]. For these reasons the porous medium is introduced and defined in this section with a double(or dual)-porosity [3, 17, 201].

2.1.2 Distribution functions and volume fractions

The medium considered consists of fracture/rock-mass structures composed of porous matrix void/grain structures occupied by CO_2 and brine. That is, a system of solid, wetting and nonwetting phases (Section 2.7).

On the microscopic level, inhomogeneities as defined at the grain and pore scale l_{i}, Figure 2.1(a), require that any field variable for a particular phase be defined precisely at the points it occupies. This level of detail is undesirable given the scales necessary for assessment and the extent of

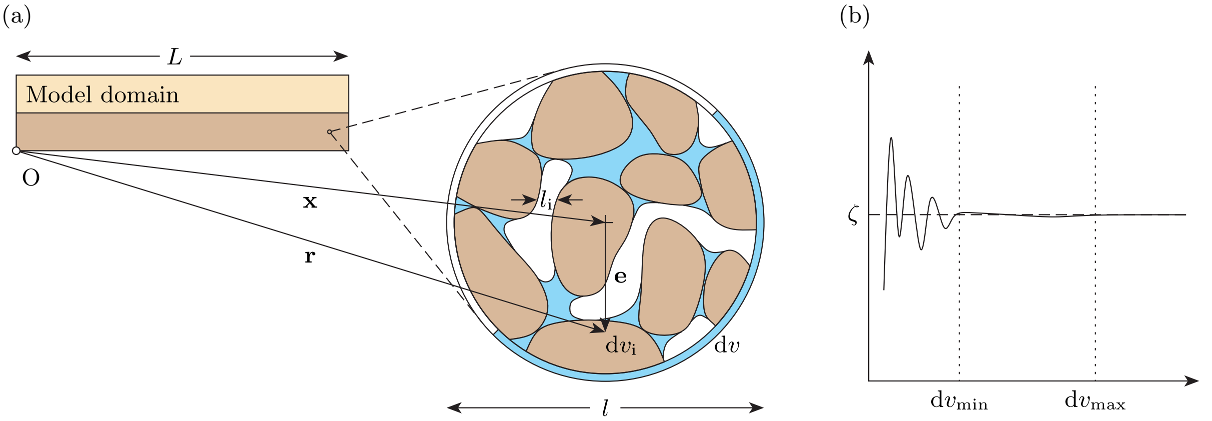

Figure 2.1: (a) Porous medium of three phases constituting a macroscopic averaging volume $\mathrm{d}v$ of internal microscopic volumes $\mathrm{d}v_\mathrm{i}$ as located by the position vectors, $\mathbf{r} = \mathbf{x} + \mathbf{e}$. The annulus represents a hypothetical smeared fracture network. (b) Typical depiction of variation of an averaged field variable ζ against averaging volume size [80].

geometric and material information that would be required.

On the macroscopic level the actual multiphase layout is replaced by a model which assumes the phases to be interpenetrating continua occupying the same characteristic macro-space. The applicability of this assumption is observed to hold over certain material dependent length scales, where the averaged field variable ζ homogenises within a certain range of averaging volume $\mathrm{d}v$, a differential/infinitesimal element of the domain, Figure 2.1(b). To ensure that the averaged values are meaningful, the characteristic length l should be such that $l_i \ll l \ll L$. That is, $\mathrm{d}v$ has to be small enough such that the governing equations make sense, and large enough such that the media may be considered homogeneous yielding stationary averages. For large scale processes in geological materials, the interest is in homogenising at the scale of pore-grain-fracture structures such that the resolution of inhomogeneities is focused at the scale of e.g. strata and wellbores.

A multiphase domain of total volume V_d, with s*olid*, w*etting* and n*onwetting* phases ($\pi = \mathrm{s}, \mathrm{w}, \mathrm{n}$) is occupied by partial volumes V_d^π. Referring to Figure 2.1(a), each point in the domain is considered as the centre of a macroscopic average volume element $\mathrm{d}v$ located by $\mathbf{x}$, in which microscopic volume elements $\mathrm{d}v_\mathrm{i}$ are located by $\mathbf{r}$, and by $\mathbf{e}$ relative to the local microscopic origin, such that $\mathbf{r} = \mathbf{x} + \mathbf{e}$. By defining a phase distribution function γ^π, the key concept of volume fractions η^π is introduced:

$$\gamma^\pi(\mathbf{x}, t) = \begin{cases} 1 & : \mathbf{r} \in \mathrm{d}v^\pi \\ 0 & : \mathbf{r} \notin \mathrm{d}v^\pi \end{cases} \tag{2.1}$$

$$\eta^\pi(\mathbf{x}, t) = \frac{\mathrm{d}v^\pi}{\mathrm{d}v} = \frac{1}{\mathrm{d}v} \int_{\mathrm{d}v} \gamma^\pi(\mathbf{r}, t)\, \mathrm{d}v_\mathrm{i}. \tag{2.2}$$

The integration is performed over the local $\mathbf{e}$-coordinate system, and may be carried out similarly for the surface area of the average volume element in contact with the π phase. Accordingly, primary and secondary porosities along with their degree of saturation, and the corresponding volume fraction of each phase are identified in Table 2.1 and illustrated in Figure 2.2.

Table 2.1: Porosity, saturation and volume fraction relationships for each phase of the representative porous medium.

	Porosity	Saturation	Volume fraction
Solid			$\eta^{\mathrm{s}} = 1 - (n_1 + n_2)$
Primary	$n_1 = (\mathrm{d}v^{\mathrm{w}_1} + \mathrm{d}v^{\mathrm{n}_1})/\mathrm{d}v$	$S_{\mathrm{w}_1} = \mathrm{d}v^{\mathrm{w}_1}/(\mathrm{d}v^{\mathrm{w}_1} + \mathrm{d}v^{\mathrm{n}_1})$	$\eta^{\mathrm{w}_1} = n_1 S_{\mathrm{w}_1}$
		$S_{\mathrm{n}_1} = \mathrm{d}v^{\mathrm{n}_1}/(\mathrm{d}v^{\mathrm{w}_1} + \mathrm{d}v^{\mathrm{n}_1})$	$\eta^{\mathrm{n}_1} = n_1 S_{\mathrm{n}_1}$
Secondary	$n_2 = (\mathrm{d}v^{\mathrm{w}_2} + \mathrm{d}v^{\mathrm{n}_2})/\mathrm{d}v$	$S_{\mathrm{w}_2} = \mathrm{d}v^{\mathrm{w}_2}/(\mathrm{d}v^{\mathrm{w}_2} + \mathrm{d}v^{\mathrm{n}_2})$	$\eta^{\mathrm{w}_2} = n_2 S_{\mathrm{w}_2}$
		$S_{\mathrm{n}_2} = \mathrm{d}v^{\mathrm{n}_2}/(\mathrm{d}v^{\mathrm{w}_2} + \mathrm{d}v^{\mathrm{n}_2})$	$\eta^{\mathrm{n}_2} = n_2 S_{\mathrm{n}_2}$

Throughout, subscripts 1 and 2 denote that the property belongs to the primary and secondary porous regions respectively. The substitute continua occupy the whole domain of interest in an overlapping sense (Figure 2.3) and will therefore have a reduced density as determined by the volume fractions. In order to acquire macroscopic variables, in what follows, the microscopic quantities are integrated/averaged over the volume $\mathrm{d}v$ as associated with the material points of the macroscopic domain.

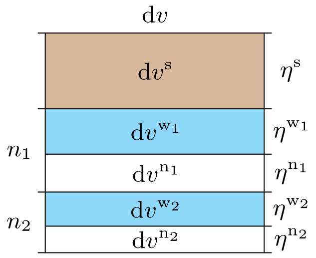

$$S_{\mathrm{w}_1} + S_{\mathrm{n}_1} = 1$$
$$S_{\mathrm{w}_2} + S_{\mathrm{n}_2} = 1$$
$$\sum_{\pi=1}^{n} \mathrm{d}v^{\pi} = \mathrm{d}v$$
$$\sum_{\pi=1}^{n} \eta^{\pi} = 1$$

Figure 2.2: Illustration of porosity, saturation and volume fraction relations within an averaged volume element.

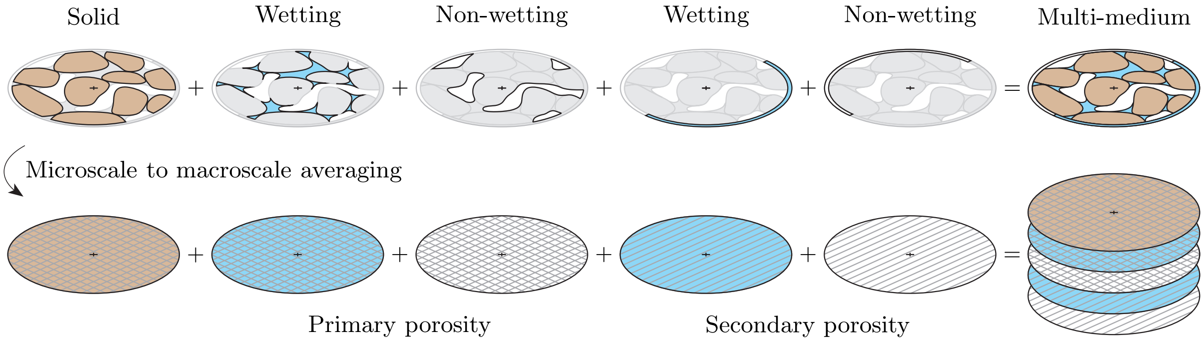

Figure 2.3: Illustration of the macroscopic (averaged) overlapping continua.

2.1.3 Averaging functions/operators

Given a microscopic field variable function (or property), $\zeta(\mathbf{r}, t)$, utilising Equations (2.1 & 2.2), the *extrinsic volume average* operator, $\langle\ \rangle_\pi$, is given by

$$\langle \zeta \rangle_\pi(\mathbf{x}, t) = \frac{1}{\mathrm{d}v} \int_{\mathrm{d}v} \zeta(\mathbf{r}, t)\, \gamma^{\pi}(\mathbf{r}, t)\, \mathrm{d}v_{\mathrm{i}}, \tag{2.3}$$

and the *intrinsic volume average* operator, $\langle\ \rangle^\pi_\pi$, is given similarly by

$$\langle\zeta\rangle^\pi_\pi(\mathbf{x},t) = \frac{1}{\mathrm{d}v^\pi}\int_{\mathrm{d}v}\zeta(\mathbf{r},t)\,\gamma^\pi(\mathbf{r},t)\,\mathrm{d}v_\mathrm{i} = \frac{1}{\eta^\pi(\mathbf{x},t)\,\mathrm{d}v}\int_{\mathrm{d}v}\zeta(\mathbf{r},t)\,\gamma^\pi(\mathbf{r},t)\,\mathrm{d}v_\mathrm{i}, \tag{2.4}$$

with the relationship $\langle\zeta\rangle_\pi(\mathbf{x},t) = \eta^\pi(\mathbf{x},t)\langle\zeta\rangle^\pi_\pi(\mathbf{x},t)$. The *mass average* operator, $\bar{\ }^\pi$, is given by

$$\bar{\zeta}^\pi(\mathbf{x},t) = \frac{\int_{\mathrm{d}v}\rho(\mathbf{r},t)\zeta(\mathbf{r},t)\,\gamma^\pi(\mathbf{r},t)\,\mathrm{d}v_\mathrm{i}}{\int_{\mathrm{d}v}\rho(\mathbf{r},t)\,\gamma^\pi(\mathbf{r},t)\,\mathrm{d}v_\mathrm{i}} = \frac{1}{\langle\rho\rangle_\pi(\mathbf{x},t)\,\mathrm{d}v}\int_{\mathrm{d}v}\rho(\mathbf{r},t)\zeta(\mathbf{r},t)\,\gamma^\pi(\mathbf{r},t)\,\mathrm{d}v_\mathrm{i} \tag{2.5}$$

which uses the microscopic density as a weighting function with (2.3). Lastly, the *area average* operator, $\bar{\bar{\ }}^\pi$, is defined by

$$\bar{\bar{\zeta}}^\pi(\mathbf{x},t) = \frac{1}{\mathrm{d}a}\int_{\mathrm{d}a}\zeta(\mathbf{r},t)\cdot\mathbf{n}\gamma^\pi(\mathbf{r},t)\,\mathrm{d}a_\mathrm{i}. \tag{2.6}$$

It can be seen that volume and mass averages are the same if constant microscopic density is present. Volume and area averages are the same if no anisotropic distribution of the phases is present, in the sense that Delesse's law is observed [55].

The mass and area averaging operators may be applied to a partial quantity relating to a component within a phase, namely ζ^κ and ρ^κ. Utilising the operators in this fashion means that partial values for each component would be given, which on summation would give the average of the phase they constitute, as follows,

$$\langle\zeta\rangle^\pi_\pi(\mathbf{x},t) = \sum_\kappa\langle\zeta^\kappa\rangle^\pi_\pi(\mathbf{x},t). \tag{2.7}$$

An averaged representative $\langle\zeta\rangle$ of the volume element $\mathrm{d}v$ is now given by the summations,

$$\langle\zeta\rangle(\mathbf{x},t) = \sum_\pi\langle\zeta\rangle_\pi(\mathbf{x},t) = \sum_\pi\eta^\pi\langle\zeta\rangle^\pi_\pi(\mathbf{x},t), \tag{2.8}$$

where the spatial variations of ζ for the individual phases within $\mathrm{d}v$ are now lost and an emergent macroscopic alternative is presented. The averaged representative value of the property ζ becomes important for building suitable macroscopic physics applications (Section 2.5) from general principles.

2.2 Kinematics

The kinematics of the substitute continua of the multiphase medium may be examined independently as follows. Firstly, the spatial positions of the material points of the continuum for each phase $\mathbf{x}^\pi$, at time t, are related to an original reference configuration $\mathbf{x}^\pi_0$, by $\mathbf{x}^\pi = \mathbf{x}^\pi(\mathbf{x}^\pi_0,t)$ and inversely by $\mathbf{x}^\pi_0 = \mathbf{x}^\pi_0(\mathbf{x}^\pi,t)$, which present material (Lagrangian) and spatial (Eulerian) descriptions of motion, respectively. That is $\mathbf{x}^\pi = \mathbf{x}^\pi(\mathbf{x}^\pi_0,t) = \mathbf{x}^\pi_0 + \mathbf{u}^\pi(\mathbf{x}^\pi_0,t)$, where $\mathbf{u}^\pi$ may be visualised as displacements of the π phase.

Considering a differentiable function in terms of spatial positions and time $\zeta^\pi(\mathbf{x},t)$, the changes of which experienced by a material point (Lagrangian description) are expressed in Eulerian notation/variables by the vectorial addition of the change with time at a fixed point and the change with distance at a fixed time. This gives the material time derivative, which is also expressed through the chain rule as

$$\underbrace{\frac{D^\pi \zeta^\pi}{Dt}}_{\text{Lagrangian}} = \frac{\partial \zeta^\pi}{\partial t} + \frac{\partial \zeta^\pi}{\partial \mathbf{x}} \cdot \frac{\partial \mathbf{x}}{\partial t} = \underbrace{\frac{\partial \zeta^\pi}{\partial t}}_{\text{Eulerian}} + \underbrace{\nabla \zeta^\pi \cdot \mathbf{v}^\pi}_{\text{Convective}}. \tag{2.9}$$

where $\mathbf{v}^\pi$ is the velocity of phase π. The following important relation for the spatial velocities $\mathbf{v}^\pi(\mathbf{x}, t)$ is now taken from (2.9) in order to give the acceleration of the π phase, by definition,

$$\mathbf{a}^\pi = \frac{D^\pi \mathbf{v}^\pi}{Dt} = \frac{\partial \mathbf{v}^\pi}{\partial t} + \nabla \mathbf{v}^\pi \cdot \mathbf{v}^\pi. \tag{2.10}$$

2.3 Identities

The following divergence ($\nabla\cdot$) and gradient (∇) operator relationships are of importance,

$$\nabla \cdot (s\mathbf{M}) = \mathbf{M} \cdot (\nabla s) + s(\nabla \cdot \mathbf{M}), \tag{2.11}$$

$$\nabla \cdot (\mathbf{u} \otimes \mathbf{v}) = (\nabla \mathbf{u}) \cdot \mathbf{v} + (\nabla \cdot \mathbf{v})\mathbf{u}, \tag{2.12}$$

where s is an arbitrary scalar, $\mathbf{u}$ and $\mathbf{v}$ are arbitrary vectors, and $\mathbf{M}$ is an arbitrary matrix. Note also that the symbols '$\cdot$' and '$\otimes$' denote the dot and tensor product operators respectively.

2.4 General microscopic balance equations

The microscopic description of a component κ within a given phase π is done with the classical balance equations of continuum mechanics. Treating the component as a continuum is permissible given that the characteristic pore and grain sizes are much greater than the mean free path of the discrete molecules (solid or fluid) of the component species [84]. It is also assumed that the species composing a phase are mixed at the molecular level so that in the continuum approach they are treated as part of a miscible mixture of components relative to the pore/grain sizes. The component is therefore viewed as having its own continuous motion defined throughout the domain where it may undergo processes of momentum, energy and chemical exchange/reaction with the other components[1]. Thus, for a typical conserved thermodynamic variable ψ belonging to a component κ, the balance equations are generically described at the point $\mathbf{r}$ in the classical form [84, 81],

$$\frac{\partial(\rho^\kappa \psi^\kappa)}{\partial t} + \nabla \cdot (\rho^\kappa \psi^\kappa \mathbf{v}^\kappa) - \nabla \cdot \mathbf{i}^\kappa - \rho^\kappa g^\kappa = \rho^\kappa G^\kappa, \tag{2.13}$$

where the symbols are described in Table 2.2 for ease of reference and clarity.

For each component, balance equations for mass, momentum, energy and entropy may now be

---

[1] The component materials within the domain are considered non-polar, as is typical in classical continuum mechanics. The stress tensors are therefore considered symmetric by ignoring the size effects and rotational interactions between particles. For materials which should be considered as polar, a couple-stress theory would be required [45, 54].

obtained from Equation (2.13) with the appropriate allocations from Table 2.3, the symbols of which are described thereafter in Table 2.4.

Table 2.2: Nomenclature for the general microscopic balance equation (2.13).

Symbol	Description	Units
ρ^κ	microscopic mass density function of κ (per unit volume of the phase π)	kg/m^3
$\mathbf{v}^\kappa$	mass-weighted mean velocity of the molecules of κ	m/s
ψ^κ	typical conserved thermodynamic property of κ	$\star$
$\mathbf{i}^\kappa$	surface flux vector of ψ^κ	$\star$ kg/m^2 s
g^κ	external supply of ψ^κ	$\star$ /s
G^κ	internal and molecular supply of ψ^κ	$\star$ /s

Table 2.3: Physical microscopic balance equation variables.

Quantity	$\psi^\kappa/\boldsymbol{\psi}^\kappa$	$\mathbf{i}^\kappa$	g^κ	G^κ	$G^{\kappa\prime}$
Mass	1	0	0	$\hat{r}^\kappa$	0
Momentum	$\mathbf{v}^\kappa$	$\boldsymbol{\sigma}^\kappa$	$\mathbf{g}^\kappa$	$\hat{r}^\kappa\boldsymbol{\psi}^\kappa + \hat{\mathbf{t}}^\kappa$	0
Energy	$u^\kappa + \frac{1}{2}\mathbf{v}^\kappa \cdot \mathbf{v}^\kappa$	$\boldsymbol{\sigma}^\kappa \cdot \mathbf{v}^\kappa + \mathbf{q}^\kappa$	$\mathbf{g}^\kappa \cdot \mathbf{v}^\kappa + \bar{h}^\kappa$	$\hat{r}^\kappa\psi^\kappa + \hat{\mathbf{t}}^\kappa \cdot \mathbf{v}^\kappa + \hat{q}^\kappa$	0
Entropy	s^κ	$\boldsymbol{\phi}^\kappa$	$\bar{b}^\kappa$	$\hat{r}^\kappa\psi^\kappa + \hat{\boldsymbol{\phi}}^\kappa + \Gamma^\kappa$	Γ^κ

Restrictions apply to exchanges of the conserved properties between components, in that summation over all components for each equation (Table 2.3) amounts to zero, $\sum_\kappa \rho^\kappa G^\kappa = 0$ (omitting any internal supply, here the entropy supply Γ^κ), such that there is no net production [84].

If components within the phases are considered to stay together during any of the modelled processes, such that they do not move/exchange amongst the fluids and/or rock grains, then the prescriptions under $G^{\kappa\prime}$ in Table 2.3 are alternatively adopted.

Table 2.4: Description of physical microscopic balance equation variables.

Symbol	Description	Units
$\hat{r}^\kappa$	molecular supply of mass of κ due to chemical reactions and decay/growth	s^{-1}
$\boldsymbol{\sigma}_\kappa$	microscopic partial stress tensor of κ	N/m^2
$\mathbf{g}^\kappa$	external body force/supply of momentum to κ (gravity and/or ionic attractions)	m/s^2
$\hat{\mathbf{t}}^\kappa$	internal body force/molecular supply of momentum to κ	m/s^2
u^κ	specific internal energy of κ (internal energy density function)	J/kg
$\mathbf{q}^\kappa$	surface flux vector of heat within the κ continuum	J/m^2 s
$\bar{h}^\kappa$	external supply of energy to κ	J/kg s
$\hat{q}^\kappa$	molecular supply/exchange of energy to κ	J/kg s
s^κ	specific entropy of component (internal entropy density function)	J/kg K
$\boldsymbol{\phi}^\kappa$	surface flux vector of entropy within the κ continuum	J/K m^{2}s
$\bar{b}^\kappa$	external supply of entropy to κ	J/kg s K
$\hat{\boldsymbol{\phi}}^\kappa$	molecular supply/exchange of entropy to κ	J/kg s K
Γ^κ	internal supply of entropy to κ	J/kg s K

It is at the boundaries of the phases (fluid-solid and fluid-fluid interfaces) that material properties and thermodynamic quantities are potentially discontinuous. Several important processes in the scope of GCS such as dissolution/precipitation, heat exchange, and viscous drag are mentioned in this context as mechanisms of interface interaction. Equations governing such interactions between adjacent phases are of the following form

$$[\rho^\kappa \psi^\kappa (\mathbf{w} - \mathbf{v}^\kappa) + \mathbf{i}^\kappa]\big|_a \cdot \mathbf{n}^{ab} + [\rho^\kappa \psi^\kappa (\mathbf{w} - \mathbf{v}^\kappa) + \mathbf{i}^\kappa]\big|_b \cdot \mathbf{n}^{ba} = 0 \tag{2.14}$$

where ab represents an interface between two different phases, $\mathbf{n}$ is the usual unit normal vector, and $\mathbf{w}$ is the velocity of the interface. An inequality sign should be introduced, for the balance of entropy, instead in (2.14) to allow for the potential production of entropy as a result of interface processes. The equations so far have ignored the thermodynamic properties of the interfaces themselves, such as interface tension and mass accumulation, for a more thorough consideration of which in this general context references [80, 81, 82] and particularly [85] are given. For an interface with surface properties, (2.14) will be non-zero. Interface behaviour is incorporated indirectly in this work via appropriate constitutive relations, as introduced through Section 2.6.

2.5 General mean macroscopic balance equations

General balance equations for a macroscopic thermodynamic property are obtained by averaging the microscopic balance equations by multiplying the general microscopic equations (2.13) and their exchange restrictions with a distribution function and then integrating them over the averaging volume. Additionally, the interface interaction (2.14) is integrated over the averaging area of surfaces within the averaging volume. This is done such that the resulting equations are localised as macroscopic point equations, with the averaging operators (2.3–2.6) defining the macroscopic quantities. Equations are produced for each component κ in each phase π. This averaging procedure is explored more thoroughly in the work referenced [83, 84, 131], wherein considerations are also made on the linking in physical meaning between the respective micro- and macroscopic quantities.

The next step is to produce convenient mean versions of these general balance equations for each phase. This is done such that the mean thermodynamic property of a phase is primarily described with the relative contributions of the separate components in respect of that mean. Particularly, any partial densities may be summed to give an average intrinsic density of the phase, as of (2.7),

$$\rho^\pi = \langle \rho \rangle^\pi_\pi = \sum_\kappa \langle \rho^\kappa \rangle^\pi_\pi, \tag{2.15}$$

and an average velocity of the phase may be produced,

$$\mathbf{v}^\pi = \sum_\kappa \frac{\langle \rho^\kappa \rangle^\pi_\pi}{\rho^\pi} \overline{\mathbf{v}^{\kappa\pi}}, \tag{2.16}$$

where the density fraction represents a mass fraction or concentration of the component, and $\overline{\mathbf{v}^{\kappa\pi}}$ is the velocity of the component. The difference between the mean and any value of a component gives the diffusion-dispersive velocity, and the related mass flux of that component,

$$\langle \mathbf{J}^\kappa \rangle^\pi_\pi = \eta^\pi \, \langle \rho^\kappa \rangle^\pi_\pi \, (\overline{\mathbf{v}^{\kappa\pi}} - \mathbf{v}^\pi). \tag{2.17}$$

Finally, the general mean macroscopic balance equation for a macroscopic thermodynamic quantity ψ^π, for a given phase π, is given in the form,

$$\frac{\partial(\eta^\pi \rho^\pi \psi^\pi)}{\partial t} + \nabla \cdot (\eta^\pi \rho^\pi \psi^\pi \mathbf{v}^\pi) - \nabla \cdot \mathbf{i}^\pi - \eta^\pi \rho^\pi g^\pi = \eta^\pi \rho^\pi f^\pi + \eta^\pi \rho^\pi G^{\pi\pi}. \tag{2.18}$$

with the restriction $\sum_\pi \eta^\pi \rho^\pi G^{\pi\pi} = 0$. The symbols are described in the following table.

Table 2.5: Nomenclature for the general mean macroscopic balance equation (2.18).

Symbol	Description	Units
η^π	volume fraction of the π phase	-
ρ^π	intrinsic volume-averaged mass density of the π phase	kg/m^2
ψ^π	mean macroscopic conserved thermodynamic property of the π phase	$\star$
$\mathbf{v}^\pi$	average velocity vector of all components in the π phase at a fixed spatial point	m/s
$\mathbf{i}^\pi$	surface flux vector of the mean macroscopic property ψ^π	$\star$ kg/m^{2}s
g^π	external supply of the mean macroscopic property ψ^π	$\star$ /s
f^π	internal supply of the mean macroscopic property ψ^π	$\star$ /s
$G^{\pi\pi}$	mean macroscopic effect due to phase interaction on ψ^π	$\star$ /s

For each phase, macroscopic balance equations for mass, momentum, energy and entropy can be derived from (2.18) with the appropriate allocations from Table 2.6; the symbols for these equations are described in Table 2.7.

Table 2.6: Physical macroscopic balance equation variables.

Equation\Quantity	$\psi^\pi/\boldsymbol{\psi}^\pi$	$\mathbf{i}^\pi$	g^π	f^π	$G^{\pi\pi}$	$G^{\pi\pi\prime}$
Mass	1	0	0	0	$r^{\pi\pi}$	0
Momentum	$\mathbf{v}^\pi$	$\boldsymbol{\sigma}^\pi$	$\mathbf{g}^\pi$	0	$r^{\pi\pi}\boldsymbol{\psi}^\pi + \mathbf{t}^{\pi\pi}$	0
Energy	$u^\pi + \frac{1}{2}\mathbf{v}^\pi \cdot \mathbf{v}^\pi$	$\boldsymbol{\sigma}^\pi \cdot \mathbf{v}^\pi + \mathbf{q}^\pi$	$\mathbf{g}^\pi \cdot \mathbf{v}^\pi + \bar{h}^\pi$	0	$r^{\pi\pi}\psi^\pi + \mathbf{t}^{\pi\pi} \cdot \mathbf{v}^\pi + q^{\pi\pi}$	0
Entropy	s^π	$\boldsymbol{\phi}^\pi$	$\bar{b}^\pi$	Γ^π	$r^{\pi\pi}\psi^\pi + \phi^{\pi\pi}$	0

Table 2.7: Description of the physical mean macroscopic balance equation variables.

Symbol	Description	Units
$r^{\pi\pi}$	mean macroscopic supply/net production of mass related to phase interaction	s^{-1}
$\boldsymbol{\sigma}^\pi$	mean macroscopic partial stress tensor of π	N/m^2
$\mathbf{g}^\pi$	mean macroscopic external body force/supply of momentum to π	m/s^2
$\mathbf{t}^{\pi\pi}$	mean macroscopic supply of momentum to π due to phase interaction	m/s^2
u^π	mean macroscopic specific internal energy of π	J/kg
$\mathbf{q}^\pi$	mean macroscopic surface flux vector of heat of π	J/m^2 s
$\hat{h}^\pi$	mean macroscopic external supply of energy to π	J/kg s
$q^{\pi\pi}$	mean macroscopic supply of energy to π due to phase interaction	J/kg s
s^π	mean macroscopic specific entropy of π	J/kg K
$\boldsymbol{\phi}^\pi$	mean macroscopic surface flux vector of entropy of π	J/K m^2 s
$\bar{b}^\pi$	mean macroscopic external supply of entropy to π	J/kg s K
$\phi^{\pi\pi}$	mean macroscopic supply of entropy to π due to phase interaction	J/kg s K
Γ^π	mean macroscopic internal supply of entropy to π	J/kg s K

Equations (2.18) present the fundamentals for continuum modelling of macroscopic multi-phase-component porous media from which specific (coupled) applications can be built.

2.6 Equations of state and constitutive relations

To build appropriate physics applications (models) the generic balance laws are accompanied by constitutive relationships in order that they facilitate workable parametrisation and produce practical results. Essentially, constitution defines the specific materials being considered. This section explores those relationships which are particular to multiphase flow in porous media with specific reference to GCS where appropriate. An extensive review is made in this context such that a thorough account of the fundamental phenomena involved is given with respect to current state-of-the-art.

This thesis is application based and only that which is considered appropriate for now is taken forward for modelling, as is discussed. This will however provide insight into the limitations of any models developed and allow for a greater variety of potential geo-applications as well as for the benchmarking of future work encompassing the more sophisticated constitutive theories.

2.6.1 Helmholtz free energy

The first and second laws of thermodynamics combine to state that the change in internal energy U (microscopic potential and kinetic energies), for an amount of substance which undergoes a change in volume V and a change in entropy S at temperature T and pressure p, is given by the energy balance

$$\mathrm{d}U = -p\,\mathrm{d}V + T\,\mathrm{dS}, \tag{2.19}$$

which is a sum of the infinitesimal supply of mechanical work W and heat Q. By introducing the Helmholtz free energy $A = U - T\mathrm{S}$, which is the maximum energy available to produce work in a thermodynamic system at a constant temperature, into (2.19), with an additional term to account for the free energy supply due to a change in the number moles $\bar{N}$ of component κ with the molar chemical potential $\bar{\mu}_\kappa$, gives,

$$\mathrm{d}A = -p\,\mathrm{d}V - \mathrm{S}\,\mathrm{d}T + \sum_{\kappa} \hat{\mu}_\kappa\,\mathrm{d}\hat{N}_\kappa. \tag{2.20}$$

Assuming the system to be closed and isothermal, that is ignoring the last two terms in (2.20), it is seen that the infinitesimal mechanical work is stored as free energy without its deterioration or increase from the other terms.

Of importance, Coussy [47, 48] extends the general balance of free energy (2.20) for a thermo-poroelastic solid phase only, with no molecular supply[2],

$$\mathrm{d}\bar{\mathrm{a}}^{\mathrm{s}} = \sum_{\mathrm{f}} p^{\mathrm{f}}\,\mathrm{d}\phi^{\mathrm{f}} + (\sigma\,\mathrm{d}\epsilon + s_{ij}\,\mathrm{d}e_{ij}) - \bar{\mathrm{s}}^{\mathrm{s}}\,\mathrm{d}T, \tag{2.21}$$

---

[2] The porosity n is Eulerian and may be related to a Lagrangian porosity ϕ with the relationship, $\phi\,\mathrm{d}v_0 = n\,\mathrm{d}v$, where $\mathrm{d}v_0$ is the initial volume [48].

where $\bar{\mathrm{a}}^{\mathrm{s}}$ and $\bar{\mathrm{s}}^{\mathrm{s}}$ are the Helmholtz free energy and the entropy of the porous solid per unit initial volume, $\mathrm{d}v_0$. The first three terms on the r.h.s. sum to represent the infinitesimal strain work per unit initial volume of the solid, where σ is mean/hydrostatic stress, ϵ is volumetric dilation/strain, s_{ij} are deviatoric stress tensor components, and e_{ij} are deviatoric strain tensor components. The first term on the r.h.s is the infinitesimal energy contributions from the occupying immiscible fluid phases f, and may be expressed equivalently for the two fluid phase system, $\mathrm{f} = \mathrm{w}, \mathrm{n}$, given the saturation relationship $\phi^{\mathrm{f}} = S_{\mathrm{f}}\phi$, as

$$\sum_{\mathrm{f}} p^{\mathrm{f}}\,\mathrm{d}\phi^{\mathrm{f}} = (S_{\mathrm{w}}p^{\mathrm{w}} + S_{\mathrm{n}}p^{\mathrm{n}})\,\mathrm{d}\phi - \phi(p^{\mathrm{n}} - p^{\mathrm{w}})\,\mathrm{d}S_{\mathrm{w}} = p\,\mathrm{d}\phi - \phi p^{\mathrm{c}}\,\mathrm{d}S_{\mathrm{w}}, \tag{2.22}$$

which identifies p defined as the macroscopic averaged fluid pressure and p^{c} defined as the macroscopic capillary pressure which is exerted on the fluid-fluid interface. Practical interpretations of (2.22) and its terms are given in Section 2.7.

2.6.2 Entropy inequality

One particular aspect on deriving constitutive relationships is the exploitation of the so called entropy inequality (Clausius-Duhem inequality) [45, 120]. Derived in part from (2.13 & 2.18) it gives a scientific and consistent thermodynamic description of macroscopic material behaviour. As well as observing the balance laws, the inequality ensures that the second law of thermodynamics is not violated, in that for an irreversible process net entropy production/increase Γ is greater than zero (zero net entropy production/increase signifying a reversible process), $\sum_{\pi} \rho^{\pi}\Gamma^{\pi} \geq 0$ at all material points at all times. Elaborate analyses based on the systematic consequences of this thermodynamic postulate have been carried out, including those in [85, 120], from which the extent of validity has been assessed for notable relationships such as Darcy's law, Fick's law and the effective stress principle, by its provision of more general theorems on the phenomena thereof.

2.6.3 Porous media stress partition

Material stresses regulate constitutive behaviour and strength so it is essential to have them well defined. For porous multi-phase-component continua the key concept is to decompose the total stress into partial stresses carried by the solid and fluids. By exploring the entropy inequality of the bulk system with volume averaging the following macroscopic relationships are given, all forms of which presented here are simplified from their general form by ignoring the stress contribution due to the relative motion of all components κ within the fluid phases ($\mathrm{f} = \mathrm{w}, \mathrm{n}$). Also, no fluid-solid dissipation is accounted for here; the dissipative part of the fluid-solid momentum exchange due to local effects is treated in Section 2.6.6 and discussed in more detail in [120].

Solid stresses are defined as tension-positive and fluid pressures as compression-positive. The partial stress tensors of the fluid phases (force on the fluid phase per unit area of bulk medium) are given by,

$$\eta^{\mathrm{w}}\boldsymbol{\sigma}^{\mathrm{w}} = -\,\eta^{\mathrm{w}}p^{\mathrm{w}}\boldsymbol{I} \quad \text{and} \quad \eta^{\mathrm{n}}\boldsymbol{\sigma}^{\mathrm{n}} = -\,\eta^{\mathrm{n}}p^{\mathrm{n}}\boldsymbol{I} \tag{2.23}$$

where p^{f} are the thermodynamic (macroscopic) pressures, and $\boldsymbol{I}$ is a unit tensor. Shear stresses in the fluids are therefore negligible. However, for the solid phase the expression reads,

$$\eta^{\mathrm{s}}\boldsymbol{\sigma}^{\mathrm{s}} = \eta^{\mathrm{s}}(\boldsymbol{\sigma}^{\mathrm{s}} + p^{\mathrm{s}}\boldsymbol{I}) - \eta^{\mathrm{s}}p^{\mathrm{s}}\boldsymbol{I} = \boldsymbol{\sigma}' - \eta^{\mathrm{s}}p^{\mathrm{s}}\boldsymbol{I} \tag{2.24}$$

where p^{s} is the solid phase pressure and $\boldsymbol{\sigma}'$ is the effective stress tensor, responsible for deformation of the solid grain skeleton, assuming for now that the pressure on the matrix grains does not cause them to deform, i.e. the effective stress here is a function of the grain structure rearrangement.

At thermodynamic equilibrium, ignoring the contribution of the fluid interface energies, the solid pressure is equal to the averaged fluid pressures as of (2.22),

$$p^{\mathrm{s}}_{\mathrm{ave}} = S_{\mathrm{w}}p^{\mathrm{w}} + S_{\mathrm{n}}p^{\mathrm{n}}. \tag{2.25}$$

The contribution however of the thermodynamic properties of the interfaces between the phases may be taken into account directly but its implementation is impractical due to the complexity of formulation [86, 131]. Alternatively, interface properties may be accounted indirectly with a macroscopic poromechanical approach.

In Section 2.7 the experimental capillary pressure-saturation curve and the interface energy $\mathcal{U}(S_{\mathrm{w}}, T) = \int_{S_{\mathrm{w}}}^{1} p^{c}(S_{\mathrm{w}}, T)\, \mathrm{d}S_{\mathrm{w}}$ are introduced after considering (2.21) and (2.22) further. Therein, this interface energy can be identified as the area under the capillary pressure-saturation curve. In [47], (2.25) is modified accordingly, leading to

$$p^{\mathrm{s}}_{\mathrm{eqv}} = S_{\mathrm{w}}p^{\mathrm{w}} + S_{\mathrm{n}}p^{\mathrm{n}} - \mathcal{U}, \tag{2.26}$$

which accounts for the additional tensile attributions of the surface stresses along the interfaces, $\mathcal{U}$ being the macroscopic interface contribution to the solid pressure. The *averaged fluid pressure* (2.25) is often employed as a convenient overall pore pressure instead of the *equivalent pore pressure* (2.26) [47, 120] (equivalent because it acts the same as the pore pressure as of a fully saturated scenario). This is acceptable if the fluid phases generally occupy separated pores such that the phase contact is negligible, but evidence shows that this is not the case for clay or cement-based materials in particular [47], where suction can cause shrinkage with significant contribution from $\mathcal{U}$.

For modelling GCS scenarios in particular, this aspect warrants further study in terms of its applicability. In this work a total stress is given by a summation of all the partial stresses of (2.23) and (2.24) while assuming (2.25),

$$\boldsymbol{\sigma} = \boldsymbol{\sigma}' - \boldsymbol{I}p^{\mathrm{s}} = \boldsymbol{\sigma}' - \boldsymbol{I}(S_{\mathrm{w}}p^{\mathrm{w}} + S_{\mathrm{n}}p^{\mathrm{n}}). \tag{2.27}$$

This is also Bishop's extended form of Terzaqhi's effective stress principle for incompressible grains. This assumption holds typically for soils as the matrix grains are relatively incompressible compared to the grain skeleton; this is however not the case for concrete and rock materials. In order to account for the effective stress $\boldsymbol{\sigma}''$ responsible for all deformation of the solid, both grain and skeleton, Biot's coefficient b, is introduced,

$$b = 1 - \frac{K_\mathrm{T}}{K_\mathrm{s}}, \tag{2.28}$$

which relates the bulk modulus (Section 2.6.10) of the solid macroscopic grain skeleton K_s to the bulk modulus of the matrix grain solids K_s. Note that $K_\mathrm{T} = E/3(1-2\nu)$, assuming the material to be elastic and isotropic, where E and ν are the usual experimental Young's modulus and Poisson's ratio respectively (Section 2.6.4). Thorough physical and thermodynamic understandings of this term are given in [27, 47, 48] and it is introduced in various interesting contexts in [120]. Here the final form is presented,

$$\boldsymbol{\sigma} = \boldsymbol{\sigma}'' - b\,\boldsymbol{I}p^\mathrm{s} = \boldsymbol{\sigma}'' - b\,\boldsymbol{I}(S_\mathrm{w}p^\mathrm{w} + S_\mathrm{n}p^\mathrm{n}). \tag{2.29}$$

If a comparably incompressible grain material is considered, $1/K_\mathrm{s} = 0$ and $b = 1$, meaning that only rearrangement of the grains/compression of the voids/pores takes place (skeleton compressibility), (2.29) reduces to the special case of (2.27).

Considering (2.29) in one dimension, for an incompressible grain porous medium, under constant total stress conditions, a change in pore pressure causes an equal and opposite change in effective stress ($b = 1$). That is, the pore space volume expands or contracts due to the pore pressure changes, given the compressibility of the solid skeleton, while the grains remain undeformed. Similarly, if the fluid is at constant pressure during deformation of the porous medium due to changes in total stress, the fluid volume change entering or leaving the pore space is equal to the total volume change. Alternatively, if the grains are compressible, these simplified effects are inhibited. The coefficient b is essentially the ratio of pore to bulk compressibility, and thus represents the ratio of fluid volume change to total volume change during deformation at constant fluid pressure. Intuitively, introducing the coefficient ($0 \leq b < 1$) in (2.29) thereby accounts for the inhibited pore compression where the skeleton is relatively rigid or where the skeleton and grain compressibilities are comparable.

2.6.4 Effective stress and strain/deformation

Key behaviour of a GCS system is determined by the rate at which it can accommodate the fluid injection which induces various coupled phenomena, responding particularly in pressure build-up, temperature change, and system deformation/fracturing (causing measured surface uplift [29]). Various constitutive laws of deformation due to effective stress are given in the general form,

$$\mathrm{d}\boldsymbol{\sigma}'' = \mathbf{D}_\mathrm{T}(\boldsymbol{\sigma}'', \boldsymbol{\varepsilon})\,\mathrm{d}\boldsymbol{\varepsilon}, \quad \mathrm{d}\boldsymbol{\varepsilon} = \boldsymbol{L}\mathrm{d}\mathbf{u}, \tag{2.30}$$

where $\mathbf{D}_\mathrm{T}$ is the tangential stress/strain matrix, which is a challenge to accurately characterise for porous/geologic materials, $\boldsymbol{\varepsilon}$ is the overall strain tensor of the required components, $\boldsymbol{L}$ is the appropriate differential operator, and $\mathbf{u}$ are the material displacements.

The simplest stress-strain constitutive relation is for a linear elastic isotropic material, where the stress/strain matrix is constant ($\mathbf{D}_\mathrm{el}$) and the stress/strain relationship linear. Equation

(2.30) is presented explicitly for such a material domain of axisymmetry (say about a wellbore); note that the stress and strain tensors are written in vector form for ease of computation, and that the hoop strain $\varepsilon_z = 2\pi \mathrm{u}_x / 2\pi x = \mathrm{u}_x / x$,

$$\begin{Bmatrix} \sigma_x \\ \sigma_y \\ \sigma_z \\ \sigma_{xy} \end{Bmatrix} = \frac{E}{(1+\nu)(1-2\nu)} \begin{bmatrix} 1-\nu & \nu & \nu & 0 \\ \nu & 1-\nu & \nu & 0 \\ \nu & \nu & 1-\nu & 0 \\ 0 & 0 & 0 & (1-2\nu)/2 \end{bmatrix} \begin{bmatrix} \partial/\partial x & 0 \\ 0 & \partial/\partial y \\ 1/x & 0 \\ \partial/\partial y & \partial/\partial x \end{bmatrix} \begin{Bmatrix} \mathrm{u}_x \\ \mathrm{u}_y \end{Bmatrix} \tag{2.31}$$

where the terms in the stress and strain vectors represent the radial, vertical (axial), hoop (circumferential) and shear components, as depicted in Figure 2.4.

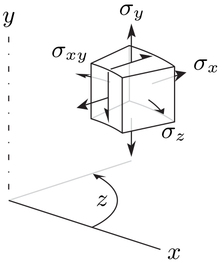

Figure 2.4: Axisymmetric elementary volume depicting radial, vertical, hoop, and shear stress components.

Linear elastic models are generally adequate for quasi-brittle materials under moderate loading and demonstrate suitable results for geo-materials undergoing a single moderate load path [120]. For more complicated material behaviour, particularly, variable elasticity, where the strains are still recoverable, and elasto- and viscoplasticity where strains are not recoverable, $\mathbf{D}_{\mathrm{T}}$ becomes dependent on the stress/strain history, and iterative methods are required[3].

2.6.5 Fick's law

Further to (2.17) the constitutive assumption for the diffusive-dispersive mass flux is that of Fick's law, which is a function of the gradient of the mass fraction,

$$\mathbf{J}^{\pi,\kappa} = -\rho^{\pi} \boldsymbol{D}^{\pi,\kappa} \nabla \left(\frac{\rho^{\pi,\kappa}}{\rho^{\pi}} \right). \tag{2.32}$$

The empirical effective dispersion tensor $\boldsymbol{D}^{\pi,\kappa}$ of κ in π, is also a function of the tortuosity of the porous pathways. This relationship is generalised in [83] via extensive consideration and linearisation of the system, where it is revealed that transport of a component or the phase as a whole is induced by pressure gradient/gravity force, density/concentration gradient, external force field (ionic system in a magnetic field), and temperature gradient. The classic

---

[3] Material failure or damage is modelled by incorporating a damage term, e.g. for isotropic damage, $\boldsymbol{\sigma}'' = (1-\omega)\mathbf{D}^{\mathrm{el}}\boldsymbol{\varepsilon}$. The damage ω, varies from 0 to 1, i.e. undamaged to fully damaged (no material coherence). The evolution of which is determined by some loading function $f(\varepsilon_{\mathrm{eq}}, \varkappa_{\mathrm{i}})$ where $\varepsilon_{\mathrm{eq}}$ is an equivalent strain (e.g. principal or modified von Mises) and $\varkappa_{\mathrm{i}}$ is a threshold material parameter for initialising damage. Other parameters may also be introduced to account for softening or hardening of the material. In [12], this is discussed further with various examples in the context of adaptive spatial discretisation (meshing) methods.

form presented here is recovered by ignoring all but the density/concentration gradient term, assuming it to be the most significant for most scenarios; this is explored and applied in more detail in [83, 120].

2.6.6 Darcy's law

Darcy flux is the discharge per unit area over a porous medium and is therefore a volume-averaged relative velocity, determined by experimental work. This is equated with the actual fluid pore velocity relative to the solid $\mathbf{v}^{\mathrm{fs}}$ via $\eta^{\mathrm{f}}\mathbf{v}^{\mathrm{fs}}$, which gives the typical extended multi-phase relationship for Darcy flux,

$$\eta^{\mathrm{f}}\mathbf{v}^{\mathrm{fs}} = \frac{k_{\mathrm{rf}}\mathbf{k}}{\mu^{\mathrm{f}}}\left[-\nabla p^{\mathrm{f}} + \rho^{\mathrm{f}}\left(\mathbf{g} - \mathbf{a}^{\mathrm{s}} - \mathbf{a}^{\mathrm{fs}}\right)\right]. \tag{2.33}$$

where $\mathbf{k}$ is the empirical intrinsic permeability tensor of the porous medium, which may also be considered as a function of porosity. Specific fluid properties are accounted for by the dynamic viscosity μ^{f} and relative permeability k_{rf}, which are discussed in Sections 2.6.9.1 and 2.7.2 respectively. Darcy's law is similarly generalised in [83, 82, 120], via the linearisation of the fluid macroscopic momentum balance, where force, density gradient, and temperature gradient terms, and coupling with the general form of (2.32) are also introduced, which warrant gauging for given modelling scenarios. Particularly, it is shown that the dissipative part of the fluid-solid and fluid-fluid momentum exchanges due to local effects is accounted for macroscopically via the viscosity, permeability and relative permeability terms, which are dependent on the fluid saturations. The movement of the fluid, as of (2.33), is governed by pressure gradient alone, and gradients due to any accelerations other than gravity are generally assumed negligible and may be further omitted. Darcy's law is therefore valid as a first assumption for the slow flow of a macroscopically inviscid fluid. It may also be arrived at without the inertial terms via reduction of Navier-Stokes equation by assuming slow incompressible flow (low Reynolds number, $\mathrm{Re} \ll 1$, $\mathrm{Re} = \rho^{\mathrm{f}}\mathrm{v}^{\mathrm{f}}l_c/\mu^{\mathrm{f}}$, ratio of inertial to viscous forces).

If velocities are however high enough the inertial effects start to have significance, the inclusion of an inertial term representative of the kinetic energy of the fluid gives the Forchheimer form,

$$\nabla p^{\mathrm{f}} = -\frac{\mu^{\mathrm{f}}}{\mathbf{k}k_{\mathrm{rf}}}\boldsymbol{q}^{\mathrm{f}} - \hat{b}\hat{b}_{\mathrm{rf}}\rho^{\mathrm{f}}\boldsymbol{q}^{\mathrm{f}}|\boldsymbol{q}^{\mathrm{f}}| \tag{2.34}$$

where $\boldsymbol{q}^{\mathrm{f}}$ is the Darcy fluid flux, and $\hat{b}$ and $\hat{b}_{\mathrm{rf}}$ are the Forchheimer and relative Forchheimer parameters, giving essentially the inertial permeability of the system, which are determined experimentally.

2.6.7 Fourier's law

Conduction is the process by which heat flows due to microscopic interactions of energetically moving/vibrating particles with those less energetic within a temperature gradient. That is, heat flows from a hotter to a colder region of substance without any net movement of the substance. This occurs until thermal equilibrium is met, unless the system is externally driven. Other forms of heat transfer are convection (due to net movements of the substance) and radiation.

The constitutive assumption for the flux of heat (supply of energy) and the temperature gradient is given by a generalised form of Fourier's law,

$$\mathbf{q}^{\pi} = -\boldsymbol{\chi}_{\text{eff}} \nabla T \tag{2.35}$$

where $\boldsymbol{\chi}_{\text{eff}}$ is an effective thermal conductivity tensor, which is introduced for the fluids in a thermodynamic context in Section 2.6.9.2, additional methods for its prediction are also given in [120].

Noteworthy, interesting relationships in this context are given in the literature for the design of various efficient (porous) building fabrics. Additionally, current additive manufacturing research is also in pursuit of more representative thermal models which will give improved automated control so that the build better matches the desired material properties and geometry. This is particularly with respect to where the formed build and surrounding sintered powder exhibit varying degrees of porosity which significantly affect the manufacturing and build performance.

2.6.8 Fluid thermodynamic properties

The thermodynamic properties of a fluid in the subsurface are dependent on the pressures and temperatures present. Cubic equations of state (EoS) for real fluids, notably, van der Waals, Redlich-Kwong and Peng-Robinson (of successive improvement), offer relatively simple and accurate relationships for volume, pressure and temperature for a variety fluids. They represent real fluids by incorporating terms which account, at the macroscopic, level for intermolecular interactions operating at the microscopic level. If such behaviour is negligible as for when the molecular sizes are small with respect to the mean distances between them, ideal gas behaviour may be assumed [48].

More modern multiparameter equations of state can represent certain pure fluids and fluid mixtures with high degrees of accuracy over the range of their states. These are typically formulated in fundamental form explicit in terms of Helmholtz free energy, as a function of density and temperature,

$$\frac{a(\rho, T)}{RT} = \frac{a^o(\rho, T) + a^r(\rho, T)}{RT} = \alpha(\delta, \tau) = \alpha^o(\delta, \tau) + \phi^r(\delta, \tau) \tag{2.36}$$

where a is the specific Helmholtz energy, R is the specific gas constant, $\delta = \rho/\rho_c$ is reduced density, and $\tau = T/T_c$ is reduced temperature. Subscripts c typically denote the fluids critical point, α therefore being a reduced (nondimensionalized) form of the Helmholtz energy. The equation is distinguished into a hypothetical ideal gas part, a^o and a residual behaviour part, a^r. By defining all the thermodynamic properties, in relation to α and its partial derivatives with respect to δ and τ, they may be determined algorithmically via weighting experimental data, multi-property interpolation, and optimisation of the function form [20, 182]. For this purpose, lists of the common thermodynamic properties are given in [182], in which the fundamental function form is used to derive EoS for important fluids and fluid mixtures. In [111] comprehensive comparisons between the mentioned EoS are made along with their validity in the context of geo-applications.

Clearly, where appropriate and/or in view of avoiding computational expense, EoS simplifications can be made from which many practical methods may be developed. To begin, the most robust case of EoS is used for accurate illustration of the following material properties, from which it may also be assessed to what extent such simplifications can be made with respect to modelling a GCS scenario.

In the following subsections, several thermodynamic properties of interest for CO_2 and Brine, namely, pressure, temperature, density (specific volume), composition and heat capacity are assessed within the potential ranges of environmental conditions of interest (Section 1.3.1).

2.6.8.1 Density: CO_2-brine mixture p-v-T-x relationship

Considering the pressure, volume, temperature and composition in mole fraction (p-v-T-x) of CO_2-brine mixtures within the ranges of interest, that is at relatively low temperatures ranging to approximately 100 °C with relatively high pressures reaching several hundred atmospheres, two distinct mutually soluble fluid phases coincide (a biphasic system). At equilibrium, the following temperature and pressure dependent reactions and equilibrium constants K_f, may be given,

$$\mathrm{CO}_{2(\mathrm{aq})} \rightleftharpoons \mathrm{CO}_{2(\mathrm{gl})}, \qquad \bar{K}_{\mathrm{CO}_2} = \bar{f}_{\mathrm{CO}_{2(\mathrm{gl})}}/\bar{a}_{\mathrm{CO}_{2(\mathrm{aq})}}, \tag{2.37}$$

$$\mathrm{H}_2\mathrm{O}_{(\mathrm{l})} \rightleftharpoons \mathrm{H}_2\mathrm{O}_{(\mathrm{g})}, \qquad \bar{K}_{\mathrm{H}_2\mathrm{O}} = \bar{f}_{\mathrm{H}_2\mathrm{O}_{(\mathrm{g})}}/\bar{a}_{\mathrm{H}_2\mathrm{O}_{(\mathrm{l})}}, \tag{2.38}$$

where $\bar{f}$ are the fugacities (effective pressures) and $\bar{a}$ are the activities (effective concentrations) of the components from which their mole fractions can be ascertained [184].

The biphasic system is typically that of a CO_2-rich supercritical phase and a H_2O-rich liquid phase, noting that pure CO_2 is supercritical beyond its critical point [181] (Figure 2.5(a)):

$T_c = 304.1282 \pm 0.015$ K (31.0 °C),
$p_c = 7.3773 \pm 0.0030$ MPa (72.8 atm),
$\rho_c = 467.6 \pm 0.6$ kg/m^3.

Although there is a degree of mutual solubility (partial miscibility), CO_2-Brine displacement is still essentially an immiscible process (primary drainage process) with phase interface tension (Section 2.7) if the fluids are mutually saturated, as is further discussed in [24]. The problem is therefore often simplified by treating the rich saturated fluids as immiscible by ignoring any diffusive and/or reactive behaviour of the species involved, in particular the dissolution of CO_2 and evaporation of H_2O.

The role of partial miscibility is however important. Notably, it has been shown to reduce near-wellbore pressures, which are of primary interest, after intermediate periods of injection. This is due to the otherwise hypothetically trapped residual brine of lower compressibility evaporating whilst also giving up more permeable pathways for the more compressible CO_2-rich phase. Hence, the assumption of immiscibility keeps the brine at a minimum residual saturation which overemphasises pressure build-up, as is quantified in [126]. This miscibility effect also leads to a slightly reduced CO_2-rich phase displacement as it is able to occupy more of the near-wellbore pore space than if immiscibility is assumed. Theory highlighting the lag between the initial front of the CO_2 and a following drying-front is given in [138].

In terms of the dissolution of the CO_2 in the H_2O-rich phase, particularly, there will be a dispersive-front of dissolved CO_2 ahead of the CO_2 shock-front. A role of this effect is that it is considered as a medium to long term trapping/storage mechanism (Section 1.3.1), the tracking of which enables a better account of the mass of CO_2 placed within the system, an interesting study on this is given by [136].

In view of GCS, detailed solubility models based on standard chemical engineering and aqueous geochemistry approaches for determining mutual solubilities involving Henry's law and/or other fundamental equilibrium constants (2.37 & 2.38), are discussed thoroughly and developed in [184]. This work is also extended in [183] to account for the brine salinity s_{sal}, to which the solubility of the phases is also a function, $x(p, T, s_{\text{sal}})$. Plots are also given therein documenting CO_2 mole fractions in H_2O in the order of 0.025, compared to H_2O in vapour phase of 0.005 at typical GCS pressures and temperatures. The miscible molecular diffusive movement thereafter is typically governed by Fick's law (Section 2.6.5) with appropriate diffusion coefficients, and is likely to be a crucial factor when considering long-term storage.

Below 100 °C the H_2O mole fraction in the CO_2-rich phase is small such that its properties can be well represented by those of pure CO_2 [184]. This simplification to the mixing rules also has the benefit of reducing what would be an iterative mutual solubility EoS module to a non-iterative one.

The p-v-T properties of pure CO_2 are plotted for demonstration in Figure 2.5(a) using a fundamental form (Helmholtz-energy) for its precision and superior range of validity [20, 111, 181, 182]. This is appropriate given that phase changes are near present within the ranges of interest for the CO_2 phase as is indicated by the sharp changes in the fluid properties over the lower pressures and temperatures in Figure 2.5(a). This is computed via

$$p(T,\rho) = -\left(\frac{\partial a}{\partial v}\right)_T \qquad \longrightarrow \qquad \frac{p(\delta,\tau)}{\rho R T} = 1 + \left(\delta \frac{\partial \alpha^r}{\partial \delta}\right)_\tau = Z. \tag{2.39}$$

The thermodynamic definition of the property pressure $p(T, \rho)$, is given with its relation to the reduced terms for fitting, where v is the specific volume and Z is the compressibility factor. Note the near ideal gas behaviour in Figure 2.5(a) around atmospheric pressures and in (2.39) when diminishing the residual term. The residual terms in such expressions are themselves the summation of many families of analytically differentiable terms, $\alpha^r = \sum_k \alpha_k^r$ [20].

The p-v-T-x behaviour of the H_2O-rich phase is plotted for comparison in Figure 2.5(b), again this is simplified by ignoring the effects of any miscible component from the opposite phase. These effects are however more significant in this phase and are considered in detail in [183, 184]. The effect of salinity, % of dissolved NaCl in solution, is however illustrated here, where more salinity indicates higher densities for the same pressures and temperatures. The fundamental form was used for the pure 0% case for best representation, for the 10% and 20% cases the experimental interpolation formulae of [161] are used, as derived from experimental data within 0–175 °C, 0.1–34 MPa, 0–25% salinity.

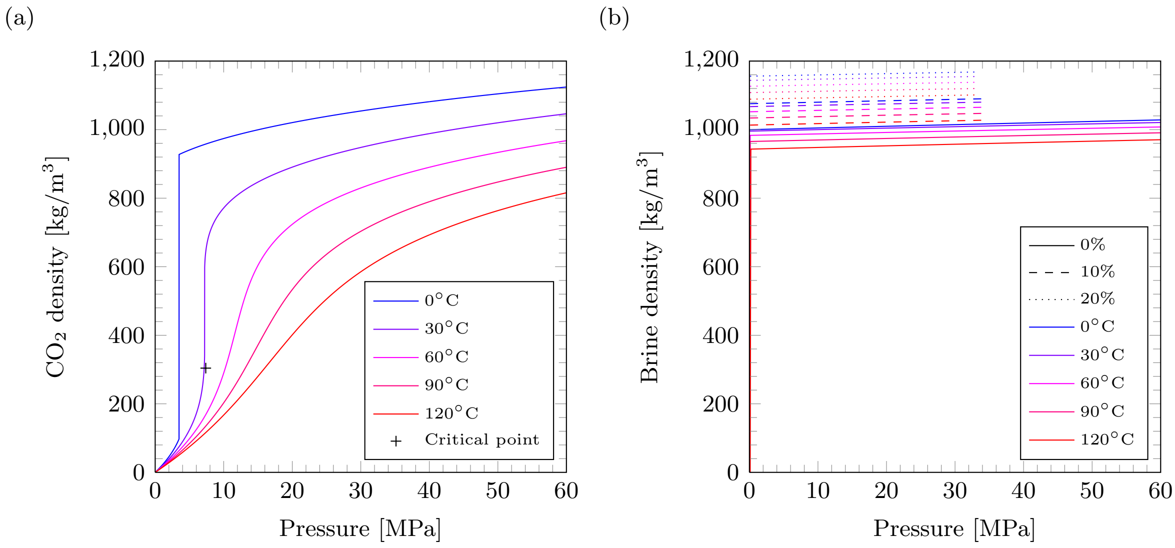

Figure 2.5: (a) CO$_2$ p-v-T relationships over applicable ranges with the critical point highlighted at $T_c = 304.1282 \pm 0.015$ K (31.0 °C), $p_c = 7.3773 \pm 0.0030$ MPa (72.8 atm), $\rho_c = 467.6 \pm 0.6$ kg/m^3 [181]. The plots are derived via Helmholtz function form. (b) Brine p-v-T-x relationships over practical ranges with mass fractions of salinity given at specified intervals: 0% is plotted via Helmholtz function form, 10% and 20% are plotted via extrapolation.

In practice, simpler and potentially more efficient cubic and/or experimentally extrapolated EoS/formulae, which account for the mixing in a more straightforward and well practised manner, are usually adopted. The usual constants for these EoS characterising intermolecular repulsion and attraction are adapted for the mixed phases using mixing rules [153]. The relationships as of Figure 2.5 may therefore be further adapted to account for the miscibility of the phases, however this may become computational excessive if a full compositional formulation is sought. If the scenario for modelling is well considered, the miscible fluid EoS may be simplified for engineering purposes. One example is by assuming miscible pseudo-phases as with the simplified black-oil formulation (widely used in reservoir engineering), a GCS methodology for which is achieved in reference [87].

Another area of investigation in this context is on the matter of impurities or co-contaminants in the injected CO$_2$ phase, particularly SO$_2$, H$_2$S, CH$_4$ and N$_2$ admixtures retained from the point source flue-gases. An EoS model in view of this is developed in [206]. A spectrum of possibilities arises as this will impact thermodynamic and transport properties within the system, for instance, initial analysis shows that the amount of dissolved CO$_2$ is sensitive to the presence of CH$_4$. This aspect is also a legislative issue, a concern at the front end of the carbon capture and storage (CCS) chain, and a particularly open area warranting further study.

2.6.8.2 Heat capacity

The supply of energy (heat) required to produce a unit temperature rise in a body is defined as the heat capacity. It is dependent on temperature and pressure, however this is generally slight over moderate changes, except at low temperatures. Both isobaric and isochoric heat capacities are fundamentally defined,

$$C_p(T,p) = \left(\frac{\partial Q}{\partial T}\right)_p = \left(\frac{\partial H}{\partial T}\right)_p \qquad C_V(T,\rho) = \left(\frac{\partial Q}{\partial T}\right)_V = \left(\frac{\partial U}{\partial T}\right)_V \tag{2.40}$$

where H is the enthalpy (total energy content of system). These relationships can be derived noting $H = U + pV$ and observing the relationships of (2.19 & 2.20).

An effective macroscopic heat capacity may be given for a multiphase medium [120], in terms of the specific isobaric heat capacities c_p^{π}, for the present phases, with reference to Table 2.1,

$$(\rho c_p)_{\text{eff}} = (1-n)\rho_{\text{s}} c_p^{\text{s}} + nS_{\text{w}}\rho^{\text{w}} c_p^{\text{w}} + nS_{\text{n}}\rho^{\text{n}} c_p^{\text{n}}. \tag{2.41}$$

Heat capacity is also fundamentally defined in Helmholtz energy explicit form for correlation [182]. Variability of the heat capacities for CO_2 and brine as a function of pressure and temperature are illustrated in [111].

Note that the temperature front due to the subsurface injection of CO_2 is behind the advection front due to a retardation caused by the specific heat capacities of the in situ brine and rock [125].

2.6.8.3 Joule-Thomson coefficient and cooling

The Joule-Thomson coefficient is described fundamentally as,

$$\mu_{\text{JT}} = \left(\frac{\partial T}{\partial p}\right)_H, \tag{2.42}$$

arising from the Joule-Thomson thermodynamic process which occurs along an insulated constant/conserved enthalpy (isenthalpic) curve in the p-T plane, that is, a steady adiabatic process with no exchange of heat with the surrounding environment. Along this curve an inversion point occurs, where $\mu_{\text{JT}} = 0$, due to a change in the dominant molecular interaction behaviour, which all real gases have, μ_{JT} being always zero for an ideal gas. If the fluid is below the maximum inversion temperature such that $\mu_{\text{JT}} > 0$, then a reduction in pressure coincides with a reduction in temperature, from (2.42).

This expansive cooling (known as throttling) is central to many thermal machines (refrigerators, air conditioners, etc.) and is achieved by an insulated value or porous plug which causes the fluid to pass from a high to lower pressure region and thus expand.

The process is a particular concern for GCS. Shallow reservoirs and particularly depleted oil and gas reservoirs de-pressurised during exploitation are characterised by low pore pressures. Injecting into a low pressured formations with high pressured CO_2 will result in large pressure gradients, from which significant Joule-Thomson cooling (JTC) may occur. It is believed that the drop in pressure here would cause freezing of the pore fluids and form CO_2 hydrates both of which could cause significant loss of injectivity and reservoir performance. Cooling effects are unlikely to pose a problem for initially moderately warm and permeable reservoirs at low pressures ($T_0 > 40$°C , $k > 10^{-14}$ m^2, $p_0 > 2$ MPa) [125, 141].

The effects of JTC in the context of GCS are discussed further in [141], where the results of a coupled non-linear hydro-thermal model capturing the transient behaviour of the problem are assessed. Later [125, 129] produced good agreement with a simplified analytical assessment. This is achieved by assuming constant and uniform material properties (in particularly μ_{JT}, which is appropriate given that it is approximately constant for CO_2 at the relatively low pressures of interest), and steady-state behaviour, which are particularly conservative assumptions in that they overestimate the spatial pressure gradient and cooling. The behaviour of a single fluid phase is also assumed in the analytical assessment, which is appropriate given that the cooling front lags within the CO_2 phase behind the advection front. An objective of this thesis is therefore to account for this hydro-thermal behaviour during the model formulation and to extend on this work by additionally coupling mechanical deformation and a double-porosity network within the formulation for assessment.

2.6.9 Fluid transport properties

Viscosity, thermal conductivity and surface energy are introduced here. The state-of-the-art is less mature in predicting theses properties from the state variables, compared to the thermodynamic properties of Section 2.6.8.

2.6.9.1 Dynamic viscosity

Fluid passing through a porous medium is generally slow such that non-turbulent or laminar flow (low Reynolds number) is primarily considered. A proportionality exists for the shear stress between laminar planes and the change in velocity between the planes with respect to their distance apart, this is given by the dynamic (shear) viscosity, $\sigma_{zy} = \mu(\partial \mathrm{v}/\partial z)$. This property is therefore a measure of the fluid's resistance to deformation by internal shear in overcoming friction that is caused by intermolecular forces.

Dynamic viscosity is an important property when considering fluid flow through porous media (Section 2.1.1) and interface stability/mobility (Section 2.7.3) when multiple phases are present. Its variation for CO_2 and brine with respect to pressure and temperature is given in Figures 2.6(a) and 2.6(b). For CO_2, with its near present critical point, at lower pressures and temperatures sharp changes in viscosity are identified. Both phases demonstrate particular sensitivity to temperature, with brine additionally becoming more viscous with increased salinity. For pure CO_2 and H_2O the enhanced relationships discussed by [20] are used. For those of brine with varying salinity the relationships of [105, 106] are used, as were derived therein with experimental data within 20–150 °C, 0.1–30 MPa, and 0–25% salinity. Note also the difference of an order of magnitude between the two phases over the ranges of interest.

Correlation for the equations plotted takes the general form,

$$\mu = \mu^{o}(\tau) + \mu^{r}(\tau, \delta) + \mu^{c}(\tau, \delta), \tag{2.43}$$

where the three terms of summations capture, respectively, dependence on temperature at zero density limits, residual dependence on temperature and density, and any dependence enhance-

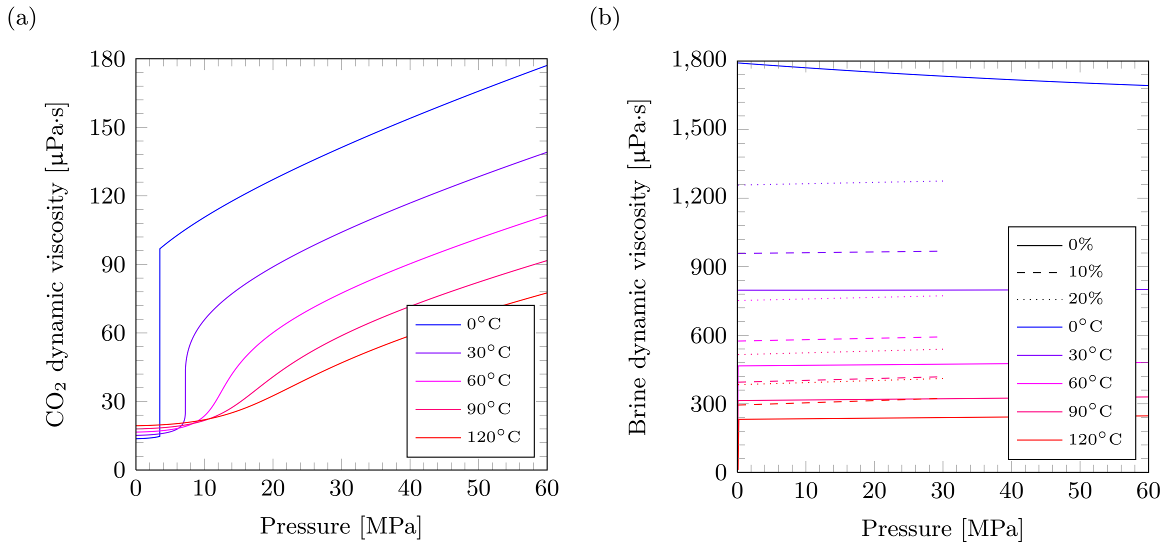

Figure 2.6: (a) CO$_2$ viscosity as a function of pressure and temperature. (b) Brine viscosity as a function of pressure, temperature and salinity with mass fractions of salinity given at specified intervals: 0% is plotted via [20], 10% and 20% are via [105, 106].

ment required over critical region temperatures and densities. Sufficient information for the last term is only available from a very limited set of fluids. Overviews are given in [111].

2.6.9.2 Thermal conductivity

The thermal conductivity of the phases are required in order to parametrise Fourier's law (2.35). Thermal conductivity is dependent on pressure and temperature, predictive correlations for fluids are also given in the three term form,

$$\chi = \chi^o(\tau) + \chi^r(\tau, \delta) + \chi^c(\tau, \delta) \tag{2.44}$$

where the three terms of summations capture, respectively, dependence on temperature at zero density limits, residual dependence on temperature and density, and any enhancement required over critical region temperatures and densities. The last term here is more significant than with viscosity and is non-negligible away from the critical points [20]. Illustrations of the variability of thermal conductivity are given in [111].

Note that formation waters have far higher thermal conductivities than CO$_2$, a property which also aids GCS monitoring via thermal perturbation sensing [72].

2.6.9.3 Surface tension and energy

The surface tension of a fluid is also a thermodynamic transport property, and is key to many natural phenomena including capillary in porous media (Section 2.7). Surface energy is a more general term as it also applies to solids. The subject of surface and interface energy due to the imbalance of intermolecular forces at a surface/interface is explored in the context of porous media in detail by [48], where interesting relationships are presented on the separation/fracturing energies for fluids and solids. An overview of the fundamental thermodynamic relations for correlation with respect to fluids is given in [20]. Note that the surface tension and surface energy density for a liquid are the same.

2.6.10 Compressibility & thermal expansion coefficients

For either solid or fluid, the compressibility coefficient c or its inverse bulk modulus K present a measure of a material's elasticity, relating relative volume change (volume strain) and pressure (or mean stress) change at constant temperature,

$$c = \frac{1}{K} = -\frac{1}{V}\left(\frac{\partial V}{\partial p}\right)_T = \frac{1}{\rho}\left(\frac{\partial \rho}{\partial p}\right)_T . \tag{2.45}$$

Similarly, the thermal expansion coefficient presents a useful relationship for the relative volumetric change (volume strain) and change in temperature at constant pressure,

$$\beta = \frac{1}{V}\left(\frac{\partial V}{\partial T}\right)_p = -\frac{1}{\rho}\left(\frac{\partial \rho}{\partial T}\right)_p . \tag{2.46}$$

As thermodynamic properties, these coefficients are dependent on pressure, temperature and composition. The partial differentials are therefore to be taken within reasonable ranges depending on the material's behaviour if these coefficients are to be adopted as constant material properties.

The isothermal compressibility (2.45) is the basis of all primary recovery mechanisms in hydrocarbon reservoirs [50]. This is seen by considering a reservoir initially overpressured with trapped hydrocarbons, where a fall in fluid pressure, Δp, due to drilling will cause the fluid to expand, ΔV, to the surface manifesting as hydrocarbon production. The assumption of isothermal behaviour in this context is also permissible given that the production process occurs slow enough such that heat taken by convection within the produced fluids and so forth is replaced by conduction from the surrounding formation, thus keeping the reservoir at a constant temperature.

2.6.10.1 Fluid density

By considering the conservation of mass in the form, $D(\rho V)/Dt = 0$, and given that $\rho(p, T)$, carrying out manipulation with the product rule and substituting (2.45) and (2.46) gives,

$$\frac{1}{\rho}\frac{D\rho}{Dt} = \frac{1}{K}\frac{Dp}{Dt} - \beta\frac{DT}{Dt}, \tag{2.47}$$

which presents a useful first-order expansion or linear approximation of the real equation of state for a given material at some reference point, Figures 2.5(a) and 2.5(b).

2.6.10.2 Solid density

For a porous solid, changes in volume of a unit mass are due to compression of the grains and/ or rearrangement of the grains. Again the conservation of mass in the from, $D(\rho V)/Dt = 0$, is considered, assuming the density of the solid phase to be a function of the solid pressure, temperature, and the first invariant of effective stress. Following a similar procedure as for (2.47), introducing the bulk modulus of the grains via the stress invariant, then applying (2.28), reference [120] produces the following solid density material derivative function for a porous solid with compressible skeleton and grains,

$$\frac{1}{\rho^{\mathrm{s}}}\frac{D^{\mathrm{s}}\rho^{\mathrm{s}}}{Dt} = \frac{1}{1-n}\left[(b-n)\frac{1}{K_{\mathrm{s}}}\frac{D^{\mathrm{s}}p^{\mathrm{s}}}{Dt} - \beta_{\mathrm{s}}(b-n)\frac{D^{\mathrm{s}}T}{Dt} - (1-b)\nabla\cdot\mathbf{v}^{\mathrm{s}}\right], \tag{2.48}$$

which reduces to the simple form of (2.47) when the grains are considered incompressible ($b = 1$). This reduction is often assumed in petroleum engineering when the compressibility of the pore volume is taken to represent that of the bulk medium, that is, $\mathrm{d}V_{\mathrm{s}} = 0$, then $\mathrm{d}V = \mathrm{d}V_{\mathrm{v}}$.

2.7 Capillarity

Due to the action of surface energy (Section 2.6.9.3), a fluid (gas/liquid)-liquid interface is potentially curved combining a difference in pressure $p^{\mathrm{a}} - p^{\mathrm{b}}$ between the two phases. The work produced by this pressure difference applying to some initial infinitesimal spherical segment through an infinitesimal increase in curvature radius is $(p^{\mathrm{a}} - p^{\mathrm{b}})\, a\,\mathrm{dR}$. Also, the change in interface energy here due the change in surface area of the spherical segment is $\gamma_{ab}\,\mathrm{d}a$. As two surfaces of the same fluid would tend to merge losing their surface energies to an (original) state of lower energy, two different surfaces equilibrate minimising the total potential energy of the interface, that is the two previous terms should be equal [48]. This leads to the Young-Laplace equation,

$$p^{\mathrm{a}} - p^{\mathrm{b}} = \frac{2\gamma_{\mathrm{ab}}}{\mathrm{R}}, \tag{2.49}$$

where γ_{ab} is the interface energy (per unit area) for the fluids, assumed constant, and R is the (mean) radius of interface curvature.

If a solid interface is also involved, a contact angle results at the point where all three phases meet due the relative intermolecular interactions between them. The contact angle θ is a measure of the relative wettability of the fluids with regard to the solid and is related by the Young-Dupré equation, which is derived by similar considerations towards interfacial energy balances,

$$\gamma_{\mathrm{sn}} = \gamma_{\mathrm{sw}} + \gamma_{\mathrm{nw}}\cos\theta. \tag{2.50}$$

Assuming the spherically curved interface invades a cylindrical pore space with radius r, the curvature R is related by $\mathrm{r} = \mathrm{R}\sin(\pi/2 - \theta)$. Combined with (2.49) this gives the specific form

$$p^{\mathrm{n}} - p^{\mathrm{w}} = \frac{2\gamma_{\mathrm{nw}}\cos\theta}{\mathrm{r}}. \tag{2.51}$$

The capillary pressure is now defined as the difference in pressure between the nonwetting and wetting phases, $p^{\mathrm{c}} = p^{\mathrm{n}} - p^{\mathrm{w}}$. Note that the capillary pressure behaviour is dependent on the property specific relative wettability between the fluid phases and the solid present. For $\mathrm{CO_2}$ and brine in the presence of one another in contact with rock, the wetting phase, which preferentially wets the solid matrix, is generally brine, in which case the $\mathrm{CO_2}$ is therefore the nonwetting phase. This phenomena is illustrated in Figure 2.1(a).

The free energy of a porous solid alone, through which a nonwetting phase invades displacing a wetting phase, is considered after (2.21). Parametrising the first r.h.s. term to account for two immiscible fluids (Equation (2.22)), while ignoring the other terms by assuming the system to be undeformable and isothermal, reduces $\mathrm{d}\bar{\mathrm{a}}^{\mathrm{s}}$ to be the infinitesimal change in free energy of the interface between the porous solid and the fluids [48],

$$\mathrm{d}\bar{\mathrm{a}}^{\mathrm{s}} = p^{\mathrm{w}}(\phi_0\,\mathrm{d}S_{\mathrm{w}}) + p^{\mathrm{n}}(\phi_0\,\mathrm{d}S_{\mathrm{n}}) = -\phi_0\,(p^{\mathrm{n}} - p^{\mathrm{w}})\,\mathrm{d}S_{\mathrm{w}}, \tag{2.52}$$

where inside the first two brackets the changes in volume fraction are observed for each fluid phase in relation to the free energy. If $\mathcal{U} = \bar{\mathrm{a}}^{\mathrm{s}}/\phi_0$ is introduced as the free energy of the interfaces per unit porous volume then,

$$p^{\mathrm{n}} - p^{\mathrm{w}} = -\frac{\mathrm{d}\mathcal{U}}{\mathrm{d}S_{\mathrm{w}}}. \tag{2.53}$$

This result is also found by extending (2.51) by considering the energy balance of a moving interface as it invades an isolated conical pore space [48]. The implication is that the capillary pressure p^{c} is a function of the saturation S_{w} and interface energy $\mathcal{U}$ associated with the specific fluids and porous solid involved.

Equation (2.53) gives a fundamental interpretation of the prevalent experimental relationships of $p^{\mathrm{c}}(S_{\mathrm{w}})$ which give macroscopic functions (capillary pressure or retention curves) relating specific fluids with porous media. An interpretation is also given on the microscale with regard to (2.51). The function $p^{\mathrm{c}}(S_{\mathrm{w}})$ is a maximum when the wetting saturation is zero and a minimum until some entry pressure is breached. The entry pressure p_{entry}, in accord with (2.51), is the minimum pressure requisite for the nonwetting phase to enter pores of the largest radius, the threshold at which S_{w} starts decreasing from 1. Essentially, by increasing p^{c} the pore space is invaded (desaturated) by the nonwetting phase. Conversely, imbibition or suction in the sense of capillary rise takes place, of which the height of a capillary fringe or column above a phreatic surface would be given by $p_{\mathrm{entry}}/\rho^{\mathrm{w}}\mathrm{g}$.

2.7.1 Capillary pressure-saturation relationship

A commonly used [120] capillary pressure curve is the Brooks-Corey model [34, 35], based on the theory of [37], which proposes a convenient approximation of an effective saturation, $S_{\mathrm{e}} = (p_{\mathrm{entry}}/p^{\mathrm{c}})^{\lambda}$, for $p^{\mathrm{c}} \geq p_{\mathrm{entry}}$, where λ is a fitting parameter to the typical concave curve of p^{c} against S_{e}, essentially characterising the pore-size distribution. A generally more representative concave-convex curve (with a nonwetting regressive entry gradient, Figure 2.7(a)), which is more challenging to implement numerically, is given by the van Genuchten model [194] based on the theory of [133],

$$S_\mathrm{e} = \frac{S_\mathrm{w} - S_\mathrm{rw}}{S_\mathrm{s} - S_\mathrm{rw}} = \left[1 + \left(\frac{p^\mathrm{c}}{p_\mathrm{v}}\right)^{\mathrm{n_v}}\right]^{-\mathrm{m_v}}, \qquad \mathrm{n_v} = \frac{1}{1 - \mathrm{m_v}}, \qquad \text{for } p^\mathrm{c} > 0 \\ = 1, \qquad \text{for } p^\mathrm{c} \le 0 \tag{2.54}$$

The wetting and nonwetting phase residual saturations S_rw and S_rn are irreducible portions undisplaceable by viscous forces. Below these residuals the associated phase becomes discontinuous through the pores, unable to flow, unless transported due to diffusive and phase transition processes (miscible dissolution and evaporation). The saturated wetting phase content $S_\mathrm{s} = 1 - S_\mathrm{rn}$ is initially taken as 1 if there is no residual to the nonwetting phase initially present.

The reference pressure p_v and the exponent $\mathrm{m_v}$ are experimentally determined parameters characterising the capillarity for a given system. Insightful parameter equivalences and conversions between the Brooks-Corey and van Genuchten models are given in references [117, 132].

During drainage-reimbibition cycles hysteresis is observed (Figure 2.6(a)) where drainage occurs at a higher capillary pressures than imbibition over the same range of saturation. Noting that the area under the curves is the free energy $\mathcal{U}$, the difference between the curves is the stored interface energy dissipated as heat and not as mechanical work during a given hysteresis loop. Therefore, more precisely, $p^\mathrm{c}_\mathrm{imbibition} \le -(\mathrm{d}\mathcal{U}/\mathrm{d}S_\mathrm{w}) \le p^\mathrm{c}_\mathrm{drainage}$.

Reincorporating deformation of the solid in (2.52) the result of (2.53), is still obtained for small transformations of linear unsaturated poroelasticity [48]. The p^c-S_w relationship is however dependent on temperature. A particular form is given by [174],

$$p^\mathrm{c} = p^\mathrm{c}_\mathrm{r}\left(\frac{B + T}{B + T_\mathrm{r}}\right) \tag{2.55}$$

which may be substituted into (2.54), subscripts r denote properties at a reference point and B is related to the temperature dependence of the interface tension and contact angle.

In a fracture network (a second porosity) the p^c-S_w relationship is commonly modelled assuming zero capillary pressure within the fractures. For low to zero entry and capillary pressures the second porosity will exhibit a sharp interface between the two phases. This assumption is however known to give significant oil-recovery modelling errors in particular [56]. In addition, pseudo curves have been used [120], and similar p^c-S_w relationships as those used for the porous continuum may be used for the fracture continuum, this is explored by [186] and the references therein.

2.7.2 Relative permeability-saturation relationship

Two immiscible fluids in a porous volume naturally occupy separate regions and thereby impede each other's potential flow channels, meaning that each cannot recruit the full (intrinsic) permeability. Thereby an increase in saturation of a phase increases its access to flow channels at the other phase's detriment. This is accounted for by scaling the intrinsic permeability $\mathbf{k}$

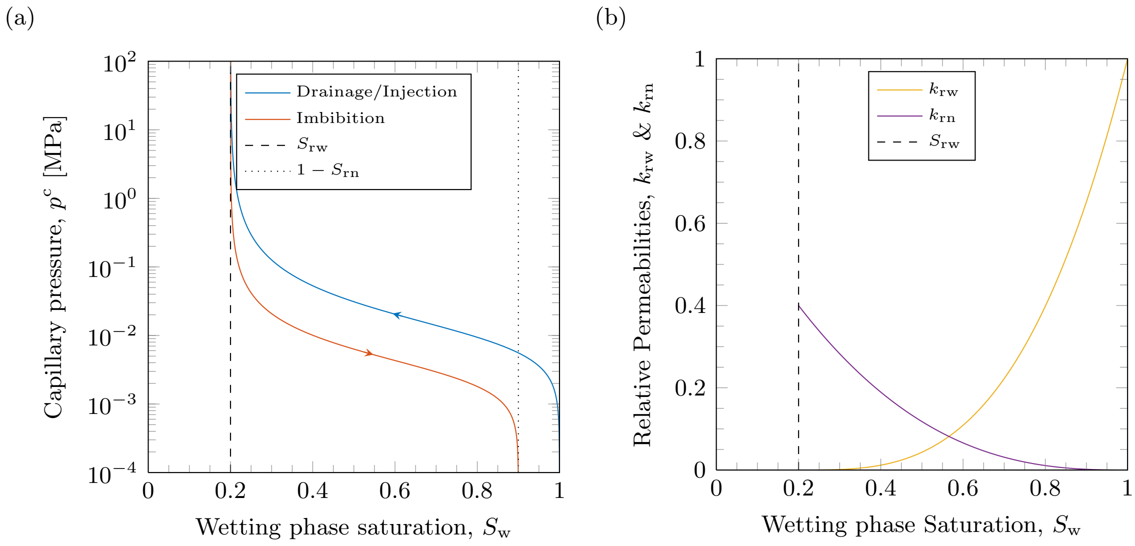

Figure 2.7: (a) van Genuchten p^c-S_{w} correlation for primary drainage, $p_{\mathrm{v}} = 0.01$ MPa, $m_{\mathrm{v}} = 0.45$, $S_{\mathrm{rw}} = 0.2$, for which a hypothetical secondary imbibition curve is also plotted for comparison demonstrating hysteresis with the immobility $S_{\mathrm{rn}} = 0.1$. (b) A corresponding correlation of relative permeability as a function of saturation during primary drainage alone, $m_{\mathrm{k}} = 3.2$, $n_{\mathrm{k}} = 2.6$, $k_{\mathrm{rw0}} = 1.0$, $k_{\mathrm{rn0}} = 0.4$.

by saturation dependent relative permeabilities, $0 \leq k_{\mathrm{rf}} \leq 1$ $(\mathrm{f} = \mathrm{w}, \mathrm{n})$, to give the effective permeabilities $k_{\mathrm{rw}}(S_{\mathrm{w}})\mathbf{k}$ and $k_{\mathrm{rn}}(S_{\mathrm{n}})\mathbf{k}$. The functions $k_{\mathrm{rf}}(S_{\mathrm{f}})$ are correlated experimentally and are given a theoretical basis in [37, 133] which lead to the p^c-S_{w} models discussed. In practice the following simplified power laws are generally correlated for use in numerical simulation, for which there is various experimental data available [128],

$$k_{\mathrm{rw}} = k_{\mathrm{rw0}} \left(\frac{S_{\mathrm{w}} - S_{\mathrm{rw}}}{1 - S_{\mathrm{rn}} - S_{\mathrm{rw}}} \right)^{m_{\mathrm{k}}}, \qquad k_{\mathrm{rn}} = k_{\mathrm{rn0}} \left(\frac{S_{\mathrm{n}} - S_{\mathrm{rn}}}{1 - S_{\mathrm{rn}} - S_{\mathrm{rw}}} \right)^{n_{\mathrm{k}}}, \tag{2.56}$$

where k_{rw0} and k_{rn0} are end-point relative permeabilities, and m_{k} and n_{k} are power law exponents for the respective phases. These particularly sensitive parameters and their uncertainty are studied in the context of GCS in [128]. The representation of the nonwetting phase entry behaviour is important, especially when long term trapping and storage capacity are of interest. Examples of $k_{\mathrm{rf}}(S_{\mathrm{f}})$ are given in Figure 2.7(b).

For the fracture network a linear dependence is often assumed ($m_{\mathrm{k}} = n_{\mathrm{k}} = 1$) with zero capillary pressure. Furthermore, this extended Darcy approach ignores viscous coupling effects, whereby one phase may enhance the flow of another.

2.7.3 Interface stability and phase mobility contrast

Viscous stability and the onset of viscous fingering at the interface during drainage for GCS is of interest. A stable interface is better for prediction and monitoring, and utilising macroscopic pore storage space. Displacement instabilities occur due to channelling by consequence of the spatial variation of rock properties, and due to viscous fingering by consequence of hydrodynamic instability. Both effects may also intensify in combination.

Various criteria for the onset of unstable displacement are discussed in [24]. The key aspects for perturbations in interface stability are the phase mobility $k_{\mathrm{r}\pi}/\mu^{\pi}$, capillary pressure p^{c}, gravity and length scale. Capillary pressure is known to stabilise immiscible displacement on shorter length scales, however larger length scales are those practical for GCS. This stabilisation is particularly a result of capillarity causing the shock-front (Section 3.2.6) to disperse; this acts to decrease the mobility contrast and therefore suppresses instability, it also follows that capillarity suppresses on the same length scale of this dispersion. It is the ratio of viscous to capillary forces which determines the gradient or sharpness to the shock-front (Darcy macroscopic capillary number), where low and high flow rates may be associated with capillary and viscous dominated flows respectively.

A simple form of the shock-front mobility contrast ratio is given by the following, which is discussed as an appropriate criterion for the onset of instability in [24],

$$M = \frac{k_{\mathrm{rn}}(S_{\mathrm{shock}})/\mu^{\mathrm{n}}}{k_{\mathrm{rw}}(S_{\mathrm{w}} = 1)/\mu^{\mathrm{w}}} > 1, \tag{2.57}$$

where instability occurs when the displacing phase is more mobile than the displaced phase evaluated at the shock-front. In the context of GCS initial study shows the viscosity ratio $\mu^{\mathrm{w}}/\mu^{\mathrm{n}}$, exponents n_{k} and m_{k}, and endpoints k_{rw0} and k_{rn0}, to be the principal sensitive parameters. Representative storage site data is therefore specifically required in order to assess stability in a given system. Hypothetical stability maps are given in [25], which are based on (2.57) and simple uncoupled simulations where finger nucleation/perturbation is caused by superimposed random permeabilities. During the temporal and spatial discretion of the system a degree of extra refinement is required to adequately capture this interface behaviour.

2.8 Further HTMC Processes

In Section 1.3.1 the trapping mechanisms for CO_2 sequestration were outlined. So far the key physical mechanisms have been reviewed for modelling. Static trapping (CO_2 restricted by structural/stratigraphic low-permeability barriers) by way of Section 2.6.6, and residual trapping (CO_2 restricted in pore spaces at irreducible saturation) by Section 2.7. These mechanisms contribute the most to sequestration at the earlier stages of injection, however they offer the least storage security. At the later stages the chemical mechanisms contribute more, potentially offering more storage security.

2.8.1 Dissolution (solubility and ionic) mechanisms

As discussed in Section 2.6.8.1 the solubility of CO_2 is a potential trapping mechanism, where CO_2 would be stored dissolved in solution as aqueous CO_2 and carbonic acid, this solubility is given by,

$$\mathrm{CO_{2(g)}} \rightleftharpoons \mathrm{CO_{2(aq)}} \quad \text{and} \quad \mathrm{CO_{2(aq)}} + \mathrm{H_2O} \rightleftharpoons \mathrm{H_2CO_{3(aq)}}. \tag{2.58}$$

The amount of dissolution is state dependent (Section 2.6.8.1), future changes of which may therefore cause the carbon to return back out of solution. The carbonic acid partially disassociates presenting an additional ionic form of trapping,

$$H_2CO_{3(aq)} + H_2O \rightleftharpoons HCO^-_{3\,(aq)} + H_3O^+. \tag{2.59}$$

The extent of this dissociation determines the acidity of the solution and may be determined by a state dependent acid dissociation constant, in terms of concentrations, $K_a = [H^+][HCO_3^-]/[H_2CO_3]$.

2.8.2 Mineral mechanisms

Further reactions with the host rock which is likely to be rich in Fe, Mg, and Ca minerals would also affect the system performance, for instance the following typical reaction,

$$Ca^{2+} + HCO^-_{3\,(aq)} + OH^- \rightleftharpoons Ca^{2+} + CO^{2-}_{3\,(aq)} + H_2O \rightleftharpoons CaCO_{3(s)} + H_2O, \tag{2.60}$$

creates solid precipitates (carbonates). In addition to being a form of long-term storage, the precipitate may block the pores impeding further sequestration. Conversely, as this reaction is reversible, calcium carbonate already present in the host rock (particularly limestones and shales in this case) may become dissolved, which could pose a problem if it is a constituent of the sealing caprock, thus compromising the physical trapping mechanisms. It follows that the extent and kinetic rates of such reactions in the subsurface should be considered in order to account for the long-term fate and transport of the stored CO_2. To do so the sink/source terms for the individual species/components in the conservation equations must be attributed to these chemical processes, giving rise to coupled diffusion-reaction equations accounting for the $CaCO_3$-H_2O-CO_2 compositions at the fluid-solid interfaces. Further study in this context is given by [101] and with the incorporation of brine in [71].

2.8.3 Adsorption mechanisms

Adsorption becomes significant particularly in organic rocks, the sequestration of CO_2 in disused coalbeds on displacing host methane CH_4 for instance, will alter the interface stresses, even if the saturating fluid pressures are constant. CO_2 replacing CH_4 at the same fluid pressure still causes an (additional) adsorption-induced deformation of the porous solid, and in this case the adsorption of CO_2 will cause the coalbed to swell as the interface energy is significantly less. The change in interface stress is due to the difference in the dipolar nature of the fluids, the macroscopic physics of which, following (2.21), and eventually incorporating fluid dependent Langmuir's adsorption isotherms is detailed for further study in [48].

In typical brine aquifer systems the brine remains adsorbed as the mineral-wetting phase; this presents a thin water film coating the mineral grains which affects multiphase flow and mediates reactions with the solid interfaces. A study in this context which demonstrates the sensitivity of the thickness of residual water films is given by [191], which highlights the needed for further detailed study of specific mineral-H_2O-CO_2 fate and transport behaviour.

2.8.4 Density convection mixing

The dissolution of CO_2 in formation brine increases the nearby aqueous phase density, meaning that it will sink while the less dense host brine will rise, resulting in convective mixing. This results in a gravitational/density-driven instability and vertical fingering of dissolved CO_2 which present problems for numerical discretisation techniques. The onset of mixing is particularly sensitive to permeability perturbations, heterogeneities, saturation, salinity, rock mineralogy, and geochemistry [72].

2.8.5 Porosity and permeability changes

In addition to changes caused by mineral precipitation/dissolution and Joule-Thompson cooling, there are porosity and permeability changes caused by stress/strain deformability within the rock. This relationship is often determined by empirical (laboratory or field calibrated) models describing changes in porosity and permeability as functions of the stress state within the host rock [162]. Empirical relations for permeability as a function of theoretical changes in porosity are also common and have been fitted for numerous rock types [72]. For the correction of permeabilities within fractures, an exponential empirical model which is stress state dependent has also been employed [72].

2.9 Upscaling

Upscaling or homogenising spatially detailed (measured) geological data so that it may be applied to spatially coarser numerical descriptions for computer simulation is motived primarily by the demand for computational efficiency. That is, to date there is disparity between the scale of measurement and the scale of discretisation over which numerical simulations can be performed in practice. In basic, upscaling is achieved by analytical and numerical techniques which seek for suitable effective descriptions for the coarse simulation grid such that the same gross behaviour of interest is simulated. Techniques can be characterised as local or global, depending on the spatial extent used to determined the coarse scale quantities, and include various heuristic, deterministic and stochastic methods (for instance, averaging, inversion and Monte Carlo methods). Detailed reviews and comparisons of the various techniques are made in [59, 63, 88, 157, 203] and the references therein. The numerous techniques involved are demonstrated to have various advantages and limitations in various modelling scenarios, and thus constitute an extensive research area. In particular, upscaling for highly heterogeneous and fractured media are detailed in [40, 49, 73, 115, 122], in which reference is made to dual-grid and dual-porosity/permeability formulations (upscaling from discrete fracture characterisations) and CO_2 sequestration. Emphasis is generally on the scaling of porosity and permeability/transmissibility parameterisations for both porous matrix and fracture. For coupled fluid, heat and geomechanics modelling, the upscaling of the deformability/moduli of the porous media is also considered in [100, 164].

2.10 Double-porosity transfer function

In a double(or dual)-porosity model (Sections 2.1.1–2.1.2) the fluid flows within the porous matrix and the fracture network, which are governed by separate mass balance equations, require coupling. To achieve this a transfer expression [17] is introduced to the mass balances for the porous matrix and fracture network sub-domains. A function presented by [201] for naturally fractured porous networks is extended for two fluid phases [120, 186] as,

$$q^{\mathrm{f}}_{\mathrm{trans}} = \pm \frac{\bar{\alpha}\, k_{\mathrm{rf}_1} \mathrm{k}_1}{\mu^{\mathrm{f}}} (p^{\mathrm{f}_1} - p^{\mathrm{f}_2}). \tag{2.61}$$

To elaborate, (2.61) is introduced in the mass balance formulation for the fluid f as a positive term in the porous matrix continuum sub-domain (subscript 1), and as a negative term in fracture network continuum sub-domain (subscript 2), hence the symbol '±' denotes the two possible valuations depending on the appropriate sub-domain. Thus if there is a pressure difference between the two sub-domains (porous matrix and fracture network) during computation an equal and opposite transfer of mass occurs between the mass balance equations for that fluid between the sub-domains (Section 3.2). For instance, if $p^{\mathrm{f}_1} > p^{\mathrm{f}_2}$, mass for that fluid will transfer from the porous matrix to the fracture network, and is conserved within the system as a whole.

The mass transfer is therefore proportional to the difference in the fluid pressure p^{f} between the two sub-domains, and controlled/regulated by the permeability of the porous matrix, the viscosity of fluid, and the geometry of the fracture network which is characterised as follows,

$$\bar{\alpha} = \frac{4\bar{n}(\bar{n}+2)}{\bar{l}^2}; \quad \bar{l} = a, \ \bar{n} = 1; \quad \bar{l} = \frac{2ab}{a+b}, \ \bar{n} = 2; \quad \bar{l} = \frac{3abc}{ab+bc+ca}, \ \bar{n} = 3. \tag{2.62}$$

The parameter $\bar{\alpha}$ is a geometrical idealisation of the fracture network heterogeneities, in which $\bar{l}$ is a characteristic length given by the side lengths of a, b and c of an idealised porous matrix cuboid block between fractures, and $\bar{n}$ is the number of orthogonal fracture sets. Interesting elaborations on this multi-porous theory introducing geomechanical and nonisothermal behaviour are given by [3, 123] and their associated work, as well as the introduction of fracturing with a single fluid phase flow by [5].

Figure 2.8 illustrates the double-porosity concept in a geomechanical context. The mechanical deformation is attributed with the porous matrix alone and any solid deformation due to pressure in the fracture network therefore occurs indirectly via coupling of the leakage term.

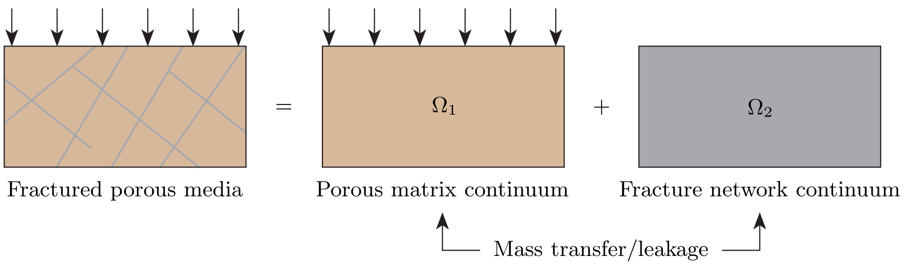

Figure 2.8: Illustration of the double-porosity concept after [120].

Figure 2.9 illustrates the coupling of system compaction and dilation with respect to the matrix and fracture pressures, assuming the conductivity of the fracture to be higher than that of the matrix. The latter dilation scenario is suggestive of a GCS injection scenario if injection was to occur through fractures intersecting the wellbore.

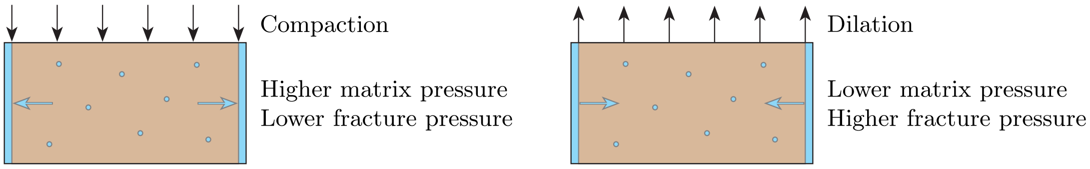

Figure 2.9: Double-porosity system compaction and dilation illustrated with respect to matrix and fracture pressures.

Note however, that these mechanisms would not occur if the fracture network was to present a lower fluid conductivity than the host porous rock. This is possible in some geological situations where the fractures have become blocked, particularly through mechanical grinding and/or subsequent plugging with finer grains and precipitate. This would mean that the fracture network would behave as a system of baffles restricting flow through the main porous body.

Intensively fissured/fractured formations are generally those consisting of carbonates rock, namely chalks, limestones and dolomites. Employing double-porosity models to predict behaviour in this type of formation has been successful in the hydrocarbon and hydrogeology engineering fields (see [38] and the reference therein). However, the application of all the features of a double-porosity formulation are not widely addressed for the study of GCS. A particular feature which is addressed in [38], is the fracture/matrix interface diffusion of CO_2 which is demonstrated to improve dissolution trapping.

2.11 Monitoring

The monitoring of GCS currently takes place for the purposes of research. On its commercialisation the focus will move towards monitoring programmes which meet regulation, i.e. Directive 2009/31/EC. In order to appropriately monitor a GCS reservoir, caprock and overburden the combined effort of subsets of techniques will be required depending on the storage site. To date, the prevalent techniques being employed in various combinations at GCS test sites are grouped generally in Table 2.8. Most of these were developed for the purposes of hydrocarbon and geothermal exploration and engineering geology, and are therefore further developed for GCS site application, a review of which along with other emerging techniques, strategies and cost/benefit analysis is given in [72].

Monitoring programmes designed for/based on these (or any future) monitoring technologies are to be used for continually validating and retooling predictive models, where assessments on site performance, security and storage strategy can then be made. Note that monitoring can be an invasive process and a balance has to be made between monitoring and security in meeting regulation at reasonable cost.

In this thesis the co-action of modelling and monitoring is developed. Two monitoring techniques are further discussed. Firstly, imaging via electrokinetics, solely for review in this context as it

Table 2.8: Potential GCS monitoring techniques, after [72].

Technique	Description
2/3/4D seismic surveys	On surface or across boreholes—assessing the reflections and refractions of induced mechanical perturbations caused by contrasts in acoustic impedance within the subsurface.
Micro-seismicity	Passive reading of CO_2 injection induced seismic events.
Surface gravity	Measurements of the gravimetric effects of the injected CO_2.
Satellite interferometry (InSAR)	Monitors surface subsistence and uplift (GCS in the order of mm/year) [29], subsurface CO_2 plume reconstruction via coupled geomechanical models [195].
Pressure and temperature gauges	Measuring hydraulic and thermal changes and connectivities between and along wells and strata.
Electrokinetics (ERT)	Assessing the changes in electrical potential between wells and strata.
Chemical & biological analyses	Various assurance monitoring and sampling techniques for determining the extent of specific chemical leakages at key locations.

demonstrates an interesting coupling with the usual governing equations for reservoir modelling. Secondly, imaging via muon tomography, which is a novel approach in the context of geological reservoirs, showing promise for GCS in particular, given the geophysical changes induced by the storage of CO_2, is to be assessed in this thesis.

2.11.1 Electrokinetic monitoring

Fluid flow through porous media due to a pressure gradient is also accompanied by a restraining effect due to electrical resistance. This is caused by the motion of the fluid dragging excess charge in the electric boundary layer at the fluid-solid/mineral interfaces, which may result in an electrical potential (electrokinetic streaming potential) [165]. Coupling these effects incorporates various electrokinetic phenomena, such as the self-potential. The electrokinetic flow is the natural movement of ions along the porous mediums electric layer, and if there is no source, the charge conservation is given by,

$$\frac{\partial \rho_Q}{\partial t} + \nabla \cdot \mathbf{j} = 0 \tag{2.63}$$

where ρ_Q is the charge density and $\mathbf{j}$ is the total electric current density. As highlighted in Sections 2.6.5 and 2.6.6, the fluid flow may be coupled with other effects. Darcy's law is coupled with electric flow (Ohm's law), after [165, 187], by

$$\boldsymbol{q}^{\mathrm{f}} = \mathbf{L}_{11}(-\nabla p^{\mathrm{f}} + \rho_{\mathrm{f}}\mathbf{g}) - \mathbf{L}_{12}\nabla \bar{V} \tag{2.64}$$

$$\mathbf{j} = \mathbf{L}_{21}(-\nabla p^{\mathrm{f}} + \rho_{\mathrm{f}}\mathbf{g}) - \mathbf{L}_{22}\nabla \bar{V} \tag{2.65}$$

where $\bar{V}$ is electric potential. The coefficient $\mathbf{L}_{11}$ represents the hydraulic conductivity, $\mathbf{L}_{22}$ the electric conductivity, and $\mathbf{L}_{12} = \mathbf{L}_{21}$ are cross coupling coefficients dependent on fluid saturation and the usual state variables, as explored by [165, 187] and the references therein. Assuming a quasi-steady state for (2.63) and substituting (2.65) presents a field continuity equation which can be additionally solved along with the usual system of coupled field equations for further investigation into subsurface flow phenomena. This is important given that electrokinetics is employed as a ground improvement and monitoring technique for various applications.

Measuring the self-potential via arrays of installed electrodes has been used as a monitoring technique for various subsurface problems. The first coupled numerical study of electrokinetics for GCS has been given recently in [186, 187], for both single- and double-porosity mechanically coupled geological systems. The coupled effect of thermal, miscible and/or chemical behaviour is however ignored therein for study purposes. The main premise is that the brine is significantly more conductive than the CO_2 and during the displacing flow the fluids can be tracked by the ensuing changes in the horizontal streaming potentials, where an electric potential peak in the horizontal profile is indicative of the fluid interface. This monitoring approach is however limited by the practicality in positioning the required electrodes.

2.11.2 Cosmic-ray muon tomographic monitoring

Muons are relatively unstable charged elementary particles belonging to the Standard Model of particle physics. They occur naturally and abundantly on Earth, mainly as a result of cosmic-rays (high-energy protons and nuclei) arriving from deep space colliding with atoms in the upper atmosphere (particularly nitrogen and oxygen). Muons are a preferred decay product of this collision, which continue at relativistic speeds able to penetrate the Earth's surface during a mean lifetime of 2.2 µs. Penetrations have been monitored at over 1×10^4 m w.e. (metres of water equivalent, the product of density and depth, 1 m w.e. $= 100$ g/cm^2) as determined in the deep underground sciences [36], that is 4 km through a subsurface bulk density of 2.5 g/cm^2. Cosmic radiation enters the atmosphere such that it gives a near constant (at a given elevation) muon flux, at sea-level of approximately 1 muon per cm^2 per minute, the small variations of which are well understood [114].

The muon flux at the Earth's surface is typically given by the standard Gaisser parametrisation [66]. This is a semi-empirical relationship for high energy muons, giving the differential muon intensity g_μ as the mean muon surface-level arrival rate per unit area, per unit solid angle per unit energy,

$$g_\mu(E_\mu, \theta) = \frac{1400}{\mathrm{m}^2 \ \mathrm{s} \ \mathrm{sr} \ \mathrm{GeV}} \left(\frac{E_\mu}{\mathrm{GeV}} \right)^{-2.7} F(E_\mu, \theta) \tag{2.66}$$

which is essentially a power law related to the muon energy spectrum, where E_μ is the muon energy, θ is zenith angle and F is the muon flux contribution due to other particle production.

A depth-intensity relation (DIR) in flux below surface level requires certain degrees of sophistication [36], the attenuation in flux with depth, while propagating through matter, is due to the wide differences in starting muon energies (0.1 to 10 GeV) and loss thereof due to a series of fundamental physical processes [113]. Particularly, as charged particles they are subject to electromagnetic (Coulomb) interactions and inelastically scatter deflecting as they pass through a material deviating from their originally trajectory.

Muons are therefore an abundant and naturally occurring form of background radiation, which on detection after having passed though the medium of interest may be used as a passive form of material detection, as is outlined in the following subsections. Muon detection occurs passively via scintillation, offering potential benefits over more active monitoring approaches (Table 2.8). In the literature monitoring studies of tunnels, pyramid vaults, volcanoes, nuclear waste storage, as well as the scanning of nuclear threats have all been reported in light of muon radiography

[150, 154, 171, 170].

2.11.2.1 Muon scattering tomography imaging

Muon Scattering Tomography (MST) is an advanced technique that uses the Multiple Coulomb Scattering (MCS) of muon radiation through material in order to detect its composition. This becomes possible when the number of interactions within the medium become high such that the angular dispersion, measured as a projected deviation angle, ϑ, may be approximated as a Gaussian distribution with a zero mean value, where the standard deviation ϑ_0 (and rms in this case) is the spread in overall scattering of many muon interactions through a given material volume. The material composition giving rise to a certain scattering is related with the following well-known formulae,

$$\vartheta_0 = \frac{13.6\ (\mathrm{MeV})}{\mathrm{p}\beta\mathrm{c}}\sqrt{\frac{L}{L_0}}\left[1 + 0.0038\ln\left(\frac{L}{L_0}\right)\right] \approx \frac{13.6\ (\mathrm{MeV})}{\mathrm{p}\beta\mathrm{c}}\sqrt{\frac{L}{L_0}} \tag{2.67}$$

$$L_0 = \frac{716.4\ (\mathrm{g/cm^2})}{\rho}\frac{\mathrm{A}}{\mathrm{Z(Z+1)}\ln(287/\sqrt{\mathrm{Z}})} \tag{2.68}$$

which shows the particle scattering proportional to the material depth L over its radiation length L_0 and inversely to the particle momentum p and relativistic velocity βc. Importantly, the radiation length L_0 is a function of the material's mass number A, atomic number Z and density ρ. It is demonstrated that a material of higher density will more readily scatter and/or attenuate particles. This phenomenon can be exploited for imaging via statistical reconstruction, whereby regions causing larger particle deflections indicate the presence of denser material.

2.11.2.2 Muon transmission imaging

The probability of muon survival over a given distance is increased primarily if less material is encountered, or similarly if material of a lower density integrated over the distance travelled is encountered. The muon flux from a given direction is thus dependent primarily on the column composition and density through which it passes. Therefore, changes in baseline flux readings due to the interference of another material entering a region of interest, causing changes in column composition and density, can be interpreted to detect the entering material.

A primary study on using this technique for monitoring GCS has recently been given in [114], wherein a basic scenario is modelled where hypothetical changes in bulk density of a geological body due to CO_2 storage are linked with statistically significant changes in simulated muon flux. It is an aim of this thesis to extend this work by facilitating the simulation of muon radiography through realistic GCS flow scenarios. This is done in order to better assess the sensitivity of the technique for monitoring bulk density changes over time in storage layers which are indicative of the presence and migration of CO_2. This may also help to design and understand the detector arrangements, locations, and responses for given injection/geological scenarios. Note that the primary limitation on employing this technique for GCS is due to the substantial storage depths, where the muon flux may become low for which the size of detector, required in order to capture the necessary muon statistics, would become impractical to install below the storage formation.

The schematic in Figure 2.10 depicts a hypothetical scenario to illustrate the potential application of muon radiography for monitoring GCS. In Figure 2.10(a) a series of cosmic-ray muon events on a trajectory towards a muon detector are depicted travelling through the atmosphere and then attenuating within the subsurface. In Figure 2.10(b) the same series of muon events are re-depicted with various trajectories taking path through a region which has undergone a reduction in density, thus increasing their survival probability, which has increased their penetration depth and rate of detection. Note that the opposite effect would occur with an increase in density within the subsurface. As a result, the muon count rates over certain angular regions with respect to the detector will change, and the statistical significance of these changes may be interpreted to detect and image the occurrence of subsurface density transitions within the angular scope of the detector.

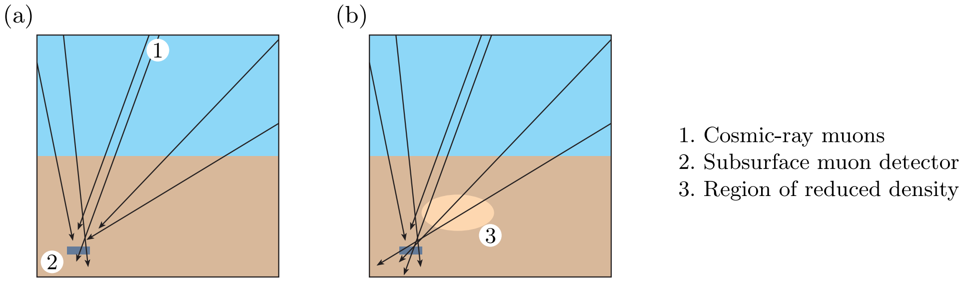

Figure 2.10: Schematic illustrating muon transmission imaging. (a) A series of muon events with trajectories toward a muon detector are depicted. (b) The same series of muon events are depicted hypothetically with various trajectories travelling through a region which has been reduced in density, thus increasing the likelihood of the survival of those muons and hence the muon flux through the detector.

2.11.2.3 Particle transport simulation

The simulation of the transport and interaction of elementary particles passing through matter is carried out by Geant4 (geometry and tracking), originally developed by CERN, it is an international collaboration of well-verified object-orientated C++ code libraries [1, 9]. This framework is widely used in the high energy physics field, and has particular application in high energy, accelerator, nuclear, and medical physics. These libraries are used to build an application to simulate the passage of muons through a geological body undergoing CO_2 storage, in order that muon radiography may be assessed and developed for the purposes of monitoring the stored CO_2. For the application, a novel computational workflow is developed that embeds an appropriate coupled rock-CO_2-brine flow model, as is also developed in this thesis.

2.12 Modelling

So far interrelated hydraulic, thermal, mechanical and chemical phenomena have been discussed to account for the key processes co-occurring in a GCS system. The most representative modelling approach is coupled hydro-thermo-mechanical-chemical (HTMC) modelling. However, such a complete approach appears to be over-demanding, and GCS simulations in the literature generally account for certain aspects of primary interest under simplifying assumptions. In view of the interrelated and interdisciplinary nature, and given that GCS is to occur on evermore unprecedented scales of inherent unpredictability, a staged learn-as-you-go approach is emerging in the CCS industry.

Analytical, semi-analytical and numerical models form part of the framework for the risk analysis of GCS. Essentially, they are to account for the migration and storage capacity of the injected fluid, which involves modelling, in particular: physical, dissolution, residual, precipitation and sorption trapping mechanisms; pore pressure breaching and fracturing of the seals; density convection mixing; CO_2 impurities; changes in formation porosity and permeability; and any additional vertical leakage risks (e.g. abandoned boreholes and faults).

Analytical and semi-analytical codes employ various simplify assumptions (Chapter 3) and are computationally inexpensive. They are used for primary/first order site assessments and are therefore useful for screening sites and form a valuable component of risk assessment. They may also be used for benchmarking special cases of more elaborate numerical codes.

The forefront numerical simulators currently employed for modelling GCS scenarios based on various coupled HTMC approaches are summarised in Table 2.9. Additionally, the simulators as listed generally employ implicit time integration and Newton-type methods for linearisation. A more extensive review is given in the respective references and comparatively by [42, 72], where the scenarios to which they have been applied (and compared) are also discussed.

In most subsurface flow modelling, the geochemical and geomechanical effects are often not taken into account, due to the matter of significance for engineering purposes, as the calculations are complex, computationally expensive, and the necessary theoretical and empirical/field information is limited [72]. However, for the injection of CO_2 it is anticipated that there will be important chemical mechanisms and significant increases in system pressure inducing site deformation. As a result there is a research interest growing for coupling these effects (Table 2.9). There are two main classes of numerical codes that couple HTMC behaviour:

2.12.1 Modular Class: Sequential coupling of a flow simulator with other software

This class consists mainly of general purpose simulators developed primarily for industrial oil and gas reservoir engineering purposes. Essentially incorporating multiple (modular) software programs via sequential coupling [172, 163]. The main benefit is that existing sophisticated models, being developed and verified within their disciplines can be incorporated cost-effectively.

2.12.2 Fully Coupled Class: Fully coupled (simultaneous) behaviour

Full coupling takes place through a simultaneous (monolithic) solution of the system of governing equations. However, if certain weak partial system couplings are present, they may be partitioned and solved in a staggered form for improving computational performance [120]. These models appear to be developed mainly for research purposes on specific HTMC problems. Those which are researchable have been developed and applied mainly to geotechnical (consolidation and settlement) and to geological nuclear waste repository problems. Notably for GCS, the

Table 2.9: Numerical simulators developed/employed for modelling GCS scenarios [42, 72].

Code	Description/key aspects	Ref.
Multiphase flow with coupled heat transport		
COORES	GCS specific research code, multiphase, multicomponent, FVM in space.	[42, 61]
ECLIPSE	BlackOil: General-purpose commercial code, multiphase, IFDM in space. Compositional: multiphase, multicomponent, cubic EoS, pressure dependent permeability.	[42, 175]
FEHM	Coupled mass-heat balance, multiphase, multicomponent, CVFEM in space.	[159]
CMG-GEM	Commercial code, EoS based, compositional simulator, multiphase, multicomponent, IFDM in space, adaptive solver.	[42, 72]
MUFTE	Compositional, multiphase, multicomponent, non-isothermal, fully coupled mass balance, Box/FVM in space.	[41]
DuMu^x	Open-source framework based on DUNE, multiphysics, multiphase, multicomponent, Box/FVM in space.	[42]
STOMP	Multiphase, multicomponent, coupled mass-energy balance, IVFDM in space.	[204]
MRST	Open-source research toolbox for prototyping reservoir simulation problems.	[112]
Coupled geochemical reactive transport		
CRUNCH	Multicomponent, non-isothermal, reactive transport, no restriction on species and reactions, kinetic mineral precipitation/dissolution, microbial Monod-type reactions, reactions and transports solved sequentially or coupled.	[109]
OpenGeoSys-ChemApp/ IPhreeqc	Open-source FEM simulator interfaced with commercial and open-source geochemical simulators for multiphase multicomponent geo-thermohydrochemical simulation, kinetic reactions and solid-solution equilibria.	[89, 121]
STOMP-ECKEChem	Integrates an efficient specifically designed batch chemistry module, equilibria, conservation, kinetics.	[72, 204]
PFLOTRAN	Parallel simulator, multiphase, multicomponent, reactive flow and transport, aqueous complexing, precipitation/dissolution and sorption, equilibria and kinetics, colloid-facilitated transport.	[79]
TOUGHREACT	Multiphase, multicomponent, reactive chemistry, fractured media, equilibria and kinetics, precipitation/dissolution.	[205]
Coupled geomechanics		
TOUGH-FLAC	Externally couples multiphase multicomponent fluid flow and heat transport code with a commercial code designed specifically for rock and soil mechanics, compatible grids coupled via external modules passing primary/state variables between field equations, surface deformations.	[162, 163]
OpenGeoSys	Scientific object-orientated open-source code for coupled mass-momentum-energy balance, based on RockFlow, multiphysics, multiphase, FEM in space, explicit fracture.	[72, 110]
CODE_BRIGHT	Hydromechanical coupling, multiphase, assessment of mechanical failure mechanisms, viscoplastic modelling, FEM in space.	[197, 197]

application of a fully coupled methodology is being applied by [110] as listed in Table 2.9. A study comparing sequentially coupled with fully coupled models is given in [57].

2.13 Review on fractures/fracturing—initiation and propagation

Early discontinuous modelling approaches made use of LEFM (Linear Elastic Fracture mechanics) and NLFM (Non-Linear Fracture Mechanics) in order to predict fracture prorogation. These methods use an energy based criterion that gives a stress intensity factor or J-integral, which if exceeding the material fracture toughness allows for the prediction of fracture propagation. However, these methods do not accurately describe the stress state ahead of the fracture, where singularities occur at the fracture tip. To overcome this, the notion of replacing this inelastic region with cohesive traction forces was introduced [16]. This is done with a discrete model and has brought about the concept of fracture energy and cohesive fracture growth. Mainly, the strategies for numerically modelling this have been developed within the finite element method framework. One strategy involves incorporating interface elements, which initially have no thickness, between the usual finite elements. In this instance fracturing will be highly mesh dependent (occurring along element boundaries) and the interface elements initially have fake stiffness which could also cause computational issues [131].

In order to better predict arbitrary fracture propagation, work was extended to this field by reference [142]. As a result, embedded discontinuities in the way of strain jumps in the formulations meant that the effect of the discontinuity can be accounted for without modelling it. Work was then incorporated using special shape functions for certain situations, following this the Partition of Unity Finite Element Method (PU-FEM) was developed [130]. Use of this theory with discontinuous approximations has been termed the Extended Finite Element Method (X-FEM) where the quadrature rule is altered for elements intersected by discontinuities. This theory has been incorporated with cohesive traction laws by reference [202], in order that a traction-separation model governing the non-linear behaviour in the fracture region is given with an elastic continuum.

In [5] the double-porosity numerical technique has been incorporated with the partition of unity method [130] in order to account for the fracturing process of a porous medium. It is essentially the partition of unity that describes the fracturing, and the double-porosity model is used to describe the resulting fluid flow. This approach, by coupling the two independent techniques, provides means for better simulations of the complex processes involved. However, this work covers for only a single fluid phase. This theoretical point of view has also be used to track fluid interfaces [187].

Additionally, [131] gives a review on fracturing in porous media that concludes on the lack of maturity in this field with regards to a global framework for continuous (unfractured)-discontinuous (fractured)-transition (fracturing)-strategies. Therein modelling approaches utilising damage mechanics, as developed in [142, 143, 144, 202], are also incorporated with the existing methodologies as outlined.

2.14 Summary of key research needs

This literature review has been carried out from various fundamental perspectives, and it is hoped that it may also be applied where applicable for developing physics applications beyond the scope of this thesis. The following research needs are identified in order to highlight the innovative aspects and findings of this work. These needs are also to be addressed during further in depth review within the respective chapters.

A comprehensive fully-coupled hydro-thermo-mechanical two-phase double-porosity Biot-type formulation is to be devised in order to complement existing industry and research formulations in the context of CGS. This is to be developed from first principles and is thus to form an extensive basis from which to capture and study various coupled phenomena which are of particular concern with respect to CO_2 sequestration, as have been reviewed. In particular, CO_2-brine displacement, solid deformation, porous matrix/fracture and Joule-Thomson cooling (JTC) effects.

The formulation of this work will present a highly nonlinear coupled system of governing equations. The numerical solution of such subsurface formulations over realistic domains are computationally intensive. Effort is therefore to be made on the study and development of the numerical methods employed in order to provide an effective means of solving the system of governing equations. The finite element method is to be employed in space and assessed in terms of its refinement for the various coupled physics involved. The finite difference method is to be employed in time, for which adaptive control theoretical and acceleration techniques are to be explored and adopted.

The various monitoring technologies leave scope for the innovation of an efficient, passive and continuous monitoring system for the purposes of CCS. Muon radiography has been reviewed as potential technology for this. In order to further assess the feasibility of employing this technology in the context of CCS, the realistic modelling of CO_2 sequestration and muon radiography are to be incorporated into a single computational framework for simulation.

Chapter 3

Model Formulations

A system of governing field equations for modelling fully coupled hydro-thermal-mechanical behaviour within a double-porosity (porous matrix and natural fracture/fissure network) multiphase (solid, wetting and nonwetting) medium is developed. This occurs following the fundamental principles introduced in Chapter 2, with particular reference to modelling a GCS system. This is done from general principles so that the assumptions in developing such a model, from the theoretical standpoint of this work, for describing a GCS system are highlighted comprehensively. The general approach given also allows for further development and application.

The development is a first attempt at accounting for such a system, the primary aim of which is to cover the hydro-thermal-mechanical-chemical bases in the coupled sense, and present a framework for study and further development. This work utilises and extends upon the following notable formulations and explores their application for modelling a GCS system. In [120] a fully coupled system accounting for miscible water and air flow within a deformable single porous geological medium is thoroughly developed. This approach is also extended for a multiphase water, gas and oil double-porosity system in [70, 120, 118], which neglect phase miscibility, fracture network deformability, and any thermal effects. Later, in [119, 146] the fracture network deformability is addressed. The thermal behaviour within a double-porosity system is also addressed for a single fluid phase in [123] neglecting fracture network deformability. These fully coupled formulation approaches which place particular emphasis on the mechanical behaviour of the system, have been extended in order to model a GCS system, particularly in [110], which accounts for thermal behaviour in a single porosity system, and [186] which accounts for a double-porosity system without thermal behaviour.

3.1 Model description

In this work, the following chief formulation aspects are itemised with their consequences and limitations. These aspects are detailed further during the derivation of the coupled governing field equations.

- The porous medium is described with a double-porosity model consisting of two distinct overlapping sub-domains, representing an interconnected porous matrix and fracture network. The physical properties of each sub-domain are considered independently and any coupling is controlled via the mass transfer/leakage function.

- The volume of fractures is considered to occupy a relatively small fraction of the total volume of the system. It can therefore be assumed that the fracture compressibility does not substantially alter the compressibility of the system as a whole [120], and only the solid deformation of the porous matrix and the multiphase fluid flows are directly coupled. The porous matrix sub-domain alone therefore carries the boundary and body forces.
- As the fracture compressibility is neglected, the intrinsic (or absolute) fracture network permeability, which is related to its compressibility through its geometry, does not change. Note that the modelling approach assumes a smeared fracture network of small volume relative to the total void space, and thus any prescribed intrinsic permeability may be viewed as an effective or averaged value of its actual performance. This is appropriate given the vast extent of typical geological reservoir models and that the fracture/geology is largely unknown for determining the actual effects of changes in stress state. It is however a point for further research to comment further on the scope of sensitivity of this behaviour, as well as for that of the porous matrix, within this context [118]. This aspect would be more prevalent for large distinct opening and closing geological fractures (or faults) which would however require that the faults be modelled explicitly.
- The solid deformation behaviour is assumed to undergo only small displacements which are linear elastic. Other constitutive material models may however be employed.
- The processes involved are considered to happen slow enough such that the inertial effects may be ignored.
- The two sub-domains are assumed to be fully saturated with a wetting and nonwetting phase.
- The phase components do not interact, transfer between the phases (condensation evaporation and dissolution) or undergo chemical reactions. The thermophysical behaviour of the phases may however be parametrised accurately given a physical state and composition for each phase.
- A single thermodynamic continuum (energy balance) is assumed appropriate for describing the temperature evolution over both sub-domains and the phases they constitute. Therefore, all the phases of both sub-domains are considered to be in local thermodynamic equilibrium at any point in the system domain. This means that the system temperature varies in space and time, but all the overlapping continua coexisting at a point are at the same temperature. This is generally acceptable given the interconnectedness of the distinct fluids and grains such that heat may diffuse by conduction instantly on the local scale relative to the space and time scales of geological interest [137]. A double temperature approach may be advocated between the porous matrix and fracture network continua, however the supply and transfer terms are extremely difficult to formulate and parameterise. For engineering purposes the single temperature approach after [123] is considered here.
- An effective saturation dependent bulk conductivity tensor is assumed appropriate. The convective heat fluxes over both sub-domains are however considered separately due to the potential difference in fluid velocities between the sub-domains. The notion of energy

transfer between the sub-domains is untreated as a single representative energy balance is assumed; this transfer is absorbed in the effective conductive and convective terms.

In what follows, a consistent formulation for the system mass, momentum and energy balance is given for a double-porosity multiphase deformable nonisothermal system. Firstly, two mass balance equations are derived for the two fluids phases for each sub-domain. As an intermezzo, a simplified single mass balance equation is solved for several GCS scenarios in order to present some useful benchmarks and relationships. Afterwards, single multiphase momentum and energy balance equations are derived.

3.2 Mass balance

The multiphase medium is described via the superposition of all the π phases in both sub-domains. An accurate kinematic description of relative motion is obtained by taking the material time derivative for the fluid phase f moving with the solid phase s, after the manipulation of (2.9) that is,

$$\frac{D^{\mathrm{s}}\zeta^{\mathrm{f}}}{Dt} = \frac{\partial \zeta^{\mathrm{f}}}{\partial t} + \nabla\zeta^{\mathrm{f}} \cdot \mathbf{v}^{\mathrm{s}}. \tag{3.1}$$

For practicality the convective component of this derivative is typically neglected for geomechanical applications, given that the solid displacements are usually small, hence,

$$\nabla\zeta^{\pi} \cdot \mathbf{v}^{\mathrm{s}} \ll \frac{\partial \zeta^{\pi}}{\partial t} \therefore \frac{D^{\mathrm{s}}\zeta^{\pi}}{Dt} \approx \frac{\partial \zeta^{\pi}}{\partial t}. \tag{3.2}$$

This simplifying approach is adopted prior to derivation, however material derivatives are easily reintroduced.

3.2.1 Primary/state variables

The following relationship involving the specific moisture content/fluid saturation capacity (Section 2.7.1),

$$\frac{\partial S_{\mathrm{w}}}{\partial t} = \frac{\partial S_{\mathrm{w}}}{\partial p^{\mathrm{c}}}\frac{\partial p^{\mathrm{c}}}{\partial t} + \frac{\partial S_{\mathrm{w}}}{\partial T}\frac{\partial T}{\partial t} = \frac{\partial S_{\mathrm{w}}}{\partial p^{\mathrm{c}}}\left(\frac{\partial p^{\mathrm{n}}}{\partial t} - \frac{\partial p^{\mathrm{w}}}{\partial t}\right) + \frac{\partial S_{\mathrm{w}}}{\partial T}\frac{\partial T}{\partial t}, \tag{3.3}$$

is employed in order to bring about different sequences of primary variables, from primarily $\mathbf{u}$, p^{w}, p^{n}, p^{c}, S_{w}, S_{n}, and T for each sub-domain. In this work it is employed in order to derive a $\mathbf{u}$-p^{w_1}-p^{n_1}-p^{w_2}-p^{n_2}-T (solid displacement-fluid pressure-temperature) primary variable set, directing the others as secondary variables within the final system of equations. Note that subscripts 1 and 2 refer to the matrix and fracture sub-domains respectively. Different variable sets will present different numerical properties [120, 167, 168] and warrant further study. In the context of modelling GCS some other interesting variable sets and elaborations are explored in [110, 187].

3.2.2 Solid mass balance for a porous continuum

From the general mean macroscopic balance equation (2.18), the mass balance for the solid phase taking the volume fraction for the intrinsic phase averaged density to be $(1 - n_1)$, given the relative small magnitude of the secondary porosity [5, 17, 119, 187],

$$\frac{\partial (1 - n_1)\rho^{\mathrm{s}}}{\partial t} + \nabla \cdot \{(1 - n_1)\rho^{\mathrm{s}}\mathbf{v}^{\mathrm{s}}\} = 0. \tag{3.4}$$

Expanding via the product rule, employing identity (2.11), and ignoring the gradient of macroscopic solid density [120],

$$\frac{(1 - n_1)}{\rho^{\mathrm{s}}}\frac{\partial \rho^{\mathrm{s}}}{\partial t} - \frac{\partial n_1}{\partial t} + (1 - n_1)\nabla \cdot \mathbf{v}^{\mathrm{s}} = 0. \tag{3.5}$$

The balance sums to zero as there is no mass exchanged with the solid phase for now.

3.2.3 Generic biphasic fluid and solid phase mass balance in a porous continuum

For a fluid phase f within the porous matrix, the mass balance, after (2.18) reads,

$$\frac{\partial (n_1 S_{\mathrm{f}_1}\rho^{\mathrm{f}_1})}{\partial t} + \nabla \cdot \{n_1 S_{\mathrm{f}_1}\rho^{\mathrm{f}_1}\mathbf{v}^{\mathrm{f}_1}\} = \pm\, m^{\mathrm{f}}, \tag{3.6}$$

where m is any mass exchanged with a particular overlapping sub-domain continua. The only exchange is assumed to happen via mass transfer/leakage between the matrix and fracture sub-domains controlled by some transfer function (2.61) [116]. An alternate formulation may also elaborate on this term in order to account for mass rate of evaporation or dissolution between the phases.

Following the choice of fluid-spatial solid-material reference systems the fluid velocity is conveniently considered consisting of two components,

$$\mathbf{v}^{\mathrm{f}_1} = \mathbf{v}^{\mathrm{s}} + \mathbf{v}^{\mathrm{f}_1\mathrm{s}}, \tag{3.7}$$

which introduces the velocity of the fluid relative to the porous solid, which is consistent with experimental valuations for Darcy's law (2.33). The divergence term of (3.6) is expanded after the substitution of (3.7), to which identity (2.11) is carried out on the term involving the solid motion,

$$\nabla \cdot \{n_1 S_{\mathrm{f}_1}\rho^{\mathrm{f}_1}(\mathbf{v}^{\mathrm{s}} + \mathbf{v}^{\mathrm{f}_1\mathrm{s}})\} = \mathbf{v}^{\mathrm{s}} \cdot \nabla\{n_1 S_{\mathrm{f}_1}\rho^{\mathrm{f}_1}\} + n_1 S_{\mathrm{f}_1}\rho^{\mathrm{f}_1}(\nabla \cdot \mathbf{v}^{\mathrm{s}}) + \nabla \cdot \{n_1 S_{\mathrm{f}_1}\rho^{\mathrm{f}_1}\mathbf{v}^{\mathrm{f}_1\mathrm{s}}\}, \tag{3.8}$$

from which emerge isolated components of fluid and solid motion for coupling. The gradient term is typically neglected as of, and including, the literature following [120], given that the solid velocities are anticipated to be small and the fluid density gradient negligible. The later two terms allow for the substitution of constitutive relationships involving respectively the solid strain rate and fluid movement.

Introducing the development of (3.8) and (2.61) into (3.6), while again carrying out the product rule for the time derivative gives,

$$n_1 S_{\mathrm{f}_1} \frac{\partial \rho^{\mathrm{f}_1}}{\partial t} + S_{\mathrm{f}_1} \rho^{\mathrm{f}_1} \frac{\partial n_1}{\partial t} + n_1 \rho^{\mathrm{f}_1} \frac{\partial S_{\mathrm{f}_1}}{\partial t} + n_1 S_{\mathrm{f}_1} \rho^{\mathrm{f}_1} (\nabla \cdot \mathbf{v}^{\mathrm{s}}) + \nabla \cdot \{ n_1 S_{\mathrm{f}_1} \rho^{\mathrm{f}_1} \mathbf{v}^{\mathrm{f}_1 \mathrm{s}} \} = \rho^{\mathrm{f}_1} q^{\mathrm{f}_1}_{\mathrm{trans}}. \quad (3.9)$$

Substituting the solid mass balance (3.5) into the fluid mass balance (3.9) cancelling the rate of change of porosity, $\partial n_1 / \partial t$, forms a coupling continuity equation of the solid and wetting fluid phases, presented,

$$\frac{(1 - n_1)}{\rho^{\mathrm{s}}} \frac{\partial \rho^{\mathrm{s}}}{\partial t} + \nabla \cdot \mathbf{v}^{\mathrm{s}} + \frac{n_1}{\rho^{\mathrm{f}_1}} \frac{\partial \rho^{\mathrm{f}_1}}{\partial t} + \frac{n_1}{S_{\mathrm{f}_1}} \frac{\partial S_{\mathrm{f}_1}}{\partial t} + \frac{1}{S_{\mathrm{f}_1} \rho^{\mathrm{f}_1}} \nabla \cdot \{ n_1 S_{\mathrm{f}_1} \rho^{\mathrm{f}_1} \mathbf{v}^{\mathrm{f}_1 \mathrm{s}} \} = \frac{q^{\mathrm{f}_1}_{\mathrm{trans}}}{S_{\mathrm{f}_1}}, \quad (3.10)$$

as the final form before any constitutive relationships are introduced. The terms represent sequentially the solid density rate, the rate of solid movement, the fluid density rate, the rate of change of the fluid saturation, the rate of fluid movement, and the rate of transfer between the sub-domains.

3.2.4 Wetting and nonwetting phase mass balance in the porous continuum

To build the two governing field equations for the mass balance of wetting and nonwetting phases in the porous matrix, the following constitutive relations are substituted with the appropriate terms of (3.10) for each phase:

- The solid (2.48) and fluid (2.47) density rates of change are assumed representative of the thermodynamic behaviour for the solid and for both the fluid phases respectively. It is here that the solid is formulated to behave with compressible solid grains, a compressible porous matrix skeleton, and an incompressible fracture network.
- The solid pressure p^{s} is taken as the averaged fluid pressure $S_{\mathrm{w}_1} p^{\mathrm{w}_1} + S_{\mathrm{n}_1} p^{\mathrm{n}_1}$ (2.25), which cross-couples this behaviour of the nonwetting phase within the mass balance of the wetting phase and vice-versa.
- The divergence of the solid velocity (rate of solid volume change) is treated via the summation of a unit vectorisation of the orthogonal strain rates, from which displacements may be derived with an appropriate differential operator, as of,

  $$\nabla \cdot \mathbf{v}^{\mathrm{s}} = \mathbf{m}^{\mathrm{T}} \frac{\partial \boldsymbol{\varepsilon}}{\partial t} = \mathbf{m}^{\mathrm{T}} \boldsymbol{L} \frac{\partial \mathbf{u}}{\partial t}, \quad (3.11)$$

  which allows for the coupling of the porous solid displacements $\mathbf{u}$ with those typically derived via momentum balance (Section 3.3). An axisymmetric stress/strain relation for (3.11) is given in (2.30) & (2.31), the unit vector for which being $\mathbf{m} = [1\ 1\ 1\ 0]^{\mathrm{T}}$ for the summation of the radial, vertical (axial) and hoop (circumferential) orthogonal components (Figure 2.4).
- The extended Darcy's law (2.33) is assumed to govern the multiphase fluid motion, where the inertial terms are considered negligible.
- The double-porosity transfer function (2.61) is assumed to govern the leakage of both fluid phases between the porous matrix and fracture network sub-domains.

After substitution, the equations are expanded and the coefficients to similar primary variable partial derivatives are grouped. This is simplified by assuming local thermodynamic equilibrium at the representative elementary points, and also noting that $\partial S_{\mathrm{n}_1}/\partial t = -\partial S_{\mathrm{w}_1}/\partial t$ and $p^{\mathrm{c}} = p^{\mathrm{n}} - p^{\mathrm{w}}$. Multiplying through the wetting phase balance equation by S_{w_1}, leads to,

$$\begin{aligned}
&\left[\frac{b-n_1}{K_\mathrm{s}}S_{\mathrm{w}_1}^2 + \frac{n_1 S_{\mathrm{w}_1}}{K_{\mathrm{w}_1}}\right]\frac{\partial p^{\mathrm{w}_1}}{\partial t} + \left[\frac{b-n_1}{K_\mathrm{s}}S_{\mathrm{n}_1}S_{\mathrm{w}_1}\right]\frac{\partial p^{\mathrm{n}_1}}{\partial t} \\
&\quad + \left[n_1 - \frac{b-n_1}{K_\mathrm{s}}S_{\mathrm{w}_1}p^{\mathrm{c}_1}\right]\frac{\partial S_{\mathrm{w}_1}}{\partial t} + bS_{\mathrm{w}_1}\mathbf{m}^{\mathrm{T}}\boldsymbol{L}\frac{\partial \mathbf{u}}{\partial t} - S_{\mathrm{w}_1}\left[\beta^{\mathrm{s}}\left(b-n_1\right) + n_1\beta^{\mathrm{w}_1}\right]\frac{\partial T}{\partial t} \\
&\qquad + \nabla\cdot\left\{\frac{k_{\mathrm{rw}_1}\mathbf{k}_1}{\mu^{\mathrm{w}_1}}\left(-\nabla p^{\mathrm{w}_1} + \rho^{\mathrm{w}_1}\mathbf{g}\right)\right\} = -\frac{\bar{\alpha}\,k_{\mathrm{rw}_1}\mathrm{k}_1}{\mu^{\mathrm{w}_1}}\left(p^{\mathrm{w}_1} - p^{\mathrm{w}_2}\right),
\end{aligned} \tag{3.12}$$

and multiplying through the nonwetting phase balance equation by S_{n_1}, leads to,

$$\begin{aligned}
&\left[\frac{b-n_1}{K_\mathrm{s}}S_{\mathrm{w}_1}S_{\mathrm{n}_1}\right]\frac{\partial p^{\mathrm{w}_1}}{\partial t} + \left[\frac{b-n_1}{K_\mathrm{s}}S_{\mathrm{n}_1}^2 + \frac{n_1 S_{\mathrm{n}_1}}{K_{\mathrm{n}_1}}\right]\frac{\partial p^{\mathrm{n}_1}}{\partial t} \\
&\quad - \left[n_1 + \frac{b-n_1}{K_\mathrm{s}}S_{\mathrm{n}_1}p^{\mathrm{c}_1}\right]\frac{\partial S_{\mathrm{w}_1}}{\partial t} + bS_{\mathrm{n}_1}\mathbf{m}^{\mathrm{T}}\boldsymbol{L}\frac{\partial \mathbf{u}}{\partial t} - S_{\mathrm{n}_1}\left[\beta^{\mathrm{s}}\left(b-n_1\right) + n_1\beta^{\mathrm{n}_1}\right]\frac{\partial T}{\partial t} \\
&\qquad + \nabla\cdot\left\{\frac{k_{\mathrm{rn}_1}\mathbf{k}_1}{\mu^{\mathrm{n}_1}}\left(-\nabla p^{\mathrm{n}_1} + \rho^{\mathrm{n}_1}\mathbf{g}\right)\right\} = -\frac{\bar{\alpha}\,k_{\mathrm{rn}_1}\mathrm{k}_1}{\mu^{\mathrm{n}_1}}\left(p^{\mathrm{n}_1} - p^{\mathrm{n}_2}\right).
\end{aligned} \tag{3.13}$$

These equations are also each simplified in part by assuming again the variation in fluid density within each phase to be negligible, meaning that the pressure gradient is the overriding factor within the fluid divergence term.

In order to rearrange for the desired $\mathbf{u}$-p^{w_1}-p^{n_1}-p^{w_2}-p^{n_2}-T primary variable set for solution, for each equation, (3.3) is employed whilst assuming for simplicity that $\partial S_\mathrm{w}/\partial T = 0$; $\partial S_\mathrm{w}/\partial p^\mathrm{c}$ being of prime concern for now (Section 2.7.1). This gives for the wetting phase,

$$\begin{aligned}
&\left[\frac{b-n_1}{K_\mathrm{s}}S_{\mathrm{w}_1}\left(S_{\mathrm{w}_1} + p^{\mathrm{c}_1}\frac{\partial S_{\mathrm{w}_1}}{\partial p^{\mathrm{c}_1}}\right) + \frac{n_1 S_{\mathrm{w}_1}}{K_{\mathrm{w}_1}} - n_1\frac{\partial S_{\mathrm{w}_1}}{\partial p^{\mathrm{c}_1}}\right]\frac{\partial p^{\mathrm{w}_1}}{\partial t} \\
&\quad + \left[\frac{b-n_1}{K_\mathrm{s}}S_{\mathrm{w}_1}\left(S_{\mathrm{n}_1} - p^{\mathrm{c}_1}\frac{\partial S_{\mathrm{w}_1}}{\partial p^{\mathrm{c}_1}}\right) + n_1\frac{\partial S_{\mathrm{w}_1}}{\partial p^{\mathrm{c}_1}}\right]\frac{\partial p^{\mathrm{n}_1}}{\partial t} \\
&\qquad + b\,S_{\mathrm{w}_1}\,\mathbf{m}^{\mathrm{T}}\boldsymbol{L}\frac{\partial \mathbf{u}}{\partial t} \\
&\qquad - S_{\mathrm{w}_1}\left[\beta^{\mathrm{s}}\left(b-n_1\right) + n_1\beta^{\mathrm{w}_1}\right]\frac{\partial T}{\partial t} \\
&\qquad + \nabla\cdot\left\{\frac{k_{\mathrm{rw}_1}\mathbf{k}_1}{\mu^{\mathrm{w}_1}}\left(-\nabla p^{\mathrm{w}_1} + \rho^{\mathrm{w}_1}\mathbf{g}\right)\right\} \\
&\qquad = -\frac{\bar{\alpha}\,k_{\mathrm{rw}_1}\mathrm{k}_1}{\mu^{\mathrm{w}_1}}\left(p^{\mathrm{w}_1} - p^{\mathrm{w}_2}\right),
\end{aligned} \tag{3.14}$$

and for the nonwetting phase,

$$\begin{aligned}
&\left[\frac{b-n_1}{K_\mathrm{s}} S_{\mathrm{n}_1}\left(S_{\mathrm{w}_1}+p^{\mathrm{c}_1}\frac{\partial S_{\mathrm{w}_1}}{\partial p^{\mathrm{c}_1}}\right)+n_1\frac{\partial S_{\mathrm{w}_1}}{\partial p^{\mathrm{c}_1}}\right]\frac{\partial p^{\mathrm{w}_1}}{\partial t}\\
&+\left[\frac{b-n_1}{K_\mathrm{s}} S_{\mathrm{n}_1}\left(S_{\mathrm{n}_1}-p^{\mathrm{c}_1}\frac{\partial S_{\mathrm{w}_1}}{\partial p^{\mathrm{c}_1}}\right)+\frac{n_1 S_{\mathrm{n}_1}}{K_{\mathrm{n}_1}}-n_1\frac{\partial S_{\mathrm{w}_1}}{\partial p^{\mathrm{c}_1}}\right]\frac{\partial p^{\mathrm{n}_1}}{\partial t}\\
&\qquad + b\, S_{\mathrm{n}_1}\,\mathbf{m}^\mathrm{T}\boldsymbol{L}\frac{\partial \mathbf{u}}{\partial t}\\
&\qquad - S_{\mathrm{n}_1}\left[\beta^\mathrm{s}\left(b-n_1\right)+n_1\beta^{\mathrm{n}_1}\right]\frac{\partial T}{\partial t}\\
&\qquad + \nabla\cdot\left\{\frac{k_{\mathrm{rn}_1}\mathbf{k}_1}{\mu^{\mathrm{n}_1}}\left(-\nabla p^{\mathrm{n}_1}+\rho^{\mathrm{n}_1}\mathbf{g}\right)\right\}\\
&\qquad = -\frac{\bar{\alpha}\, k_{\mathrm{rn}_1}\mathrm{k}_1}{\mu^{\mathrm{n}_1}}\left(p^{\mathrm{n}_1}-p^{\mathrm{n}_2}\right).
\end{aligned} \tag{3.15}$$

3.2.5 Wetting and nonwetting phase mass balance in the fracture continuum

The fluid mass balances within the fracture network are unassociated (uncoupled) at this point from that of the solid, flow within the fracture network is assumed not to cause any direct deformation of the solid, other than through leakage from the fracture network to the porous matrix as prescribed by the transfer function.

The derivation of wetting and nonwetting phase mass balances in the fracture network proceed as was carried out for (3.10) with the volume fractions generalised, however the first two solid terms are neglected (assumed zero) as constitutive relations for deforming fractures has not been introduced for these terms in this work, whereby fracture pressures cause solid deformation and so forth. Potential formulations for instance could however stem from extending the isothermal approach of deforming fractures-skeleton-grain in [119, 146]. In this work, the fracture volume, as is typically the case, is considered to be small compared with that of the porous matrix which permits this uncoupled assumption. Considering therefore a fracture network as a pervading flow route through the porous matrix unaffected by and unaffecting (uncoupled from) the solid deformation other than from being partially coupled through leakage, the following generic continuity equation is given,

$$\frac{n_2}{\rho^{\mathrm{f}_2}}\frac{\partial \rho^{\mathrm{f}_2}}{\partial t}+\frac{n_2}{S_{\mathrm{f}_2}}\frac{\partial S_{\mathrm{f}_2}}{\partial t}+\frac{1}{S_{\mathrm{f}_2}\rho^{\mathrm{f}_2}}\nabla\cdot\left\{n_2 S_{\mathrm{f}_2}\rho^{\mathrm{f}_2}\mathbf{v}^{\mathrm{f}_2\mathrm{s}}\right\}=\pm\frac{q^{\mathrm{f}_2}_{\mathrm{trans}}}{S_{\mathrm{f}_2}}. \tag{3.16}$$

Note the subscripts for this sub-domain have been alternated. The terms represent sequentially the fluid density rate, the rate of change of the fluid saturation, the rate of fluid movement, and the rate of transfer between sub-domains. Given the relative modest magnitude of the secondary porosity (fracture network) the divergence flow term is more significant than the other left-hand terms [17].

To build the two governing field equations for the mass balance of wetting and nonwetting phases in the fracture network, the following constitutive relations are substituted with the appropriate terms of (3.16) for each phase:

- The fluid (2.47) density rate of change is assumed representative of the thermodynamic behaviour for both the fluid phases.

- The extended Darcy's law (2.33) is assumed to govern the multiphase fluid motion within the fractures, the inertial terms of which are also considered negligible.
- The double-porosity transfer function (2.61) is assumed to govern the leakage of both fluid phases between the fracture network and the porous matrix sub-domains.

Again after substitution, the equations are expanded and the coefficients to similar primary variable partial derivatives are grouped. This is simplified by assuming local thermodynamic equilibrium at the representative elementary points, and noting that $\partial S_{\mathrm{n}_2}/\partial t = -\partial S_{\mathrm{w}_2}/\partial t$ and $p^{\mathrm{c}} = p^{\mathrm{n}} - p^{\mathrm{w}}$. Multiplying through the wetting phase balance equation by S_{w_2}, leads to,

$$\frac{n_2 S_{\mathrm{w}_2}}{K_{\mathrm{w}_2}}\frac{\partial p^{\mathrm{w}_2}}{\partial t} - S_{\mathrm{w}_2} n_2 \beta^{\mathrm{w}_2}\frac{\partial T}{\partial t} + n_2\frac{\partial S_{\mathrm{w}_2}}{\partial t} + \nabla\cdot\left\{\frac{k_{\mathrm{rw}_2}\mathbf{k}_2}{\mu^{\mathrm{w}_2}}\left(-\nabla p^{\mathrm{w}_2} + \rho^{\mathrm{w}_2}\mathbf{g}\right)\right\} = \frac{\bar{\alpha}\, k_{\mathrm{rw}_1}\mathrm{k}_1}{\mu^{\mathrm{w}_1}}(p^{\mathrm{w}_1} - p^{\mathrm{w}_2}), \tag{3.17}$$

and multiplying through the nonwetting phase balance equation by S_{n_2}, leads to,

$$\frac{n_2 S_{\mathrm{n}_2}}{K_{\mathrm{n}_2}}\frac{\partial p^{\mathrm{n}_2}}{\partial t} - S_{\mathrm{n}_2} n_2 \beta^{\mathrm{n}_2}\frac{\partial T}{\partial t} - n_2\frac{\partial S_{\mathrm{w}_2}}{\partial t} + \nabla\cdot\left\{\frac{k_{\mathrm{rn}_2}\mathbf{k}_2}{\mu^{\mathrm{n}_2}}\left(-\nabla p^{\mathrm{n}_2} + \rho^{\mathrm{n}_2}\mathbf{g}\right)\right\} = \frac{\bar{\alpha}\, k_{\mathrm{rn}_1}\mathrm{k}_1}{\mu^{\mathrm{n}_1}}(p^{\mathrm{n}_1} - p^{\mathrm{n}_2}). \tag{3.18}$$

Again the variation in fluid density within each phase has been assumed negligible, and the desired $\mathbf{u}$-p^{w_1}-p^{n_1}-p^{w_2}-p^{n_2}-T primary variable set for solution is obtained in the same manner for each equation via (3.3), whilst assuming for simplicity that $\partial S_{\mathrm{w}}/\partial T = 0$. This finally gives for the wetting phase,

$$\begin{aligned}
&\left[\frac{n_2 S_{\mathrm{w}_2}}{K_{\mathrm{w}_2}} - n_2\frac{\partial S_{\mathrm{w}_2}}{\partial p^{\mathrm{c}_2}}\right]\frac{\partial p^{\mathrm{w}_2}}{\partial t} \\
&\quad + n_2\frac{\partial S_{\mathrm{w}_2}}{\partial p^{\mathrm{c}_2}}\frac{\partial p^{\mathrm{n}_2}}{\partial t} \\
&\quad - S_{\mathrm{w}_2} n_2 \beta^{\mathrm{w}_2}\frac{\partial T}{\partial t} \\
&\quad + \nabla\cdot\left\{\frac{k_{\mathrm{rw}_2}\mathbf{k}_2}{\mu^{\mathrm{w}_2}}\left(-\nabla p^{\mathrm{w}_2} + \rho^{\mathrm{w}_2}\mathbf{g}\right)\right\} \\
&\quad = \frac{\bar{\alpha}\, k_{\mathrm{rw}_1}\mathrm{k}_1}{\mu^{\mathrm{w}_1}}(p^{\mathrm{w}_1} - p^{\mathrm{w}_2}),
\end{aligned} \tag{3.19}$$

and for the nonwetting phase,

$$\begin{aligned}
&n_2\frac{\partial S_{\mathrm{w}_2}}{\partial p^{\mathrm{c}_2}}\frac{\partial p^{\mathrm{w}_2}}{\partial t} \\
&\quad + \left[\frac{n_2 S_{\mathrm{n}_2}}{K_{\mathrm{n}_2}} - n_2\frac{\partial S_{\mathrm{w}_2}}{\partial p^{\mathrm{c}_2}}\right]\frac{\partial p^{\mathrm{n}_2}}{\partial t} \\
&\quad - S_{\mathrm{n}_2} n_2 \beta^{\mathrm{n}_2}\frac{\partial T}{\partial t} \\
&\quad + \nabla\cdot\left\{\frac{k_{\mathrm{rn}_2}\mathbf{k}_2}{\mu^{\mathrm{n}_2}}\left(-\nabla p^{\mathrm{n}_2} + \rho^{\mathrm{n}_2}\mathbf{g}\right)\right\} \\
&\quad = \frac{\bar{\alpha}\, k_{\mathrm{rn}_1}\mathrm{k}_1}{\mu^{\mathrm{n}_1}}(p^{\mathrm{n}_1} - p^{\mathrm{n}_2}).
\end{aligned} \tag{3.20}$$

3.2.6 Illustration: 1D axisymmetric mass balance solutions

A simplified radially symmetric quasi one dimensional problem based on mass balance is defined about a vertical injection well, and is solved both analytically and numerically. This is done to explore the development in (semi-)analytical theory [124, 127, 138, 139], to highlight and evaluate the primary displacing/storage behaviour within a potential realistic GCS system, and in order to provide a benchmark for the verification of more elaborate numerical models. Such simplified models are computationally efficient and are important for large scale risk and optimisation analyses. Detailed studies on this topic are given in [19, 44, 74].

The problem is defined as an axisymmetric region with a single porosity, confined upper and lower with impermeable boundaries. The injecting wellbore is at the centre with a radius r, at the radial extent x_{extent} is a far field boundary. The region has a height H from the base, in which a sharp interface is located at h propagating through the region over time t. The interface has CO_2 and immobile brine (at residual saturation, S_{rw}) on one side and mobile and immobile brine on the other. The CO_2 will have a lower density than brine (Figures 2.5(a) & 2.5(b)) and the CO_2 zone is assumed therefore to be on the upper side of the interface. This problem definition is illustrated in Figure 3.1.

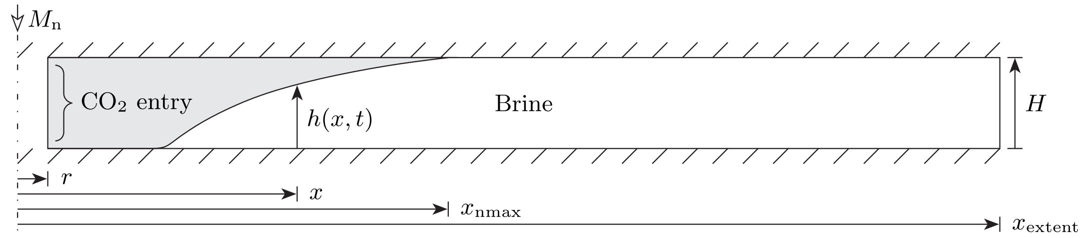

Figure 3.1: Schematic of a one-dimensional x axisymmetric system illustrating a typical stable CO_2-Brine interface profile $h(x,t)$ propagating from the wellbore delivering a mass injection rate, M_n around the wellbore interface at a radius of x_{well} along the height of the confined storage aquifer, H. The top and bottom of the domain represent no-flow boundaries and the far end is modelled as a far field Dirichlet boundary at constant pressure permitting flow.

This problem simplification essentially ignores capillary pressure and assumes a single fluid pressure p which is in vertical equilibrium. Saturation S_{f}, relative permeability k_{rf}, viscosity μ^{f} and density ρ^{f} are assumed constant and uniform within the respective zones either side of the interface. The system is therefore undeformable, immiscible, non-reactive and isothermal. These simplifications are discussed further in [124, 127, 138, 139]. Considering a control volume over time in one (radial) spatial dimension of the region described with a circumferential cross-sectional area (Figure 3.2), through which pass a flux of brine, q^{w} [m/s] and CO_2, q^{n} [m/s], the mass balance for the brine and CO_2 components, scripted w and n respectively, may be

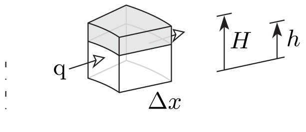

Figure 3.2: Simplified problem axisymmetric control volume.

visualised by assuming step changes in space Δx and time Δt,

$$\{\Delta[\mathrm{q}^{\mathrm{w}} h x \rho^{\mathrm{w}}]_{x}^{x+\Delta x}\}\Delta t = -\{\Delta[(1-S_{\mathrm{rw}})hxn\rho^{\mathrm{w}} + S_{\mathrm{rw}}Hxn\rho^{\mathrm{w}}]_{t}^{t+\Delta t}\}\Delta x \tag{3.21}$$

$$\{\Delta[\mathrm{q}^{\mathrm{n}}(H-h)x\rho^{\mathrm{n}}]_{x}^{x+\Delta x}\}\Delta t = -\{\Delta[(1-S_{\mathrm{rw}})(H-h)xn\rho^{\mathrm{n}}]_{t}^{t+\Delta t}\}\Delta x \tag{3.22}$$

which reduce when $\Delta x \to 0$ and $\Delta t \to 0$ to a set of coupled continuity equations, which may also be derived by expressing the general fluid mass balance (3.6) in one dimension with the saturations in terms of the interface height.

After [124], in order to facilitate the solution of (3.21) and (3.22), the concept of small compressibilities are introduced for the porous medium and fluids. Further to Section 2.6.10, the concept of compressibility is extended for a porous medium in this context, using the notation of [209], where subscripts b, c, and p denote bulk, confining and pore. Firstly, bulk compressibilities are further defined for both constant pore and confining pressures, respectively,

$$c_{\mathrm{bc}} = -\frac{1}{V_{\mathrm{b}}}\left(\frac{\partial V_{\mathrm{b}}}{\partial p_{\mathrm{c}}}\right)_{p_{\mathrm{p}}}, \qquad c_{\mathrm{bp}} = \frac{1}{V_{\mathrm{b}}}\left(\frac{\partial V_{\mathrm{b}}}{\partial p_{\mathrm{p}}}\right)_{p_{\mathrm{c}}}. \tag{3.23}$$

Secondly, pore compressibilities are introduced, likewise for both constant pore and confining pressures,

$$c_{\mathrm{pc}} = -\frac{1}{V_{\mathrm{p}}}\left(\frac{\partial V_{\mathrm{p}}}{\partial p_{\mathrm{c}}}\right)_{p_{\mathrm{p}}}, \qquad c_{\mathrm{pp}} = \frac{1}{V_{\mathrm{p}}}\left(\frac{\partial V_{\mathrm{p}}}{\partial p_{\mathrm{p}}}\right)_{p_{\mathrm{c}}}. \tag{3.24}$$

Note that c_{bc} is taken equivalent to $1/K_{\mathrm{T}}$ (2.28), which is the reciprocal of the dry (drained) bulk modulus of the solid grain skeleton (matrix). The compressibility of the solid grain mineralogy constituting the matrix is therefore defined,

$$c_{\mathrm{r}} = -\frac{1}{V_{\mathrm{r}}}\left(\frac{\partial V_{\mathrm{r}}}{\partial p}\right)_{\Delta p_{\mathrm{c}}=\Delta p_{\mathrm{p}}}, \tag{3.25}$$

where c_{r} is taken equivalent to $1/K_{\mathrm{s}}$ (2.28).

In reservoir sciences and engineering the deformation of the rock formation is often taken in the form of a porosity compressibility, where the confining (overburden) pressures may be considered constant,

$$c_{n\mathrm{p}} = \frac{1}{n}\left(\frac{\partial n}{\partial p_{\mathrm{p}}}\right)_{p_{\mathrm{c}}}. \tag{3.26}$$

For a given material model the various forms of system compressibility, as have been outlined, are interrelated. For a linear poroelastic solid model, as discussed in [209], since $n = V_{\mathrm{p}}/V_{\mathrm{b}}$, the relationships $c_{\mathrm{bp}} = c_{\mathrm{bc}} - c_{\mathrm{r}}$ and $c_{\mathrm{pp}} = [c_{\mathrm{bc}} - (1+n)c_{\mathrm{r}}]/n$ may be derived. Expanding (3.26) and introducing the compressibility relationships, considering that $c_{\mathrm{bc}} = 1/K_{\mathrm{T}}$ and $c_{\mathrm{bc}} = c_{\mathrm{r}}/(1-b)$ after (2.28), the following expression is given,

$$c_{n\mathrm{p}} = \frac{1}{n}\left(\frac{\partial n}{\partial p_{\mathrm{p}}}\right)_{p_{\mathrm{c}}} = \frac{1}{K_{\mathrm{T}}}\left(\frac{b}{n} - 1\right). \tag{3.27}$$

This expression relates the porosity compressibility, as utilised in the following semi-analytical formulations, to parameters describing the compressibility of a porous medium which are often employed in more elaborate numerical models [120], namely the dry (drained) bulk modulus and the Biot parameter (2.28). Equation (3.27) thus allows for a comparison between different formulation strategies involving the deformation of a reservoir system. It is also demonstrated that the porosity compressibility is related to the bulk compressibility factored by the Biot parameter (2.28) and the system porosity. Further in depth assessments within this context are given in [209] and the references therein.

After (2.45) the associated isothermal compressibilities of the fluid phases are given by

$$c_{\mathrm{w}} = \frac{1}{\rho^{\mathrm{w}}}\left(\frac{\partial \rho^{\mathrm{w}}}{\partial p_{\mathrm{p}}}\right), \qquad c_{\mathrm{n}} = \frac{1}{\rho^{\mathrm{n}}}\left(\frac{\partial \rho^{\mathrm{n}}}{\partial p_{\mathrm{p}}}\right). \tag{3.28}$$

As is typical in hydro-geological investigations, theses compressibilities are small such that they may be considered constant along with n, ρ^{w}, and ρ^{n}. The compressibility relationships (3.27) and (3.28) are introduced into the continuity equations (3.21) and (3.22). The fluxes are related to an assumed vertically averaged pressure p gradient via the Forchheimer equation (2.34) which introduces the extended Darcy behaviour accounting for both viscous and inertial flow resistances. Lastly, the continuity equations are simplified with the dimensionless terms [127],

$$\begin{aligned}
x_D &= \frac{x}{r}, & x_{\mathrm{e}D} &= \frac{x}{x_{\mathrm{extent}}}, & t_D &= \frac{M_{\mathrm{n}} t}{2\pi r^2 H n(1-S_{\mathrm{rw}})\rho^{\mathrm{n}}}, & p_D &= \frac{2\pi H \rho^{\mathrm{n}} k k_{\mathrm{rn}} p}{M_{\mathrm{n}} \mu^{\mathrm{n}}}, \\
h_D &= \frac{h}{H}, & q_D^{\mathrm{n}} &= \frac{2\pi r H \rho^{\mathrm{n}} \mathrm{q}^{\mathrm{n}}}{M_{\mathrm{n}}}, & q_D^{\mathrm{w}} &= \frac{2\pi r H \rho^{\mathrm{n}} \mathrm{q}^{\mathrm{w}}}{M_{\mathrm{n}}}, & \hat{\alpha} &= \frac{M_{\mathrm{n}} \mu^{\mathrm{n}} (c_{n\mathrm{p}} + c_{\mathrm{w}})}{2\pi H (1-S_{\mathrm{rw}})\rho^{\mathrm{n}} k k_{\mathrm{rn}}}, \\
\hat{\beta} &= \frac{M_{\mathrm{n}} k k_{\mathrm{rn}} \hat{b}\hat{b}_{\mathrm{rn}}}{2\pi H r \mu^{\mathrm{n}}}, & \hat{\gamma} &= \frac{\mu^{\mathrm{n}}}{\mu^{\mathrm{w}} k_{\mathrm{rn}}}, & \hat{\epsilon} &= \frac{(1-S_{\mathrm{rw}})(c_{\mathrm{n}} - c_{\mathrm{w}})}{(c_{n\mathrm{p}} + c_{\mathrm{w}})}, & \hat{\sigma} &= \frac{\rho^{\mathrm{n}} \hat{b}_{\mathrm{rn}}}{\rho^{\mathrm{w}}}.
\end{aligned} \tag{3.29}$$

Note that the relative and end-point permeabilities of the wetting phase are taken constant at unity, $k_{\mathrm{rw}} = 1$, and the respective nonwetting values are taken constant at some prescribed value k_{rn}, as the phases are assumed to be at their extreme saturations each side of the interface. Cast in a useful format, the final set of equations in dimensionless form becomes,

$$\frac{\partial h_D}{\partial t_D} = -\frac{1}{x_D}\frac{\partial}{\partial x_D}\{x_D h_D q_D^{\mathrm{w}}\} - \hat{\alpha}\left[S_{\mathrm{rw}} + (1-S_{\mathrm{rw}})h_D\right]\frac{\partial p_D}{\partial t_D} \tag{3.30}$$

$$\frac{\partial p_D}{\partial t_D} = -\frac{1}{\hat{\alpha}\left[1+\hat{\epsilon}(1-h_D)\right] x_D}\frac{\partial}{\partial x_D}\{\left[(1-h_D)q_D^{\mathrm{n}} + h_D q_D^{\mathrm{w}}\right] x_D\} \tag{3.31}$$

where the fluxes are related to the pressure gradient after (2.34) in dimensionless form by,

$$\frac{\partial p_D}{\partial x_D} = -q_D^{\mathrm{n}} - \hat{\beta} q_D^{\mathrm{n}} |q_D^{\mathrm{n}}| \tag{3.32}$$

$$\frac{\partial p_D}{\partial x_D} = -\frac{1}{\hat{\gamma}} q_D^{\mathrm{w}} - \frac{\hat{\beta}}{\hat{\sigma}} q_D^{\mathrm{w}} |q_D^{\mathrm{w}}| \tag{3.33}$$

with the dimensionless boundary conditions at $t_D > 0$,

$$q_D^{\mathrm{n}} = 1,\ q_D^{\mathrm{w}} = 0 \quad \text{at } x_D = 1, \tag{3.34}$$

$$h_D = 1,\ p_D = 0 \quad \text{at } x_D \to \infty, \tag{3.35}$$

and the dimensionless initial conditions at $t_D = 0$,

$$h_D = 1,\ p_D = 0 \quad \text{at } x_D > 1. \tag{3.36}$$

This system of ordinary differential equations may now be solved for h_D and p_D.

An approximate analytical solution to this problem is derived by introducing the similarity transform $\chi = x_D^2/t_D$, while assuming for simplicity that the fluid interface front moves much slower than the pressure front, the flow is non-inertial, the difference between fluid compressibilities is negligible relative to the overall system compressibility, and the well boundary is diminished: $\hat{\alpha} \to 0$, $\hat{\beta} = 0$, $\hat{\epsilon} \to 0$, and $r_D = 1 \to 0$, respectively. By doing so an asymptotic expansion is carried out which leads to [127, 124],

$$h_D(x,t) \approx \begin{cases} 0, & \text{for} \quad \chi \leq 2\hat{\gamma}, \\ \left(\sqrt{\dfrac{2\hat{\gamma}}{\chi}} - 1\right)\dfrac{1}{\hat{\gamma}-1}, & \text{for} \quad 2\hat{\gamma} < \chi < 2/\hat{\gamma}, \\ 1, & \text{for} \quad \chi \geq 2/\hat{\gamma}, \end{cases} \tag{3.37}$$

valid for $\hat{\gamma} \geq 1$. Note that $\hat{\gamma}$ is a reintroduction of the mobility contrast (Section 2.7.3), taking the limit at which $h_D = 1$ for $\chi = 2/\hat{\gamma}$ that represents the point of maximum radial extent of the CO_2 interface x_{nmax}. Re-dimensionalising therefore gives,

$$x_{\mathrm{nmax}}(t) \approx \sqrt{\frac{M_{\mathrm{n}} t}{\pi H n (1 - S_{\mathrm{rw}}) \rho^{\mathrm{n}}} \frac{k_{\mathrm{rn}} \mu^{\mathrm{w}}}{\mu^{\mathrm{n}}}}. \tag{3.38}$$

Given a constant mass injection rate and constant material properties, it follows $x_{\mathrm{nmax}} \propto \sqrt{t}$, hence the time steps and interface layouts in Figures 3.3–3.4, which is a useful approximate relationship to know from the standpoint of developing monitoring technologies. Note that for a mobility contrast $\hat{\gamma}$ of unity, (3.38) becomes simply the radial expansion of a cylinder undergoing a constant rate of volumetric increase, here through a volume of porous space.

Note that in this work the more recent analytical and semi-analytical expressions of [124, 127] are employed. The formulations therein build on the important and widely establish work of [139, 138]. This was done largely by incorporating fluid and formation compressibilities, facilitating the solution of the governing equations, in particular the pressure distribution, and also by incorporating inertial fluid flow effects.

Both (3.37) and (3.38) present useful relationships for benchmarking and giving preliminary estimates of key reservoir system behaviour. A particular interest, with regard to developing muon detection technologies [114], is in estimating a profile of change in the aquifer system bulk density due to the injection of CO_2. This is in order to simulate and assess the corresponding changes in muon flux through the system for the design of the detector. A vertically averaged bulk density may be given extending (3.37), by taking into account the appropriate volume fractions after (2.8),

$$\rho_{\mathrm{vert}}(x,t) = (1-n)\rho^{\mathrm{s}} + n(1 - S_{\mathrm{rw}})(1 - h_D)\rho^{\mathrm{n}} + n(S_{\mathrm{rw}} + h_D - S_{\mathrm{rw}} h_D)\rho^{\mathrm{w}}. \tag{3.39}$$

Instances of valuations for which, demonstrating potential changes in the vertically averaged bulk density profile, are given alongside Figures 3.3–3.4.

The system of equations (3.30–3.34) may also be solved numerically. To do so the central finite difference in space and adaptive in time methodology of [124] is programmed with slight modification in order to account for the inclusion of an irreducible wetting saturation.

Both analytical and numerical methods are applied to four extreme GCS scenarios, extended after [139] (Table 3.1). Firstly for a cold aquifer system at limiting shallow (1 km) and deep (3 km) depths, and secondly likewise for a warm aquifer system. The temperature gradients are respectively 25 °C/km with a surface temperature of 10 °C, and 45 °C/km with a surface temperature of 20 °C. The fluid pressure gradient is 10.5 MPa/km with mean atmospheric pressure. The corresponding ambient pressure and temperature combinations give rise to the accurate fluid properties (programmed after Chapter 2) as listed. The rock properties are characteristic of a typical sandstone aquifer, though $k_{\mathrm{rn}} = b_{\mathrm{rn}} = 1$ and $S_{\mathrm{r}} = 0$ for illustration. The Forchheimer parameter is given by [124],

$$\hat{b} = 0.005(n^{-5.5})(k^{-0.5}), \tag{3.40}$$

which is an empirical relationship which is particularly sensitive to the formation porosity. The CO_2 mass rate is at a lower limit of that deemed practical (3–120 kg/s) for commercial CCS purposes [126].

In Figure 3.3 each of the four reservoir type parameter sets are assessed while varying extremely the important rock permeability parameter. For Figure 3.4 the four sets are assessed again while varying extremely the important rock compressibility parameter. In Figures 3.3 and 3.4 the solid lines represent the base case (Table 3.1) and are therefore the same in both figures, the dashed and dash-dot lines demonstrate the effects of rock permeability and compressibility within the respective figures.

Overall, with respect to depth for both the cold and warm basins, it is observed that the extent of CO_2 migration is reduced. This is due primarily to the decrease in contrast ($\hat{\gamma}$) between the wetting and nonwetting fluid viscosities brought about by the increases in temperature and pressure affecting the phase viscosities, (Figures 2.6(a) and 2.6(b)), where the brine viscosity behaviour is particularly sensitive to changes in temperature. Additionally, for the warm basin scenarios CO_2 migration is increased overall, due primarily to the significant reduction in CO_2 density (Figures 2.5(a)), as this affects the dimensionless t_D term in a way that extends the radial extent of the interface.

In Figure 3.3 finite difference solutions are presented for a sequence of reduced system permeabilities deviating from the base case (Table 3.1). As a consequence $\hat{\alpha}$ increases and the results divert from the analytical solutions which assume $\hat{\alpha} \to 0$. In all cases the interface representing the same injected mass is observed to lag with successive reductions in permeability. This is a result of the lower permeability presenting a greater viscous resistance to fluid flow, meaning greater well pressures and pressure gradients become necessary in order to inject the prescribed mass of CO_2; the CO_2 will compress more and occupy less volume with in the aquifer under the higher pressures. This effect is therefore more pronounced in the warm and shallow case where

Table 3.1: Storage formation parameter sets for extreme brine aquifer scenarios: Cool & Shallow (CS), Cool & Deep (CD), Warm & Shallow (WS), and Warm & Deep (WD) basins. The scenarios present alternate ambient pressures and temperatures, due to hydrostatic and geothermal gradients, used as reference to determine the constant material properties (Chapter 2) as itemised. The hydrostatic gradient for all cases is 10.5 MPa/km with mean atmospheric pressure, and the geothermal gradients for the cold and warm basins are 25 °C/km with a surface temperature of 10 °C and 45 °C/km with a surface temperature of 20 °C respectively. The tildes ($\sim$) indicate adjacent values for the rock parameters are carried over.

			Storage system parameters				
Scenario			Cool basin		Warm basin		
			Shallow	Deep	Shallow	Deep	
Parameter	Sym.		CS (a)	CD (c)	WS (b)	WD (d)	Units
Reservoir depth			1	3	1	3	km
Reference pressure			10.5	31.5	10.5	31.5	MPa
Reference temperature			35	85	65	155	°C
Brine density	ρ^{w}		1069	1050	1054	1000	kg/m^3
Brine viscosity	μ^{w}		872	441	543	264	µPa s
Brine compressibility	c_{w}		3.75	3.77	3.86	4.64	$\times 10^{-10}$ Pa^{-1}
CO$_2$ density	ρ^{n}		730	740	292	499	kg/m^3
CO$_2$ viscosity	μ^{n}		60.0	63.2	24.2	41.1	µPa s
CO$_2$ compressibility	c_{n}		422	131	1867	262	$\times 10^{-10}$ Pa^{-1}
Rock density	ρ^{s}	2670	$\sim$	$\sim$	$\sim$	$\sim$	kg/m^3
Rock compressibility	$c_{n\mathrm{p}}$	5.00	$\sim$	$\sim$	$\sim$	$\sim$	$\times 10^{-10}$ Pa^{-1}
Porosity	n	0.2	$\sim$	$\sim$	$\sim$	$\sim$	-
Permeability	k	1.875	$\sim$	$\sim$	$\sim$	$\sim$	$\times 10^{-13}$ m^2
End-point relative permeability	k_{rn}	1	$\sim$	$\sim$	$\sim$	$\sim$	-
Forchheimer	$\hat{b}$	(3.40)	$\sim$	$\sim$	$\sim$	$\sim$	m^{-1}
Relative Forchheimer	$\hat{b}_{\mathrm{rn}}$	1	$\sim$	$\sim$	$\sim$	$\sim$	-
Brine residual saturation	S_{rw}	0	$\sim$	$\sim$	$\sim$	$\sim$	-
Well/Reservoir height	H	100	$\sim$	$\sim$	$\sim$	$\sim$	m
Well radius	r	0.2	$\sim$	$\sim$	$\sim$	$\sim$	m
CO$_2$ Mass injection rate	M_{n}	20	$\sim$	$\sim$	$\sim$	$\sim$	kg/s

the CO$_2$ is significantly more compressible. In addition to the viscous resistance of the system, the inertial resistance may also be assessed, in this instance by increasing the Forchheimer parameter the well pressures and pressure gradients will also increase in order to inject the same prescribed mass of CO$_2$, this is evaluated in [124]. The $\hat{\beta}$ term becomes influential for systems with low porosities which are characteristic of high Forchheimer parameter valuations (3.40).

In Figure 3.4 finite difference solutions are presented for a sequence of exaggerated increasing rock compressibilities deviating from the base case (Table 3.1). As a consequence $\hat{\alpha}$ increases and the results divert from the analytical solutions which assume $\hat{\alpha} \to 0$. In all cases, the results highlight effects of increasing the system compressibility, where the storage capacity increases as the rock expands more readily such that the furthest extent of the CO$_2$ interface is reduced for the same injected mass, the profiles are however more vertical. As the system is more readily able to accommodate the injected mass of CO$_2$, the required well pressures and pressure gradients in this instance therefore decrease with increasing rock compressibility.

Pressure as well as temperature changes within the system along with the corresponding solid/rock stress state/deformation are of particular interest in this work, and are to be evaluated further. To do so, momentum and energy balance equations are now developed in succession for coupling with the mass balance equations as developed earlier for a double-porosity system.

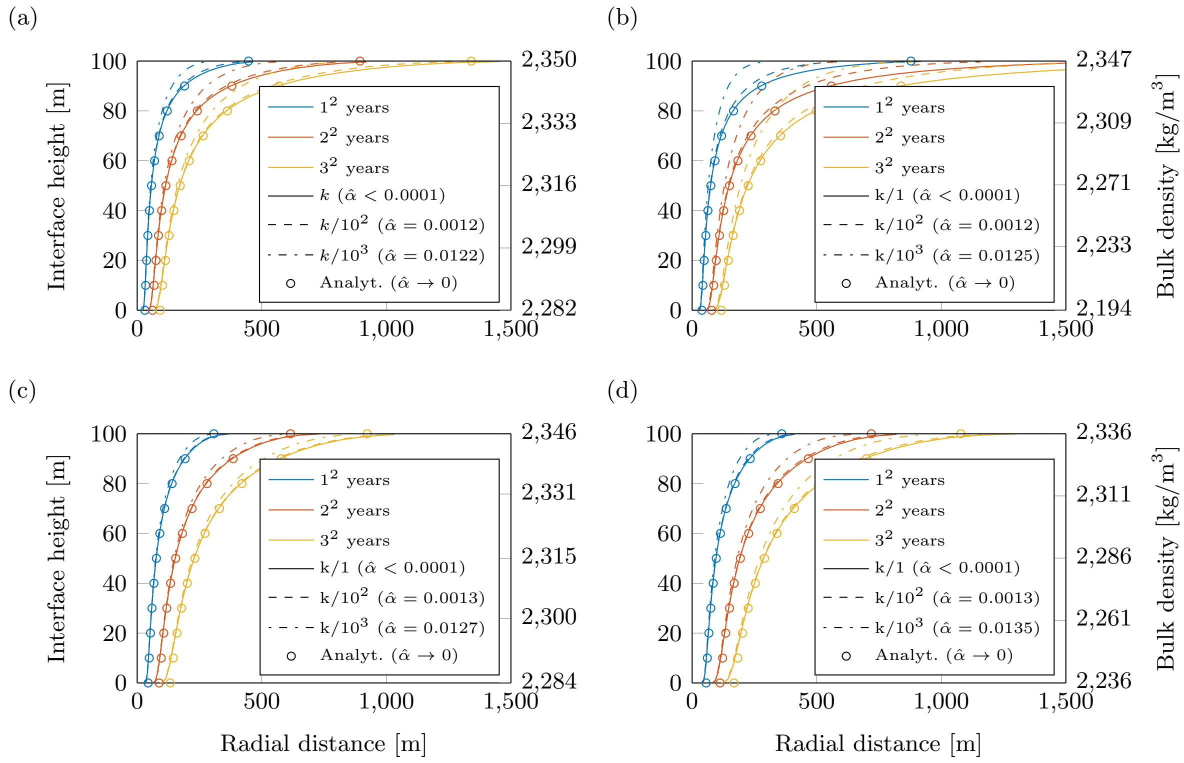

Figure 3.3: Analytical and FD solutions for interface and bulk density profiles for varying permeability of the cases: (a) CS, (b) WS, (c) CD, & (d) WD. $\hat{\beta} < 0.1$ for all cases. Note the differences in axis range between sub-figures which is the maximum and minimum density due to the variation in fluid densities between cases.

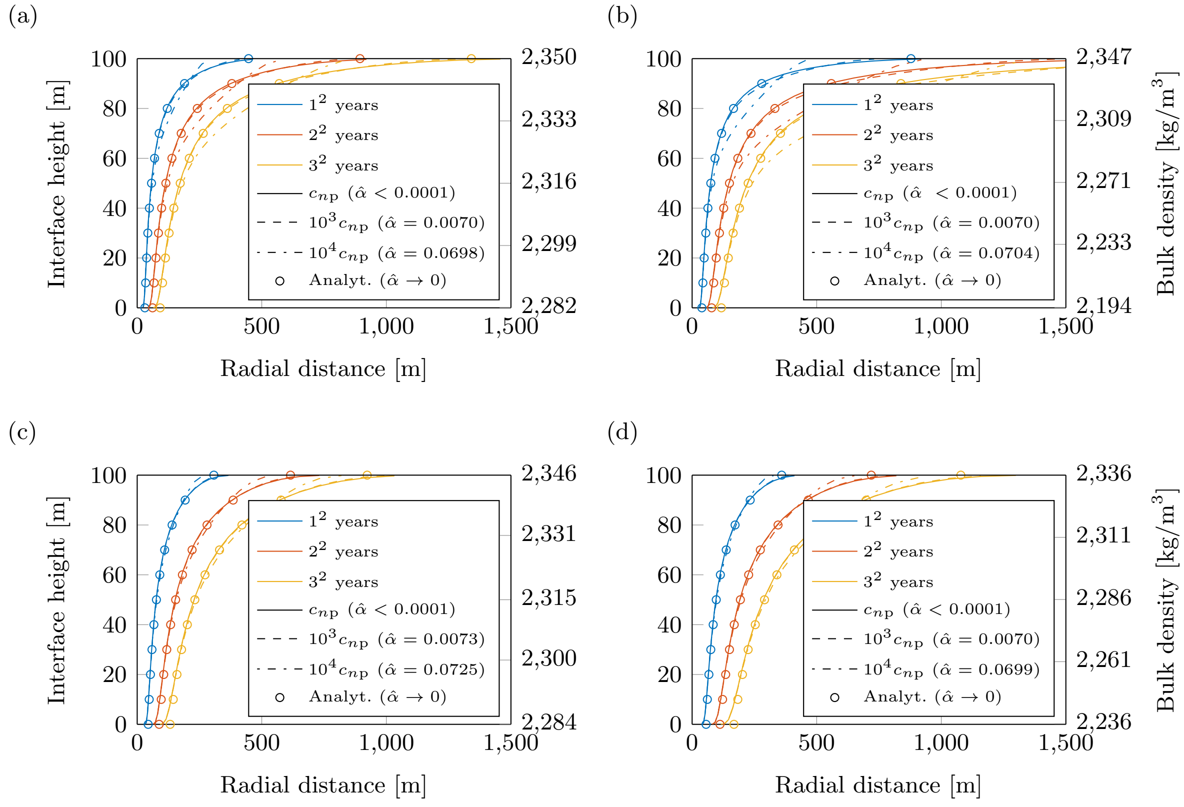

Figure 3.4: Analytical and FD solutions for interface and bulk density profiles for varying compressibility of the four cases: (a) CS, (b) WS, (c) CD, & (d) WD. $\hat{\beta} < 0.1$ for all cases. Note the differences in axis range between sub-figures which is the maximum and minimum density due to the variation in fluid densities between cases.

3.3 Momentum balance

It is of interest in this work to couple the multiphase linear momentum of the system in order to understand the associated material behaviour especially with respect to the solid stress state within the host porous medium. As discussed this is only coupled to the porous matrix subdomain. The conservation of linear momentum for a generic macroscopic phase, after (2.18), reads,

$$\frac{\partial\left(\eta^\pi \rho^\pi \mathbf{v}^\pi\right)}{\partial t}+\nabla\cdot\left(\eta^\pi \rho^\pi \mathbf{v}^\pi \otimes \mathbf{v}^\pi\right)-\nabla\cdot\boldsymbol{\sigma}^\pi-\eta^\pi \rho^\pi \mathbf{g}^\pi=\mathbf{0}, \tag{3.41}$$

omitting the phase interaction terms for ease of presentation, given that they are constrained to zero on summation over all the π phases. The utilisation of the interaction terms is discussed extensively in [83, 120], in particular, considering the momentum balance of the fluid phases in isolation with their phase interaction terms, the extended form of Darcy's law is derived as a special case as discussed in (Section 2.6.6).

The first two terms of (3.41) are the inertial components, which reduce to the phase acceleration after applying the identities (2.11 & 2.12), the kinematic definition of the phase acceleration (2.10), and the macroscopic mass balance with no mass supply. After which the form of (3.41) becomes,

$$\nabla\cdot\boldsymbol{\sigma}^\pi+\eta^\pi \rho^\pi \mathbf{g}^\pi=\eta^\pi \rho^\pi \mathbf{a}^\pi, \tag{3.42}$$

which is the usual compact form describing the linear momentum balance for a single material. Here a multiphase linear momentum balance is sought, summing all π phase momentum balances, within an including the porous matrix, relative to the solid phase after the introduction of the appropriate volume fractions gives,

$$\nabla\cdot\boldsymbol{\sigma}+\rho\mathbf{g}=\rho\mathbf{a}^s+n_1 S_{\mathrm{w}_1}\rho^{\mathrm{s}}\mathbf{a}^{\mathrm{sw}_1}+n_1 S_{\mathrm{n}_1}\rho^{\mathrm{s}}\mathbf{a}^{\mathrm{sn}_1}, \tag{3.43}$$

where $\boldsymbol{\sigma}$ is now the summation of all the partial stress tensors, the total stress, in line with the derivation of the constitutive relationship of (2.29), and ρ arises as an apparent or macroscopic bulk density,

$$\rho=\left(1-n_1\right)\rho^{\mathrm{s}}+n_1 S_{\mathrm{w}_1}\rho^{\mathrm{w}_1}+n_1 S_{\mathrm{n}_1}\rho^{\mathrm{n}_1}, \tag{3.44}$$

which, conveniently, is also the bulk property detectable by muon radiographic techniques (Section 2.11.2).

In the formulation of this system of equations the inertial effects are ignored. This occurs for now, and (3.43) reduces to the static stress equilibrium for macroscopic total stresses, in tensorial form,

$$\nabla\cdot\boldsymbol{\sigma}+\rho\mathbf{g}=\mathbf{0}, \tag{3.45}$$

which is vectorised (vector notation is now adopted for this balance equation) for ease of coupling and computation to,

$$\boldsymbol{L}_{\mathrm{eq}}^{\mathrm{T}}\boldsymbol{\sigma}+\rho\mathbf{g}=\mathbf{0}. \tag{3.46}$$

The vectorised equilibrium differential operator $L_{\mathrm{eq}}^{\mathrm{T}}$ is to be cast appropriately depending on the domain being considered, that is three dimensional, two dimensional or axisymmetric [60].

To build a multiphase governing field equation for the momentum balance of the system, the following constitutive relations are substituted with the appropriate terms of (3.46):

- The total stress tensor is decomposed as of (2.29), into an effective stress component responsible for the deformation of the solid skeleton and grains, and fluid pressure components. The unit tensor and pressure tensors here are vectorised in line with the vectorisation at (3.45) and with (3.11).
- The effective stress may now be related to solid displacements by selecting an appropriate constitutive solid model extended in order to account for thermal effects,

  $$\boldsymbol{\sigma}'' = \mathbf{D}_{\text{el}}(\boldsymbol{\varepsilon} - \boldsymbol{\varepsilon}^{\text{Th}}) \quad \text{or} \quad \mathrm{d}\boldsymbol{\sigma}'' = \mathbf{D}_{\text{T}}(\mathrm{d}\boldsymbol{\varepsilon} - \mathrm{d}\boldsymbol{\varepsilon}^{\text{Th}}), \tag{3.47}$$

  where for the latter,

  $$\mathrm{d}\boldsymbol{\varepsilon} = \boldsymbol{L}\mathrm{d}\mathbf{u} \quad \text{and} \quad \mathrm{d}\boldsymbol{\varepsilon}^{\text{Th}} = \mathbf{m}\,(\beta^{\text{s}}/3)\,\mathrm{d}T. \tag{3.48}$$

  The total strain vector is represented by $\boldsymbol{\varepsilon}$ and the thermal strain vector by $\boldsymbol{\varepsilon}^{\text{Th}}$, $\mathbf{D}_{\text{el}}$ and $\mathbf{D}_{\text{T}}$ are the linear elastic and tangential stress/strain matrices, β^{s} is again the solid thermal expansion coefficient, and $\mathbf{m}$ is the unit vector. The primary variables being the solid displacements $\mathbf{u}$ and the multiphase temperature T. Note that within the parenthesis of (3.47) other strain effects may be incorporated such as creep strains and initial strains.
- The external body force vector is taken as the acceleration due to the Earth's gravitational field.

Noting that the mechanical loads are carried only by the porous matrix continuum as discussed, expanding puts the primary variables into the following form,

$$\boldsymbol{L}_{\text{eq}}^{\text{T}}\left[\mathbf{D}_{\text{el}}\boldsymbol{L}\mathbf{u} - \mathbf{D}_{\text{el}}\mathbf{m}\,(\beta^{\text{s}}/3)\,T - b\mathbf{m}S_{\text{w1}}p^{\text{w1}} - b\mathbf{m}S_{\text{n1}}p^{\text{n1}}\right] + \rho\mathbf{g} = \mathbf{0}, \tag{3.49}$$

which may also be cast in an incremental/time differentiated form for symmetry of the system of balance equations and in order to incorporate non-linear material behaviour. This treatment is carried out in Chapter 4.

3.4 Energy/enthalpy balance

For the balance of energy, any surplus mean macroscopic effects due to phase interaction are neglected. It is demonstrated that these terms may be subjected to a summation of zero over all the overlapping phases [120] when prescribing a multiphase energy balance for the system as a whole for which there is no net increase of energy due to phase interaction. For the individual phase equations these terms are therefore omitted for ease of presentation. The external energy supply terms which are not required are also omitted. That is, any chemical, electromagnetic, radiative and nuclear forms of external energy supply are neglected. Reduced from the general macroscopic balance (2.18), an appropriate energy balance for a single phase is therefore given. The terms of which express sequentially, the rate of change of internal and kinetic energies, the rate of change of internal and kinetic energies by convective transport, the rate of work done by stresses/pressures and energy change by heat conduction, and the rate of work done by external/gravitational forces, as follows,

$$\frac{\partial \eta^\pi \rho^\pi \left(u^\pi + {}^1\!/_2\, \mathbf{v}^\pi \cdot \mathbf{v}^\pi\right)}{\partial t} + \nabla \cdot \left[\eta^\pi \rho^\pi \left(u^\pi + {}^1\!/_2\, \mathbf{v}^\pi \cdot \mathbf{v}^\pi\right) \mathbf{v}^\pi\right] - \nabla \cdot \left(\boldsymbol{\sigma}^\pi \cdot \mathbf{v}^\pi - \mathbf{q}^\pi\right) - \eta^\pi \rho^\pi \left(\mathbf{g}^\pi \cdot \mathbf{v}^\pi\right) = 0. \quad (3.50)$$

Manipulating the energy balance (3.50), and substituting both the general mass and momentum balance equations, leads to an expression of the rate of change of internal energy,

$$\frac{\partial \eta^\pi \rho^\pi u^\pi}{\partial t} + \nabla \cdot \left(\eta^\pi \rho^\pi u^\pi \mathbf{v}^\pi\right) + \nabla \cdot \mathbf{q}^\pi + \eta^\pi p^\pi \left(\nabla \cdot \mathbf{v}^\pi\right) - \tau^\pi : \nabla \mathbf{v}^\pi = 0. \quad (3.51)$$

This manipulation essentially subtracts the rate of change of kinetic energy within the system from (3.50), leaving an equation of the rate of change of internal energy [28, 120]. Note that the partial stress tensor has also become decomposed into a partial pressure and deviatoric stress. The terms now conveniently express, sequentially, the rate of change of internal energy, the rate of change of internal energy by convective transport, the rate of internal energy change by heat conduction, the reversible rate of internal energy change by compression/expansion, and the irreversible rate of internal energy change by viscous dissipation (mechanical into internal energy). Energy may be recoverable from this last term if the material is viscoelastic and therefore able to store elastic energy. Using the identity (2.11) and the material derivative (2.9) with the equation of continuity, (3.51) is transformed into the useful form,

$$\eta^\pi \rho^\pi \frac{D u^\pi}{D t} + \nabla \cdot \mathbf{q}^\pi + \eta^\pi p^\pi \left(\nabla \cdot \mathbf{v}^\pi\right) - \tau^\pi : \nabla \mathbf{v}^\pi = 0. \quad (3.52)$$

To build a multiphase governing field equation to account for the thermal behaviour of the system, the following developments are made for (3.52):

- First, the specific internal energy u is modified to the specific enthalpy h. As stated for (2.40), in terms of specific (intensive) properties,

  $$u^\pi = h^\pi - p^\pi v^\pi = h^\pi - \frac{p^\pi}{\rho^\pi}, \quad (3.53)$$

  making the standard assumption that the thermodynamic relationships derived for a system in equilibrium is appropriate for use in a non-equilibrium system if it is applied locally. The pressure term is the intrinsic hydrostatic component of the stress tensor (fluid pressure) and v is specific volume. Differentiating, applying the quotient/reciprocal rule, and expanding (3.53) yields,

  $$\rho^\pi \frac{D u^\pi}{D t} = \rho^\pi \frac{D h^\pi}{D t} + \frac{p^\pi}{\rho^\pi} \frac{D \rho^\pi}{D t} - \frac{D p^\pi}{D t}, \quad (3.54)$$

  which presents a relationship that may be introduced into (3.52) in order to produce a balance of enthalpy.
- The enthalpy balance allows for the introduction of system temperature. As enthalpy is a function of pressure and temperature (an ideal gas being a function of temperature only),

$h^\pi = h^\pi(p^\pi, T^\pi)$, therefore taking the total differential,

$$\mathrm{d}h^\pi = \left(\frac{\partial h^\pi}{\partial T^\pi}\right)_p \mathrm{d}T^\pi + \left(\frac{\partial h^\pi}{\partial p^\pi}\right)_T \mathrm{d}p^\pi, \tag{3.55}$$

and on substituting the specific heat capacity relationship after (2.40) for the first differential and using Maxwell's standard thermodynamic relation [39] for the second along with (2.46) after some manipulation, gives,

$$\mathrm{d}h^\pi = c_p^\pi \mathrm{d}T^\pi + \left[v^\pi - T^\pi \left(\frac{\partial v^\pi}{\partial T^\pi}\right)_p\right] \mathrm{d}p^\pi = c_p^\pi \mathrm{d}T^\pi + \frac{1}{\rho^\pi}\left(1 - T^\pi \beta^\pi\right) \mathrm{d}p^\pi. \tag{3.56}$$

The density rate term of (3.54) is treated by expanding the mass balance $D(\eta^\pi \rho^\pi)/Dt + \eta^\pi \rho^\pi \left(\nabla \cdot \mathbf{v}^\pi\right)$. Introducing this along with (3.56), into (3.54), finally gives,

$$\rho^\pi \frac{Du^\pi}{Dt} = \rho^\pi c_p^\pi \frac{DT^\pi}{Dt} - T^\pi \beta^\pi \frac{Dp^\pi}{Dt} - \frac{p^\pi}{\eta^\pi}\frac{D\eta^\pi}{Dt} - p^\pi \left(\nabla \cdot \mathbf{v}^\pi\right). \tag{3.57}$$

The assumption that the enthalpy is a function of pressure and temperature restricts the formulation to Newtonian fluids, which is a practical assumption for small/low-weight molecule fluids, such as those under prime consideration here within the ranges of interest [90]. Note that,

$$T^\pi \beta^\pi = -\frac{T^\pi}{\rho^\pi}\left(\frac{\partial \rho^\pi}{\partial T^\pi}\right)_p = -\left(\frac{\partial \ln \rho^\pi}{\partial \ln T^\pi}\right)_p \tag{3.58}$$

is a volume coefficient of expansion. Note also that the Joule-Thomson coefficient (Section 2.6.8.3) can be derived form (3.56) assuming constant enthalpy $\mathrm{d}h^\pi = 0$, for further developments therefore,

$$\mu_{\mathrm{JT}}^\pi = \left(\frac{\partial T^\pi}{\partial p^\pi}\right)_h = -\frac{1}{c_p^\pi}\left[v^\pi - T^\pi \left(\frac{\partial v^\pi}{\partial T^\pi}\right)_p\right] = \frac{v^\pi}{c_p^\pi}\left(T^\pi \beta^\pi - 1\right). \tag{3.59}$$

- The constitutive relationship adopted for the heat flux vector $\mathbf{q}^\pi$ is Fourier's law (2.44), which introduces the thermal conductivities of the media. However, when dealing with a porous multiphase medium an effective conductivity is generally prescribed [120, 129, 137, 208] due to the complex geometrical mixture of the phases. Considering the phases to be in parallel an upper-bound overall effective thermal conductivity is given by,

$$\boldsymbol{\chi}_{\mathrm{eff}} = (1 - n_{12})\boldsymbol{\chi}^{\mathrm{s}} + (n_1 S_{\mathrm{w}_1} + n_2 S_{\mathrm{w}_2})\boldsymbol{\chi}^{\mathrm{w}} + (n_1 S_{\mathrm{n}_1} + n_2 S_{\mathrm{n}_2})\boldsymbol{\chi}^{\mathrm{n}}. \tag{3.60}$$

Alternatively, considering the phases to be in series, a lower-bound overall effective thermal conductivity is given by,

$$\frac{1}{\boldsymbol{\chi}_{\mathrm{eff}}} = \frac{(1 - n_{12})}{\boldsymbol{\chi}^{\mathrm{s}}} + \frac{(n_1 S_{\mathrm{w}_1} + n_2 S_{\mathrm{w}_2})}{\boldsymbol{\chi}^{\mathrm{w}}} + \frac{(n_1 S_{\mathrm{n}_1} + n_2 S_{\mathrm{n}_2})}{\boldsymbol{\chi}^{\mathrm{n}}}. \tag{3.61}$$

Further developments to this effect are discussed in [129, 137, 208] for single porosity media with single and multiple fluid phases, for a double-porosity multiple fluid phase model further research is warranted. The upper bound is assumed in this work for now.

Applying the relationships, as itemised above, sequentially to (3.52) presents,

$$\eta^\pi \rho^\pi c_p^\pi \frac{DT^\pi}{Dt} - \eta^\pi \beta^\pi T^\pi \frac{Dp^\pi}{Dt} - p^\pi \frac{D\eta^\pi}{Dt} - \nabla \cdot (\boldsymbol{\chi}_{\text{eff}}^\pi \nabla T^\pi) - \tau^\pi : \nabla \mathbf{v}^\pi = 0. \tag{3.62}$$

The second and third terms, giving change due to mechanical work by pressure/temperature and volume fraction variation, and the fifth term, giving change due to viscous dissipation (an irreversible part of the internal energy increase which may be characterised for a fluid by its viscosity and dilatational viscosity [28]), are usually neglected for geo-applications [120]. The volume coefficient of expansion in the second term for an incompressible material (constant density), is $\partial \ln \rho / \partial \ln T = 0$, which is the same result for a system with constant pressure, $Dp/Dt = 0$. Also, for an ideal gas $\partial \ln \rho / \partial \ln T = -1$. Neglecting these terms presents the basic classical energy balance for multiphase media to which additional terms are generally added depending on the application.

For the consideration of energy balance the compressibility of the system is typically ignored, particularly in coupled geomechanical models [120], as its effect is generally negligible and therefore left uncoupled. In order to assess the extent of validity of such simplifications for fully coupled GCS model applications marks a point for further research. From the discussion in Section 2.6.8.3 on the importance of understanding the thermal effects of pressure variation within the CO_2 phase, the variation of phase pressure and the viscous dissipation terms are retained in this work from the general equation (3.62) for the CO_2 phase alone, assuming these effects to be negligible in the less compressible phases. The negligibility of the pressure changes may be assessed by the condition $\beta T(\mathrm{g}\beta/c_p)l_c \ll 1$, and the viscous dissipation by the condition $(\mathrm{g}\beta/c_p)l_c \ll 1$, if not met the respective differential terms are required [95, 137]. This is potentially the case for various CO_2 thermodynamic parametrisations. On retained these terms an additional relationship is needed for the viscous dissipation term, for flow in porous media governed by Darcy's law, this is given by the term, $\eta^\pi \mathbf{v}^\pi \cdot \nabla p^\pi$ [4, 95, 137].

In essence, the isobaric thermal expansion coefficients of the solid and wetting phases, as derived here, are considered negligible in the energy balance formulation, noting that they are orders of magnitude lower than for the nonwetting phase, over the pressures and temperatures of interest. A similar assumption is made in [129]. The convective heat flux of the solid is also ignored as its movement is negligible with respect to the fluids. Given that all the phases are considered to be in local thermodynamic equilibrium,

$$T^{\text{s}} = T^{\text{w}_1} = T^{\text{w}_2} = T^{\text{n}_1} = T^{\text{n}_2} = T. \tag{3.63}$$

In all therefore, for the solid phase the enthalpy balance is

$$\eta^{\text{s}} \rho^{\text{s}} c_p^{\text{s}} \frac{\partial T}{\partial t} - \nabla \cdot (\boldsymbol{\chi}_{\text{eff}}^{\text{s}} \nabla T) = 0, \tag{3.64}$$

for the wetting phase,

$$\eta^{\text{w}_\text{i}} \rho^{\text{w}_\text{i}} c_p^{\text{w}_\text{i}} \frac{\partial T}{\partial t} + \eta^{\text{w}_\text{i}} \rho^{\text{w}_\text{i}} c_p^{\text{w}_\text{i}} \mathbf{v}^{\text{w}_\text{i}} \cdot \nabla T - \nabla \cdot \left(\boldsymbol{\chi}_{\text{eff}}^{\text{w}_\text{i}} \nabla T\right) = 0, \tag{3.65}$$

and for the nonwetting phase,

$$\eta^{\mathrm{n_i}}\rho^{\mathrm{n_i}}c_p^{\mathrm{n_i}}\frac{\partial T}{\partial t}+\eta^{\mathrm{n_i}}\rho^{\mathrm{n_i}}c_p^{\mathrm{n_i}}\mathbf{v}^{\mathrm{n_i}}\cdot\nabla T-\eta^{\mathrm{n_i}}\beta^{\mathrm{n_i}}T\frac{\partial p^{\mathrm{n_i}}}{\partial t}-\eta^{\mathrm{n_i}}\left(\beta^{\mathrm{n_i}}T-1\right)\mathbf{v}^{\mathrm{n_i}}\cdot\nabla p^{\mathrm{n_i}}-\nabla\cdot\left(\boldsymbol{\chi}_{\mathrm{eff}}^{\mathrm{n_i}}\nabla T\right)=0, \tag{3.66}$$

where i = 1, 2. Hence, on summation of all the enthalpy balance equations the following multiphase macroscopic balance equation is given, conveniently in terms of the desired primary variables,

$$\begin{aligned}(\rho c_p)_{\mathrm{eff}}\frac{\partial T}{\partial t}+(\rho c_p\mathbf{v})_{\mathrm{eff}}\cdot\nabla T-\sum_{\mathrm{i}=1}^{2}n_{\mathrm{i}}S_{n_{\mathrm{i}}}\beta^{\mathrm{n_i}}T\frac{\partial p^{\mathrm{n_i}}}{\partial t}&\\ -\sum_{\mathrm{i}=1}^{2}n_{\mathrm{i}}S_{n_{\mathrm{i}}}\left(\beta^{\mathrm{n_i}}T-1\right)\mathbf{v}^{\mathrm{n_i}}\cdot\nabla p^{\mathrm{n_i}}-\nabla\cdot\left(\boldsymbol{\chi}_{\mathrm{eff}}\nabla T\right)&=0,\end{aligned} \tag{3.67}$$

where,

$$(\rho c_p)_{\mathrm{eff}}=(1-n_{12})\,\rho^{\mathrm{s}}c_p^{\mathrm{s}}+(n_1S_{\mathrm{w_1}}+n_2S_{\mathrm{w_2}})\,\rho^{\mathrm{w}}c_p^{\mathrm{w}}+(n_1S_{\mathrm{n_1}}+n_2S_{\mathrm{n_2}})\,\rho^{\mathrm{n}}c_p^{\mathrm{n}} \tag{3.68}$$

$$(\rho c_p\mathbf{v})_{\mathrm{eff}}=\rho^{\mathrm{w}}c_p^{\mathrm{w}}\left(n_1S_{\mathrm{w_1}}\mathbf{v}^{\mathrm{w_1}}+n_2S_{\mathrm{w_2}}\mathbf{v}^{\mathrm{w_2}}\right)+\rho^{\mathrm{n}}c_p^{\mathrm{n}}\left(n_1S_{\mathrm{n_1}}\mathbf{v}^{\mathrm{n_1}}+n_2S_{\mathrm{n_2}}\mathbf{v}^{\mathrm{n_2}}\right) \tag{3.69}$$

$$\boldsymbol{\chi}_{\mathrm{eff}}=(1-n_{12})\boldsymbol{\chi}^{\mathrm{s}}+(n_1S_{\mathrm{w_1}}+n_2S_{\mathrm{w_2}})\boldsymbol{\chi}^{\mathrm{w}}+(n_1S_{\mathrm{n_1}}+n_2S_{\mathrm{n_2}})\boldsymbol{\chi}^{\mathrm{n}}. \tag{3.70}$$

The respective fluid material properties of density, specific isobaric heat capacity, and thermal/heat conductivity, in the porous matrix and the fissure/fracture network, are considered to be the same ($\rho^{\mathrm{f_1}}=\rho^{\mathrm{f_2}}$, $c_p^{\mathrm{f_1}}=c_p^{\mathrm{f_2}}$, $\boldsymbol{\chi}^{\mathrm{f_1}}=\boldsymbol{\chi}^{\mathrm{f_2}}$) for tractability. All phases are considered to be in local thermodynamic equilibrium, and the pressure variations are assumed to be within a reasonable range such that the material properties in each sub-domain vary negligibly from one another with respect to temperature and pressure changes. The volume fraction velocities of the fluids may be given by substituting Darcy's law (2.6.6). The solid velocity is left uncoupled as the associated heat convection is assumed negligible as mentioned.

Efficient preliminary solutions to simplified governing equations extended for GCS application were presented for the key mass balance equations. Such extension with solutions for the momentum balance, assessing for instance any first order uplift over a GCS reservoir due to prescribed pressure changes, appear more open for study with direct reference to GCS. Solutions are however given for simple geotechnical consolidation/deformation problems as of [120] and the references therein. For the energy balance, research has presented solutions for simplified energy balance equations extended for GCS, which also highlight the prominent thermal considerations as adopted here, for reference [128, 129].

For designing a muon detection system an estimation of density change due to injection is required [114]. In determining this, the mass balance of the system is the most influential aspect, unless the coupled mechanical and/or thermal effects become severe. Simple uncoupled single-porosity mass balance solutions have therefore been presented in Section 3.2.6 as of (3.39) for the purposes of simple first-order estimation. A coupled or uncoupled momentum balance solution is of indirect importance because an estimate of mechanical/pressure changes would indicate if the muon detection equipment would become damaged, and therefore what installation tolerances should be set. Likewise, the energy balance is also of importance because components currently under development, to be installed subsurface as part of the muon detector system, are sensitive to temperature, therefore, estimates of thermal fluctuations around the muon detection system are desirable. Any (thermal-electrical) coupling or response to this effect is also demanded and unresearched.

3.5 Summary of governing field equations

The six non-linear governing field equations as derived are given in compact form. This is to highlight the coupling between terms and equations, for ease of reference, and for further numerical computation. The mass balances within the porous continuum, for the wetting phase,

$$\lambda_{\mathrm{w_1}} \frac{\partial p^{\mathrm{w_1}}}{\partial t} + \lambda_{\mathrm{w_1 n_1}} \frac{\partial p^{\mathrm{n_1}}}{\partial t} + \lambda_{\mathrm{w_1 s}} \boldsymbol{L} \frac{\partial \mathbf{u}}{\partial t} - \lambda_{\mathrm{w_1 T}} \frac{\partial T}{\partial t} + \nabla \cdot \left\{ \boldsymbol{K}_{\mathrm{w_1}} \left(-\nabla p^{\mathrm{w_1}} + \rho^{\mathrm{w_1}} \mathbf{g} \right) \right\} = -\lambda_{\mathrm{w_1 l_2}} \left(p^{\mathrm{w_1}} - p^{\mathrm{w_2}} \right), \quad (3.71)$$

and for the nonwetting phase,

$$\lambda_{\mathrm{n_1 w_1}} \frac{\partial p^{\mathrm{w_1}}}{\partial t} + \lambda_{\mathrm{n_1}} \frac{\partial p^{\mathrm{n_1}}}{\partial t} + \lambda_{\mathrm{n_1 s}} \boldsymbol{L} \frac{\partial \mathbf{u}}{\partial t} - \lambda_{\mathrm{n_1 T}} \frac{\partial T}{\partial t} + \nabla \cdot \left\{ \boldsymbol{K}_{\mathrm{n_1}} \left(-\nabla p^{\mathrm{n_1}} + \rho^{\mathrm{n_1}} \mathbf{g} \right) \right\} = -\lambda_{\mathrm{n_1 l_2}} \left(p^{\mathrm{n_1}} - p^{\mathrm{n_2}} \right). \quad (3.72)$$

The mass balances within the fissured/fractured continuum, for the wetting phase,

$$\lambda_{\mathrm{w_2}} \frac{\partial p^{\mathrm{w_2}}}{\partial t} + \lambda_{\mathrm{w_2 n_2}} \frac{\partial p^{\mathrm{n_2}}}{\partial t} - \lambda_{\mathrm{w_2 T}} \frac{\partial T}{\partial t} + \nabla \cdot \left\{ \boldsymbol{K}_{\mathrm{w_2}} \left(-\nabla p^{\mathrm{w_2}} + \rho^{\mathrm{w_2}} \mathbf{g} \right) \right\} = \lambda_{\mathrm{w_1 l_2}} (p^{\mathrm{w_1}} - p^{\mathrm{w_2}}), \quad (3.73)$$

and for the nonwetting phase,

$$\lambda_{\mathrm{n_2 w_2}} \frac{\partial p^{\mathrm{w_2}}}{\partial t} + \lambda_{\mathrm{n_2}} \frac{\partial p^{\mathrm{n_2}}}{\partial t} - \lambda_{\mathrm{n_2 T}} \frac{\partial T}{\partial t} + \nabla \cdot \left\{ \boldsymbol{K}_{\mathrm{n_2}} \left(-\nabla p^{\mathrm{n_2}} + \rho^{\mathrm{n_2}} \mathbf{g} \right) \right\} = \lambda_{\mathrm{n_1 l_2}} (p^{\mathrm{n_1}} - p^{\mathrm{n_2}}). \quad (3.74)$$

The multiphase momentum balance,

$$\boldsymbol{L}_{\mathrm{eq}}^{\mathrm{T}} \left[\mathbf{D}_{\mathrm{el}} \boldsymbol{L} \mathbf{u} - \mathbf{D}_{\mathrm{el}} \mathbf{m} \left(\beta^{\mathrm{s}} / 3 \right) T - b \mathbf{m} S_{\mathrm{w1}} p^{\mathrm{w_1}} - b \mathbf{m} S_{\mathrm{n1}} p^{\mathrm{n_1}} \right] + \rho \mathbf{g} = \mathbf{0}. \quad (3.75)$$

The multiphase enthalpy balance,

$$(\rho c_p)_{\mathrm{eff}} \frac{\partial T}{\partial t} + (\rho c_p \mathbf{v})_{\mathrm{eff}} \cdot \nabla T - \sum_{\mathrm{i}=1}^{2} n_{\mathrm{i}} S_{n_{\mathrm{i}}} \beta^{\mathrm{n_i}} T \frac{\partial p^{\mathrm{n_i}}}{\partial t} - \sum_{\mathrm{i}=1}^{2} n_{\mathrm{i}} S_{n_{\mathrm{i}}} \left(\beta^{\mathrm{n_i}} T - 1 \right) \mathbf{v}^{\mathrm{n_i}} \cdot \nabla p^{\mathrm{n_i}} - \nabla \cdot \left(\boldsymbol{\chi}_{\mathrm{eff}} \nabla T \right) = 0. \quad (3.76)$$

The subscripts to the λ terms additionally denote and emphasise the important direct cross-coupling relationships within the mass balance equations. For instance, the wetting phase in the porous matrix domain $\mathrm{w_1}$, sequentially, relates firstly to itself presenting a compressibility term, then to the nonwetting phase in the matrix domain -n_1, to the solid phase (porous matrix) -s, to the thermal behaviour -T, and to the wetting phase in the fracture network domain -l_2. The latter all presenting coupling terms.

Note that, as derived, the only cross-coupling term between the sub-domains is the $\lambda_{\mathrm{w}_1\mathrm{l}_2}$ transfer/leakage term. As discussed, further elaborations on solid deformation due directly to the differential pressure between matrix and fracture sub-domains would result in $\lambda_{\mathrm{f}_1\mathrm{f}_2}$ and $\lambda_{\mathrm{f}_2\mathrm{f}_1}$ terms. Here these terms are essentially zero and any additional deformation due to the fracture network is coupled solely by any transfer via the double-porosity transfer/leakage function, the fracture network itself is therefore considered undeformable, which however is largely considered appropriate given the relatively small volume fraction of the fissure/fracture network often encounter in practice. For more appreciable volume fractions thereof, clearly further formulations would be required involving constitutive relationships encompassing grain, skeleton, and the fissure/fracture network as a natural extension.

Furthermore, this system of equations may be reduced straightforwardly in order to account for a single-porosity system (with no fissure/fracture equations), an undeformable system (with no momentum balance), or an isothermal system (with no energy balance), by cancelling/uncoupling the appropriate cross-coupling terms/equations. The results by doing so are essentially special cases which coincide with the typical results explored within the literature.

Chapter 4

Spatial Discretisation

The standard Galerkin finite element procedure is employed in order to spatially discretise the developed system of equations over a domain. During this process the appropriate initial and boundary conditions for the system sub-domains are introduced. This is to allow for the numerical solution of the coupled partial differential governing field equations.

The governing equations to be solved are posed in the following general form [207], where $\mathbf{x}$ is a vector of the multiple primary variable unknowns, satisfying the differential equation set,

$$\mathbf{A}(\mathbf{x}) = \left\{ \begin{array}{c} A_1(\mathbf{x}) \\ \vdots \end{array} \right\} = \mathbf{0} \tag{4.1}$$

within the domain Ω, with boundary conditions,

$$\mathbf{B}(\mathbf{x}) = \left\{ \begin{array}{c} B_1(\mathbf{x}) \\ \vdots \end{array} \right\} = \mathbf{0} \tag{4.2}$$

on the boundaries of the domain Γ, as illustrated in Figure 4.1. $\mathbf{A}$ and $\mathbf{B}$ prescribe known operators or functions. The differential equation set may be single and can be non-linear.

The finite element method seeks a solution for unknowns in the approximate form,

$$\mathbf{x} \approx \hat{\mathbf{x}} = \sum_{n=1}^{nds} \mathbf{N}_n \bar{\mathrm{x}}_n = \mathbf{N}\bar{\mathbf{x}} \tag{4.3}$$

where $\bar{\mathbf{x}}$ are now discrete unknowns at nodal points, and $\mathbf{N}$ are appropriate shape functions for interpolating the unknowns in terms of independent spatial coordinates defined locally within elements bound by a certain number of nodal points, nds. Casting the approximating equations in integral form permits the approximation to be gathered element-wise and assembled [207], where the number of elements, els, constitute the domain,

$$\int_{\Omega} \mathbf{A}\,\mathrm{d}\Omega + \int_{\Gamma} \mathbf{B}\,\mathrm{d}\Gamma = \sum_{e=1}^{els} \left(\int_{\Omega_e} \mathbf{A}\,\mathrm{d}\Omega + \int_{\Gamma_e} \mathbf{B}\,\mathrm{d}\Gamma \right) = \mathbf{0}, \tag{4.4}$$

provided that the integrals can be performed.

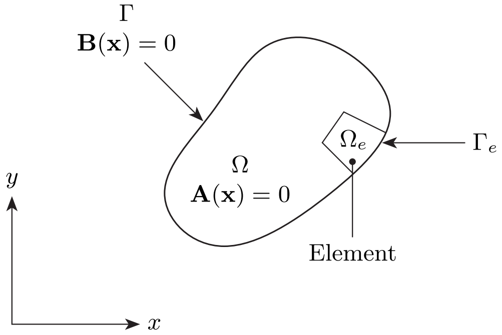

Figure 4.1: Visualisation of domain and boundary for an arbitrary problem

4.1 Method of weighted residuals (Galerkin procedure)

The *weighted residual-Galerkin procedure*, the determination of *variational functionals* for which stationarity is sought, *virtual work*, and direct *stiffness methods* are procedures for acquiring formulations giving solutions to governing equations. The first method mentioned is utilised in this work due to its generality, which makes it applicable to a variety of physical problems [118, 207].

In order to solve the differential equations an approach is taken which attempts to find an approximation by solving element-wise over a domain for equilibrium at discrete points (4.3). It generally follows that the accuracy of a solution increases with an increase in the number of discrete nodal points within the domain at an expense related to the extra computation involved.

By introducing an approximation such as (4.3) to the exact field a residual error is now defined, $\mathbf{r} = \mathbf{r}_\Omega + \mathbf{r}_\Gamma$. A solution is now sought that will minimize this error over the whole domain and its boundary. This is done by forcing a zero value for an appropriate number of integrals of the residual over the domain and boundary, weighted in different ways by weighting functions.

Adopting the following reformulation of (4.1) and (4.2),

$$\int_\Omega \mathbf{v}^\mathrm{T}\mathbf{A}(\mathbf{x})\,\mathrm{d}\Omega + \int_\Gamma \tilde{\mathbf{v}}^\mathrm{T}\mathbf{B}(\mathbf{x})\,\mathrm{d}\Gamma = \mathbf{0} \tag{4.5}$$

where $\mathbf{v}^\mathrm{T}$ and $\tilde{\mathbf{v}}^\mathrm{T}$ are sets of arbitrary functions. Equations (4.5) are satisfied equivalent to the original differential equations (4.1) and their boundary conditions (4.2). Importantly, it follows that if (4.5) is satisfied for all $\mathbf{v}$ then (4.1) and (4.2) are satisfied at all points of the domain and on the boundary [207].

It is assumed here that the integrals can be evaluated. To this effect the continuity (differentiability class) of $\mathbf{A}$ and $\mathbf{B}$ must be considered. If in any term nth-order derivatives are present then the function $\mathbf{x}$ must have continuous $n-1$ derivatives, otherwise difficulties are encountered when integrating. As is generally applicable, carrying out an integration by parts over the desired spatial dimensions for region Ω bounded by Γ gives Green's theorem, which states

$$\int_{\Omega} \varPhi \frac{\partial \varPsi}{\partial x} \, \mathrm{d}\Omega = - \int_{\Omega} \frac{\partial \varPhi}{\partial x} \varPsi \, \mathrm{d}\Omega + \int_{\Gamma} \varPhi \varPsi n_x \, \mathrm{d}\Gamma. \tag{4.6}$$

By removing the derivatives from $\mathbf{x}$ and placing them on the weighting function $\mathbf{v}$ results in terms on the boundary and lowers the order of the original operators on $\mathbf{x}$. It follows that a lower order of continuity is applicable for the choice of the $\mathbf{x}$ function at the cost of higher continuity for the shape function. Applying (4.6) to (4.5) illustrates the important alternate weak form,

$$\int_{\Omega} \mathbf{C}(\mathbf{v})^{\mathrm{T}} \mathbf{D}(\mathbf{x}) \, \mathrm{d}\Omega + \int_{\Gamma} \mathbf{E}(\tilde{\mathbf{v}})^{\mathrm{T}} \mathbf{F}(\mathbf{x}) \, \mathrm{d}\Gamma = \mathbf{0}. \tag{4.7}$$

Now if the unknown $\mathbf{x}$ is approximated via substitution of expansion (4.3) (noting that this gives formulae representing the residual error obtained by this substitution and that it is the weighted integral of this residual that is being defined), and the weight function $\mathbf{v}$ is substituted by a respective finite set of similarly expanded approximate functions $\mathbf{w}$, the following is given

$$\int_{\Omega} \mathbf{C}^{\mathrm{T}}(\mathbf{w}) \mathbf{D}(\mathbf{N}\bar{\mathbf{x}}) \, \mathrm{d}\Omega + \int_{\Gamma} \mathbf{E}^{\mathrm{T}}(\tilde{\mathbf{w}}) \mathbf{F}(\mathbf{N}\bar{\mathbf{x}}) \, \mathrm{d}\Gamma = \mathbf{0}. \tag{4.8}$$

Finally, out of the frequently employed weighting functions; *point collocation*, giving rise to finite difference methods; *Subdomain collocation*, giving rise to finite volume methods; *the Galerkin method* is adopted, whereby the shape functions are used as the weight functions $\mathbf{w} = \mathbf{N}$. This procedure typically results in symmetric matrices for computation if (4.1) is symmetric. Equation (4.8) now becomes an approximation to the statement (4.5) and results in a set of simultaneous equations for the unknowns, which are to be summed in matrix form element-wise as of (4.4).

The procedure is employed in sequence for the momentum, mass and energy balance equations, on introducing the appropriate initial and boundary conditions.

4.1.1 Momentum balance initial and boundary conditions

At time $t = 0$, the initial conditions of the displacement field are

$$\mathbf{u} = \mathbf{u}_0, \tag{4.9}$$

in Ω, the domain of interest, and on Γ, its boundary.

The boundary conditions are either imposed values (Dirichlet/essential boundary conditions) or imposed fluxes (Neumann/natural boundary conditions) on the boundaries, Γ_π and Γ_π^q respectively. The Dirichlet boundary conditions for imposing displacements are

$$\mathbf{u} = \hat{\mathbf{u}} \quad \text{on } \Gamma_{\mathrm{u}}. \tag{4.10}$$

The Neumann (traction) boundary condition for stress is given by

$$\mathbf{I}_{\mathrm{eq}}^{\mathrm{T}} \boldsymbol{\sigma} = \bar{\mathbf{t}} \quad \text{on } \Gamma_{\mathrm{u}}^{q}, \tag{4.11}$$

where $\mathbf{I}_{\mathrm{eq}}$ is the appropriate matrix related to the usual unit normal vector to the boundary, which is cast in view of the domain type after (3.46).

4.1.2 Momentum balance discretisation

Applying the weighted residual method to (3.75) and (4.11) presents,

$$\int_{\Omega} \mathbf{w}^{\mathrm{T}} \left(\boldsymbol{L}_{\mathrm{eq}}^{\mathrm{T}} \boldsymbol{\sigma} + \rho \mathbf{g}\right) \mathrm{d}\Omega \ + \int_{\Gamma_{\mathrm{u}}^{q}} \tilde{\mathbf{w}}^{\mathrm{T}} \left(\mathbf{I}_{\mathrm{eq}}^{\mathrm{T}} \boldsymbol{\sigma} - \bar{\mathbf{t}}\right) \mathrm{d}\Gamma = 0. \tag{4.12}$$

Applying Green's theorem (4.6), and limiting the weighting functions such that $\mathbf{w} = \mathbf{0}$ on Γ_{u} and $\tilde{\mathbf{w}} = -\mathbf{w}$ on Γ_{u}^{q} gives,

$$\int_{\Omega} \left(\boldsymbol{L}_{\mathrm{eq}} \mathbf{w}\right)^{\mathrm{T}} \boldsymbol{\sigma} \, \mathrm{d}\Omega \ = \int_{\Omega} \mathbf{w}^{\mathrm{T}} \rho \mathbf{g} \, \mathrm{d}\Omega \ + \int_{\Gamma_{\mathrm{u}}^{q}} \mathbf{w}^{\mathrm{T}} \bar{\mathbf{t}} \, \mathrm{d}\Gamma. \tag{4.13}$$

The primary variables are interpolated and thus expressed via the following shape functions and discrete nodal values after (4.4),

$$\mathbf{u} = \mathbf{N}_{u} \bar{\mathbf{u}} \tag{4.14}$$

$$p^{\mathrm{f_i}} = \mathbf{N}_{p} \bar{\mathbf{p}}^{\mathrm{f_i}} \tag{4.15}$$

$$T = \mathbf{N}_{T} \bar{\mathbf{T}} \tag{4.16}$$

which are introduced into (4.13). The trial/weight functions are replaced with the shape functions following the Galerkin procedure. Finally, reinstating the total stress components as of (3.75), presents

$$\begin{aligned} \int_{\Omega} \left(\boldsymbol{L}_{\mathrm{eq}} \mathbf{N}_{u}\right)^{\mathrm{T}} \mathbf{D}_{\mathrm{el}} \boldsymbol{L} \mathbf{N}_{u} \, \mathrm{d}\Omega \, \bar{\mathbf{u}} - \int_{\Omega} \left(\boldsymbol{L}_{\mathrm{eq}} \mathbf{N}_{u}\right)^{\mathrm{T}} b \mathbf{m} S_{\mathrm{w1}} \mathbf{N}_{p} \, \mathrm{d}\Omega \, \bar{\mathbf{p}}^{\mathrm{w_1}} - \int_{\Omega} \left(\boldsymbol{L}_{\mathrm{eq}} \mathbf{N}_{u}\right)^{\mathrm{T}} b \mathbf{m} S_{\mathrm{n1}} \mathbf{N}_{p} \, \mathrm{d}\Omega \, \bar{\mathbf{p}}^{\mathrm{n_1}} \\ - \int_{\Omega} \left(\boldsymbol{L}_{\mathrm{eq}} \mathbf{N}_{u}\right)^{\mathrm{T}} \mathbf{D}_{\mathrm{el}} \mathbf{m} \left(\beta_{\mathrm{s}}/3\right) \mathbf{N}_{T} \, \mathrm{d}\Omega \, \bar{\mathbf{T}} \ = \int_{\Omega} \mathbf{N}_{u}^{\mathrm{T}} \rho \mathbf{g} \, \mathrm{d}\Omega \ + \int_{\Gamma_{\mathrm{u}}^{q}} \mathbf{N}_{u}^{\mathrm{T}} \bar{\mathbf{t}} \, \mathrm{d}\Gamma. \end{aligned} \tag{4.17}$$

The discretised primary variables have been taken out of the integrals because they are nodal values and do not depend on the volume integration.

4.1.3 Mass balance initial and boundary conditions

At time $t = 0$, the initial conditions of the pressure fields are

$$p^{\mathrm{f_i}} = p_{0}^{\mathrm{f_i}}, \tag{4.18}$$

in Ω, the domain of interest, and on Γ, its boundary.

The Dirichlet boundary conditions for imposing pressures are

$$p^{\mathrm{f_i}} = \hat{p}^{\mathrm{f_i}} \quad \text{on } \Gamma_{\mathrm{f}}. \tag{4.19}$$

The Neumann boundary condition for the fluids, imposing a mass flux across the boundary, after (2.33), is given by,

$$q^{\mathrm{f_i}} = \rho^{\mathrm{f_i}} \frac{k_{\mathrm{rf_i}}\mathbf{k}_{\mathrm{i}}}{\mu^{\mathrm{f_i}}} \left(-\nabla p^{\mathrm{f_i}} + \rho^{\mathrm{f_i}}\mathbf{g}\right)^{\mathrm{T}} \cdot \mathbf{n} \quad \text{on } \Gamma_{\mathrm{f}}^{q}. \tag{4.20}$$

where $\mathbf{n}$ is the usual unit normal vector to the boundary.

4.1.4 Mass balance discretisation

Applying the weighted residual method to a generic version of the mass balances for the porous matrix continua (3.71) and (3.72), and to the boundary condition (4.20) presents,

$$\int_{\Omega} \mathbf{w}^{\mathrm{T}} \left[\lambda \frac{\partial p^{\mathrm{w_1}}}{\partial t} + \lambda \frac{\partial p^{\mathrm{n_1}}}{\partial t} + \lambda \boldsymbol{L} \frac{\partial \mathbf{u}}{\partial t} - \lambda \frac{\partial T}{\partial t} + \nabla \cdot \left\{\boldsymbol{K}_{\mathrm{f_1}} \left(-\nabla p^{\mathrm{f_1}} + \rho^{\mathrm{f_1}}\mathbf{g}\right)\right\} + \lambda \left(p^{\mathrm{f_1}} - p^{\mathrm{f_2}}\right)\right] \mathrm{d}\Omega$$
$$+ \int_{\Gamma_{\mathrm{f}}^{q}} \tilde{\mathbf{w}}^{\mathrm{T}} \left[\boldsymbol{K}_{\mathrm{f_1}} \left(-\nabla p^{\mathrm{f_i}} + \rho^{\mathrm{f_i}}\mathbf{g}\right)^{\mathrm{T}} \cdot \mathbf{n} - \frac{q^{\mathrm{f_i}}}{\rho^{\mathrm{f_i}}}\right] \mathrm{d}\Gamma = 0. \tag{4.21}$$

Applying Green's theorem (4.6) to the divergence operator, and limiting the weighting functions such that $\mathbf{w} = 0$ on Γ_{f} and $\tilde{\mathbf{w}} = -\mathbf{w}$ on Γ_{f}^{q}, whilst expanding in part and rearranging, gives

$$\int_{\Omega} \left[\mathbf{w}^{\mathrm{T}} \lambda \frac{\partial p^{\mathrm{w_1}}}{\partial t} + \mathbf{w}^{\mathrm{T}} \lambda \frac{\partial p^{\mathrm{n_1}}}{\partial t} + \mathbf{w}^{\mathrm{T}} \lambda \boldsymbol{L} \frac{\partial \mathbf{u}}{\partial t} - \mathbf{w}^{\mathrm{T}} \lambda \frac{\partial T}{\partial t} + \mathbf{w}^{\mathrm{T}} \lambda \left(p^{\mathrm{f_1}} - p^{\mathrm{f_2}}\right)\right] \mathrm{d}\Omega$$
$$+ \int_{\Omega} (\nabla \mathbf{w})^{\mathrm{T}} \boldsymbol{K}_{\mathrm{f_1}} \nabla p^{\mathrm{f_1}} \, \mathrm{d}\Omega = \int_{\Omega} (\nabla \mathbf{w})^{\mathrm{T}} \boldsymbol{K}_{\mathrm{f_1}} \rho^{\mathrm{f_1}} \mathbf{g} \, \mathrm{d}\Omega - \int_{\Gamma_{\mathrm{f}}^{q}} \mathbf{w}^{\mathrm{T}} \frac{q^{\mathrm{f_i}}}{\rho^{\mathrm{f_i}}} \, \mathrm{d}\Gamma. \tag{4.22}$$

The primary variables are interpolated and thus expressed via shape functions and discrete nodal values, as of (4.4), which are introduced into (4.22). The trial/weight functions are also replaced with the shape functions, giving the following form for both porous matrix continuity equations,

$$\int_{\Omega} \mathbf{N}_p^{\mathrm{T}} \lambda \mathbf{N}_p \, \mathrm{d}\Omega \, \frac{\partial \bar{\mathbf{p}}^{\mathrm{w_1}}}{\partial t} + \int_{\Omega} \mathbf{N}_p^{\mathrm{T}} \lambda \mathbf{N}_p \, \mathrm{d}\Omega \, \frac{\partial \bar{\mathbf{p}}^{\mathrm{n_1}}}{\partial t} + \int_{\Omega} \mathbf{N}_p^{\mathrm{T}} \lambda \boldsymbol{L} \mathbf{N}_u \, \mathrm{d}\Omega \, \frac{\partial \bar{\mathbf{u}}}{\partial t} - \int_{\Omega} \mathbf{N}_p^{\mathrm{T}} \lambda \mathbf{N}_T \, \mathrm{d}\Omega \, \frac{\partial \bar{\mathbf{T}}}{\partial t}$$
$$+ \int_{\Omega} \mathbf{N}_p^{\mathrm{T}} \lambda \mathbf{N}_p \, \mathrm{d}\Omega \, \bar{\mathbf{p}}^{\mathrm{f_1}} - \int_{\Omega} \mathbf{N}_p^{\mathrm{T}} \lambda \mathbf{N}_p \, \mathrm{d}\Omega \, \bar{\mathbf{p}}^{\mathrm{f_2}} + \int_{\Omega} (\nabla \mathbf{N}_p)^{\mathrm{T}} \boldsymbol{K}_{\mathrm{f_1}} \nabla \mathbf{N}_p \, \mathrm{d}\Omega \, \bar{\mathbf{p}}^{\mathrm{f_1}}$$
$$= \int_{\Omega} (\nabla \mathbf{N}_p)^{\mathrm{T}} \boldsymbol{K}_{\mathrm{f_1}} \rho^{\mathrm{f_1}} \mathbf{g} \, \mathrm{d}\Omega - \int_{\Gamma_{\mathrm{f}}^{q}} \mathbf{N}_p^{\mathrm{T}} \frac{q^{\mathrm{f_1}}}{\rho^{\mathrm{f_1}}} \, \mathrm{d}\Gamma. \tag{4.23}$$

Carrying out the same procedure for the fissured/fractured domain continua (3.73) and (3.74), gives the following form for the two continuity equations,

$$\int_{\Omega} \mathbf{N}_p^{\mathrm{T}} \lambda \mathbf{N}_p \, \mathrm{d}\Omega \, \frac{\partial \bar{\mathbf{p}}^{\mathrm{w_2}}}{\partial t} + \int_{\Omega} \mathbf{N}_p^{\mathrm{T}} \lambda \mathbf{N}_p \, \mathrm{d}\Omega \, \frac{\partial \bar{\mathbf{p}}^{\mathrm{n_2}}}{\partial t} - \int_{\Omega} \mathbf{N}_p^{\mathrm{T}} \lambda \mathbf{N}_T \, \mathrm{d}\Omega \, \frac{\partial \bar{\mathbf{T}}}{\partial t}$$
$$- \int_{\Omega} \mathbf{N}_p^{\mathrm{T}} \lambda \mathbf{N}_p \, \mathrm{d}\Omega \, \bar{\mathbf{p}}^{\mathrm{f_1}} + \int_{\Omega} \mathbf{N}_p^{\mathrm{T}} \lambda \mathbf{N}_p \, \mathrm{d}\Omega \, \bar{\mathbf{p}}^{\mathrm{f_2}} + \int_{\Omega} (\nabla \mathbf{N}_p)^{\mathrm{T}} \boldsymbol{K}_{\mathrm{f_2}} \nabla \mathbf{N}_p \, \mathrm{d}\Omega \, \bar{\mathbf{p}}^{\mathrm{f_2}}$$
$$= \int_{\Omega} (\nabla \mathbf{N}_p)^{\mathrm{T}} \boldsymbol{K}_{\mathrm{f_2}} \rho^{\mathrm{f_2}} \mathbf{g} \, \mathrm{d}\Omega - \int_{\Gamma_{\mathrm{f}}^{q}} \mathbf{N}_p^{\mathrm{T}} \frac{q^{\mathrm{f_2}}}{\rho^{\mathrm{f_2}}} . \, \mathrm{d}\Gamma. \tag{4.24}$$

The λ and $\boldsymbol{K}_{\mathrm{f_i}}$ coefficients will be stipulated for their respective terms when the system of equations is cast fully in matrix form in Section 4.2.

4.1.5 Energy balance initial and boundary conditions

At time $t = 0$, the initial conditions of the temperature field are

$$T = T_0, \tag{4.25}$$

in Ω, the domain of interest, and on Γ, its boundary.

The Dirichlet boundary conditions for imposing temperature are

$$T = \hat{T} \quad \text{on } \Gamma_{\mathrm{T}}. \tag{4.26}$$

The Neumann boundary condition for heat transfer across the boundary, after (2.32), is given by,

$$\left(-\boldsymbol{\chi}_{\mathrm{eff}} \nabla T\right)^{\mathrm{T}} \cdot \mathbf{n} = \mathrm{q}^T \quad \text{on } \Gamma_T^q. \tag{4.27}$$

where $\mathbf{n}$ is the usual unit normal vector to the boundary and q^T is the prescribed heat flux.

4.1.6 Energy balance discretisation

Applying the weighted residual method to the energy balance equation for the bulk medium (3.76) presents,

$$\begin{aligned}
&\int_\Omega \mathbf{w}^{\mathrm{T}} \left[(\rho c_p)_{\mathrm{eff}} \frac{\partial T}{\partial t} + (\rho c_p \mathbf{v})_{\mathrm{eff}} \cdot \nabla T - \nabla \cdot (\boldsymbol{\chi}_{\mathrm{eff}} \nabla T) \right] \mathrm{d}\Omega \\
&\quad - \int_\Omega \mathbf{w}^{\mathrm{T}} \left[\sum_{\mathrm{i}=1}^{2} n_{\mathrm{i}} S_{n_{\mathrm{i}}} \beta^{\mathrm{n_i}} T \frac{\partial p^{\mathrm{n_i}}}{\partial t} + \sum_{\mathrm{i}=1}^{2} n_{\mathrm{i}} S_{n_{\mathrm{i}}} \left(\beta^{\mathrm{n_i}} T - 1\right) \mathbf{v}^{\mathrm{n_i}} \cdot \nabla p^{\mathrm{n_i}} \right] \mathrm{d}\Omega \\
&\qquad + \int_{\Gamma_T^q} \tilde{\mathbf{w}}^{\mathrm{T}} \left[\left(-\boldsymbol{\chi}_{\mathrm{eff}} \nabla T\right)^{\mathrm{T}} \cdot \mathbf{n} - \mathrm{q}^T \right] \mathrm{d}\Gamma = 0.
\end{aligned} \tag{4.28}$$

Applying Green's theorem (4.6) to the divergence operator, and limiting the weighting functions such that $\mathbf{w} = 0$ on Γ_T and $\tilde{\mathbf{w}} = -\mathbf{w}$ on Γ_T^q, whilst expanding in part and rearranging gives,

$$\begin{aligned}
&\int_\Omega \mathbf{w}^{\mathrm{T}} \left[(\rho c_p)_{\mathrm{eff}} \frac{\partial T}{\partial t} + (\rho c_p \mathbf{v})_{\mathrm{eff}} \cdot \nabla T \right] \mathrm{d}\Omega + \int_\Omega (\nabla \mathbf{w})^{\mathrm{T}} \boldsymbol{\chi}_{\mathrm{eff}} \nabla T \, \mathrm{d}\Omega \\
&- \int_\Omega \mathbf{w}^{\mathrm{T}} \left[\sum_{\mathrm{i}=1}^{2} n_{\mathrm{i}} S_{n_{\mathrm{i}}} \beta^{\mathrm{n_i}} T \frac{\partial p^{\mathrm{n_i}}}{\partial t} + \sum_{\mathrm{i}=1}^{2} n_{\mathrm{i}} S_{n_{\mathrm{i}}} \left(\beta^{\mathrm{n_i}} T - 1\right) \mathbf{v}^{\mathrm{n_i}} \cdot \nabla p^{\mathrm{n_i}} \right] \mathrm{d}\Omega + \int_{\Gamma_T^q} \mathbf{w}^{\mathrm{T}} \mathrm{q}^T \mathrm{d}\Gamma = 0.
\end{aligned} \tag{4.29}$$

The primary variables are interpolated with shape functions from discrete nodal values, after (4.4), which are incorporated into (4.29). The trial/weight functions are replaced with the shape functions, following the Galerkin procedure, giving finally,

$$\begin{aligned}
&\int_\Omega \mathbf{N}_T^{\mathrm{T}} \left(\rho c_p\right)_{\mathrm{eff}} \mathbf{N}_T \,\mathrm{d}\Omega \,\frac{\partial \bar{\mathbf{T}}}{\partial t} + \int_\Omega \mathbf{N}_T^{\mathrm{T}} \left(\rho c_p \mathbf{v}\right)_{\mathrm{eff}} \cdot \nabla \mathbf{N}_T \,\mathrm{d}\Omega \,\bar{\mathbf{T}} + \int_\Omega \left(\nabla \mathbf{N}_T\right)^{\mathrm{T}} \boldsymbol{\chi}_{\mathrm{eff}} \nabla \mathbf{N}_T \,\mathrm{d}\Omega \,\bar{\mathbf{T}} \\
&\qquad - \int_\Omega \mathbf{N}_T^{\mathrm{T}} n_1 S_{n_1} \beta^{\mathrm{n}_1} T \mathbf{N}_p \,\mathrm{d}\Omega \,\frac{\partial \bar{\mathbf{p}}^{\mathrm{n}_1}}{\partial t} - \int_\Omega \mathbf{N}_T^{\mathrm{T}} n_1 S_{n_1} \left(\beta^{\mathrm{n}_1} T - 1\right) \mathbf{v}^{\mathrm{n}_1} \cdot \nabla \mathbf{N}_p \,\mathrm{d}\Omega \,\bar{\mathbf{p}}^{\mathrm{n}_1} \\
&\qquad - \int_\Omega \mathbf{N}_T^{\mathrm{T}} n_2 S_{n_2} \beta^{\mathrm{n}_2} T \mathbf{N}_p \,\mathrm{d}\Omega \,\frac{\partial \bar{\mathbf{p}}^{\mathrm{n}_2}}{\partial t} - \int_\Omega \mathbf{N}_T^{\mathrm{T}} n_2 S_{n_2} \left(\beta^{\mathrm{n}_2} T - 1\right) \mathbf{v}^{\mathrm{n}_2} \cdot \nabla \mathbf{N}_p \,\mathrm{d}\Omega \,\bar{\mathbf{p}}^{\mathrm{n}_2} \\
&\qquad\qquad = - \int_{\Gamma_T^q} \mathbf{N}_T^{\mathrm{T}} \mathrm{q}^T \,\mathrm{d}\Gamma. \qquad (4.30)
\end{aligned}$$

Note that for all governing equations, the essential boundary conditions are automatically satisfied by the choice of functions on Γ_π, and that the natural boundary conditions are satisfied automatically during the weak formulation. During the discretisation process the gradient and divergence operators, which now operate on the shape function arrays, have become ∇ and ∇^{T} respectively, where for three dimensions

$$\nabla = \left\{ \begin{array}{c} \frac{\partial}{\partial x} \\ \frac{\partial}{\partial y} \\ \frac{\partial}{\partial z} \end{array} \right\}. \qquad (4.31)$$

4.2 The spatially discretised system of equations

Reinstating the full coefficients represented by the λ terms and casting all the spatially discretised governing equations in matrix form presents an ordinary differential equation set in respect of time, whereby the components of system coupling are conveniently highlighted,

$$\left[\begin{array}{c|cc|cc|c}
\mathbf{K}_1 & \mathbf{Q}_{\mathrm{uw1}} & \mathbf{Q}_{\mathrm{un1}} & \mathbf{0} & \mathbf{0} & \mathbf{Q}_{\mathrm{uT}} \\ \hline
\mathbf{Q}_{\mathrm{wu1}} & \mathbf{S}_{\mathrm{w1}} & \mathbf{Q}_{\mathrm{wn1}} & \mathbf{0} & \mathbf{0} & \mathbf{Q}_{\mathrm{w1T}} \\
\mathbf{Q}_{\mathrm{nu1}} & \mathbf{Q}_{\mathrm{nw1}} & \mathbf{S}_{\mathrm{n1}} & \mathbf{0} & \mathbf{0} & \mathbf{Q}_{\mathrm{n1T}} \\ \hline
\mathbf{0} & \mathbf{0} & \mathbf{0} & \mathbf{S}_{\mathrm{w2}} & \mathbf{Q}_{\mathrm{wn2}} & \mathbf{Q}_{\mathrm{w2T}} \\
\mathbf{0} & \mathbf{0} & \mathbf{0} & \mathbf{Q}_{\mathrm{nw2}} & \mathbf{S}_{\mathrm{n2}} & \mathbf{Q}_{\mathrm{n2T}} \\ \hline
\mathbf{0} & \mathbf{0} & \mathbf{Q}_{\mathrm{Tn1}} & \mathbf{0} & \mathbf{Q}_{\mathrm{Tn2}} & \mathbf{C}_{\mathrm{T}}
\end{array} \right]
\frac{\mathrm{d}}{\mathrm{d}t}
\left\{ \begin{array}{c}
\bar{\mathbf{u}} \\ \hline
\bar{\mathbf{p}}^{\mathrm{w}_1} \\
\bar{\mathbf{p}}^{\mathrm{n}_1} \\ \hline
\bar{\mathbf{p}}^{\mathrm{w}_2} \\
\bar{\mathbf{p}}^{\mathrm{n}_2} \\ \hline
\bar{\mathbf{T}}
\end{array} \right\} +$$

$$\left[\begin{array}{c|cc|cc|c}
\mathbf{0} & \mathbf{0} & \mathbf{0} & \mathbf{0} & \mathbf{0} & \mathbf{0} \\ \hline
\mathbf{0} & \mathbf{H}_{\mathrm{w1}} + \mathbf{L}_{\mathrm{w}} & \mathbf{0} & -\mathbf{L}_{\mathrm{w}} & \mathbf{0} & \mathbf{0} \\
\mathbf{0} & \mathbf{0} & \mathbf{H}_{\mathrm{n1}} + \mathbf{L}_{\mathrm{n}} & \mathbf{0} & -\mathbf{L}_{\mathrm{n}} & \mathbf{0} \\ \hline
\mathbf{0} & -\mathbf{L}_{\mathrm{w}} & \mathbf{0} & \mathbf{H}_{\mathrm{w2}} + \mathbf{L}_{\mathrm{w}} & \mathbf{0} & \mathbf{0} \\
\mathbf{0} & \mathbf{0} & -\mathbf{L}_{\mathrm{n}} & \mathbf{0} & \mathbf{H}_{\mathrm{n2}} + \mathbf{L}_{\mathrm{n}} & \mathbf{0} \\ \hline
\mathbf{0} & \mathbf{0} & \mathbf{H}_{\mathrm{Tn1}} & \mathbf{0} & \mathbf{H}_{\mathrm{Tn2}} & \mathbf{H}_{\mathrm{T}}
\end{array} \right]
\left\{ \begin{array}{c}
\bar{\mathbf{u}} \\ \hline
\bar{\mathbf{p}}^{\mathrm{w}_1} \\
\bar{\mathbf{p}}^{\mathrm{n}_1} \\ \hline
\bar{\mathbf{p}}^{\mathrm{w}_2} \\
\bar{\mathbf{p}}^{\mathrm{n}_2} \\ \hline
\bar{\mathbf{T}}
\end{array} \right\}
=
\left\{ \begin{array}{c}
\frac{\mathrm{d}}{\mathrm{d}t}\mathbf{f}_{\mathrm{u}} \\ \hline
\mathbf{f}_{\mathrm{w1}} \\
\mathbf{f}_{\mathrm{n1}} \\ \hline
\mathbf{f}_{\mathrm{w2}} \\
\mathbf{f}_{\mathrm{n2}} \\ \hline
\mathbf{f}_{\mathrm{T}}
\end{array} \right\} \qquad (4.32)$$

where the sub-matrices are

$$\mathbf{K}_1 = \int_\Omega \mathbf{B}^{\mathrm{T}} \mathbf{D}_{\mathrm{el}} \mathbf{B} \,\mathrm{d}\Omega, \qquad (4.33)$$

$$\mathbf{Q}_{\mathrm{uw1}} = - \int_\Omega \mathbf{B}^{\mathrm{T}} b S_{\mathrm{w}_1} \mathbf{m} \mathbf{N}_p \,\mathrm{d}\Omega, \qquad (4.34)$$

$$\mathbf{Q}_{\mathrm{un1}} = -\int_{\Omega} \mathbf{B}^{\mathrm{T}} b S_{\mathrm{n}_1} \mathbf{m} \mathbf{N}_p \, \mathrm{d}\Omega, \tag{4.35}$$

$$\mathbf{Q}_{\mathrm{uT}} = -\int_{\Omega} \mathbf{B}^{\mathrm{T}} \mathbf{D}_{\mathrm{el}} \mathbf{m} \left(\beta^{\mathrm{s}}/3\right) \mathbf{N}_T \, \mathrm{d}\Omega, \tag{4.36}$$

$$\mathbf{f}_{\mathrm{u}} = \int_{\Omega} \mathbf{N}_{\mathrm{u}}^{\mathrm{T}} \left[(1-n_1)\rho^{\mathrm{s}} + n_1 S_{\mathrm{w1}} \rho^{\mathrm{w1}} + n_1 S_{\mathrm{n1}} \rho^{n1}\right] \mathbf{g} \, \mathrm{d}\Omega + \int_{\Gamma_{\mathrm{u}}^q} \mathbf{N}_{\mathrm{u}}^{\mathrm{T}} \mathbf{t} \, \mathrm{d}\Gamma \tag{4.37}$$

- - - -

$$\mathbf{Q}_{\mathrm{wu1}} = \int_{\Omega} \mathbf{N}_p^{\mathrm{T}} b S_{\mathrm{w}_1} \mathbf{m}^{\mathrm{T}} \mathbf{B} \, \mathrm{d}\Omega = \mathbf{Q}_{\mathrm{uw1}}^{\mathrm{T}}, \tag{4.38}$$

$$\mathbf{S}_{\mathrm{w1}} = \int_{\Omega} \mathbf{N}_p^{\mathrm{T}} \left[\frac{b-n_1}{K_{\mathrm{s}}} S_{\mathrm{w}_1} \left(S_{\mathrm{w}_1} + p^{\mathrm{c}_1} \frac{\partial S_{\mathrm{w}_1}}{\partial p^{\mathrm{c}_1}}\right) + \frac{n_1 S_{\mathrm{w}_1}}{K_{\mathrm{w}_1}} - n_1 \frac{\partial S_{\mathrm{w}_1}}{\partial p^{\mathrm{c}_1}}\right] \mathbf{N}_p \, \mathrm{d}\Omega, \tag{4.39}$$

$$\mathbf{Q}_{\mathrm{wn1}} = \int_{\Omega} \mathbf{N}_p^{\mathrm{T}} \left[\frac{b-n_1}{K_{\mathrm{s}}} S_{\mathrm{w}_1} \left(S_{\mathrm{n}_1} - p^{\mathrm{c}_1} \frac{\partial S_{\mathrm{w}_1}}{\partial p^{\mathrm{c}_1}}\right) + n_1 \frac{\partial S_{\mathrm{w}_1}}{\partial p^{\mathrm{c}_1}}\right] \mathbf{N}_p \, \mathrm{d}\Omega, \tag{4.40}$$

$$\mathbf{Q}_{\mathrm{w1T}} = -\int_{\Omega} \mathbf{N}_p^{\mathrm{T}} \, S_{\mathrm{w}_1} \left[\beta^{\mathrm{s}} \left(b-n_1\right) + n_1 \beta^{\mathrm{w}_1}\right] \mathbf{N}_T \, \mathrm{d}\Omega, \tag{4.41}$$

$$\mathbf{H}_{\mathrm{w1}} = \int_{\Omega} \left(\nabla \mathbf{N}_p\right)^{\mathrm{T}} \frac{k_{\mathrm{rw}_1} \mathbf{k}_1}{\mu^{\mathrm{w}_1}} \nabla \mathbf{N}_p \, \mathrm{d}\Omega, \tag{4.42}$$

$$\mathbf{L}_{\mathrm{w}} = \int_{\Omega} \mathbf{N}_p^{\mathrm{T}} \frac{\bar{\alpha}\, k_{\mathrm{rw}_1} \mathrm{k}_1}{\mu^{\mathrm{w}_1}} \mathbf{N}_p \, \mathrm{d}\Omega, \tag{4.43}$$

$$\mathbf{f}_{\mathrm{w1}} = \int_{\Omega} \left(\nabla \mathbf{N}_p\right)^{\mathrm{T}} \frac{k_{\mathrm{rw}_1} \mathbf{k}_1}{\mu^{\mathrm{w}_1}} \rho^{\mathrm{w}_1} \mathbf{g} \, \mathrm{d}\Omega - \left\{\int_{\Gamma_{\mathrm{f}}^q} \mathbf{N}_p^{\mathrm{T}} \frac{q^{\mathrm{w}_1}}{\rho^{\mathrm{w}_1}} \, \mathrm{d}\Gamma\right\}, \tag{4.44}$$

- - - -

$$\mathbf{Q}_{\mathrm{nu1}} = \int_{\Omega} \mathbf{N}_p^{\mathrm{T}} b S_{\mathrm{n}_1} \mathbf{m}^{\mathrm{T}} \mathbf{B} \, \mathrm{d}\Omega = \mathbf{Q}_{\mathrm{un1}}^{\mathrm{T}}, \tag{4.45}$$

$$\mathbf{Q}_{\mathrm{nw1}} = \int_{\Omega} \mathbf{N}_p^{\mathrm{T}} \left[\frac{b-n_1}{K_{\mathrm{s}}} S_{\mathrm{n}_1} \left(S_{\mathrm{w}_1} + p^{\mathrm{c}_1} \frac{\partial S_{\mathrm{w}_1}}{\partial p^{\mathrm{c}_1}}\right) + n_1 \frac{\partial S_{\mathrm{w}_1}}{\partial p^{\mathrm{c}_1}}\right] \mathbf{N}_p \, \mathrm{d}\Omega, \tag{4.46}$$

$$\mathbf{S}_{\mathrm{n1}} = \int_{\Omega} \mathbf{N}_p^{\mathrm{T}} \left[\frac{b-n_1}{K_{\mathrm{s}}} S_{\mathrm{n}_1} \left(S_{\mathrm{n}_1} - p^{\mathrm{c}_1} \frac{\partial S_{\mathrm{w}_1}}{\partial p^{\mathrm{c}_1}}\right) + \frac{n_1 S_{\mathrm{n}_1}}{K_{\mathrm{n}_1}} - n_1 \frac{\partial S_{\mathrm{w}_1}}{\partial p^{\mathrm{c}_1}}\right] \mathbf{N}_p \, \mathrm{d}\Omega, \tag{4.47}$$

$$\mathbf{Q}_{\mathrm{n1T}} = -\int_{\Omega} \mathbf{N}_p^{\mathrm{T}} \, S_{\mathrm{n}_1} \left[\beta^{\mathrm{s}} \left(b-n_1\right) + n_1 \beta^{\mathrm{n}_1}\right] \mathbf{N}_T \, \mathrm{d}\Omega, \tag{4.48}$$

$$\mathbf{H}_{\mathrm{n1}} = \int_{\Omega} \left(\nabla \mathbf{N}_p\right)^{\mathrm{T}} \frac{k_{\mathrm{rn}_1} \mathbf{k}_1}{\mu^{\mathrm{n}_1}} \nabla \mathbf{N}_p \, \mathrm{d}\Omega, \tag{4.49}$$

$$\mathbf{L}_{\mathrm{n}} = \int_{\Omega} \mathbf{N}_p^{\mathrm{T}} \frac{\bar{\alpha}\, k_{\mathrm{rn}_1} \mathrm{k}_1}{\mu^{\mathrm{n}_1}} \mathbf{N}_p \, \mathrm{d}\Omega, \tag{4.50}$$

$$\mathbf{f}_{\mathrm{n1}} = \int_{\Omega} \left(\nabla \mathbf{N}_p\right)^{\mathrm{T}} \frac{k_{\mathrm{rn}_1} \mathbf{k}_1}{\mu^{\mathrm{n}_1}} \rho^{\mathrm{n}_1} \mathbf{g} \, \mathrm{d}\Omega - \left\{\int_{\Gamma_{\mathrm{f}}^q} \mathbf{N}_p^{\mathrm{T}} \frac{q^{\mathrm{n}_1}}{\rho^{\mathrm{n}_1}} \, \mathrm{d}\Gamma\right\}, \tag{4.51}$$

- - - -

$$\mathbf{S}_{\mathrm{w2}} = \int_{\Omega} \mathbf{N}_p^{\mathrm{T}} \left[\frac{n_2 S_{\mathrm{w}_2}}{K_{\mathrm{w}_2}} - n_2 \frac{\partial S_{\mathrm{w}_2}}{\partial p^{\mathrm{c}_2}}\right] \mathbf{N}_p \, \mathrm{d}\Omega, \tag{4.52}$$

$$\mathbf{Q}_{\mathrm{wn2}} = \int_{\Omega} \mathbf{N}_p^{\mathrm{T}} n_2 \frac{\partial S_{\mathrm{w}_2}}{\partial p^{\mathrm{c}_2}} \mathbf{N}_p \, \mathrm{d}\Omega, \tag{4.53}$$

$$\mathbf{Q}_{\mathrm{w2T}} = -\int_{\Omega} \mathbf{N}_p^{\mathrm{T}} \, S_{\mathrm{w}_2} n_2 \beta^{\mathrm{w}_2} \, \mathbf{N}_T \, \mathrm{d}\Omega, \tag{4.54}$$

$$\mathbf{H}_{\mathrm{w2}} = \int_{\Omega} \left(\nabla \mathbf{N}_p\right)^{\mathrm{T}} \frac{k_{\mathrm{rw}_2} \mathbf{k}_2}{\mu^{\mathrm{w}_2}} \nabla \mathbf{N}_p \, \mathrm{d}\Omega, \tag{4.55}$$

$$\mathbf{f}_{\mathrm{w2}} = \int_{\Omega} \left(\nabla \mathbf{N}_p\right)^{\mathrm{T}} \frac{k_{\mathrm{rw}_2} \mathbf{k}_2}{\mu^{\mathrm{w}_2}} \rho^{\mathrm{w}_2} \mathbf{g} \, \mathrm{d}\Omega - \left\{\int_{\Gamma_{\mathrm{f}}^q} \mathbf{N}_p^{\mathrm{T}} \frac{q^{\mathrm{w}_2}}{\rho^{\mathrm{w}_2}} \, \mathrm{d}\Gamma\right\}, \tag{4.56}$$

- - - -

$$\mathbf{Q}_{\mathrm{nw2}} = \int_\Omega \mathbf{N}_p^{\mathrm{T}} n_2 \frac{\partial S_{\mathrm{w2}}}{\partial p^{\mathrm{c2}}} \mathbf{N}_p \, \mathrm{d}\Omega, \tag{4.57}$$

$$\mathbf{S}_{\mathrm{n2}} = \int_\Omega \mathbf{N}_p^{\mathrm{T}} \left[\frac{n_2 S_{\mathrm{n_2}}}{K_{\mathrm{n_2}}} - n_2 \frac{\partial S_{\mathrm{w2}}}{\partial p^{\mathrm{c2}}} \right] \mathbf{N}_p \, \mathrm{d}\Omega, \tag{4.58}$$

$$\mathbf{Q}_{\mathrm{n2T}} = -\int_\Omega \mathbf{N}_p^{\mathrm{T}} \, S_{\mathrm{n_2}} n_2 \beta^{\mathrm{n_2}} \, \mathbf{N}_T \, \mathrm{d}\Omega, \tag{4.59}$$

$$\mathbf{H}_{\mathrm{n2}} = \int_\Omega \left(\nabla \mathbf{N}_p\right)^{\mathrm{T}} \frac{k_{\mathrm{rn_2}} \mathbf{k}_2}{\mu^{\mathrm{n_2}}} \nabla \mathbf{N}_p \, \mathrm{d}\Omega, \tag{4.60}$$

$$\mathbf{f}_{\mathrm{n2}} = \int_\Omega \left(\nabla \mathbf{N}_p\right)^{\mathrm{T}} \frac{k_{\mathrm{rn_2}} \mathbf{k}_2}{\mu^{\mathrm{n_2}}} \rho^{\mathrm{n_2}} \mathbf{g} \, \mathrm{d}\Omega - \int_{\Gamma_{\mathrm{f}}^q} \mathbf{N}_p^{\mathrm{T}} \frac{q^{\mathrm{n_2}}}{\rho^{\mathrm{n_2}}} \, \mathrm{d}\Gamma, \tag{4.61}$$

\- - - -

$$\mathbf{Q}_{\mathrm{Tn1}} = -\int_\Omega \mathbf{N}_T^{\mathrm{T}} n_1 S_{\mathrm{n_1}} \beta^{\mathrm{n_1}} T \, \mathbf{N}_p \, \mathrm{d}\Omega, \tag{4.62}$$

$$\mathbf{Q}_{\mathrm{Tn2}} = -\int_\Omega \mathbf{N}_T^{\mathrm{T}} n_2 S_{\mathrm{n_2}} \beta^{\mathrm{n_2}} T \, \mathbf{N}_p \, \mathrm{d}\Omega, \tag{4.63}$$

$$\mathbf{C}_{\mathrm{T}} = \int_\Omega \mathbf{N}_T^{\mathrm{T}} \left(\rho c_p\right)_{\mathrm{eff}} \mathbf{N}_T \, \mathrm{d}\Omega, \tag{4.64}$$

$$\mathbf{H}_{\mathrm{Tn1}} = -\int_\Omega \mathbf{N}_T^{\mathrm{T}} n_1 S_{\mathrm{n_1}} \left(\beta^{\mathrm{n_1}} T - 1\right) \mathbf{v}^{\mathrm{n_1}} \cdot \nabla \mathbf{N}_p \, \mathrm{d}\Omega, \tag{4.65}$$

$$\mathbf{H}_{\mathrm{Tn2}} = -\int_\Omega \mathbf{N}_T^{\mathrm{T}} n_2 S_{\mathrm{n_2}} \left(\beta^{\mathrm{n_2}} T - 1\right) \mathbf{v}^{\mathrm{n_2}} \cdot \nabla \mathbf{N}_p \, \mathrm{d}\Omega, \tag{4.66}$$

$$\mathbf{H}_{\mathrm{T}} = \int_\Omega \mathbf{N}_T^{\mathrm{T}} \left(\rho c_p \mathbf{v}\right)_{\mathrm{eff}} \cdot \nabla \mathbf{N}_T + \left(\nabla \mathbf{N}_T\right)^{\mathrm{T}} \boldsymbol{\chi}_{\mathrm{eff}} \nabla \mathbf{N}_T \, \mathrm{d}\Omega, \tag{4.67}$$

$$\mathbf{f}_{\mathrm{T}} = -\int_{\Gamma_T^q} \mathbf{N}_T^{\mathrm{T}} \mathrm{q}^T \, \mathrm{d}\Gamma. \tag{4.68}$$

The listed matrices distribute the associated properties over the domain and on its boundaries, where the subscripts denote the associated primary variable, sub-domain, and therefore any coupling. Symbols **K**, **Q**, **S**, **C**, **H**, and **L**, refer to stiffness, coupling, compressibility, thermal capacity, conductivity, and leakage matrices respectively. Note that $\mathbf{B} = \boldsymbol{L}\mathbf{N}_u$ is the strain operator, and **f** are forcing vectors, distributing body and traction forces, and fluid/thermal fluxes.

4.3 Shape functions & isoparametric finite elements

The primary variables $\mathbf{u}$, $p^{\mathrm{f_i}}$ and T, are expressed in terms of values at a finite number of discrete nodal points in space as an approximate representation of the continuum in that space. This involves the partitioning of the continuum into finite elements for separate integration before assembly with the other elements constituting the domain of interest. Within an element the primary variables are expressed in terms of values on the element's boundary, whereby those nodes on the boundary are to ensure continuity between the elements. This is to be satisfied by the choice of element nodal shape functions $\mathbf{N}$.

In this work, the system of equations is solved over a 2D axisymmetric domain as rotated about some vertical extent along which a mass flux may be applied, representative of an idealised body of prospective reservoir with a central wellbore. This is typically assumed in both 1D

(Section 3.2.6) and 2D in the literature for simplicity when testing theory for an injection/extraction or heave/consolidation problem of this type [120]. Solving (4.32) over a 3D domain is however a natural extension of what follows.

To mesh the displacement, pressure and temperature fields, computationally flexible isoparametric finite elements are considered. Doing so makes it possible for arbitrary domain shapes to be meshed with arbitrary refinement (these elements may also be developed for fracture mechanics [46]). In formulating these elements both global (physical) and natural (isoparametric) coordinate systems are described. The shape functions are the same for both coordinates systems, where the coordinates within the element are interpolated the same as for the variables. From the isoparametric family, 2D quadrilateral finite elements are adopted. For the pressure and temperature fields a basic 4 node linear finite element is employed. For the displacement field a higher order quadratic 9 node finite element is employed, which overlaps with specially coinciding nodes only at the vertices (Figure 4.2(a)). This is to overcome numerical difficulties encountered at certain limit state conditions, ensuring that convergence criteria are satisfied [120, 207]. The effect in this context and the choice of elements is a point for further study.

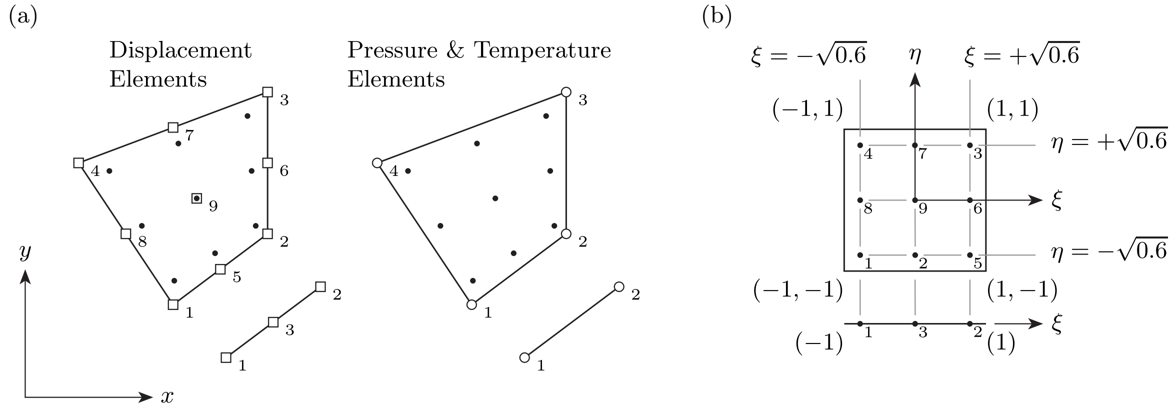

Figure 4.2: (a) In global coordinates with numbered nodes, the displacement and pressure/temperature field 1D and 2D finite elements used for computational interpolation. The square and circular marks denote the quadratic and linear finite element nodes respectively, and the dot marks denote the Gauss integration points. (b) In natural coordinates, 3 point 1D and 3×3 point 2D Gauss quadrature rule components, with the integration point coordinates and numbering. The weights of the integration points are respectively $w_{1\&3} = 5/9$, $w_2 = 8/9$ for the 1D case, and multi-dimensionally $w_{1\text{-}4} = 25/81$, $w_{5\text{-}8} = 40/81$, $w_9 = 64/81$ for the 2D case.

Furthermore, a 9 node Lagrange element has a central node. An element that has one or more central nodes offers better accuracy. This is desirable for the displacement elements given that the mechanical behaviour/stress state of the GCS system is of key interest in this work. All isoparametric elements lose accuracy once deviated from a rectangular shape, but the Lagrange element is much less sensitive to non-rectangularity than a serendipity element with no central nodes [46]. The cost is that larger element matrices are produced demanding greater computation for the same element size. The higher order displacement element also ensures that a reasonably accurate 4 node element may be selected for the pressure and temperature fields.

The corresponding shape functions for the 4 and 9 node elements are given in Tables 4.3 and 4.4 respectively. For the 4 and 9 node elements the shape functions are derived by the appropriate multiplication of respectively linear and quadratic Lagrangian polynomials (Tables 4.1 and 4.2) such that unity is given at the nodes [207], where ξ and η are the local coordinates of the element ranging from -1 to 1 (Figure 4.2(b)).

Table 4.1: 1D 2 node linear line finite element shape functions and derivatives, $-1 \leq \xi \leq 1$.

2 node shape functions	Derivative w.r.t. ξ
$\bar{N}^1 = \frac{1}{2}(1-\xi)$	$\frac{\partial \bar{N}^1}{\partial \xi} = -\frac{1}{2}$
$\bar{N}^2 = \frac{1}{2}(1+\xi)$	$\frac{\partial \bar{N}^2}{\partial \xi} = \frac{1}{2}$

Table 4.2: 1D 3 node quadratic line finite element shape functions and derivatives, $-1 \leq \xi \leq 1$.

3 node shape functions	Derivative w.r.t. ξ
$\bar{N}^1 = \frac{1}{2}(\xi^2-\xi)$	$\frac{\partial \bar{N}^1}{\partial \xi} = \xi - \frac{1}{2}$
$\bar{N}^2 = \frac{1}{2}(\xi^2+\xi)$	$\frac{\partial \bar{N}^2}{\partial \xi} = \xi + \frac{1}{2}$
$\bar{N}^3 = (1-\xi^2)$	$\frac{\partial \bar{N}^3}{\partial \xi} = -2\xi$

Table 4.3: 2D 4 node quadrilateral finite element shape functions and derivatives, $-1 \leq \xi, \eta \leq 1$.

4 node shape functions	Derivative w.r.t. ξ	Derivative w.r.t. η
$N^1 = \frac{1}{4}(1-\xi)(1-\eta)$	$\frac{\partial N^1}{\partial \xi} = -\frac{1}{4}(1-\eta)$	$\frac{\partial N^1}{\partial \eta} = -\frac{1}{4}(1-\xi)$
$N^2 = \frac{1}{4}(1+\xi)(1-\eta)$	$\frac{\partial N^2}{\partial \xi} = \frac{1}{4}(1-\eta)$	$\frac{\partial N^2}{\partial \eta} = -\frac{1}{4}(1+\xi)$
$N^3 = \frac{1}{4}(1+\xi)(1+\eta)$	$\frac{\partial N^3}{\partial \xi} = \frac{1}{4}(1+\eta)$	$\frac{\partial N^3}{\partial \eta} = \frac{1}{4}(1+\xi)$
$N^4 = \frac{1}{4}(1-\xi)(1+\eta)$	$\frac{\partial N^4}{\partial \xi} = -\frac{1}{4}(1+\eta)$	$\frac{\partial N^4}{\partial \eta} = \frac{1}{4}(1-\xi)$

Table 4.4: 2D 9 node quadrilateral finite element shape functions and derivatives, $-1 \leq \xi, \eta \leq 1$.

9 node shape functions	Derivative w.r.t. ξ	Derivative w.r.t. η
$N^1 = \frac{1}{4}(\xi^2-\xi)(\eta^2-\eta)$	$\frac{\partial N^1}{\partial \xi} = \frac{1}{4}(2\xi-1)(\eta^2-\eta)$	$\frac{\partial N^1}{\partial \eta} = \frac{1}{4}(\xi^2-\xi)(2\eta-1)$
$N^2 = \frac{1}{4}(\xi^2+\xi)(\eta^2-\eta)$	$\frac{\partial N^2}{\partial \xi} = \frac{1}{4}(2\xi+1)(\eta^2-\eta)$	$\frac{\partial N^2}{\partial \eta} = \frac{1}{4}(\xi^2+\xi)(2\eta-1)$
$N^3 = \frac{1}{4}(\xi^2+\xi)(\eta^2+\eta)$	$\frac{\partial N^3}{\partial \xi} = \frac{1}{4}(2\xi+1)(\eta^2+\eta)$	$\frac{\partial N^3}{\partial \eta} = \frac{1}{4}(\xi^2+\xi)(2\eta+1)$
$N^4 = \frac{1}{4}(\xi^2-\xi)(\eta^2+\eta)$	$\frac{\partial N^4}{\partial \xi} = \frac{1}{4}(2\xi-1)(\eta^2+\eta)$	$\frac{\partial N^4}{\partial \eta} = \frac{1}{4}(\xi^2-\xi)(2\eta+1)$
$N^5 = -\frac{1}{2}(\xi^2-1)(\eta^2-\eta)$	$\frac{\partial N^5}{\partial \xi} = -\xi(\eta^2-\eta)$	$\frac{\partial N^5}{\partial \eta} = -\frac{1}{2}(\xi^2-1)(2\eta-1)$
$N^6 = -\frac{1}{2}(\xi^2+\xi)(\eta^2-1)$	$\frac{\partial N^6}{\partial \xi} = -\frac{1}{2}(2\xi+1)(\eta^2-1)$	$\frac{\partial N^6}{\partial \eta} = -(\xi^2+\xi)\eta$
$N^7 = -\frac{1}{2}(\xi^2-1)(\eta^2+\eta)$	$\frac{\partial N^7}{\partial \xi} = -\xi(\eta^2+\eta)$	$\frac{\partial N^7}{\partial \eta} = -\frac{1}{2}(\xi^2-1)(2\eta+1)$
$N^8 = -\frac{1}{2}(\xi^2-\xi)(\eta^2-1)$	$\frac{\partial N^8}{\partial \xi} = -\frac{1}{2}(2\xi-1)(\eta^2-1)$	$\frac{\partial N^8}{\partial \eta} = -(\xi^2-\xi)\eta$
$N^9 = (\xi^2-1)(\eta^2-1)$	$\frac{\partial N^9}{\partial \xi} = 2\xi(\eta^2-1)$	$\frac{\partial N^9}{\partial \eta} = 2(\xi^2-1)\eta$

The interpolating expressions are defined in such a way that over a single element,

$$\left\{ \begin{array}{c} 1 \\ x(\xi,\eta) \\ y(\xi,\eta) \\ \mathrm{u}_x(\xi,\eta) \\ \mathrm{u}_y(\xi,\eta) \end{array} \right\} = \left[\begin{array}{cccc} 1 & 1 & \dots & 1 \\ x_1 & x_2 & \dots & x_9 \\ y_1 & y_2 & \dots & y_9 \\ \mathrm{u}_{x1} & \mathrm{u}_{x2} & \dots & \mathrm{u}_{x9} \\ \mathrm{u}_{y1} & \mathrm{u}_{y2} & \dots & \mathrm{u}_{y9} \end{array} \right] \left\{ \begin{array}{c} N^1_{\mathrm{u}}(\xi,\eta) \\ N^2_{\mathrm{u}}(\xi,\eta) \\ \vdots \\ N^9_{\mathrm{u}}(\xi,\eta) \end{array} \right\}, \tag{4.69}$$

$$\left\{\begin{array}{c} 1 \\ x(\xi,\eta) \\ y(\xi,\eta) \\ p^{\mathrm{f_i}}(\xi,\eta) \\ T(\xi,\eta) \end{array}\right\} = \left[\begin{array}{cccc} 1 & 1 & 1 & 1 \\ x_1 & x_2 & x_3 & x_4 \\ y_1 & y_2 & y_3 & y_4 \\ p_1^{\mathrm{f_i}} & p_2^{\mathrm{f_i}} & p_3^{\mathrm{f_i}} & p_4^{\mathrm{f_i}} \\ T_1 & T_2 & T_3 & T_4 \end{array}\right] \left\{\begin{array}{c} N^1_{p/T}(\xi,\eta) \\ N^2_{p/T}(\xi,\eta) \\ N^3_{p/T}(\xi,\eta) \\ N^4_{p/T}(\xi,\eta) \end{array}\right\}, \tag{4.70}$$

where the subscript numbers refer to the node of the element (Figure 4.2(a)). Note that C_0 continuity is achieved across element boundaries.

The shape function matrix for the 9 node finite element with the same number of shape functions is given for computation as

$$\mathbf{N}_{\mathrm{u}} = \left[\begin{array}{cccccccc} N^1_{\mathrm{u}} & 0 & N^2_{\mathrm{u}} & 0 & \dots & N^9_{\mathrm{u}} & 0 \\ 0 & N^1_{\mathrm{u}} & 0 & N^2_{\mathrm{u}} & \dots & 0 & N^9_{\mathrm{u}} \end{array}\right], \tag{4.71}$$

allocated in such a way that

$$\left\{\begin{array}{c} x(\xi,\eta) \\ y(\xi,\eta) \end{array}\right\} = \mathbf{N}_{\mathrm{u}} \left\{\begin{array}{c} x_1 \\ y_1 \\ \vdots \\ x_9 \\ y_9 \end{array}\right\} = \left\{\begin{array}{c} \sum\limits_{n=1}^{9} N^n_{\mathrm{u}} x_n \\ \sum\limits_{n=1}^{9} N^n_{\mathrm{u}} y_n \end{array}\right\}, \tag{4.72}$$

and likewise for displacements u_x and u_y acting in the global x and y coordinates respectively,

$$\left\{\begin{array}{c} \mathrm{u}_x \\ \mathrm{u}_y \end{array}\right\} = \mathbf{N}_{\mathrm{u}} \left\{\begin{array}{c} \mathrm{u}_{x1} \\ \mathrm{u}_{y1} \\ \dots \\ \mathrm{u}_{x9} \\ \mathrm{u}_{y9} \end{array}\right\}. \tag{4.73}$$

4.3.1 2D Jacobian matrix and determinant

It is required that the shape function derivatives over the local parent element be related to the derivatives over the distorted global element. To achieve this, $\{\xi, \eta\} \to \{x, y\}$ mapping is carried out using an elemental Jacobian matrix, $\mathbf{J}$. It is derived here using the chain rule which immediately gives the relationship

$$\left\{\begin{array}{c} \frac{\partial N}{\partial \xi} \\ \frac{\partial N}{\partial \eta} \end{array}\right\} = \underbrace{\left[\begin{array}{cc} \frac{\partial x}{\partial \xi} & \frac{\partial y}{\partial \xi} \\ \frac{\partial x}{\partial \eta} & \frac{\partial y}{\partial \eta} \end{array}\right]}_{\mathbf{J}} \left\{\begin{array}{c} \frac{\partial N}{\partial x} \\ \frac{\partial N}{\partial y} \end{array}\right\}. \tag{4.74}$$

The derivatives $\{\partial N/\partial\xi \;\, \partial N/\partial\eta\}^{\mathrm{T}}$ may be determined readily due to the regular structure of the parent element (Figure 4.2(b), and Tables 4.3 and 4.4), in order that the derivatives $\{\partial N/\partial x \;\, \partial N/\partial y\}^{\mathrm{T}}$ may be determined for the global element satisfying the governing equations, the inverse of the Jacobian is required such that

$$\left\{ \begin{array}{c} \frac{\partial N}{\partial x} \\ \frac{\partial N}{\partial y} \end{array} \right\} = \mathbf{J}^{-1} \left\{ \begin{array}{c} \frac{\partial N}{\partial \xi} \\ \frac{\partial N}{\partial \eta} \end{array} \right\}. \tag{4.75}$$

Knowing the shape function derivatives at some point in the parent element, and a given global element's nodal (vertices) coordinates $[\mathbf{x}, \mathbf{y}]_e$ (independent of ξ and η), in view of (4.72), differentiating x and y with respect to ξ and η is possible. The Jacobian components at the point within the given element are therefore obtained numerically via,

$$\mathbf{J} = \left[\begin{array}{cc} \frac{\partial x}{\partial \xi} & \frac{\partial y}{\partial \xi} \\ \frac{\partial x}{\partial \eta} & \frac{\partial y}{\partial \eta} \end{array} \right] = \sum_{n=1}^{nds} \left[\begin{array}{cc} \frac{\partial N_n}{\partial \xi} x_n & \frac{\partial N_n}{\partial \xi} y_n \\ \frac{\partial N_n}{\partial \eta} x_n & \frac{\partial N_n}{\partial \eta} y_n \end{array} \right] = \left[\begin{array}{ccc} \frac{\partial N_1}{\partial \xi} & \cdots & \frac{\partial N_{nds}}{\partial \xi} \\ \frac{\partial N_1}{\partial \eta} & \cdots & \frac{\partial N_{nds}}{\partial \eta} \end{array} \right] \left[\begin{array}{cc} x_1 & y_1 \\ \vdots & \vdots \\ x_{nds} & y_{nds} \end{array} \right] \tag{4.76}$$

where the diagonal terms account for the rate of stretching along the coordinate axes and the off-diagonal terms map the shearing of the element. The inverse of the Jacobian is obtained by,

$$\mathbf{J}^{-1} = \frac{1}{|\mathbf{J}|} \left[\begin{array}{cc} \frac{\partial y}{\partial \eta} & -\frac{\partial y}{\partial \xi} \\ -\frac{\partial x}{\partial \eta} & \frac{\partial x}{\partial \xi} \end{array} \right] = \frac{1}{|\mathbf{J}|} \left[\begin{array}{cc} J_{22} & -J_{12} \\ -J_{21} & J_{11} \end{array} \right] \tag{4.77}$$

where the Jacobian determinant,

$$|\mathbf{J}| = \frac{\partial x}{\partial \xi}\frac{\partial y}{\partial \eta} - \frac{\partial x}{\partial \eta}\frac{\partial y}{\partial \xi} = J_{11}J_{22} - J_{12}J_{21}. \tag{4.78}$$

The following important derivatives may now be computed,

$$\frac{\partial N}{\partial x} = \frac{1}{|\mathbf{J}|}\left(\frac{\partial y}{\partial \eta}\frac{\partial N}{\partial \xi} - \frac{\partial y}{\partial \xi}\frac{\partial N}{\partial \eta}\right) = \frac{1}{|\mathbf{J}|}\left(J_{22}\frac{\partial N}{\partial \xi} - J_{12}\frac{\partial N}{\partial \eta}\right), \tag{4.79}$$

$$\frac{\partial N}{\partial y} = \frac{1}{|\mathbf{J}|}\left(\frac{\partial x}{\partial \xi}\frac{\partial N}{\partial \eta} - \frac{\partial x}{\partial \eta}\frac{\partial N}{\partial \xi}\right) = \frac{1}{|\mathbf{J}|}\left(J_{11}\frac{\partial N}{\partial \eta} - J_{21}\frac{\partial N}{\partial \xi}\right). \tag{4.80}$$

4.3.2 Gauss-Legendre quadrature for axisymmetric numerical integration

The evaluation of the complex integral equations of (4.32) is carried out via numerical integration through a multi-dimension Gauss-Legendre quadrature rule [46]. The quadrature rule employed is illustrated in Figure 4.2(a) for the 2D case with

$$\iint_{-1}^{1} f(\xi,\eta)\,\mathrm{d}\xi\mathrm{d}\eta = \sum_{i=1}^{ips} f(\xi_i,\eta_i)\,w_i, \tag{4.81}$$

where i is the Gauss integration point as weighted by w_i over the summation. Note that a 3 point rule has been selected for the appropriate accuracy, meaning that there are 9 Gaussian integration points within each element. The coupled displacement, pressure and temperature elements are occupied by the same 9 integration points during computation.

Within an axisymmetric domain, each element is essentially a 3D ring-element about the central axis, meaning, $\mathrm{d}\Omega = 2\pi x \mathrm{d}x\mathrm{d}y$, where x is the radial extent (Figure 2.4) and $\mathrm{d}x\mathrm{d}y$ is the infinitesimal cross-sectional area at the point of interest. As 2π is constant it may be taken out of all the integrals and cancelled throughout the system of equations. Hence, $\mathrm{d}\Omega$ may be interpreted $x\mathrm{d}x\mathrm{d}y$, and similarly $\mathrm{d}\Gamma$ as $x\mathrm{d}y$.

In order to apply the quadrature rule to the irregular global axisymmetric elements they have to be transformed into the canonical from,

$$\int_{\Omega_e} f(x,y)\, x\, \mathrm{d}x\mathrm{d}y\mathrm{d}\theta \Rightarrow \int_0^{2\pi}\int_{-1}^{1}\int_{-1}^{1} f[x(\xi,\eta),y(\xi,\eta)]\, x(\xi,\eta)\, |\mathbf{J}(\xi,\eta)|\, d\xi d\eta \mathrm{d}\theta$$
$$= 2\pi \sum_{i=1}^{ips} f[x(\xi_i,\eta_i),y(\xi_i,\eta_i)]\, x(\xi_i,\eta_i)\, |\mathbf{J}(\xi_i,\eta_i)|\, w_i. \quad (4.82)$$

Note that the integration is now expressed entirely in terms of ξ and η by an area transformation, where the area of the differential quadrilateral is computed via the geometric cross product

$$\mathrm{d}x\mathrm{d}y = \frac{\partial x}{\partial \xi}\mathrm{d}\xi\, \frac{\partial y}{\partial \eta}\mathrm{d}\eta - \frac{\partial x}{\partial \eta}\mathrm{d}\eta\, \frac{\partial y}{\partial \xi}\mathrm{d}\xi = \begin{vmatrix} \frac{\partial x}{\partial \xi} & \frac{\partial y}{\partial \xi} \\ \frac{\partial x}{\partial \eta} & \frac{\partial y}{\partial \eta} \end{vmatrix} \mathrm{d}\xi\mathrm{d}\eta = |\mathbf{J}|\, \mathrm{d}\xi\mathrm{d}\eta, \quad (4.83)$$

which reintroduces the Jacobian determinant, as gathered by the computation (4.76) which may now be employed at the integration points for the purpose of (4.77–4.80) and (4.82).

4.4 General Finite Element Formulations

The following subsections itemise and compute the various general matrix and vector types which constitute the full system of equations (4.32).

4.4.1 Tangential stiffness element matrix

The tangential stiffness matrix of (4.32), element-wise after (4.4) is of the form,

$$\boldsymbol{\mathcal{S}}^e = \int_{\Omega_e} \mathbf{B}^{\mathrm{T}}\mathbf{D}\mathbf{B}\, d\Omega, \quad (4.84)$$

based on the global coordinate system (Figure 4.2(a)), which is to be transformed in terms the natural coordinate system (Figure 4.2(b)) for computation. Employing therefore the Gauss quadrature rule (4.82) presents

$$\boldsymbol{\mathcal{S}}^e = \sum_{i=1}^{ips} \mathbf{B}_i^{\mathrm{T}}\mathbf{D}\,\mathbf{B}_i\, x(\xi_i,\eta_i)\, |\mathbf{J}(\xi_i,\eta_i)|\, w_i. \quad (4.85)$$

For the axisymmetric case, $\mathbf{D}$ (illustrated here as being constant over the domain) relates axisymmetric stress-strains as covered in Section 2.6.4, and $\mathbf{B}$ is the kinematic relationship of element strains to nodal displacements which is given by $\boldsymbol{L}\mathbf{N}_{\mathrm{u}}$, where

$$\boldsymbol{L} = \begin{bmatrix} \frac{\partial}{\partial x} & 0 \\ 0 & \frac{\partial}{\partial y} \\ \frac{1}{x} & 0 \\ \frac{\partial}{\partial y} & \frac{\partial}{\partial x} \end{bmatrix}. \tag{4.86}$$

Hence, the differential operator matrix given for the 2D axisymmetric case is therefore

$$\mathbf{B} = \boldsymbol{L}\mathbf{N}_{\mathrm{u}} = \left[\begin{array}{cc|c|cc} \frac{\partial N_{\mathrm{u}}^1}{\partial x} & 0 & \cdots & \frac{\partial N_{\mathrm{u}}^9}{\partial x} & 0 \\ 0 & \frac{\partial N_{\mathrm{u}}^1}{\partial y} & \cdots & 0 & \frac{\partial N_{\mathrm{u}}^9}{\partial y} \\ \frac{N_{\mathrm{u}}^1}{x} & 0 & \cdots & \frac{N_{\mathrm{u}}^9}{x} & 0 \\ \frac{\partial N_{\mathrm{u}}^1}{\partial y} & \frac{\partial N_{\mathrm{u}}^1}{\partial x} & \cdots & \frac{\partial N_{\mathrm{u}}^9}{\partial y} & \frac{\partial N_{\mathrm{u}}^9}{\partial x} \end{array}\right]. \tag{4.87}$$

Utilising the Jacobian formulation leading to (4.79) and (4.80), the isoparametric mapping formulation for computation is given as

$$\mathbf{B}_i = \left[\begin{array}{cc|c} \frac{1}{|\mathbf{J}|}\left(J_{22}\frac{\partial N_{\mathrm{u}}^1}{\partial \xi} - J_{12}\frac{\partial N_{\mathrm{u}}^1}{\partial \eta}\right) & 0 & \cdots \\ 0 & \frac{1}{|\mathbf{J}|}\left(J_{11}\frac{\partial N_{\mathrm{u}}^1}{\partial \eta} - J_{21}\frac{\partial N_{\mathrm{u}}^1}{\partial \xi}\right) & \cdots \\ \frac{N_{\mathrm{u}}^1}{x} & 0 & \cdots \\ \frac{1}{|\mathbf{J}|}\left(J_{11}\frac{\partial N_{\mathrm{u}}^1}{\partial \eta} - J_{21}\frac{\partial N_{\mathrm{u}}^1}{\partial \xi}\right) & \frac{1}{|\mathbf{J}|}\left(J_{22}\frac{\partial N_{\mathrm{u}}^1}{\partial \xi} - J_{12}\frac{\partial N_{\mathrm{u}}^1}{\partial \eta}\right) & \cdots \end{array}\right]_{(\xi_i,\eta_i)}. \tag{4.88}$$

The radius x is also taken at the integration point, and is interpolated from the element nodal coordinates $\{\mathbf{x}\}_e$,

$$x(\xi_i, \eta_i) = \mathbf{N}_{\mathrm{u}}(\xi_i, \eta_i)\{\mathbf{x}\}_e. \tag{4.89}$$

Note that a partial derivative is not required for the kinematic relationship of the circumferential hoop strain, after (2.31). The $1/x$ terms however cause a diverging near-singular or singular integral as the elements approach the axis of symmetry ($x \to 0$). This may exhibit strong behaviour when integrating numerically and requires consideration when implementing, as is discussed in [43] and the references therein.

4.4.2 Laplace element matrix

The Laplace matrices of (4.32) element-wise after (4.4) are of the form,

$$\boldsymbol{\mathcal{L}}^e = \int_{\Omega_e} \left(\nabla\mathbf{N}_{p/T}\right)^{\mathrm{T}} \boldsymbol{\Pi}\, \nabla\mathbf{N}_{p/T}\, \mathrm{d}\Omega, \tag{4.90}$$

which are based on the global coordinate system (Figure 4.2(a)) and are to be transformed with the natural coordinate system (Figure 4.2(b)) for computation. Employing the Gauss quadrature rule (4.82) presents

$$\boldsymbol{\mathcal{L}}^e = \sum_{i=1}^{ips} \left(\nabla\mathbf{N}_{p/T}\right)_i^{\mathrm{T}} \boldsymbol{\Pi}(\xi_i, \eta_i)\, \left(\nabla\mathbf{N}_{p/T}\right)_i\, x(\xi_i, \eta_i)\, |\mathbf{J}(\xi_i, \eta_i)|\, w_i. \tag{4.91}$$

For the axisymmetric case, after (4.31) the ∇ operator is reduced as follows, given that by definition no gradient is present in the z (Figure 2.4) circumferential sense,

$$\nabla = \left\{ \begin{array}{c} \frac{\partial}{\partial x} \\ \frac{\partial}{\partial y} \end{array} \right\}, \tag{4.92}$$

with respect to the 4 node finite element (4.70), hence

$$\nabla \mathbf{N}_{p/T} = \left[\begin{array}{cccc} \frac{\partial N^1}{\partial x} & \frac{\partial N^2}{\partial x} & \frac{\partial N^3}{\partial x} & \frac{\partial N^4}{\partial x} \\ \frac{\partial N^1}{\partial y} & \frac{\partial N^2}{\partial y} & \frac{\partial N^3}{\partial y} & \frac{\partial N_4}{\partial y} \end{array} \right]. \tag{4.93}$$

Utilising the Jacobian formulation leading to (4.79) and (4.80), the isoparametric mapping of the global derivatives for computation at the integration points is therefore

$$\left(\nabla \mathbf{N}_{p/T}\right)_i = [\mathbf{J}(\xi_i, \eta_i)]^{-1} \left[\begin{array}{cccc} \frac{\partial N^1}{\partial \xi} & \frac{\partial N^2}{\partial \xi} & \frac{\partial N^3}{\partial \xi} & \frac{\partial N^4}{\partial \xi} \\ \frac{\partial N^1}{\partial \eta} & \frac{\partial N^2}{\partial \eta} & \frac{\partial N^3}{\partial \eta} & \frac{\partial N^4}{\partial \eta} \end{array} \right]_{(\xi_i, \eta_i)}, \tag{4.94}$$

where the natural derivatives of the polynomial shape functions are gathered as of Table 4.3 for the integration points.

The generic $\mathbf{\Pi}$ term is tensorial in the computation as it includes either the 2D permeability or conductivity tensor, respectively of the form

$$\mathbf{k}_{1/2} = \left[\begin{array}{cc} k^x_{1/2} & 0 \\ 0 & k^y_{1/2} \end{array} \right], \quad \boldsymbol{\chi}_{\text{eff}} = \left[\begin{array}{cc} \chi^x_{\text{eff}} & 0 \\ 0 & \chi^y_{\text{eff}} \end{array} \right]. \tag{4.95}$$

4.4.3 Mass element matrix

The mass matrices of (4.32) element-wise after (4.4) are of the form,

$$\boldsymbol{\mathcal{M}}^e = \int_{\Omega_e} \left(\mathbf{N}_{p/T}\right)^{\mathrm{T}} \Pi \, \mathbf{N}_{p/T} \, \mathrm{d}\Omega, \tag{4.96}$$

which is transformed after (4.82) in terms of the natural coordinate system (Figure 4.2(b)), in order that the Gauss quadrature rule may be employed,

$$\boldsymbol{\mathcal{M}}^e = \sum_{i=1}^{ips} \left(\mathbf{N}_{p/T}\right)_i^{\mathrm{T}} \Pi(\xi_i, \eta_i) \left(\mathbf{N}_{p/T}\right)_i x(\xi_i, \eta_i) \left|\mathbf{J}(\xi_i, \eta_i)\right| w_i. \tag{4.97}$$

where,

$$\left(\mathbf{N}_{p/T}\right)_i = \left[\begin{array}{cccc} N^1 & N^2 & N^3 & N^4 \end{array} \right]_{(\xi_i, \eta_i)}. \tag{4.98}$$

In this instance, the generic Π term is scalar, and the term ‘mass matrix’ is used here in a generic sense but is formally only applicable if Π contains the mass density of the material.

4.4.4 Advection element matrix

The advective matrices of (4.32) element-wise after (4.4) are of the form,

$$\boldsymbol{\mathcal{A}}^e = \int_{\Omega_e} \left(\mathbf{N}_{p/T}\right)^{\mathrm{T}} \boldsymbol{\Pi} \cdot \nabla \mathbf{N}_{p/T} \, \mathrm{d}\Omega, \tag{4.99}$$

which is transformed after (4.82) in terms of the natural coordinate system (Figure 4.2(b)), in order that the Gauss quadrature rule may be employed,

$$\boldsymbol{\mathcal{A}}^e = \sum_{i=1}^{ips} \left(\mathbf{N}_{p/T}\right)_i^{\mathrm{T}} \boldsymbol{\Pi}(\xi_i, \eta_i) \cdot \left(\nabla \mathbf{N}_{p/T}\right)_i \, x(\xi_i, \eta_i) \, |\mathbf{J}\left(\xi_i, \eta_i\right)| \, w_i. \tag{4.100}$$

where the terms $\left(\mathbf{N}_{p/T}\right)_i$ and $\left(\nabla \mathbf{N}_{p/T}\right)_i$ are determined as of (4.98) and (4.94) respectively.

The generic $\boldsymbol{\Pi}$ term is vectorial given that it incorporates the fluid velocity field, computed in the form

$$\mathbf{v}_{\mathrm{w/n}_{1/2}} = \begin{bmatrix} \mathrm{v}^x_{\mathrm{w/n}_{1/2}} \\ \mathrm{v}^y_{\mathrm{w/n}_{1/2}} \end{bmatrix}. \tag{4.101}$$

4.4.5 Displacement and pressure coupling element matrices

The matrices coupling the solid displacements with the mass balance equations in (4.32), element-wise after (4.4), are of the form,

$$\boldsymbol{\mathcal{Q}}^e_{\mathrm{u}} = -\int_{\Omega_e} \mathbf{B}^{\mathrm{T}} \, \Pi \, \mathbf{m} \, \mathbf{N}_{p/T} \, \mathrm{d}\Omega, \tag{4.102}$$

which is transformed after (4.82) in terms of the natural coordinate system (Figure 4.2(b)), in order that the Gauss quadrature rule may be employed,

$$\boldsymbol{\mathcal{Q}}^e_{\mathrm{u}} = -\sum_{i=1}^{ips} \mathbf{B}_i^{\mathrm{T}} \, \Pi(\xi_i, \eta_i) \, \mathbf{m} \left(\mathbf{N}_{p/T}\right)_i \, x(\xi_i, \eta_i) \, |\mathbf{J}\left(\xi_i, \eta_i\right)| \, w_i. \tag{4.103}$$

where the terms $\mathbf{B}_i$ and $\left(\mathbf{N}_{p/T}\right)_i$ are determined as of (4.88) and (4.98) respectively.

The pressure coupling matrix is related accordingly via transposing (4.103), that is $\boldsymbol{\mathcal{Q}}^e_p = -(\boldsymbol{\mathcal{Q}}^e_{\mathrm{u}})^{\mathrm{T}}$, where the negative sign has arisen because of the alternate convention between solid stress and fluid pressure, which have been defined and carried throughout as tension-positive and compression-positive respectively (Section 2.6.3).

4.4.6 Body force/source element vectors

The vector distributing body forces (source vector) within the system (4.32), element-wise after (4.4), is of the form,

$$\boldsymbol{\mathcal{B}}^e_{\mathrm{u}} = \int_{\Omega_e} \mathbf{N}_{\mathrm{u}}^{\mathrm{T}} \, \mathbf{b} \, \mathrm{d}\Omega, \tag{4.104}$$

which is transformed after (4.82) in terms of the natural coordinate system (Figure 4.2(b)), in order that the Gauss quadrature rule may be employed,

$$\boldsymbol{\mathcal{B}}^e_{\mathrm{u}} = \sum_{i=1}^{ips} (\mathbf{N}_{\mathrm{u}})_i^{\mathrm{T}}\ \mathbf{b}(\xi_i,\eta_i)\,x(\xi_i,\eta_i)\,|\mathbf{J}\,(\xi_i,\eta_i)\,|\,w_i. \tag{4.105}$$

where $(\mathbf{N}_{\mathrm{u}})_i$ is determined after (4.71) via,

$$(\mathbf{N}_{\mathrm{u}})_i = \begin{bmatrix} N^1_{\mathrm{u}} & 0 & N^2_{\mathrm{u}} & 0 & \dots & N^9_{\mathrm{u}} & 0 \\ 0 & N^1_{\mathrm{u}} & 0 & N^2_{\mathrm{u}} & \dots & 0 & N^9_{\mathrm{u}} \end{bmatrix}_{(\xi_i,\eta_i)}, \tag{4.106}$$

For the mass balance equations the gradient operator may also be incorporated, as of the form

$$\boldsymbol{\mathcal{B}}^e_{p} = \int_{\Omega_e} (\nabla\mathbf{N}_p)^{\mathrm{T}}\ \mathbf{b}\,\mathrm{d}\Omega, \tag{4.107}$$

which is transformed after (4.82) in terms of the natural coordinate system (Figure 4.2(b)), in order that the Gauss quadrature rule may be employed,

$$\boldsymbol{\mathcal{B}}^e_{p} = \sum_{i=1}^{ips} (\nabla\mathbf{N}_p)_i^{\mathrm{T}}\ \mathbf{b}(\xi_i,\eta_i)\,x(\xi_i,\eta_i)\,|\mathbf{J}\,(\xi_i,\eta_i)\,|\,w_i, \tag{4.108}$$

where $(\nabla\mathbf{N}_p)_i$ is determined as of (4.71).

4.4.7 Surface force/flux element vectors

Finally, the surface force/flux vectors in (4.32) element-wise after the second boundary term in (4.4) are of the form

$$\boldsymbol{\mathcal{T}}^e_{\mathrm{u}} = \int_{\Gamma_e} \mathbf{N}^{\mathrm{T}}_{\mathrm{u}}\,\mathbf{t}\,\mathrm{d}\Gamma, \qquad \boldsymbol{\mathcal{T}}^e_{p/T} = \int_{\Gamma_e} \mathbf{N}^{\mathrm{T}}_{p/T}\,\mathrm{q}\,\mathrm{d}\Gamma, \tag{4.109}$$

which are transformed after applying (4.82) one dimensionally in terms of the natural coordinate system (Figure 4.2(b)), in order that the Gauss quadrature rule may be employed,

$$\boldsymbol{\mathcal{T}}^e_{\mathrm{u}} = \sum_{i=1}^{ips} \left(\bar{\mathbf{N}}_{\mathrm{u}}\right)_i^{\mathrm{T}}\,\mathbf{t}(\xi_i)\,x(\xi_i)\,|\mathbf{J}\,(\xi_i)\,|\,w_i, \qquad \boldsymbol{\mathcal{T}}^e_{p/T} = \sum_{i=1}^{ips} \left(\bar{\mathbf{N}}_{p/T}\right)_i^{\mathrm{T}}\ \mathrm{q}(\xi_i)\,x(\xi_i)\,|\mathbf{J}\,(\xi_i)\,|\,w_i, \tag{4.110}$$

where,

$$\left(\bar{\mathbf{N}}_{\mathrm{u}}\right)_i = \begin{bmatrix} \bar{N}^1_{\mathrm{u}} & 0 & \bar{N}^2_{\mathrm{u}} & 0 & \bar{N}^3_{\mathrm{u}} & 0 \\ 0 & \bar{N}^1_{\mathrm{u}} & 0 & \bar{N}^2_{\mathrm{u}} & 0 & \bar{N}^3_{\mathrm{u}} \end{bmatrix}_{(\xi_i,\eta_i)}, \qquad \left(\bar{\mathbf{N}}_{p/T}\right)_i = \begin{bmatrix} \bar{N}^1_{p/T} & \bar{N}^2_{p/T} \end{bmatrix}_{(\xi_i,\eta_i)}, \tag{4.111}$$

which are the 1D cases given that the functions (4.110) are applied to the domain boundary via line elements. The Jacobian is also computed in the 1D sense from components of (4.76) depending on the orthogonality of the surface line to which the function is applied.

4.5 Global matrix assembly and programming aspects

The quadrature rule summations for the general element matrices and vectors applied with the corresponding coefficients may now be carried out over the element integration points as located and weighted in Figure 4.2(b). The corresponding valuations of the shape functions and their derivatives may be gathered as of Tables 4.1–4.4.

The numerical integration processes as detailed are carried out over each element, the resulting element matrices and vectors are to be assembled globally in a numerical form representative of (4.32) and solved for the primary and secondary variable set over time. Due to the numerous physics and couplings which have been formulated and the potentially large domain sizes of geological interest, care is taken in programming for the assembly and solution of the multi-field initial-boundary value problem encountered. The Matlab programming environment is employed for coding the numerical formulations developed in this thesis because of its high-level language which is designed for effective prototyping and efficient matrix/vector operations. The C/C++ language is also employed for low-level collaborative coding in order to model and integrate the muon transport physics (Section 2.11.2.3).

The system of equation (4.32) has three coefficient arrays which may be assembled as follows,

$$\boldsymbol{\mathcal{C}}_{\mathbf{kl}} = \sum_{e=1}^{els} \boldsymbol{\mathcal{C}}^{e}_{\mathbf{kl}}, \qquad \boldsymbol{\mathcal{K}}_{\mathbf{kl}} = \sum_{e=1}^{els} \boldsymbol{\mathcal{K}}^{e}_{\mathbf{kl}}, \qquad \boldsymbol{\mathcal{F}}_{\mathbf{k}} = \sum_{e=1}^{els} \boldsymbol{\mathcal{F}}^{e}_{\mathbf{k}}, \tag{4.112}$$

where **k** and **l** index the rows and columns respectively corresponding to the degrees of freedom belonging to all the primary variables at all the finite element nodes within the system. If constructed explicitly in this fashion for the large coefficient matrices of (4.32), particularly large sparse numerical arrays are encountered which pose computational problems, principally in term of memory (re)allocation. To overcome this the element matrices are assembled vectorised into a triplicate storage form of three full columns for each coefficient matrix, that is $[\,\mathbf{k}\ \mathbf{l}\ \check{\boldsymbol{\mathcal{C}}}\,]$ and $[\,\mathbf{k}\ \mathbf{l}\ \check{\boldsymbol{\mathcal{K}}}\,]$, which in turn are leveraged easily within the Matlab environment.

Research on improving the efficiency in implementing the finite element method in the Matlab environment is ongoing, see [6, 155] amongst others, including development of the environment itself. Several approaches are observed to this effect, which are based both generally in application and on specific physics applications and finite element types. The novel implementations involve full vectorisation of the finite element procedures, as discussed in Section 4.4, via an embedding of simultaneous linear algebra rule matrix operations and element by element array operations, which apply well with nodal element iso-parametrisation. Application with respect to coupled multi-physics and finite elements discussed in this work extends naturally and has been employed in part. However, further study is warranted and would demonstrate even greater efficiencies for the competitive implementation of research finite element code involving large coupled arrays. For now, the standard approaches are generally used which follow Section 4.4 accordingly, for the purposes of initially benchmarking the development of the modelled physics.

4.6 Meshing and mesh refinement

The element mesh of overlapping 4 and 9 node elements is constructed in the global coordinate system with Blossom quadrilaterals for the purposes of mesh refinement and adaptation (hence the choice of iso-parametrisation as discussed). These refined/adapted mesh elements are realised through an indirect quadrilateralisation method, whereby a refined Delaunay triangulation of some appropriate spatial function is merged into unstructured quadrilaterals through the Blossom algorithm [156]. This produces a high-quality refined (Blossom-Quad) mesh, efficient in terms of both element shape and field size.

For numerical accuracy and efficiency, modelling injection scenarios often requires that the elements be refined around the wellbore to an extent which lessens outwards, often as a logarithmic function. This is particularly due to the convergence of flow lines (due to the pressure gradient) about the wellbore, and given that the initial stages of fluid injection will also present high gradients across the induced fluid interface before it begins to disperse as it moves outwards. Furthermore, localised high gradients will continue to occur across the fluid interface as it migrates through the domain. By refining the mesh in these locations and unrefining it in others, where and when appropriate, significant improvements would be presented by directly capturing more detail as required. In order to refine the mesh appropriately, the mesh density may be correlated with an error indicator over the spatial domain. The view is that the high gradient in capillary pressure (and relatedly saturation) at the fluid interface denotes a region requiring mesh refinement. Therefore, a capillary pressure (or saturation) gradient criterion norm may be suggested in order to adapt the mesh,

$$\|\nabla p^{\mathrm{c}}\| = \sqrt{\left(\frac{\partial p^{c}}{\partial x}\right)^{2} + \left(\frac{\partial p^{c}}{\partial y}\right)^{2} + \left(\frac{\partial p^{c}}{\partial z}\right)^{2}}. \tag{4.113}$$

Note that this gradient is highest at the start of injection around the wellbore (for a homogeneous medium), and as the fluid interface migrates outward the gradient is lessened as the fluid interface disperses, which is a non-linear function of the van Genuchten (pressure-saturation) parametrisation. In this work a basic mesh design is carried out in view of these observations in Section 6.3.

With respect to adaptive spatial discretisation, interesting level-set and extended finite element methods have been employed in order to track and model the high gradient fluid interface (saturation front) phenomena within coupled (isothermal hydro-mechanical) multiphase fluid systems. These methods however introduce complication and require the extra computation of additional sub-vectors within the system of equations containing the necessary extra degrees of freedom [187, 186].

Chapter 5

Temporal Integration & Solution Control

The finite element formulations discretising the space domain now presents a system of nonlinear first-order ordinary differential equations, concisely of the form

$$\boldsymbol{\mathcal{C}}(\mathbf{X})\,\frac{\mathrm{d}\mathbf{X}}{\mathrm{d}t} + \boldsymbol{\mathcal{K}}(\mathbf{X})\,\mathbf{X} = \boldsymbol{\mathcal{F}}(\mathbf{X}), \tag{5.1}$$

where $\boldsymbol{\mathcal{C}}$ denotes a capacity matrix, $\boldsymbol{\mathcal{K}}$ a conductivity matrix, and $\boldsymbol{\mathcal{F}}$ a supply vector.

The system of differential equations is typical of a 'non-structural' problem (heat transfer, field problems and fluid flows). These 'non-structural' (first-order) problems are different from 'structural' (second-order) problems primarily because the time integration of the governing equation is concerned only with first-order derivatives in time. It has arisen in this form due to the omission of inertial effects within the model formulation, in assuming the physical processes involved behave slow enough such that any acceleration terms are approximately zero. That is, $\ddot{\mathbf{X}} \approx \mathbf{0}$.

Finite difference schemes in time are well practised for the temporal integration of numerical equations in the form of (5.1), for which a discretising time-step size Δt is selected. Coupled subsurface consolidation/heave and extraction/injection scenarios simulated over large time domains, certainly at the scales necessary for modelling GCS, present behaviour that warrant the selection of a vast range of time-step sizes during a single simulation. This is prominent with respect to (5.1) because the capacity term will generally dissipate over time as the displacements, pressures and temperatures often exhibit steady-state and/or limit-state behaviour, depending on the system, some time after the initial supply or loading on the system. Uniform time-stepping is observed to be either inefficient and/or inaccurate as it essentially assumes that the system behaves constantly throughout. Also, heuristically changing the step size does not give a clear indication for controlling or indeed optimising successive time-step sizes. Therefore, an automatic and adaptive time-stepping scheme is desired in this work over uniform stepping and/or heuristic methods for the selection of Δt.

A sensible method for adapting the time-step sizes is through control of the local truncation error of the solution scheme discretising the time domain [77, 78, 178]. Firstly, an estimate of the local truncation error must be acquired. Two main approaches which determine an error estimate though comparing solutions of different accuracy are:

- Step-doubling (Richardson extrapolation), where the temporal integration is performed twice with the same method, once for a full initial time-step size and then again for two half step sizes of the original [78, 173].
- Embedded methods, where multiple methods of different consistency order operate over the same time-step size [78].

The later approach is adopted in this work due to a series of inherent benefits which will be discussed. A requirement is that the two embedded integration methods are single-step (though may be multiple-stage) procedures so that the time-step size can be easily adjusted as the integration proceeds. Two such temporal integration methods of adjacent order are therefore described below and embedded. The embedded scheme utilised is one advocated by [102, 176], where it is employed for solving consolidation problems with a single pore fluid phase, and for Richards flow equations. It is developed in this work for the case of multiphase flow in deforming porous media in the context of a GCS scenario (Equation 5.1).

From estimating the local truncation errors during the temporal integration it is then demonstrated that successive time-step sizes can be coordinated effectively through control theory [178]. Here further constraints in line with PI (proportional and integral feedback) control strategies for nonlinear systems [75, 76] are incorporated. The notion of PI control theory for multiple processes in porous media is also highlighted in [200]. The importance in behaviour of the different sub-vectors in the solution vector $\mathbf{X}$ on error control is also a point for further study, particularly with respect to staggering the system of equations (4.32) depending on the degree of coupling between the various system components [120].

Additionally, the coefficients (constitutive functions) $\boldsymbol{\mathcal{C}}$ and $\boldsymbol{\mathcal{K}}$ as well as the non-trivial forcing conditions of $\boldsymbol{\mathcal{F}}$ are dependent on $\mathbf{X}$. This nonlinearity of the system is dealt with during the integration of each time-step via linearisation with iterative methods. For this, a fixed-point (Picard) iteration procedure is incorporated into the workflow. This procedure is known to be robust for coupled nonlinear problems but demonstrates slow, at best linear, convergence rates. To improve on this an acceleration method is also incorporated. Anderson mixing [11] is researched for this purpose as it improves performance with minimal intrusion. This acceleration method has been used successfully in electronic structure computations [198], and has emerged more recently for significantly improving the modelling of certain FSI problems over other acceleration methods [68]. Its formulation appears to be unresearched in the context of coupled porous media HTMC modelling.

Newton-type procedures can however be employed in order to give quadratic convergence rates, but require the computation of Jacobian information in order to linearise the system of equations. This Jacobian is computationally expensive to acquire, and efficient convergence also requires that it has certain continuity properties. Such continuity is not shown in some parametrisations of van Genuchten models [199], where it is noted that fixed-point methods have lower requirements for continuity. It is also noted that Brooks-Corey saturation models are used with direct Newton methods extensively, potentially due to their more straightforward linearisation. It is preferred that a van Genuchten model is employed as it highlights more realistic behaviour (Section 2.7.1) in the computation of a saturated to unsaturated flow transition. Therefore, in this work the Newton method in not adopted.

Ultimately, a modified Newton method is sough on the basis that formal/analytical tangent linearisation (which would lead to Newton-Raphson iterations and quadratic convergence) is potentially prohibited by the complexity of the governing coupled formulation and/or its future development. One particular alternative using numerical differentiation in order to determine tangent matrices for plasticity models is given in [148, 149] for reference. Another interesting alternative general purpose technique being employed for large scale reservoirs simulations is algorithmic/automatic differentiation [112, 135].

In what follows, the theoretical approaches as discussed are developed and integrating into a workflow and then schemed into a computational algorithm for the solution of (5.1).

5.1 Method 1: The $\boldsymbol{\theta}$-method

The simplest general method for time integration is the θ-method. It is essentially given by the finite difference assumptions of

$$\left(\frac{\mathrm{d}\mathbf{X}}{\mathrm{d}t}\right)_{t_n+\theta\Delta t} \approx \frac{\mathbf{X}_{t_n+\Delta t} - \mathbf{X}_{t_n}}{\Delta t} \tag{5.2}$$

$$\mathbf{X}_{t_n+\theta\Delta t} \approx (1-\theta)\mathbf{X}_{t_n} + \theta\mathbf{X}_{t_n+\Delta t} \tag{5.3}$$

which are illustrated in Figure 5.1. For brevity, following the notation of [207], the backward, theta-point and forward values in time are subscripted $n, n+\theta$, and $n+1$ respectively. Note Δt is Δt_{n+1} from $t_n \to t_{n+1}$, which is notation necessary for when adaptive time-stepping is of concern.

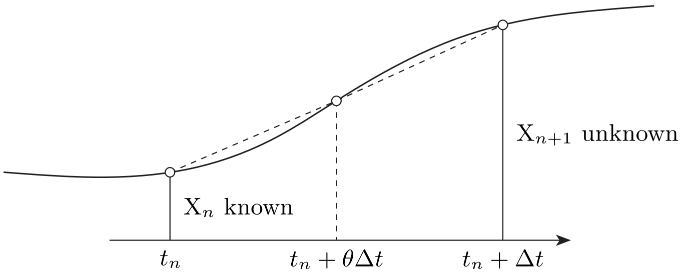

Figure 5.1: Illustration of primary variable approximations in the time domain for the θ-method of time integration, depicted is the $(n+1)$th step.

A finite difference approximation of the derivative of $\mathbf{X}$ at $n+\theta$ is given by (5.2), and by (5.3) a linear interpolation between values of $\mathbf{X}$ at n and $n+1$ gives an approximation for $\mathbf{X}$ at $n+\theta$. The numerical parameter θ is an algorithmic integration constant chosen in order to yield different integration schemes for desired performances. The following values for θ result in the given properties of the well-known integration procedures [18]:

$\theta = 0$, *explicit* Euler forward method, conditionally stable, first-order accurate in Δt,
$\theta = 0.5$, *implicit* trapezoidal rule, unconditionally stable, second-order accurate in Δt,
$\theta = 1$, *implicit* Euler backward method, unconditionally stable, first-order accurate in Δt.

In order to develop a scheme for a solution at $n+1$ with a known or initial value at n, consider (5.1) at $n+\theta$,

$$\boldsymbol{\mathcal{C}}_{n+\theta}\left(\frac{\mathrm{d}\mathbf{X}}{\mathrm{d}t}\right)_{n+\theta} + \boldsymbol{\mathcal{K}}_{n+\theta}\,\mathbf{X}_{n+\theta} = \boldsymbol{\mathcal{F}}_{n+\theta}, \tag{5.4}$$

where the discretised forms (5.2) and (5.3) are substituted giving,

$$\boldsymbol{\mathcal{C}}_{n+\theta}\left(\frac{\mathbf{X}_{n+1} - \mathbf{X}_n}{\Delta t}\right) + \boldsymbol{\mathcal{K}}_{n+\theta}\left[(1-\theta)\mathbf{X}_n + \theta\mathbf{X}_{n+1}\right] = \boldsymbol{\mathcal{F}}_{n+\theta}. \tag{5.5}$$

Expanding and grouping the terms gives the following common single-stage single-step schemes for the solution of $\mathrm{X}_{\mathrm{n+1}}$, which belong to the weighted Euler difference family,

$$\left[\boldsymbol{\mathcal{C}} + \theta\Delta t\boldsymbol{\mathcal{K}}\right]_{n+\theta}\mathbf{X}_{n+1} = \left[\boldsymbol{\mathcal{C}} - (1-\theta)\Delta t\boldsymbol{\mathcal{K}}\right]_{n+\theta}\mathbf{X}_n + \Delta t\boldsymbol{\mathcal{F}}_{n+\theta}. \tag{5.6}$$

The coefficient matrices and forcing conditions here are evaluated as

$$\boldsymbol{\mathcal{C}}_{n+\theta} = \boldsymbol{\mathcal{C}}(\mathbf{X}_n + \theta\Delta t\dot{\mathbf{X}}_{n+\theta}) \tag{5.7}$$

$$\boldsymbol{\mathcal{K}}_{n+\theta} = \boldsymbol{\mathcal{K}}(\mathbf{X}_n + \theta\Delta t\dot{\mathbf{X}}_{n+\theta}) \tag{5.8}$$

$$\boldsymbol{\mathcal{F}}_{n+\theta} = \boldsymbol{\mathcal{F}}(\mathbf{X}_n + \theta\Delta t\dot{\mathbf{X}}_{n+\theta}) \tag{5.9}$$

which are strongly dependent on the primary/state variables, highlighting the requirement for an appropriate iterative strategy for the solution of (5.10).

This result is also derived via a more general weighted residual form [207], and is denoted as the SS11 algorithm. In SSpj notation this is a Single-Step method of a polynomial approximation/expansion of degree one, $p = 1$, to solve a differential equation of first-order, $j = 1$ ($\mathcal{O}(\Delta t^j)$). It is now presented in the more computationally/algorithmically useful two-stage single-step form of

$$\left[\boldsymbol{\mathcal{C}} + \theta\Delta t\boldsymbol{\mathcal{K}}\right]_{n+\theta}\dot{\mathbf{X}}_{n+\theta} = -\boldsymbol{\mathcal{K}}_{n+\theta}\mathbf{X}_n + \boldsymbol{\mathcal{F}}_{n+\theta} \tag{5.10}$$

$$\mathbf{X}_{n+1} = \mathbf{X}_n + \Delta t\dot{\mathbf{X}}_{n+\theta} \tag{5.11}$$

where $\dot{\mathbf{X}}_{n+\theta}$ is the $\mathcal{O}(\Delta t)$ approximation of $(\mathrm{d}\mathbf{X}/\mathrm{d}t)_{n+\theta}$ over the time-step Δt, (5.2). This two-stage form also follows from rearranging (5.5) in terms of $\dot{\mathbf{X}}_{n+\theta}$ and on inspection again of (5.2).

5.2 Method 2: The Thomas-Gladwell method

A class of algorithms proposed in [207] deals with multi-stage single-step methods for both first- and second-order differential equations. A particular method known as the SS21 algorithm of which [190] proposes a more generalised form is incorporated. This method has three integration parameters which makes it flexible for efficient embedding with the θ-method. The method is presented as a two-stage single-step procedure as follows,

$$[\varphi_2 \Delta t \boldsymbol{\mathcal{C}} + \varphi_3 \Delta t^2 \boldsymbol{\mathcal{K}}]\ddot{\bar{\mathbf{X}}}_n = -\boldsymbol{\mathcal{C}}\dot{\bar{\mathbf{X}}}_n - \boldsymbol{\mathcal{K}}[\bar{\mathbf{X}}_n + \varphi_1 \Delta t \dot{\bar{\mathbf{X}}}_n] + \boldsymbol{\mathcal{F}}_{n+\varphi_1} \tag{5.12}$$

$$\bar{\mathbf{X}}_{n+1} = \bar{\mathbf{X}}_n + \Delta t \dot{\bar{\mathbf{X}}}_n + \frac{1}{2}\Delta t^2 \ddot{\bar{\mathbf{X}}}_n \tag{5.13}$$

where

$$\ddot{\bar{\mathbf{X}}}_n = (\dot{\bar{\mathbf{X}}}_{n+1} - \dot{\bar{\mathbf{X}}}_n)/\Delta t \tag{5.14}$$

is the approximation of $(\mathrm{d}^2\mathbf{X}/\mathrm{d}t^2)_n$ as an average estimate over the time step Δt. The coefficent matrices and forcing conditions are evaluated as

$$\boldsymbol{\mathcal{C}}_{n+\varphi} = \boldsymbol{\mathcal{C}}(\bar{\mathbf{X}}_n + \varphi_1 \Delta t \dot{\bar{\mathbf{X}}}_n + \varphi_3 \Delta t^2 \ddot{\bar{\mathbf{X}}}_n) \tag{5.15}$$

$$\boldsymbol{\mathcal{K}}_{n+\varphi} = \boldsymbol{\mathcal{K}}(\bar{\mathbf{X}}_n + \varphi_1 \Delta t \dot{\bar{\mathbf{X}}}_n + \varphi_3 \Delta t^2 \ddot{\bar{\mathbf{X}}}_n) \tag{5.16}$$

$$\boldsymbol{\mathcal{F}}_{n+\varphi} = \boldsymbol{\mathcal{F}}(\bar{\mathbf{X}}_n + \varphi_1 \Delta t \dot{\bar{\mathbf{X}}}_n + \varphi_3 \Delta t^2 \ddot{\bar{\mathbf{X}}}_n). \tag{5.17}$$

The schemes of (5.12) are unconditionally stable given $2\varphi_3 \geq \varphi_1 \geq 0.5$ and $\varphi_2 \geq 0.5$ [190]. They are also second-order accurate, $\mathcal{O}(\Delta t^2)$ convergent, for first-order ODEs given $\varphi_1 = \varphi_2$ [104].

Equation (5.12) is rearranged such that it can be embedded with the Euler schemes via the substitution of (5.14) as follows

$$[\varphi_2 \boldsymbol{\mathcal{C}} + \varphi_3 \Delta t \boldsymbol{\mathcal{K}}]\dot{\bar{\mathbf{X}}}_{n+1} = [(\varphi_2 - 1)\boldsymbol{\mathcal{C}}\dot{\bar{\mathbf{X}}}_n + (\varphi_3 - \varphi_1)\Delta t \boldsymbol{\mathcal{K}}\dot{\bar{\mathbf{X}}}_n] - \boldsymbol{\mathcal{K}}\bar{\mathbf{X}}_n + \boldsymbol{\mathcal{F}}_{n+\varphi_1} \tag{5.18}$$

$$\bar{\mathbf{X}}_{n+1} = \bar{\mathbf{X}}_n + \frac{1}{2}\Delta t(\dot{\bar{\mathbf{X}}}_n + \dot{\bar{\mathbf{X}}}_{n+1}) \tag{5.19}$$

The SS11 equation (5.10) and the rearranged Thomas-Gladwell equation (5.18) are of the same form and can be made the same by setting $\theta = \varphi_1 = \varphi_3$ and $\varphi_2 = 1$. However, updates to the schemes (5.11) and (5.19) approximate with adjacent $\mathcal{O}(\Delta t)$ and $\mathcal{O}(\Delta t^2)$ accuracies respectively, given $\theta \neq 0.5$. Setting in this manner where the derivatives $\dot{\bar{\mathbf{X}}}_{n+1} \equiv \dot{\mathbf{X}}_{n+\theta}$ coincide, means that the solution of one nonlinear system is required at each time-step thereby promoting considerable efficiency.

5.3 Embedded backward-Euler/Thomas-Gladwell pair

The two integration methods are embedded via setting $\theta = \varphi_{1,2,3} = 1$. This employs the fully implicit backward Euler method which is prevalent in hydrogeology and in engineering practice due to its robustness in the face of stiff ODE systems (typical of the discretisations in this work), unconditional stability, damping behaviour towards unwanted oscillations[1], and resilience to abrupt changes in forcing/boundary conditions. Its first-order accuracy is also sufficient for the practicalities involved with subsurface modelling. However, embedded with the Thomas-Gladwell method an estimate of its local truncation error can be given for adaptive purposes.

Combining the methods as outlined the embedded system is now given,

$$[\boldsymbol{\mathcal{C}} + \Delta t\boldsymbol{\mathcal{K}}]_{n+1}\,\dot{\mathbf{X}}_{n+1} = [\boldsymbol{\mathcal{F}}_{n+1} - \boldsymbol{\mathcal{K}}_{n+1}\mathbf{X}_n] \tag{5.20}$$

$$\mathbf{X}_{n+1} = \mathbf{X}_n + \Delta t\dot{\mathbf{X}}_{n+1} \tag{5.21}$$

$$\hat{\mathbf{X}}_{n+1} = \mathbf{X}_n + \frac{1}{2}\Delta t(\dot{\mathbf{X}}_{n+1} + \dot{\mathbf{X}}_n) \tag{5.22}$$

where $\mathbf{X}_{n+1}$ and $\hat{\mathbf{X}}_{n+1}$ are now the local first- and second-order estimates. The coefficent matrices and forcing conditions are evaluated as

$$\boldsymbol{\mathcal{C}}_{n+1} = \boldsymbol{\mathcal{C}}(\mathbf{X}_{n+1}) \tag{5.23}$$

$$\boldsymbol{\mathcal{K}}_{n+1} = \boldsymbol{\mathcal{K}}(\mathbf{X}_{n+1}) \tag{5.24}$$

$$\boldsymbol{\mathcal{F}}_{n+1} = \boldsymbol{\mathcal{F}}(\mathbf{X}_{n+1}). \tag{5.25}$$

Essentially, by averaging the derivatives as of (5.22) the accuracy of the approximation is raised locally. Note however that the backward Euler method is employed as the solution and thus the evaluation of (5.21) is carried to the next time-step as $\mathbf{X}_n$ throughout. It is the $\mathcal{O}(\Delta t^2)$ estimate of the local truncation error of (5.21), occurring at the $n+1$ step, that is given by the difference

$$|\mathbf{X}_{n+1} - \hat{\mathbf{X}}_{n+1}| = \frac{1}{2}\Delta t|\dot{\mathbf{X}}_{n+1} - \dot{\mathbf{X}}_n| = \frac{1}{2}\Delta t^2|\ddot{\mathbf{X}}_n|, \tag{5.26}$$

which can also be shown through Taylor expansion.

5.4 Nonlinear solver

The coupled problem (5.20) is to be solved at a fixed point in time. In abstract form it can be viewed as a fixed-point problem

$$\mathbf{X}_{n+1} = f(\mathbf{X}_{n+1}) \tag{5.27}$$

which is equivalent to the nonlinear system

$$g(\mathbf{X}_{n+1}) = 0 \tag{5.28}$$

given by the residual operator g as defined by

$$g(\mathbf{X}_{n+1}) \equiv f(\mathbf{X}_{n+1}) - \mathbf{X}_{n+1}. \tag{5.29}$$

This problem can be solved by successive substitution in the way of

$$\mathbf{X}^{s+1}_{n+1} = f(\mathbf{X}^{s}_{n+1}) \tag{5.30}$$

---

[1] This seems in apparent contradiction with Section 5.1, where $\theta = 0.5$ demonstrates better performance than $\theta = 1$. However explanation is that the accuracy of discretisation is judged both in time and space.

where s denotes the iteration count within each time-step. For any initial input vector, $\mathbf{X}^0_{n+1}$, this process is convergent if the function f satisfies the assumption of the Banach contraction mapping theorem [145]. A fixed-point iteration is also described as a self-consistent field (SCF) iteration, which finds $\mathbf{x} \in \mathbb{R}^n$ such that $\mathbf{x} = f(\mathbf{x})$ given $f : \mathbb{R}^n \rightarrow \mathbb{R}^n$. Self-consistence is achieved when the input and output vectors coincide or, equivalently, when the residual vector tends to zero [145].

5.4.1 Solver

At each iteration the set of linearised equations to be solved are of the form $\mathbf{Ax} = \mathbf{b}$ (Equation 5.20). Due to the formulation as it stands which is typical of a monolithic coupled finite element problem, $\mathbf{A}$ is sparse and unsymmetric. This burden on solving for $\mathbf{x}$ is placed on the UMFPACK (Unsymmetrical Multi-Frontal) solver [51]. These routines use direct sparse **LU** factorisation (Cholesky decomposition) where the matrix is computed as an assemblage of sub-matrices (which can be referred to as elements analogous with the FE method) which coordinate as a front [98] of subsets to which dense matrix operations can then be applied. This process can be carried out with multiple fronts [52] in order to save time and allow for work to be carried out parallelised if desired amongst other efficiencies as explored in associated work. UMFPACK is written in ANSI/ISO C and is interfaced in this work within the Matlab environment.

If larger (and potentially 3D) domains are modelled, partitioned and/or projected (conjugate gradient-like) iterative methods may be required such as the biconjugate gradient stabilised method (Bi-CGSTAB). Pre-conditioning may also be required in order to prevent ill-conditioning, however such methods show potential for coupled consolidation equations [67].

5.4.2 Anderson acceleration and mixing

A straightforward fixed-point procedure alone gives slow convergence. Noting that calls to the solver for coupled and generally for subsurface (large-scale) problems are particularly expensive, fixed-point procedures are sometimes not an option, particularly when many solver calls do not bring about convergence. On the other hand difficulties also arise using standard Newton methods because the Jacobian is explicitly required at each iteration. The Jacobian in some instances is unavailable analytically or difficult and/or expensive to obtain numerically.

An effective nonlinear solver is devised in this work through selective time-stepping, as discussed in the following section, and via a modified fixed-point method which employs Anderson mixing in order to improve and accelerate convergence of the iterations for each selected time-step.

Firstly, a simple mixing scheme is introduced. Consider 'mixing' the input and output vectors of a fixed-point iteration in the following linear fashion in order to produce an input vector for the forthcoming iteration, $s + 1$,

$$\mathbf{X}^{s+1} = \mathbf{X}^s + \beta^s(f(\mathbf{X}^s) - \mathbf{X}^s) \tag{5.31}$$

$$= \mathbf{X}^s + \beta^s\mathbf{R}^s \tag{5.32}$$

where $\mathbf{R}$ now denotes the residual vector as of (5.29), and $0 \leq \beta^s \leq 1$ is a mixing or damping parameter which can be altered over the iterations. Note that field operator f was introduced in (5.27) to denote the operation performed on the primary variables in order to solve (5.20), however it may also be considered as a general nonlinear operation. Setting $\beta^s = 0$ will take the old input vector through again and $\beta^s = 1$ will take the output vector directly through, essentially undamped. This factor is beneficial for systems which are prone to producing oscillations or divergence when the initial estimates are far from the solution. Again convergence is relatively slow, however it is to be viewed that this is due to (5.32) taking information only from the immediate iteration vectors.

Anderson acceleration mixing improves on this notion by processing information of the vectors from previous successive iterations powerfully in order to bring about faster convergence. The processing may begin after some initial iterations have been computed s_{startA}, as some initial iterations may not pose as useful a degree of information on indicating system convergence as the iterations which follow. For the same reason some maximum number of the latest iterations $m_{\max}$ may be specified for processing alone if/once reached. Considering therefore a modified form of Anderson acceleration where the latest $m+1$ iteration inputs $(\mathbf{X}^{s-m}, \ldots, \mathbf{X}^s)$, are processed with the corresponding residual outputs $(\mathbf{R}^{s-m}, \ldots, \mathbf{R}^s)$ via the linear combinations,

$$\tilde{\mathbf{X}}^s = \mathbf{X}^s - \sum_{i=s-m}^{s-1} \gamma^i_{(s)} \Delta\mathbf{X}^i = \mathbf{X}^s - \boldsymbol{\mathcal{X}}^s \boldsymbol{\gamma}_{(s)} \tag{5.33}$$

$$\tilde{\mathbf{R}}^s = \mathbf{R}^s - \sum_{i=s-m}^{s-1} \gamma^i_{(s)} \Delta\mathbf{R}^i = \mathbf{R}^s - \boldsymbol{\mathcal{R}}^s \boldsymbol{\gamma}_{(s)} \tag{5.34}$$

where $\Delta\mathbf{X}^i = \mathbf{X}^{i+1} - \mathbf{X}^i$ and $\Delta\mathbf{R}^i = \mathbf{R}^{i+1} - \mathbf{R}^i$, and the arrays $\boldsymbol{\mathcal{X}}^s = [\Delta\mathbf{X}^{s-m}, \ldots, \Delta\mathbf{X}^{s-1}]$ and $\boldsymbol{\mathcal{R}}^s = [\Delta\mathbf{R}^{s-m}, \ldots, \Delta\mathbf{R}^{s-1}]$. Essentially, $\tilde{\mathbf{X}}^s$ and $\tilde{\mathbf{R}}^s$ are weighted averages of the previous vectors $\mathbf{X}^{s-m}, \ldots, \mathbf{X}^s$ and $\mathbf{R}^{s-m}, \ldots, \mathbf{R}^s$ respectively, weighted through the arguments $\boldsymbol{\gamma}^{(s)} = (\gamma^{s-m}, \ldots, \gamma^{s-1})^{\mathrm{T}}$ determined by the minimisation

$$\min_{\boldsymbol{\gamma}^{(s)} = (\gamma^{s-m}, \ldots, \gamma^{s-1})^{\mathrm{T}}} \| \mathbf{R}^s - \boldsymbol{\mathcal{R}}^s \boldsymbol{\gamma}^{(s)} \|_2, \tag{5.35}$$

which minimises the weighted average of the corresponding residuals in order to find a tangent/Newton direction for the next iteration from the optimal linear combination of vectors, $\mathbf{X}$ and $\mathbf{R}$, within the space spanned by previous iterations. The successive unconstrained least-squares problem (5.35) is solved efficiently by updating factors in a $\boldsymbol{\mathcal{R}} = \boldsymbol{QR}$ decomposition [198]. Note that the notion of weighted averages is visualised easier on expanding (5.33 & 5.34), and had the formulation begun in this manner a constrained least-squares problem would be encountered. On solving the unconstrained version, the accelerated update is then given by combining the results of (5.33), (5.34) and (5.35) in the form of (5.32) giving

$$\mathbf{X}^{s+1} = \tilde{\mathbf{X}}^s + \beta^s \tilde{\mathbf{R}}^s \tag{5.36}$$

$$= \mathbf{X}^s + \beta^s \mathbf{R}^s - (\boldsymbol{\mathcal{X}}^s + \beta^s \boldsymbol{\mathcal{R}}^s) \boldsymbol{\gamma}^{(s)}, \tag{5.37}$$

which weights the latest specified m vector iterations and residuals in a manner that minimises the weighted average residual for accelerated convergence. On setting $m_{\max} = 0$, the scheme defaults to simple mixing as no iterations are processed/weighted. Anderson acceleration mixing (5.37) is also shown to be equivalent to a multisecant quasi-Newton (secant updating) method [62, 198], where Newton steps are shown to be formed in the way of implicitly approximated inverse Jacobians, for $g(\mathbf{X}) \equiv f(\mathbf{X}) - \mathbf{X}$, (potentially better than updating the Jacobian itself) from all the available secant information depending on m. This different but complementary point of view happens to derive an equivalent Broyden update (second Broyden method), a vantage which might prove useful for further developments.

This non-intrusive device for improving the convergence of vector sequences is employed at each time-step and is also able to benefit from receiving improved initial estimates from the embedded temporal integration scheme due to the higher order information available.

5.4.3 Tolerance

A residual tolerance, τ_{R} must be specified in order for the convergence procedure to terminate when

$$\|\mathbf{X}_{n+1}^{s+1} - \mathbf{X}_{n+1}^{s}\| \leq \tau_{\mathrm{R}} = \tau_{\mathrm{R}}^{\mathrm{r}}\|\mathbf{X}_{n+1}^{s+1}\| + \tau_{\mathrm{R}}^{\mathrm{a}}. \tag{5.38}$$

The convergence check combines both a relative, $\tau_{\mathrm{R}}^{\mathrm{r}}$ and a much smaller absolute, $\tau_{\mathrm{R}}^{\mathrm{a}}$ tolerance [180] such that any ill-conditioning with the relative measure is avoided if any near zero values were to appear in the solution vector. It is also sensible to monitor the sub-vectors of each of the coupled domains independently, such that

$$\max_{\mathbf{X}=\mathbf{u},\mathbf{p}^{\mathrm{f_i}},\mathbf{T}} \left\{ \frac{\|\mathbf{X}_{n+1}^{s+1} - \mathbf{X}_{n+1}^{s}\|}{\tau_{\mathrm{R}}^{\mathrm{r}}\|\mathbf{X}_{n+1}^{s+1}\| + \tau_{\mathrm{R}}^{\mathrm{a}}} \right\} \leq 1 \tag{5.39}$$

benefits the formulation, especially if the sub-vectors are computed in a staggered manner where each may undergo different rates of time stepping depending on their respective error control. It is common for either the Euclidean norm $\|\cdot\|_2$ or the maximum norm $\|\cdot\|_\infty$ (which renders a 'critical' node with the maximum error) to be used in these circumstances, for both truncation and residual errors.

5.5 Control theory: Adaptive time-step size control

5.5.1 Optimal error control for the integration procedure

From the converged iterations the local truncation error estimate can now be determined as of (5.26), which in turn can be used to control errors within the system through selective time-stepping. Firstly, following the control-theoretical techniques for time-step size selection for differential equations [76, 179], the elementary local error control algorithm is given. For an integration method of order p the local truncation error ε is asymptotically proportional to the time-step size Δt. This is shown via Taylor expansion [78], considering

$$\varepsilon = y(t_0 + \Delta t) - y_1 \tag{5.40}$$

expanded by

$$y(t_0 + \Delta t) = y(t_0) + \dot{y}(t_0)\Delta t + \ddot{y}(t_0)\frac{\Delta t^2}{2!} + \dots \tag{5.41}$$

hence, while introducing appropriate subscript indices,

$$\varepsilon_n = \mathit{\Phi}_n \Delta t_n^{p+1} + \mathcal{O}(\Delta t_n^{p+2}) \tag{5.42}$$

where $\mathit{\Phi}$ contains error coefficients and differentials of the method, which may also be regarded as a function, $\mathit{\Phi}(t, x)$. If it is assumed that $\mathit{\Phi}$ varies slowly (and is therefore assumed constant), a discrepancy between the local truncation error at n and a desired tolerance τ_{T} can therefore be eliminated via the elementary controller:

$$\Delta t_{n+1} = \Delta t_n \left(\frac{\tau_{\mathrm{T}}}{\varepsilon_n}\right)^{\frac{1}{1+p}}. \tag{5.43}$$

This control strategy can also be demonstrated more directly with the proposed embedded methods. From (5.26) and (5.14), if the error to be controlled is

$$\mathbf{X}_{n+1} - \hat{\mathbf{X}}_{n+1} = \frac{1}{2}\Delta t_{n+1}(\dot{\mathbf{X}}_{n+1} - \dot{\mathbf{X}}_n) = \frac{1}{2}(\Delta t_{n+1})^2 \ddot{\mathbf{X}}_n \approx (\Delta t_{n+1})^2 \frac{\mathbf{X}_n - \hat{\mathbf{X}}_n}{(\Delta t_n)^2}, \tag{5.44}$$

if $\ddot{\mathbf{X}}_n \approx \ddot{\mathbf{X}}_{n-1}$, which is permissible while considering $\mathcal{O}(\Delta t)$ accuracy and slow variation, and if it is required that this error at $n+1$ is to be less than a tolerance τ_{T}, then

$$(\Delta t_{n+1})^2 \frac{\|\mathbf{X}_n - \hat{\mathbf{X}}_n\|}{(\Delta t_n)^2} \leq \tau_{\mathrm{T}} = \tau_{\mathrm{T}}^{\mathrm{r}} \|\mathbf{X}_n\| + \tau_{\mathrm{T}}^{\mathrm{a}}, \tag{5.45}$$

from which

$$\Delta t_{n+1} \leq \Delta t_n \left(\frac{\tau_{\mathrm{T}}^{\mathrm{r}} \|\mathbf{X}_n\| + \tau_{\mathrm{T}}^{\mathrm{a}}}{\|\mathbf{X}_n - \hat{\mathbf{X}}_n\|}\right)^{\frac{1}{2}} \tag{5.46}$$

gives an appropriate indication for the next time-step size with information gathered from the current time-step n [103].

If after initial step size control on computation of $\mathbf{X}_{n+1}$, $\varepsilon_{n+1} > \tau_{\mathrm{T}}$, then the step is rejected and repeated with the new more accurate error estimate ε_{n+1} replacing ε_n, along with Δt_{n+1} replacing Δt_n in the control equation. This is such that the step is repeated with a smaller step size and so on until the step is accepted. Hence, where large truncation errors are prevalent then the scheme will reduce the step sizes accordingly.

Clearly rejected steps give unwanted computational expense, so a more stable scheme which can anticipate step size reductions before rejection is desirable. The elementary scheme may lead to poor error control due to:

- The properties of the system of equation may change significantly with the solution such that $\varPhi_n$ and $\varPhi_{n-1}$ do not approximate.

- The error may behave as if $p+1$ is either smaller or larger than expected due to the stiffness of the problem or if higher-order terms become dominant [178].

In order to account more robustly for the error trends during computation both integral and proportional factors are incorporated into the controller [77]:

$$\Delta t_{n+1} = \Delta t_n \left(\frac{\tau_{\mathrm{T}}}{\varepsilon_n}\right)^{k_I} \left(\frac{\varepsilon_{n-1}}{\varepsilon_n}\right)^{k_P} . \tag{5.47}$$

The PI controller accounts for error trends whereby if ε is progressively decreasing over the steps the proportional factor will be become greater than 1, and provided $k_P > 0$, a faster step size growth will occur than with the integral factor alone, and conversely for a progressively increasing error a faster step size reduction will occur. The integral and proportional gain parameters k_I and k_P are an area of study for a given system of equations and should be chosen to obtain suitable dynamics for that system.

The PI controller is incorporated into the design of the time integration algorithm, complementing the acceleration method, as discussed.

5.5.2 Optimal convergence control for an accelerated fixed-point iteration method

It is sought that the step size be further restricted (if necessary) such that there is optimal convergence. To do so the controller must aim for a convergence rate C_{opt} that provides the most efficient integration [75, 145]. The convergence rate C is proportional to the size of time-step and the (unknown) Jacobian, and if the change in Jacobian is small then a successive step size can be given by

$$\Delta t^C_{n+1} = \Delta t_n \frac{C_{\mathrm{opt}}}{C_n}, \tag{5.48}$$

such that in the next step $C_{n+1} \to C_{\mathrm{opt}}$. A more sophisticated control is generally not sought given the significant approximations in estimating the parameters involved.

A inexpensive option for determining the convergence rate is through considering three consecutive iterations, whereby

$$C_n = \max C^s_n = \max_s \frac{\|\mathbf{X}^{s+1}_n - \mathbf{X}^s_n\|}{\|\mathbf{X}^s_n - \mathbf{X}^{s-1}_n\|} \tag{5.49}$$

which gives an estimate of the asymptotic convergence rate that is generally linear for both fixed-point and modified newton-methods [75].

An optimal convergence rate C_{opt}, is however still required such that the controller can aim for the most efficient integration. In the literature [75, 145] methods are demonstrated for estimating its value for given systems, with estimates given for both fixed-point and modified newton-methods. There is therefore potential scope for formulation specifically for the accelerated fixed-point procedure by considering the quasi-Newton Jacobian information as is discussed. In this work, control is dictated by computational accuracy for now, balancing computational accuracy with computational effort per unit step is therefore a point for further study as is discussed further in Section 6.8. The view is that a step size increase should not cause an increase in computational effort per unit step, a value of C should therefore be sought that minimises $s/\Delta t$.

5.5.3 Management of truncation error and convergence control

In order that an optimal selection of time-step size is made in terms of balancing accuracy and unnecessary computational effort per unit step, the minimum Δt_{n+1} from both control criteria (if known) is selected,

$$\Delta t_{n+1} = \min(\Delta t^{\varepsilon}_{n+1},\ \Delta t^{C}_{n+1}). \tag{5.50}$$

For the final algorithm, filtering by judicious coding is applied in order to prevent any aggressive stepping,

$$\Delta t_{+} = \Delta t \cdot \max(f_{\min}, \min(f_{\max},\ \mathrm{s} \cdot f_{\varepsilon},\ \mathrm{s} \cdot f_{C})). \tag{5.51}$$

This ensures that stepping will progress in a controlled manner, or as desired for investigation, due to the lower and upper factor bounds, $f_{\min}$ and $f_{\max}$ respectively, with none to minimal rejected steps, enforced by a safety factor, $\mathrm{s} \approx 0.5^{1/1+p}$ [77, 78, 102, 173]. Tighter enforcement may also follow after rejected steps and the error values should also be coordinated in this filter with the machine precision, on which the code runs.

5.6 Initial variable values and time-step size

5.6.1 Initial derivative

An initial derivative $\dot{\mathbf{X}}_n$ is required for the update (5.22) at the first time-step. This is provided by solving (5.20) for $\Delta t = 0$ with the initial and boundary conditions, that is

$$[\boldsymbol{\mathcal{C}}_0]\dot{\mathbf{X}}_0 = [\boldsymbol{\mathcal{F}}_0 - \boldsymbol{\mathcal{K}}_0\mathbf{X}_0]. \tag{5.52}$$

Afterwards, the successive solutions for $\dot{\mathbf{X}}_{n+1}$ are substituted in the next step as $\dot{\mathbf{X}}_n$.

5.6.2 Initial time-step size

A coarse initial time-step size estimate may be selected and then handled by the controller. If the time-step size is too large it will be rejected by the controller and reduced, if too small it will be increased. A coarse estimate may therefore prove inefficient, in order to provide a more consistent estimation for Δt_0 the following is given

$$\Delta t_0 = \frac{\mathrm{s} \cdot \tau_{\mathrm{T}}^{\frac{1}{1+p}}}{\|\dot{\mathbf{X}}_0\| / \|\mathbf{X}_0\|}, \tag{5.53}$$

which is in line with (5.46) and is based on series expansion [102, 173].

5.6.3 Initial estimate for the nonlinear solver

It is clear that the selection of $\mathbf{X}^0_{n+1}$ for the first iteration of the nonlinear solver in each time-step is important for the robustness and efficiency of the solver, as it is from this value that the final solution must converge. Generally $\mathbf{X}_n$ is reused for this purpose, however with the adaptive scheme employed higher order information is available in order to give a quadratic estimate [176], simply

$$\mathbf{X}^0_{n+1} = \mathbf{X}_n + (\Delta t_{n+1})\dot{\mathbf{X}}_n + \frac{1}{2}(\Delta t_{n+1})^2\ddot{\mathbf{X}}_{n-1} \tag{5.54}$$

where the last term can be related to the truncation error (5.26) and therefore ensures accuracy while also being implicitly controlled by the adaptive scheme.

5.7 Conditioning spatial and temporal discretisation

For modelling a consolidation/heave and/or extraction/injection scenario the controller determines relatively small initial time-step sizes. This is in order to avoid the prescribed truncations errors given the order in accuracy of the time integration scheme (5.20) and the high initial variable gradients at the onset of an instantaneous forcing (traction/flux) condition. Note that the step sizes will generally increase as the system of equations steps through time due to the transient nature of equation (5.1).

For small step sizes however, in coupled Biot-type formulations, it is observed and reported (i.e. [177, 176] and the references therein) that during the early stages of loading (with particular reference to consolidation problems) spatial oscillations occur in the pore pressure distribution at free draining boundaries. These oscillations dissipate over time, however they can be avoided. The problem arises particularly due to ill-conditioning of the $[\boldsymbol{\mathcal{C}} + \Delta t \boldsymbol{\mathcal{K}}]$ matrix, where if Δt is relatively small it can exacerbate the difference in magnitude between the matrix pivots and thus cause numerical difficulties. The differences in magnitude come from the simultaneous integration of the coupled solid mechanical and fluid flow equations which in themselves bring about matrix terms of opposite numerical extremes.

So although decreasing the early step sizes controls the temporal discretisation truncation error, doing so may cause spatial oscillations. Rather than increasing the initial step sizes to placate spacial oscillations at the cost of larger truncation errors which will also stress the convergence behaviour of the nonlinear solver, it is sought to reduce the critical step size of the system at which spacial oscillations occur in order to facilitate the controller and nonlinear solver, as developed. Note also that for a nonlinear system larger uncontrolled step sizes also require more iterations which may oscillate and/or fail to converge.

A critical step size may be indicated by assessing in particular the system parameters and finite elements sizes which directly affect the ill-conditioning, as is discussed in [65, 177]. For consolidation problems in particular, the critical step size is inversely proportional to the mechanical stiffness and conductivity of the porous system and proportional to the characteristic size of the finite element mesh refinement at the boundary involved. Therefore, by refining the mesh appropriately spacial oscillations are avoided.

In this work an acceptable temporal error tolerance is specified, for which the spatial mesh is refined until any oscillations are avoided. This is done in line with the observations made in this Section and in Section 4.6. At this point any further refinement brings about the same smooth ODE system solutions and therefore the same temporal time-stepping behaviour. The interrelated effects of spatial and temporal discretisation, along with the abrupt fluid interface undergoing inter-element transitions, requires further study for the particular system of equations developed in this work. Criteria to this effect are discussed in [102] and the references therein.

In order to compute with small time-step sizes, scaling procedures may also be introduced, which raise the magnitude of the smallest pivot. This has been employed for consolidation problems as of [177, 176]. However, this approach also requires further study in this context.

5.8 Time discretisation algorithm

In simplified concise pseudo-code, Table 5.1 as follows, presents an algorithm efficiently integrating the complementing implementation of:

- The embedded backward Euler method for $\mathbf{X}_n \rightarrow \mathbf{X}_{n+1} \in \mathbb{R}^{i\times 1}$ time integration.
- Anderson accelerative mixing for each nonlinear vector solution where $\mathbf{X}_{n+1} = f(\mathbf{X}_{n+1})$ given $f : \mathbb{R}^{i\times 1} \rightarrow \mathbb{R}^{i\times 1}$, which receives enhanced information from the embedded integration.
- Adaptive time-stepping with PI control theory via assessing the local truncation error trend by the embedded backward Euler/Thomas-Gladwell pair of adjacent accuracy.

Table 5.1: Accelerated solution control algorithm.

Accelerated Fixed-Point Iterations with PI Control Adaptive Time Stepping for $\mathbf{X}_n \rightarrow \mathbf{X}_{n+1} \in \mathbb{R}^{i\times 1}$

```
Set truncation & convergence tolerances $\tau_{\mathrm{T}}^{\mathrm{r/a}} > \tau_{\mathrm{R}}^{\mathrm{r/a}} > 0$
Set mixing/acceleration parameters $\beta$, $m_{\max}, s_{\mathrm{startA}}, s_{\max}$
Set control parameters $k_I^{\mathrm{ac/rj}}$, $k_P^{\mathrm{ac/rj}}$, $C_{\mathrm{opt}}$, $f_{\min}$, $f_{\max}$, s
Initialise $t \leftarrow \Delta t_{n+1} \leftarrow 0,$ and set $t_{\mathrm{final}}$, $n_{\max}$
Initialise $(\varepsilon_{n-1}/\varepsilon_n) \leftarrow 1$
Given $\mathbf{X}_0$, initial conditions.
Initialise $\mathbf{X}_{n+1}^s \leftarrow \mathbf{X}_n \leftarrow \mathbf{X}_0$, and $\dot{\mathbf{X}}_{n+1}^{s+1} \leftarrow \dot{\mathbf{X}}_0 \leftarrow \mathbf{0}$
for $n = 0$ to $n_{\max}$
    Initialise $m \leftarrow 0$
    Initialise $\boldsymbol{\mathcal{X}} \leftarrow \mathbf{0}$
    Initialise $\boldsymbol{\mathcal{R}} \leftarrow \mathbf{0}$
    for $s = 0$ to $s_{\max}$
        Form $\boldsymbol{\mathcal{C}}(\mathbf{X}_{n+1}^s)$, $\boldsymbol{\mathcal{K}}(\mathbf{X}_{n+1}^s)$, $\boldsymbol{\mathcal{F}}(\mathbf{X}_{n+1}^s)$, FE spatial discretisation with BCs.
        if $n = 0$ & $s = 0$
            Solve $\dot{\mathbf{X}}_0 = [\boldsymbol{\mathcal{C}}_0]^{-1}[\boldsymbol{\mathcal{F}}_0 - \boldsymbol{\mathcal{K}}_0\mathbf{X}_0]$ with BCs for free DoFs.
            Determine $\Delta t_1 = \mathrm{s} \cdot \tau_{\mathrm{T}}^{1/2}/(\|\dot{\mathbf{X}}_0\|/\|\mathbf{X}_0\|)$
            Initialise $\dot{\mathbf{X}}_n \leftarrow \dot{\mathbf{X}}_0$
            Initialise $\Delta t_{n+1} \leftarrow \Delta t_1$
```

```
            Update $t \leftarrow t + \Delta t_{n+1}$
        end if
        Solve $\dot{\mathbf{X}}^{s+1}_{n+1} = [\boldsymbol{\mathcal{C}}^s_{n+1} + \Delta t_{n+1}\boldsymbol{\mathcal{K}}^s_{n+1}]^{-1}[\boldsymbol{\mathcal{F}}^s_{n+1} - \boldsymbol{\mathcal{K}}^s_{n+1}\mathbf{X}_n]$ with BCs for free DoFs.
        Determine $\mathbf{X}^{s+1}_{n+1} = f(\mathbf{X}^s_{n+1}) = \mathbf{X}_n + \Delta t_{n+1}\dot{\mathbf{X}}^{s+1}_{n+1}$
        Determine $\mathbf{R}^s_{n+1} = \mathbf{X}^{s+1}_{n+1} - \mathbf{X}^s_{n+1}$
        if $\|\mathbf{R}^s_{n+1}\| \leq \tau_{\mathrm{R}}$
            Break for
        end if
        if $m_{\max} = 0$ or $s < s_{\mathrm{startA}}$. Simple un-accelerated approximate solution update.
            Update $\mathbf{X}^s_{n+1} \leftarrow \mathbf{X}^{s+1}_{n+1}$
        else Anderson acceleration mixing.
            if $s > s_{\mathrm{startA}}$
                $\boldsymbol{\mathcal{X}} = [\boldsymbol{\mathcal{X}},\ (\mathbf{X}^s_{n+1} - \mathbf{X}^{s-}_{n+1})]$, for $m$ iterations $\leq m_{max}$.
                $\boldsymbol{\mathcal{R}} = [\boldsymbol{\mathcal{R}},\ (\mathbf{R}^s_{n+1} - \mathbf{R}^{s-}_{n+1})]$, for $m$ iterations $\leq m_{max}$.
                Update $m \leftarrow m + 1$
            end if
            Update $\mathbf{X}^{s-}_{n+1} \leftarrow \mathbf{X}^s_{n+1}$
            Update $\mathbf{R}^{s-}_{n+1} \leftarrow \mathbf{R}^s_{n+1}$
            if $m = 0$
                Update $\mathbf{X}^s_{n+1} \leftarrow \mathbf{X}^{s+1}_{n+1}$
            else
                Solve $\min_{\boldsymbol{\gamma}^{(s)}=(\gamma^{s-m},\dots,\gamma^{s-1})^{\mathrm{T}}} \|\mathbf{R}^s_{n+1} - \boldsymbol{\mathcal{R}}\boldsymbol{\gamma}^{(s)}\|_2$
                Update $\mathbf{X}^{s+1}_{n+1} = \mathbf{X}^s_{n+1} + \beta\mathbf{R}^s_{n+1} - (\boldsymbol{\mathcal{X}} + \beta\boldsymbol{\mathcal{R}})\gamma^{(s)}$
                Update $\mathbf{X}^s_{n+1} \leftarrow \mathbf{X}^{s+1}_{n+1}$
            end if
        end if
    end for
    Determine $\hat{\mathbf{X}}_{n+1} = \mathbf{X}_n + \frac{1}{2}\Delta t_{n+1}(\dot{\mathbf{X}}^{s+1}_{n+1} + \dot{\mathbf{X}}_n)$. Embedded higher order solution.
    Determine $\varepsilon_n = \|\hat{\mathbf{X}}_{n+1} - \mathbf{X}^{s+1}_{n+1}\|$
    Update $\Delta t_n \leftarrow \Delta t_{n+1}$
    if $\varepsilon_n \leq \tau_{\mathrm{T}}$ & $s \leq s_{\max}$, then $n \leftarrow n + 1$. Controller accepts step.
        Modify $\Delta t_{n+1} = \Delta t_n \cdot \mathrm{s} \cdot (\tau_{\mathrm{T}}/\varepsilon_n)^{k_I^{\mathrm{ac}}} (\varepsilon_{n-1}/\varepsilon_n)^{k_P^{\mathrm{ac}}}$ constrained by $C_{\mathrm{opt}}$, $f_{\min}$, $f_{\max}$, s.
        Update $t \leftarrow t + \Delta t_{n+1}$
        Update $\dot{\mathbf{X}}_{n-1} \leftarrow \dot{\mathbf{X}}_n$
        Update $\dot{\mathbf{X}}_n \leftarrow \dot{\mathbf{X}}^{s+1}_{n+1}$
        Update $\mathbf{X}_n \leftarrow \mathbf{X}^{s+1}_{n+1}$
    else $\varepsilon_n > \tau_{\mathrm{T}}$, then $n \circlearrowleft$. Controller rejects step.
        Modify $\Delta t_{n+1} = \Delta t_n \cdot \mathrm{s} \cdot (\tau_{\mathrm{T}}/\varepsilon_n)^{k_I^{\mathrm{rj}}} (\varepsilon_{n-1}/\varepsilon_n)^{k_P^{\mathrm{rj}}}$ constrained by $C_{\mathrm{opt}}$, $f_{\min}$, $f_{\max}$, s.
        if $n = 0$
            Set $\dot{\mathbf{X}}_{n-1} \leftarrow \dot{\mathbf{X}}_n$
        end if
        Update $t \leftarrow t - \Delta t_n + \Delta t_{n+1}$
    end if
    Update $\varepsilon_{n-1} \leftarrow \varepsilon_n$
    Determine $\ddot{\mathbf{X}}_{n-1} = (\dot{\mathbf{X}}_n - \dot{\mathbf{X}}_{n-1})/\Delta t_n$. Enhance solver/AA with embedded control data.
    Determine $\mathbf{X}^s_{n+1} = \mathbf{X}_n + (\Delta t_{n+1})\dot{\mathbf{X}}_n + \frac{1}{2}(\Delta t_{n+1})^2\ddot{\mathbf{X}}_{n-1}$
    Post process & store data.
    if $t \geq t_{\mathrm{final}}$
        Break for
    end if
end for
```

For an appropriately refined FE mesh the mixing and control parameters allow fine tuning for the effective solution of the governing system of equations. Note that the norms are calculated in both a relative-absolute sense such that all the sub-vectors are assessed with any potential ill-conditioning avoided. Appropriate numerical parameter values are discussed further and given in Section 6.2.

In practice the algorithm is coded into a series of program functions which encapsulate its various theoretical components. These include all the coupled finite element procedures as discussed in Chapter 4, the accelerative nonlinear solver, the PI controller, and the post processor (stress recovery, etc.). This programming strategy allows for ease of maintenance and development of the theoretical components which form the program. It also allows for distribution of the functions for other modelling/programming applications. Better computational performance is also achieved in this respect within the Matlab environment, as the functions may be optimised for runtime, given that the shared variables are passed by reference where possible.

The tabulated algorithm is employed in order to solve the system of coupled governing equations (4.32). This is demonstrated in Chapter 6 for various/reduced coupled configurations, which are parametrised for certain test and realistic scenarios, as is discussed. The numerical properties of the algorithm will also be assessed.

5.9 Potential matrix partitioning and solution staggering

Partitioning of the coefficient matrix operators is important for the design of coupled numerical models, whereby various advantageous simultaneous or staggered solution strategies may be implemented. Detailed studies on this aspect are given for simpler coupled numerical models in [120] and the references therein.

Considering the linear system which requires solution in (5.8), after (5.20–5.22),

$$[\boldsymbol{\mathcal{C}} + \Delta t \boldsymbol{\mathcal{K}}]_{n+1} \dot{\mathbf{X}}_{n+1} = [\boldsymbol{\mathcal{F}}_{n+1} - \boldsymbol{\mathcal{K}}_{n+1}\mathbf{X}_n], \tag{5.55}$$

the l.h.s. operator may be partitioned as follows,

$$[\boldsymbol{\mathcal{C}} + \Delta t \boldsymbol{\mathcal{K}}]_{n+1} = [\boldsymbol{\mathcal{C}} + \Delta t \boldsymbol{\mathcal{K}}]^{\mathrm{L}}_{n+1} + [\boldsymbol{\mathcal{C}} + \Delta t \boldsymbol{\mathcal{K}}]^{\mathrm{R}}_{n+1}, \tag{5.56}$$

which on substitution into (5.55), yields

$$[\boldsymbol{\mathcal{C}} + \Delta t \boldsymbol{\mathcal{K}}]^{\mathrm{L}}_{n+1} \dot{\mathbf{X}}_{n+1} = [\boldsymbol{\mathcal{F}}_{n+1} - \boldsymbol{\mathcal{K}}_{n+1}\mathbf{X}_n] - [\boldsymbol{\mathcal{C}} + \Delta t \boldsymbol{\mathcal{K}}]^{\mathrm{R}}_{n+1} \dot{\mathbf{X}}^{(\mathrm{P})}_{n+1} \tag{5.57}$$

where the R superscripted operator has been moved to the r.h.s., where $\dot{\mathbf{X}}^{(\mathrm{P})}_{n+1}$ has subsequently become a predictor which is usually a linear combination of previous solution vectors,

$$\dot{\mathbf{X}}^{(\mathrm{P})}_{n+1} = \sum_{i=0}^{n} a_i \dot{\mathbf{X}}_{n-i}. \tag{5.58}$$

For each time-step an appropriate iterative predictor-corrector method may now be carried out until subsequent vector solutions are within a given tolerance, where depending on the partitioning approach, different procedures for (5.57) may be employed.

The partitioning of $[\boldsymbol{\mathcal{C}} + \Delta t \boldsymbol{\mathcal{K}}]_{n+1}$ here can be carried out in various ways, however, the procedure is generally beneficial if the coupling is weak. On inspection of (4.32) the coupling between the solid displacement and matrix pressure fields is strong, with weaker coupling observed between the fracture pressure fields and/or, as is generally the case in consolidation problems, with the temperature field. Considering the temperature field to be weakly coupled a potential partitioning of the L superscripted operator is

$$[\boldsymbol{\mathcal{C}} + \Delta t \boldsymbol{\mathcal{K}}]^{\mathrm{L}}_{n+1} \dot{\mathbf{X}}_{n+1} =$$

$$\left[\begin{array}{c|cc|cc|c}
\mathbf{K}_1 & \mathbf{Q}_{\mathrm{uw1}} & \mathbf{Q}_{\mathrm{un1}} & \mathbf{0} & \mathbf{0} & \mathbf{0} \\
\hline
\mathbf{Q}_{\mathrm{wu1}} & \mathbf{S}_{\mathrm{w1}} + \Delta t(\mathbf{H}_{\mathrm{w1}} + \mathbf{L}_{\mathrm{w}}) & \mathbf{Q}_{\mathrm{wn1}} & -\Delta t \mathbf{L}_{\mathrm{w}} & \mathbf{0} & \mathbf{0} \\
\mathbf{Q}_{\mathrm{nu1}} & \mathbf{Q}_{\mathrm{nw1}} & \mathbf{S}_{\mathrm{n1}} + \Delta t(\mathbf{H}_{\mathrm{n1}} + \mathbf{L}_{\mathrm{n}}) & \mathbf{0} & -\Delta t \mathbf{L}_{\mathrm{n}} & \mathbf{0} \\
\hline
\mathbf{0} & -\Delta t \mathbf{L}_{\mathrm{w}} & \mathbf{0} & \mathbf{S}_{\mathrm{w2}} + \Delta t(\mathbf{H}_{\mathrm{w2}} + \mathbf{L}_{\mathrm{w}}) & \mathbf{Q}_{\mathrm{wn2}} & \mathbf{0} \\
\mathbf{0} & \mathbf{0} & -\Delta t \mathbf{L}_{\mathrm{n}} & \mathbf{Q}_{\mathrm{nw2}} & \mathbf{S}_{\mathrm{n2}} + \Delta t(\mathbf{H}_{\mathrm{n2}} + \mathbf{L}_{\mathrm{n}}) & \mathbf{0} \\
\hline
\mathbf{0} & \mathbf{0} & \mathbf{0} & \mathbf{0} & \mathbf{0} & \mathbf{C}_{\mathrm{T}} + \Delta t \mathbf{H}_{\mathrm{T}}
\end{array}\right]
\frac{\mathrm{d}}{\mathrm{d}t}
\left\{\begin{array}{c}
\bar{\mathbf{u}} \\ \hline
\bar{\mathbf{p}}^{\mathrm{w}_1} \\
\bar{\mathbf{p}}^{\mathrm{n}_1} \\ \hline
\bar{\mathbf{p}}^{\mathrm{w}_2} \\
\bar{\mathbf{p}}^{\mathrm{n}_2} \\ \hline
\bar{\mathbf{T}}
\end{array}\right\}, \tag{5.59}$$

for which the R superscripted operator is

$$[\boldsymbol{\mathcal{C}} + \Delta t \boldsymbol{\mathcal{K}}]^{\mathrm{R}}_{n+1} \dot{\mathbf{X}}_{n+1} =
\left[\begin{array}{c|cc|cc|c}
\mathbf{0} & \mathbf{0} & \mathbf{0} & \mathbf{0} & \mathbf{0} & \mathbf{Q}_{\mathrm{uT}} \\
\hline
\mathbf{0} & \mathbf{0} & \mathbf{0} & \mathbf{0} & \mathbf{0} & \mathbf{Q}_{\mathrm{w1T}} \\
\mathbf{0} & \mathbf{0} & \mathbf{0} & \mathbf{0} & \mathbf{0} & \mathbf{Q}_{\mathrm{n1T}} \\
\hline
\mathbf{0} & \mathbf{0} & \mathbf{0} & \mathbf{0} & \mathbf{0} & \mathbf{Q}_{\mathrm{w2T}} \\
\mathbf{0} & \mathbf{0} & \mathbf{0} & \mathbf{0} & \mathbf{0} & \mathbf{Q}_{\mathrm{n2T}} \\
\hline
\mathbf{0} & \mathbf{0} & \mathbf{Q}_{\mathrm{Tn1}} + \Delta t \mathbf{H}_{\mathrm{Tn1}} & \mathbf{0} & \mathbf{Q}_{\mathrm{Tn2}} + \Delta t \mathbf{H}_{\mathrm{Tn2}} & \mathbf{0}
\end{array}\right]
\frac{\mathrm{d}}{\mathrm{d}t}
\left\{\begin{array}{c}
\mathbf{0} \\ \hline
\mathbf{0} \\
\bar{\mathbf{p}}^{\mathrm{n}_1} \\ \hline
\mathbf{0} \\
\bar{\mathbf{p}}^{\mathrm{n}_2} \\ \hline
\bar{\mathbf{T}}
\end{array}\right\}^{(\mathrm{P})}. \tag{5.60}$$

This partitioning approach has made the coefficient matrix (5.59) of the linear system symmetric, if indeed the stiffness and other sub-matrices are (made) symmetric. Additionally, the system is now uncoupled into two sets of equations, namely, those of the displacement/pressure fields and the temperature field, which allows for the solution of the system to be determined in a staggered manner [120]. Matrix partitioning and solution staggering is not considered any further in this work. Note that casting the favourable partitioned forms and staggering the solution in the control algorithm, where there is potential scope for effective modification of the predictor-corrector selection, is left for further study. Such an approach is likely to be appropriate when computing a large multi-physics system of equations with weakly coupled phenomena, the degree of coupling within the present system is also a point for further research in this context given the governing energy balance equation form being considered.

Chapter 6

Model Results & Performance

In this Chapter the physical and numerical model parametrisations, as introduced and developed throughout Chapters 2–5, are first discussed further and allocated appropriate base case valuations for study. Secondly, several key modelling aspects are discussed in the following sections. Once covered, the numerical model is then trialled through a series of scenarios for the for verification and validation. This is done in a manner where various simplified subsets or sub-couplings of the full discretised system of equations are assessed in turn, increasing in complexity. This approach, along with the realistic physical parametrisations, also allows for the effects of various couplings within the numerical system to be highlighted. Finally, the numerical properties and performance of the control algorithm, as developed in Chapter 5, is also assessed.

6.1 Physical parameter base set

The system of equations (4.32) is solved with a series of model parameters which characterise the hydro-thermo-mechanical-chemical behaviour of the phases within the reservoir system, as introduced in Chapter 2 and worked into the system of governing field equations. These parameters are collected and listed in Table 6.1, along with their symbol, valuation and units. The parameters are initially valued with reference to four extreme scenarios belonging to the brine aquifer subset of potential geostorage sites, as previously introduced in Section 3.2.6. For the fluid phases in particular, the parameters are essentially thermophysical properties of the fluid and are therefore well referenced functions of pressure, temperature and composition (p-T-x), as discussed in Section 2.6.8.

Following from Chapter 2, EoS program functions are coded that process p-T-x data to give value to the required fluid properties as parametrised in this work. This stands in part for future development with respect to updating nonlinear material behaviour. For initial investigation however, unlike for the multiphase flow and saturation behaviour, the individual intrinsic material phase properties are assumed constant which is generally meaningful in this context given the extent to which they vary with respect to p-T-x over the ranges of interest. That is, the primary state variables ($\mathbf{u}$-p^{w_1}-p^{n_1}-p^{w_2}-p^{n_2}-T) are considered to vary moderately such that the material properties of the system may be considered constant. Therefore, the EoS program functions are used to initially parametrise the model accurately from reference p-T-x data based on the reservoir scenario/initial conditions. The six thermophysical properties (ρ-μ-K-β-c_p-χ) of each fluid phase are thus listed in Table 6.1 for reference only, as a numerical simulation may be parametrised via reference or initial p-T-x data alone in order to describe the fluids.

The thermophysical properties for the CO_2 phase are solved for after the work of [20, 64, 166, 181], and for the H_2O phase after [8, 7, 58, 105, 106, 151, 160, 161], in which the ranges of validity, extents of physical accuracy, and the compromise of computational demand and physical accuracy, of the equations of state developed, are discussed in detail.

For Table 6.1, the CO_2-rich phase is parametrised as pure CO_2, and the H_2O-rich (brine) phase as a H_2O-NaCl solution, both at the reference reservoir p-T values, with no cross composition/mutual solubility (miscibility), which are acceptable investigative assumptions as discussed in Section 2.6.8. Sodium chloride is selected as the dissolved component in water as it is the most common and dominate solute in this context. The salinity of the H_2O-NaCl solution (brine) is parametrised at a mass fraction of 0.1 (mass of salt solute to mass of solution), which is a molality of 1.9 mol/kg (moles of salt solute to mass of solvent). The accurate thermodynamic description of saline aqueous fluids are also of particular importance for the modelling and prediction of other engineered and natural large scale hydrogeothermal processes [58]. It is also because of this that sufficient equations of state exist that efficiently describe this fluid at the relatively high pressures, temperatures and salinities of interest.

There exist various complexities and points of inversion in the fluid property trends in response to changes in p-T-x (Section 2.6.8). In addition to the charts given in Section 2, Table 6.1 demonstrates the extent and contrast in property variation between the two fluid phases, over a realistic range of storage system scenarios. These properties alone can also be used for predicting important underling storage behaviour (Section 2.7.3). Over the range of pressures and temperatures of interest here, the brine phase properties vary in a relatively slight manner, though its viscosity shows particular sensitively to temperature. An increase in salinity has the effect of generally moderate increases in fluid density, viscosity, and bulk modulus, and reductions in the thermal capacity and conductivity. For the CO_2 phase, greater sensitivity is demonstrated overall with respect to changes in pressure and temperature, though the parameter values generally remain within the same orders of magnitude. This sensitivity is a consequence of the CO_2 phase being within scope of its critical region (Section 2.6.8).

Listed next in Table 6.1, the solid phase (porous medium) physical properties are given characterising its mechanical and thermal behaviour (Section 2.6.4). The valuations are typical of sandstone formation rock, the mechanical and thermal parameters are determined after [99] and [141, 129] respectively. Tabulated next are the saturation parameters (Section 2.7), characterising the rock-brine-CO_2 system saturation behaviour of the two (matrix and fracture) sub-domains. The parameterisations for the matrix sub-domain are typical realistic base case values, demonstrating significant saturation-capillary pressure behaviour and wetting residual saturation. Note that in practice the rock parameter values will vary in space and due to variations in pressure and temperature depending on the formation, in this chapter these parameters are initially considered constant and uniform for the purpose of investigation.

Table 6.1: Storage formation HTM parameter sets for extreme brine aquifer scenarios: cool & shallow, cool & deep, warm & shallow, and warm & deep basins. The scenarios present alternate ambient pressures and temperatures, due to lithostatic, hydrostatic and geothermal gradients, used as reference to determine the constant material properties as itemised. The lithostatic and hydrostatic gradients for all cases are 23.5 MPa/km and 10.5 MPa/km respectively with mean atmospheric pressure, and the geothermal gradients for the cold and warm basins are 25°C/km with a surface temperature of 10°C and 45°C/km with a surface temperature of 20°C respectively. The tildes (∼) indicate adjacent values for the rock parameters are carried over.

		Storage system parameters						
Scenario				Cool basin		Warm basin		
				Shlw.	Deep	Shlw.	Deep	
Porous region		Matrix$_1$	Fract.$_2$					
Physical Parameters	Sym.							Units
Reservoir depth	D			1	3	1	3	km
Ref. fluid pressure	p_{ref}			10.5	31.5	10.5	31.5	MPa
Ref. temperature	T_{ref}			35.0	85.0	65.0	155.0	°C
Ref. vertical effective stress	σ'_{v}			13.0	39.0	13.0	39.0	MPa
Brine density	ρ^{w}			1069	1050	1054	1000	kg/m^3
Brine viscosity	μ^{w}			872	441	543	264	µPa s
Brine bulk modulus	K_{w}			2.67	2.65	2.59	2.16	GPa
Brine thermal expansion coef.	β^{w}			0.416	0.585	0.536	0.793	$\times 10^{-3}$/K
Brine specific heat cap.	c_p^{w}			3810	3789	3819	3856	J/(kg K)
Brine thermal conductivity	χ^{w}			0.615	0.677	0.651	0.691	W/(m K)
CO$_2$ density	ρ^{n}			730	740	292	499	kg/m^3
CO$_2$ viscosity	μ^{n}			60.0	63.2	24.2	41.1	µPa s
CO$_2$ bulk modulus	K_{n}			0.0237	0.0764	0.00536	0.0382	GPa
CO$_2$ thermal expansion coef.	β^{n}			16.2	5.49	17.4	5.10	$\times 10^{-3}$/K
CO$_2$ specific heat cap.	c_p^{n}			3622	2018	2801	1750	J/(kg K)
CO$_2$ thermal conductivity	χ^{n}			0.0817	0.0822	0.0399	0.0586	W/(m K)
Intrinsic rock density	ρ^{s}	2670		∼	∼	∼	∼	kg/m^3
Young's modulus	E	14.4		∼	∼	∼	∼	GPa
Poisson's ratio	ν	0.2		∼	∼	∼	∼	-
Biot's parameter	b	1.0		∼	∼	∼	∼	-
Thermal expansion coef.	β^{s}	0.039		∼	∼	∼	∼	$\times 10^{-3}$/K
Specific isobaric heat cap.	c_p^{s}	1000		∼	∼	∼	∼	J/(kg K)
Thermal conductivity	χ^{s}	2.51		∼	∼	∼	∼	W/(m K)
Porosity	n	0.2	0.05	∼	∼	∼	∼	-
Brine residual saturation	S_{rw}	0.3	0.1	∼	∼	∼	∼	-
CO$_2$ residual saturation	S_{rn}	0.0	0.0	∼	∼	∼	∼	-
Intrinsic permeability	$\mathbf{k}$	1.875	varies	∼	∼	∼	∼	$\times 10^{-13}$ m^2
Brine End-point relative perm.	k_{rn}	1.0	1.0	∼	∼	∼	∼	-
CO$_2$ End-point relative perm.	k_{rn}	0.5	0.5	∼	∼	∼	∼	-
Brine relative perm. exponent	m_{k}	1.0	1.0	∼	∼	∼	∼	-
CO$_2$ relative perm. exponent	n_{k}	1.0	1.0	∼	∼	∼	∼	-
van Genuchten parameter	m_{v}	0.5	0.6	∼	∼	∼	∼	-
van Genuchten parameter	p_{v}	10.0	2.0	∼	∼	∼	∼	kPa
Fracture spacing	$\bar{l}$		varies	∼	∼	∼	∼	m
Well height/reservoir thickness	H	50		∼	∼	∼	∼	m
Well radius	r	0.2		∼	∼	∼	∼	m
CO$_2$ mass injection rate	M_{n}	20		∼	∼	∼	∼	kg/s

As discussed in Section 2.7.1, the fracture sub-domain is parametrised with a less significant though non-negligible saturation-capillary pressure behaviour for study. The saturation-relative permeability relationships for each sub-domain are assumed linear at this stage for simplicity. Listed also is the intrinsic permeability which is typical of a sandstone formation, and the fracture spacing $\bar{l}$, which are varied for investigation in the following sections. Finally, typical values for well depth/reservoir height and well radius are given along with a feasible mass rate of injection, which is within limit of valuation deemed practical (3–120 kg/s or ∼0.1–4.0 Mtpa) for commercial CCS purposes [126]. The parameters valued in Table 6.1 are base case valuations for study in the following sections, and will apply where required, unless stated otherwise.

6.2 Numerical parameter base set

Tables 6.2 and 6.3 present the base case control and acceleration parameters that are used throughout this chapter unless stated otherwise.

Table 6.2: Numerical control parameters

Numerical control parameter	Sym.	Value
Residual error tolerances	$\tau_{\mathrm{R}}^{\mathrm{r/a}}$	$10^{-7}/10^{-10}$
Truncation error tolerances	$\tau_{\mathrm{T}}^{\mathrm{r/a}}$	$10^{-3}/10^{-7}$
Integral control exponent	$k_I^{\mathrm{ac/rj}}$	0.5
Proportional control exponent	$k_P^{\mathrm{ac/rj}}$	0.0
Safety factor	s	0.8
Min control factor	$f_{\min}$	0.1
Max control factor	$f_{\max}$	1.2

Table 6.3: Numerical acceleration parameters

Numerical acceleration parameter	Sym.	Value
Acceleration starting iteration	s_{startA}	0
Max number of iterations	$s_{\max}$	10
Max iterations to accelerate	$m_{\max}$	5
Damping parameter	β	1

The relative/absolute tolerances for the residual and truncation errors (Section 5.4.3) are given conservative values which are orders of magnitude lower than would adversely affect the solution at the scales of interest. The integral gain factor exponent is dictated by the order of the temporal integration scheme (5.46), and the proportional gain control exponent behaviour is ignored at this stage for later study. The safety and min/max control factors are allocated conservative values given the general high nonlinear behaviour of the system of equations. This is because large time-step growths, though potentially permissible given the prescribed truncation error tolerance and the expected truncation errors within the system, can cause poor solution convergence. This is due partly to the initially unknown Jacobian or secant information desired for efficient convergence, which is sought through the modified fixed-point iterations themselves.

The acceleration parameters dictate a scenario where the accelerative mixing occurs from the first iteration over a maximum of 5 consecutive iterations, with the maximum total number of iterations set at 10. The damping parameter is fixed at unity, which is an undamped configuration meaning that all residual vectors are passes straight through to the next iteration un-damped (Section 5.4.2).

6.3 Mesh design

As discussed in Chapters 4 and 5 the adaptivity of spatial discretisation is important and demonstrates interrelation with the temporal discretisation. For infiltrating variably saturated flows, coarse spatial discretisation may demonstrate initial oscillations in the spatial solutions and oscillation in the time-step size adaptation, assuming that these oscillations are associated with the saturation front undergoing abrupt transition through the elements. After [102], the Courant number is trialled as a criterion in order to heuristically balance the space-time discretisation,

$$\mathrm{Cr} = \mathrm{v}\frac{\Delta t}{\Delta x}, \tag{6.1}$$

where v is the front velocity, and Δt and Δx are the step sizes to be adapted in time and space respectively. The method trialled initially requires selecting an appropriate temporal truncation error tolerance from which an initial time-step size, Δt_0 after (5.53), is acquired. Then the spacial discretisation is selected via $\mathrm{Cr} \sim 1$. This may either be done heuristically through trial or via knowledge of an estimate of the front velocity and a rate of growth, r, for Δt.

For the latter case, a 1D (quasi-2D) axisymmetric front velocity may be estimated after (3.38) which gives a relationship for the front location as $x = C\sqrt{t}$, where C is dependent on the physical system properties (assumed constant) and x is the position of the front, from which a front velocity $\mathrm{v}(x)$ may be given by differentiating, that is $\mathrm{v} = C^2/2x$. Relating the time-step size as of $\Delta t = \Delta t_0 r^n$, via geometric series the following time at n may be given,

$$t_n = \frac{x^2}{C^2} = \Delta t_0 \sum_{k=0}^{n} r^k = \Delta t_0 \frac{1 - r^{n+1}}{1 - r}, \tag{6.2}$$

which may be isolated for n in terms of the variable x, hence an expression for $\Delta t(x)$ may be given. Letting $\Delta x(x) = \mathrm{v}(x)\Delta t(x)$ from the Courant criterion, on substitution the following analytical function is derived which gives an estimate of the necessary element size Δx as a function of position x, in the space domain for its spatial discretisation (meshing) in anticipation of the front,

$$\Delta x(x) = \left(\frac{C^2}{2x}\right) \Delta t_0 r^{\frac{\ln\left(-\frac{x^2(1-r)}{C^2 \Delta t_0}+1\right)}{\ln r} - 1}. \tag{6.3}$$

The expression requires an estimate for r, which may be acquired from an initial trial run of the system of equations in order to determine an estimate of the growth behaviour of Δt, which is also dependent on the numerical settings within the controller. In practice however, the spatial refinement need only be this strict if the saturation behaviour exhibits a sharp fluid interface/transition, and the refinement criterion formulated should therefore be viewed as some maximum degree of mesh refinement necessary, particularly for the near well region. An appropriate spacial discretisation is illustrated in Figure 6.5, which is based on the guidance and approximate form of (6.3). Note finally that if r is unsteady exhibiting fluctuations during temporal integration, which is generally the case for relatively coarse meshes through which sharp fluid interfaces/high numerical gradient attempt to pass, this is generally indicative that the mesh needs refinement.

6.4 Full saturation to partial saturation flow transition

The GCS problem scenarios considered in this work initially consist of a fully saturated domain of a wetting fluid phase, into which an initially non-existent nonwetting fluid is injected causing the domain to become partially saturated. A physical transition therefore has to be modelled from a single fluid system to a multiple fluid system. Two relevant methods of air/gas-water desaturation occurring over an originally fully saturated domain are analysed in [120] relevant to hydro-mechanical coupled equations.

The first method assumes negligibly small, though finite minimum values for the desaturating nonwetting phase relative permeability and saturation. These values are prescribed and enforced within the system of equations over the domain regions which are undergoing fully saturated stages. By doing so the nonwetting phase continuity equation(s) are continuously maintained throughout computation (see [120, 168] and the references therein).

The second method proposes switching, element-by-element, solutions from single-phase to multi-phase flow at a specified saturation or capillary pressure. However, in practice there are various complications in that oscillations occur in the solutions and in the nonlinear iterations during switching of the governing equations [69, 120]. This method also requires that a minimum nonwetting phase relative permeability be set in order to avoid oscillations in the solution which would otherwise be due to very small diagonal terms in the coefficient matrices causing numerical difficulties (ill-conditioning).

This presents an interesting aspect which requires further research in this context. Given the scope of this work, the first method is adopted for its simplicity at this stage. The minimum value for the relative permeability of the wetting phase is set to a value of 0.0001 [69, 120].

6.5 Stress recovery

The solid strains of the porous medium are post-processed in order to give the effective stress state, considering (2.30), (3.47) and (4.87), from

$$\boldsymbol{\sigma}'' = \mathbf{D}_{\mathrm{el}}(\boldsymbol{\varepsilon} - \boldsymbol{\varepsilon}^{\mathrm{Th}}) = \mathbf{D}_{\mathrm{el}}\boldsymbol{L}\mathbf{N}_u\bar{\mathbf{u}} - \mathbf{D}_{\mathrm{el}}\mathbf{m}(\beta^{\mathrm{s}}/3)\mathbf{N}_T\bar{\mathbf{T}}. \tag{6.4}$$

In accordance with Section 4.4.1, this operation may be performed over the isoparametric finite elements at points within the natural coordinate system of the element. It is performed for the 9 node finite element at the 3×3 Gauss-Legendre quadrature points. These points are used for sampling as they are optimal for determining the stresses (gradients) because they have the property of superconvergence, as is discussed in [207] following the Herrmann theorem for problems of elasticity. The function (displacements) sought is demonstrated to be optimally accurate sampled at the nodes, whereas the gradients of this function (stresses) are optimally sampled at the Gauss points. This superconvergence is however lost on distortion of the (isoparametric) element.

For analysis the computed stress components may then be extrapolated from the inner Gauss points onto the finite element nodes via use of the element shape functions. Due to the degree of continuity between the elements, discrepancies in the stresses computed at nodes shared by adjacent elements will require averaging. This straight forward technique will however reintroduce inaccuracies, particularly for higher order elements [207].

For this reason superconvergent patch recovery (SPR), as described in [207], is employed for the 9 node quadratic displacement finite element. The patch of elements surrounding each node is processed by determining the Gauss point stresses over the patch through which a quadratic polynomial (same order as the displacement element shape function) is fitted via a least squares method, in order to recover stresses of superconvergent accuracy at the node for analysis. For further interesting alternate developments in this context, see [147] and the references therein.

6.6 Visualisation and data management

Model data are output in Visualization Toolkit (VTK) format and rendered with open-source VTK based libraries for quality visualisation and interaction [2, 13, 169]. This proves effective for large domains in space and time with multiple overlaid degrees of freedom, allowing additionally for the parallelisation of large data sets.

6.7 Model verification

The coupled hydro-mechanical, multiphase hydraulic, and fractured hydro-mechanical aspects of the numerical model are first benchmarked with emphasis on parametrisation taken from Table 6.1. The coupled hydro-thermal, hydro-thermo-mechanical and fractured hydro-thermo-mechanical aspects are then benchmarked with reference to a specific subset of parameters which give rise to some interesting coupled thermal effects as are discussed. This incremental benchmarking approach introducing increasing complexity, covering geometrically idealised, though realistic, engineering scenarios is also aimed at providing insight into the physical phenomena as described by the system of governing equations.

Table 6.4 summarises the engineering problems modelled in the subsections which are to follow, through which the numerical model is employed with increasing complexity.

Table 6.4: Summary of the coupled multi-physics problems assessed.

Section	Coupling	Summary
6.7.1	(1H)M	One fluid phase hydro-mechanical consolidation problem highlighting coupled system response to a footing load causing pore fluid pressure/solid stress evolution and deformation.
6.7.2	(2H)	Two fluid phase injection problem highlighting coupled system fluid pressure and saturation evolution.
6.7.3	(2H)M	Two fluid phase hydro-mechanical injection problem highlighting coupled system fluid pressure, saturation and solid deformation/caprock uplift
6.7.4	(4H)M	Double-porosity two fluid phase hydro-mechanical injection problem highlighting coupled system fluid pressure, saturation and solid deformation/caprock uplift with the effects of an additionally coupled fracture network.
6.7.5	(2H)T	Two fluid phase hydro-thermal injection problem highlighting coupled fluid pressure, saturation and site Joule-Thomson cooling effects.
6.7.6	(2/4H)TM	Single and double porosity two fluid phase hydro-thermal-mechanical injection problems highlighting coupled fluid pressure, saturation, solid deformation/caprock uplift, and site Joule-Thomson cooling effects.

6.7.1 One fluid phase Hydro-Mechanical behaviour: (1H)M

The isolated coupled system of equations (sub-matrix rows/columns 1–2 or 1–3) from (4.32), is

$$\begin{bmatrix} \mathbf{K}_1 & \mathbf{Q}_{\mathrm{uf}_1} \\ \mathbf{Q}_{\mathrm{fu}_1} & \mathbf{S}_{\mathrm{f}_1} \end{bmatrix} \frac{\mathrm{d}}{\mathrm{d}t} \begin{Bmatrix} \bar{\mathbf{u}} \\ \bar{\mathbf{p}}^{\mathrm{f}_1} \end{Bmatrix} + \begin{bmatrix} \mathbf{0} & \mathbf{0} \\ \mathbf{0} & \mathbf{H}_{\mathrm{f}_1} \end{bmatrix} \begin{Bmatrix} \bar{\mathbf{u}} \\ \bar{\mathbf{p}}^{\mathrm{f}_1} \end{Bmatrix} = \begin{Bmatrix} \frac{\mathrm{d}}{\mathrm{d}t}\mathbf{f}_{\mathrm{u}} \\ \mathbf{f}_{\mathrm{f}_1} \end{Bmatrix}, \tag{6.5}$$

where the saturation coefficients S_{w} and k_{rw} are set at 1, as a single saturating fluid f_1 within the first (porous matrix) sub-domain is considered.

This reduced system is solved for a typical consolidation/settlement problem for a circular flexible footing on a mechanically and hydraulically homogeneous isotropic porous medium assumed linear elastic. The initial conditions are $p^{\mathrm{f}_1} = p^{\mathrm{f}_1}_{\mathrm{ref}}$ and $\mathbf{u} = \mathbf{0}$. The boundary conditions are illustrated in Figure 6.1. The base to the modelled domain is assumed rigid, rough and impermeable, the radial extent rigid, smooth and impermeable, and the top surface free to deform under the loading and permeable.

An analytical solution to benchmark this problem is employed following [31] for an incompressible fluid, as similarly carried out by [120, 177]. This involves Biot's 3D consolidation formulation [26] in terms of displacements and excess pore fluid pressures, which is solved via the application of Fourier transforms in space and a Laplace transform in time.

In order to compare this solution with the solution of (6.5), the elastic mechanical behaviour described so far (in terms of Young's modulus E, Poisson's ratio ν, and Biot's parameter b) is translated to the coefficient of volume compressibility,

$$m_v = \frac{(1+\nu)(1-2\nu)}{(1-\nu)E}, \tag{6.6}$$

which is the inverse of the constrained or 1D elastic modulus. From this expression, the coefficient of consolidation [152] may be given, in terms of the porous solid intrinsic permeability and the fluid dynamic viscosity, as

$$c_v = \frac{\mathrm{k}_1}{m_v \mu^{\mathrm{f}}}. \tag{6.7}$$

The coefficient of consolidation describes a rate at which a fully saturated porous medium undergoes consolidation, and is thus a direct function of the mechanical and hydraulic properties of the porous medium. A slower settlement is the product of a system where the pore fluid pressures, built-up during loading, dissipate slower due to restriction by greater resistance to fluid flow as the load is transferred to the porous solid.

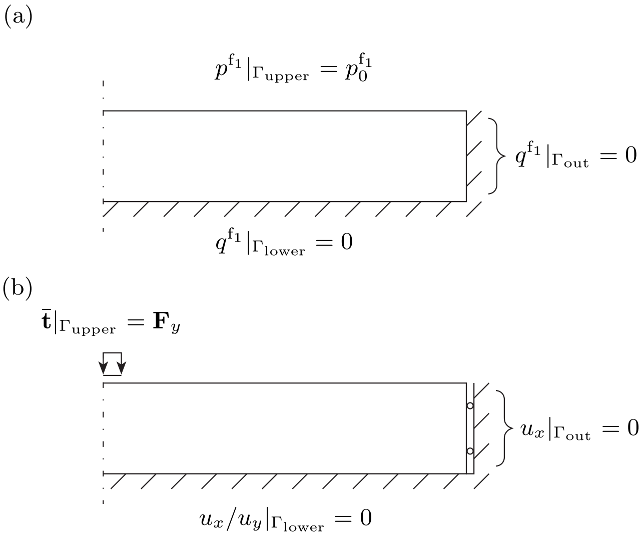

Figure 6.1: Model boundary condition for a hydro-mechanical consolidation problem of (a) fluid pressure and flux (mass balance) and (b) displacement and traction (momentum balance) boundary conditions.

The predicted normalised settlement $(s_t - s_i)/(s_f - s_i)$, where subscripts i and f denote initial and final, may be plotted against the dimensionless time factor $c_v t/H^2$, where H is the height of the consolidating porous body/layer. A point undergoing settlement on the axisymmetric centreline directly under the footing is sampled for s.

A footing radial extent to layer depth of 0.2 is trialled, this is computed as a 1 m radial load on a 5 m deep layer, the radial extent of the layer is computed at 20 m. Due to the nondimensionalisation of settlement and time, only Poisson's ratio and a loading (as a fraction of the Young's modulus) need be specified further. A Poisson's ratio of 0.25 and a surface footing load of $-100/E$ are therefore trialled.

An initial instantaneous (undrained) system response to the loading is given on multiplying through (6.5) by dt as d$t \to 0$, and then integrating assuming elastic behaviour,

$$\begin{bmatrix} \mathbf{K}_1 & \mathbf{Q}_{\mathrm{uf}_1} \\ \mathbf{Q}_{\mathrm{fu}_1} & \mathbf{S}_{\mathrm{f}_1} \end{bmatrix} \begin{Bmatrix} \bar{\mathbf{u}} \\ \bar{\mathbf{p}}^{\mathrm{f}_1} \end{Bmatrix} = \begin{Bmatrix} \mathbf{f}_{\mathrm{u}} \\ \mathbf{0} \end{Bmatrix}, \tag{6.8}$$

which for an incompressible grain and fluid, $\mathbf{S}_{\mathrm{f}_1} = \mathbf{0}$, and is subsequently a form originally derived for nearly-incompressible/incompressible elastic behaviour, see [120] and the references therein. The final steady-state (drained) response gives for the second and first equations of

(6.5), respectively,

$$\mathbf{H}_{\mathrm{f}_1}\bar{\mathbf{p}}^{\mathrm{f}_1} = \mathbf{f}_{\mathrm{f}_1} \quad \text{and} \quad \mathbf{K}_1\bar{\mathbf{u}} = \mathbf{f}_{\mathrm{u}} - \mathbf{Q}_{\mathrm{uf}_1}\bar{\mathbf{p}}^{\mathrm{f}_1}, \tag{6.9}$$

assuming that the coefficient matrices are independent of any system responses.

In between the limit states, consolidation occurs due to compression of the void spaces as load is transferred from the pore fluid to the solid skeleton. This occurs as the instantaneous fluid pressure on loading dissipates, coupled with the fluid flow from the pore space due to the induced dissipating pore pressure gradient. This process is plotted over time for the sampled s in Figure 6.2 for the system described. Agreement is demonstrated between the distinct solution methods; one employing transforms (solid black line) and the other employing the finite element method in space and finite differencing in time (dotted marks as discretised in time). In [120], a similar comparison is made with a coarse mesh, where at the early (faster rate) stages of settlement, oscillations in the solution occur, which slightly overestimate the settlement while gradually correcting.

The mesh is refined in the present investigation using the Blossom-quadrilateral elements (Section 4.6), with an element size of 0.05 m below the footing to a size of 1.0 m at the far boundary. The numerical control parameters of Table 6.5 are specified in order to examine the effect of the solution control algorithm (Section 5.8) on the time-stepping. Note that this problem requires no nonlinear convergence due to the coefficient matrices remaining constant as only one fluid phase is considered.

Table 6.5: Consolidation problem numerical control parameters

Numerical control parameter	Sym.	Value
Truncation error tolerance	$\tau_{\mathrm{T}}^{\mathrm{r}}$	10^{-2}
Integral control exponent	$k_I^{\mathrm{ac/rj}}$	0.5
Safety factor	s	0.9
Max control factor	$f_{\max}$	10

For this problem the controller is allocated to adapt the time-stepping only for truncation errors occurring at the degree of freedom corresponding to the vertical displacement (settlement) of the sample point centrally located under the footing. Referring to Figure 6.2, beginning with an initial time-step size estimate from (5.53), the step size changes are controlled by the maximum permitted control factor of $f_{\max} = 10$. This is because the initial system computes well below the truncation error tolerance of $\tau_{\mathrm{T}}^{\mathrm{r}} = 10^{-2}$ (blue dot marks). However, when the time-steps begin to step over greater changes in settlement with respect to time, the truncation errors rise and subsequent decreases in the control factor occur to a minimum of $f \approx 1.3$ along the region at highest gradient before relaxing again at the end of the consolidation process. Note that further reduction in the truncation error tolerance brings about even further refinement in this manner.

For comparison the controller is allocated to time-step at a fixed control factor rate of $f = 10$ (red cross marks), which is thus unresponsive to any change in the local truncation error. It is observed that the settlement prediction becomes increasingly underestimated with respect to time.

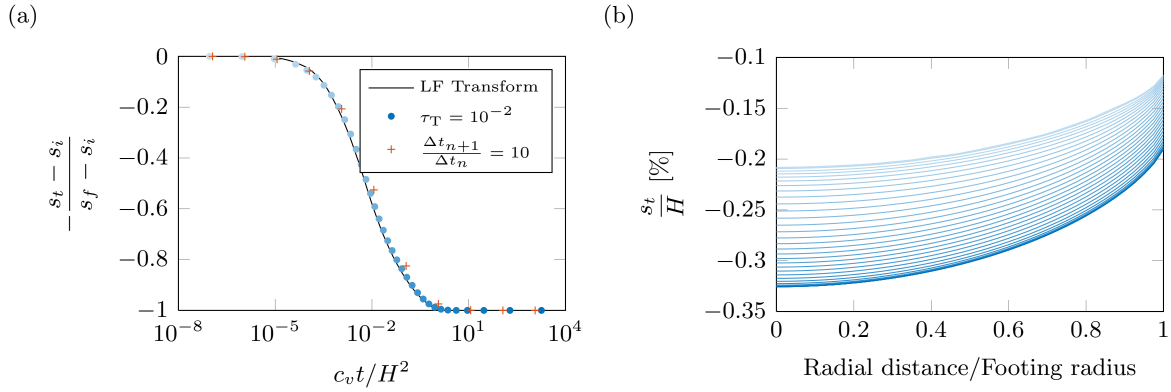

Figure 6.2: (a) Fourier/Laplace transform (solid line) and finite element/finite difference (dot marks) consolidation problem solutions. (b) Settlement/deformed profile predictions under the footing load corresponding to the $\tau_T = 10^{-2}$ controlled solution points.

In Figure 6.3, the final static steady-state of the porous layer is illustrated as a quarter symmetric rendering of the computed axisymmetric results. Depicted is the final deformed shape below the footing, magnified by a factor of 25, with the vertical effective stresses within the porous solid structure. This highlights the expected Boussinesq stress contours [152], which along with the deformed profile (Figure 6.2(b)) can be verified with known elastic solutions, for instance [120, 152]. For this case the initial displacement computed was −0.010 m settling to −0.016 m.

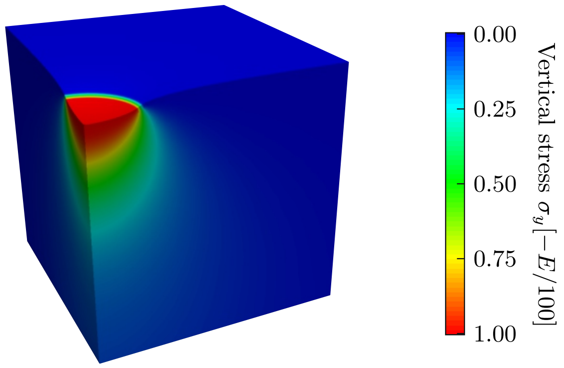

Figure 6.3: Quarter symmetric section, rendered from the computed axisymmetric domain, illustrating the final deformed shape (magnified by a factor of 25) and the vertical effective stress profile after consolidation directly below the circular footing.

6.7.2 Two fluid phase Hydraulic behaviour: (2H)

From the main discretised system of governing equations (4.32), the coupled mass balance components for the fluids in both the sub-domains (sub-matrix rows/columns 2–3 and 4–5) may be isolated with no/zeroed leakage terms,

$$\begin{bmatrix} \mathbf{S}_{\mathrm{w_i}} & \mathbf{Q}_{\mathrm{wn_i}} \\ \mathbf{Q}_{\mathrm{nw_i}} & \mathbf{S}_{\mathrm{n_i}} \end{bmatrix} \frac{\mathrm{d}}{\mathrm{d}t} \begin{Bmatrix} \bar{\mathbf{p}}^{\mathrm{w_i}} \\ \bar{\mathbf{p}}^{\mathrm{n_i}} \end{Bmatrix} + \begin{bmatrix} \mathbf{H}_{\mathrm{w_i}} & \mathbf{0} \\ \mathbf{0} & \mathbf{H}_{\mathrm{n_i}} \end{bmatrix} \begin{Bmatrix} \bar{\mathbf{p}}^{\mathrm{w_i}} \\ \bar{\mathbf{p}}^{\mathrm{n_i}} \end{Bmatrix} = \begin{Bmatrix} \mathbf{f}_{\mathrm{w_i}} \\ \mathbf{f}_{\mathrm{n_i}} \end{Bmatrix}, \tag{6.10}$$

which describes the main hydraulic compressible two-phase fluid flow and displacing behaviour of the sub-domains ($\mathrm{i} = 1, 2.$) within the system of equations.

It is sought to verify these system components with the axisymmetric 1D/quasi-2D analytical solution (3.37) which describes the fluid interface positioning (saturation profile) and on extension the corresponding vertically averaged fluid pressure [124] via exponential integral function. To do so the initial and boundary conditions illustrated in Figure 6.4 are prescribed after the conditions (3.34–3.36). An appropriate FE mesh is also illustrated in Figure 6.5. The numerical domain is 2D axisymmetric, so lower and upper impermeable (no flux) boundary conditions are also prescribed, which are to be viewed as the necessary sealing layers to the storage system. The mass rate of injection is related to the wellbore surface fluid flux q^{n}, and the imposed mass flux q^{n} via,

$$q^{\mathrm{n}} = \mathrm{q}^{\mathrm{n}}\rho^{\mathrm{n}} = \frac{M_{\mathrm{n}}}{2\pi r H}, \tag{6.11}$$

which is the mass rate of injection divided by the inner injection wellbore surface area along the formation height. Additionally, the domain has to behave as if the far-field boundary is at an infinite extent. This is achieved by extending the domain radially such that the pressure waves/disturbances computed for each scenario do not reach the far-field boundary during simulation. For a continuous flux/injection scenario on the inner boundary with an outer boundary at infinite extent the pressures will continuously rise and a steady-state will not be met. For a system with a far-field boundary a steady-state will begin to ensue once the pressure wave meets the far field boundary. This means that the analytical and numerical solutions will become incomparable at this point. Note that for an open (constant pressure) outer boundary (for instance a far-field abandoned well or production well), once met by the pressure wave, monotonically rising pressures diverging from the well would in turn fall/stabilise. Conversely, for a confined (no flux) outer boundary (for instance a low permeability geological structure), once met by the pressure wave, the well pressures will in turn begin to rise asymptotically. The initial pressure conditions are given in Table 6.1, which are also used as reference pressures in order to parametrise the fluid properties of the model.

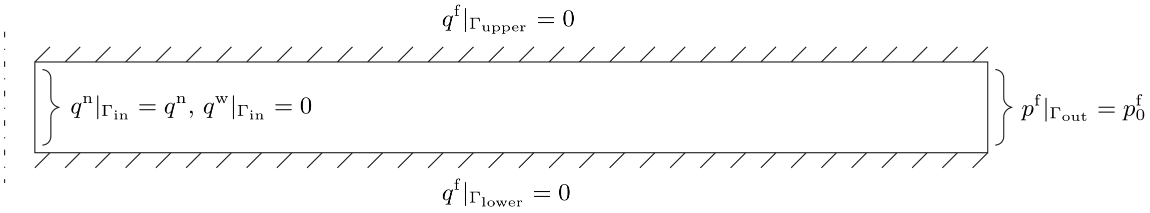

Figure 6.4: Model boundary condition schematic for multiphase hydraulic behaviour of fluid pressure and flux (mass balance) boundary conditions. Superscript f denotes both fluid phases ($\mathrm{f} = \mathrm{w}, \mathrm{n}.$).

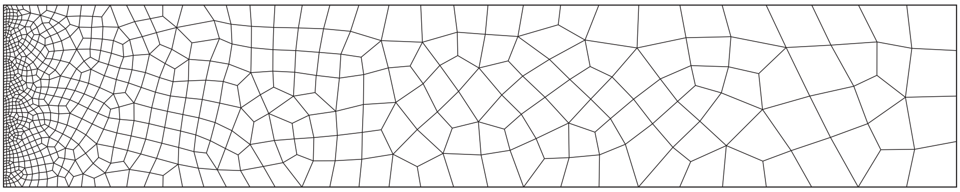

Figure 6.5: Example finite element mesh of the inner 262.5 m by 50 m portion of the domain. The radial extent shown is arbitrary and in practice continues to a greater extent depending on the requirements of the model.

To enact the analytical solution (3.37) its key simplifying assumptions are outlined and carried out within the numerical model by reducing it as follows.

- Immiscible (non-reactive) fluid displacement: this assumption is already inherent in the current numerical formulation where the extra degrees of freedom necessary in order to capture the miscible mass fractions evaporated/dissolved within the fluid phases have been omitted for future study (Section 2.6.8).
- Constant thermodynamic fluid properties: the fluid properties which are a function of the primary state variables are fixed at values which correspond to the (initial) reference pressure and temperature, and are thus not updated within the coefficient matrices during computation.
- Gravity associated effects are neglected: the gravitational terms appearing in Darcy's equation as derived from momentum balance are omitted. Essentially, vertical flow is assumed negligible and is neglected for tractability. Thus the system is considered to be in vertical equilibrium whereby vertically-integrated governing equations may be employed (as was carried out for the analytical formulation), which is appropriate when the system horizontal length scale is much greater than the vertical. This is demonstrated to be a reasonable assumption, in the context of GCS, for horizontally injected fluid flows (from a vertical injection well) in [124, 127]. See also [139, 138] for in-depth details on capturing the effects of gravity override (buoyancy) and mobility contrast Section 2.7.3 with respect to employing vertically-integrated governing equations.
- Negligible capillary pressure effects: negligible capillary pressure-saturation behaviour is modelled by assuming, $p_{\mathrm{v}} \to 0$ and $\mathrm{m}_{\mathrm{v}} \to 1$, for the van Genuchten parametrisation (Section 2.7.1), and the relative permeability exponents are set linear, $m_{\mathrm{k}} = 1$ and $n_{\mathrm{k}} = 1$ (Section 2.7.2 and [124, 140]).

The behaviour of this system as reduced from the full set of equations (4.32), is additionally isothermal, non-deformable, and non-inertial. The contrast in compressibilities of the fluids is however retained, where for the analytical solution it is assumed that there is a negligible difference in fluid compressibility relative to the compressibility of the system as a whole (see Section 3.2.6 and Section 6.1 with Table 6.1 in order to quantify these compressibilities). The latter two itemised simplifying assumptions are acceptable given that the viscous forces are generally more significant than the gravity and capillary forces, in terms of driving the fluid motion.

Reducing the effects of the capillary pressure causes the fluid interface to become less physically dispersed and the finite element mesh for the numerical model is refined with Section 6.3 as guidance. Both models are parametrised accordingly for the four extreme scenarios given in Table 6.1 with the required parameters (omitting those which have cancelled along with the physics which has been uncoupled) and given the reductions as itemised above. The solution of these models for the fluid saturation profile and the corresponding pressure evolutions are compared in Figures 6.6 and 6.7 for the same constant 20 kg/s mass rate of injection for a study time period of just over a year (400 days). Solutions are shown at intervals of $(4n)^2$ days where $n = 1 \to 5$, this is because the radial extent of the $\mathrm{CO_2}$ has the relationship with time of $x_{\mathrm{nmax}} \propto \sqrt{t}$, see (3.38). That is, 16, 64, 144, 256, and 400 days. Note that the controller (Section 5.8) is augmented in order to compute solutions precisely at these specified time intervals during temporal integration, while it is within tolerance to do so.

The analytical solution considers 1D vertically integrated mass/volume conservation, and thus arrives at a solution for a sharp fluid interface height and a single averaged fluid pressure which is in vertical equilibrium. The interface height is essentially a radial fluid saturation profile as integrated over the storage height H, which represents an effective depth of brine underneath, and an effective depth of $\mathrm{CO_2}$ and immobile brine above. This configuration is assumed and enforced due to the effect of strong gravity override given that the $\mathrm{CO_2}$ is less dense and viscous than the resident brine. However, the 2D axisymmetric formulation is not vertically integrated and thus the fluid interface is smeared along the domain to an extent depending on the system properties, and there also co-exists multiple phase pressures. For comparison, the 2D axisymmetric numerical solutions are post-processed accordingly, whereby the 2D saturation profile is vertically integrated and the multiphase fluid pressures are averaged. The interface height/saturation profile, h, for the numerical model (as plotted along the radial distances in the following figures) is therefore given by vertically integrating the $\mathrm{CO_2}$ saturation by numerically solving $\int_0^H S_{\mathrm{n}}\,\mathrm{d}y = (H - h)(1 - S_{\mathrm{rw}})$. Once solved for h (the unknown in the numerical model solution) a comparison can be made between the numerical and analytical versions at each time interval. The averaged fluid pressures are given by taking $p_{\mathrm{ave}} = S_{\mathrm{w}} p^{\mathrm{w}} + S_{\mathrm{n}} p^{\mathrm{n}}$ along the radial centreline of the domain for each time interval. Note that the pressures plotted in the figures are excess pressures over the initial formation conditions (Table 6.1).

In Figure 6.6, the shallow depth cool and warm formation scenario results are displayed. Due to the higher temperature present in the warm reservoir and the corresponding thermodynamics properties of the fluids, the $\mathrm{CO_2}$ viscosity has reduced more significantly in comparison to that of the brine (Table 6.1). This has brought about a larger contrast in mobility between the phases (Section 2.7.3), which has caused the larger spreading and radial extent of the $\mathrm{CO_2}$ plume interfaces compared to those in the cool formation. These conditions are taken into account in both the numerical and analytical models by simply changing the system parameters (Table 6.1). Relatively high mobility ratio fluid displacements are generally unfavourable as they make inefficient and more unpredictable use of the pore storage space, due particularly to the increased potential onset of unstable viscous fingering (Section 2.7.3). For the same mass injected, higher well pressures also develop in the shallow warm reservoir due to the significantly lower $\mathrm{CO_2}$ density which means that a larger volume has to be injected and subsequently a larger volume of brine displaced. Such an increase in fluid flux is therefore accompanied by an increase in pressure gradient. At this lower density, the $\mathrm{CO_2}$ compressibility is also significantly higher than in the other scenarios and becomes non-negligible. This causes the appreciable discrepancy between the analytical and numerical pressure profiles (Figure 6.6(b)), where the numerical solution, which accounts directly for the fluid compressibilities, is predicting a lower pressure profile, as would be expected relative to the analytical solution which assumes a negligible difference in compressibility between the fluid phases.

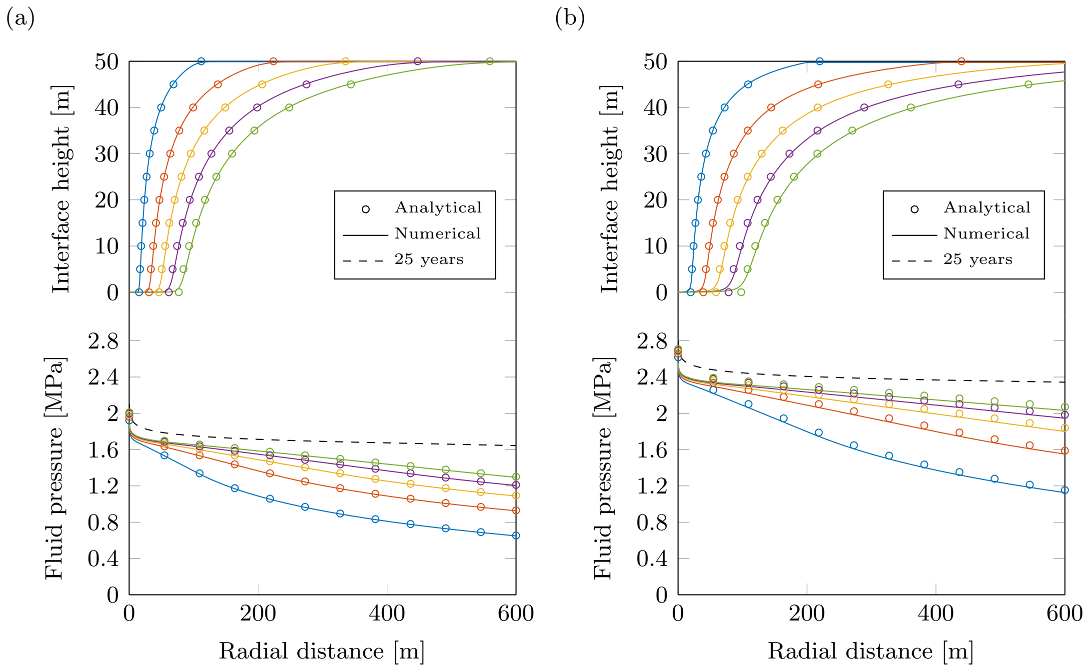

Figure 6.6: Shallow depth (a) cool and (b) warm formation corresponding saturation and pressure distributions. The time steps are plotted at intervals of $(4n)^2$ days where $n = 1$ (blue) → 5 (green), that is 16, 64, 144, 256, and 400 days.

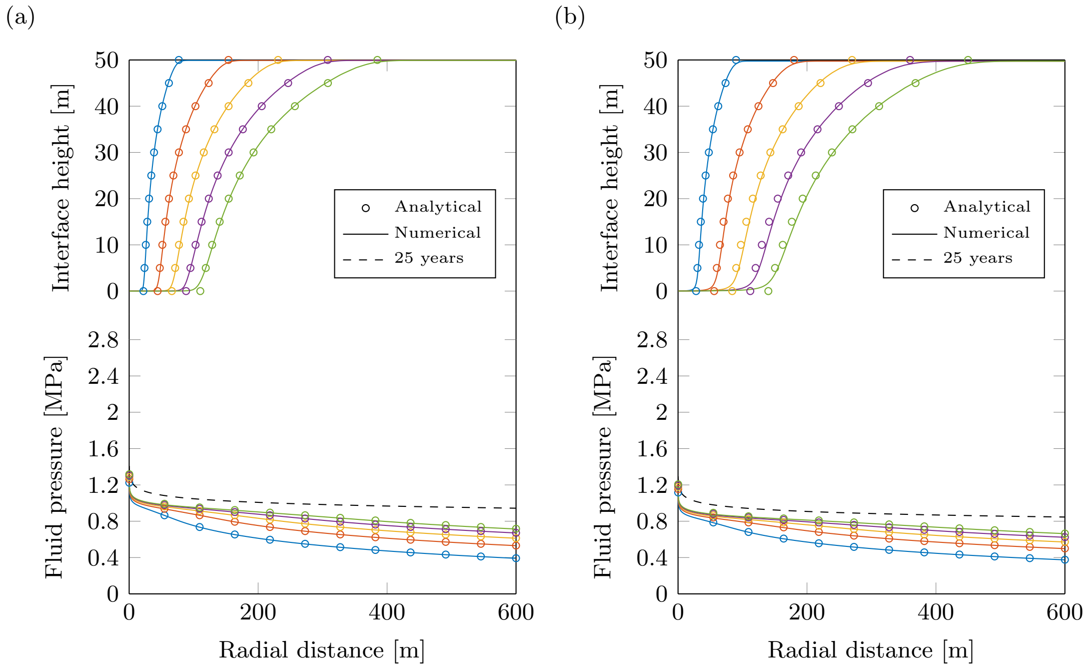

Figure 6.7: Deep depth (a) cool and (b) warm formation corresponding saturation and pressure distributions. The time steps are plotted at intervals of $(4n)^2$ days where $n = 1$ (blue) → 5 (green), that is 16, 64, 144, 256, and 400 days.

In Figure 6.7, the deep depth cool and warm reservoir scenario results are presented. Given the thermodynamic behaviour of the fluid phases, the increases with depth in both temperature and pressures have reduced the contrast in the fluid mobilities. This has reduced the spreading of the fluid interfaces. In particular, the brine viscosity has reduced significantly in relation to the other thermodynamic parameters (Table 6.1), which has meant that there is less resistance to its flow and hence less excess well pressures are computed in order to facilitate the same mass rate of injection compared with the shallow reservoir scenarios.

In each of Figures 6.6 and 6.7, the excess pressure evolution plots also include a profile at 25 years of injection for comparison (dashed lines), which has a near steady state distribution that may be viewed as a potential state towards the end of a long-term injection phase. The final steady state of the reservoir system may be viewed as a single moving CO_2 phase with a fluid flux, $q^{\mathrm{n}}(x) = M_{\mathrm{n}}/2\pi x H \rho^{\mathrm{n}}$, as a function of the radial distance, x. As this fluid flux is due to the pressure gradient, on substituting Darcy's equation (2.33) ignoring the gravitational/inertial terms, then integrating w.r.t. x gives a steady-state system pressure profile of

$$p(x) - p_r = \frac{M_{\mathrm{n}}\mu^{\mathrm{n}}}{2\pi H \rho^{\mathrm{n}} k_{\mathrm{rn}} k} \ln\left(\frac{r}{x}\right), \tag{6.12}$$

where p_r is the undefined pressure at the well face located at the radial distance r. This is known as the Thiem formula [125, 196], which indicates that pressure draw-down is prominent at the near-well region. The extent of pressure build-up is therefore primarily proportional to the volume rate of injection per unit height of the injection well and inversely proportional to the conductivity of the system. Note that the system behaviours demonstrated so far are in response to the porous solid and engineering parameters having typical mid-range values. Thus, the pressures would become substantial, relative to the overburden, for systems with particularly low conductivities with relatively high mass rates of injection. Note also that the well pressures (inner nodal pressure values) must continually rise in order to maintain a constant flux across the boundary.

In all, the analytical and numerical solutions demonstrate good agreement, where the saturation profiles indicate importantly the conservation of CO_2 mass within the numerical system. The analytical approach is also benchmarked favourably against industry standard commercial software [126, 139]. This conveys the appropriateness in applying the coupled consolidation theory (Chapter 3) and the numerical methods (Chapters 4–5) as has been extended from the work centrally of [120], for further fully coupled analysis in the context of GCS modelling. Reinstating the gravitational terms and accurate capillary pressure-saturation behaviour, the solution of (6.10) is benchmarked favourably with the open-source numerical reservoir simulation prototyping framework [112], which is based largely on traditional incompressible continuity and Darcy fluid flow processes on unstructured grids.

6.7.3 Two phase Hydro-Mechanical behaviour: (2H)M

From the main discretised system of governing equations (4.32), the coupled momentum and mass balance components for the solid and the two fluid phases in the primary sub-domain (sub-matrix rows/columns 1–3) may be isolated with no/zeroed leakage terms.

The same reduced GCS model scenarios as introduced in Section 6.7.2 are used for comparison, now with the inclusion of the coupled mechanical behaviour of the porous solid. Initial and boundary conditions for the momentum balance equation are therefore further specified. In order to model a locked-in geological body, an initial field stress state is determined given the depth, and lithostatic and hydrostatic gradients of the reservoir scenarios. Accordingly, a vertical effective stress σ'_{v} is given in Table 6.1, the horizontal stress is given as a ratio of the vertical stress, assumed for simplicity to be related to the Poisson effect,

$$\sigma'_{\mathrm{h}} = \frac{\nu}{(1-\nu)}\sigma'_{\mathrm{v}}. \tag{6.13}$$

The increase in the stress components due to the body forces over the depth of the domain are also accounted for if the gravitational effects are incorporated. In practice, σ'_{v} and σ'_{h} may be complex due particularly to the effect of far-field tectonic stresses, and are typically determined by measurement on site, statistically, and/or via integrating estimates of the unit weights of the overlying strata [92, 99]. The vertical compression of the formation wants to cause an associated horizontal dilation (Poisson effect). Assuming that the formation is confined horizontally from movement/dilation, a resultant compressive horizontal stress will ensue instead of horizontal dilation. This practically expresses the situation of Equation (6.13). Note that a Poisson ratio of 0.2 gives a horizontal-vertical stress relationship of $\sigma'_{\mathrm{h}} = 0.25\sigma'_{\mathrm{v}}$. In basic, this means that the highest (principal) compressive stresses is orientated vertically, and if the pore space is pressurised to fracture the formation rock, the fracture-plane would be orientated vertically, perpendicular to the horizontal least principal stress. Conversely, if the factor relating horizontal-vertical stresses is greater than 1 (due to high compressive tectonic stresses), the fracture-plane would be orientated horizontally, perpendicular to the vertical least principal stress. This is noteworthy in the context of GCS, given that vertical fractures may pose a greater risk as they may promote unwanted vertical fluid migration.

The boundary conditions are illustrated in Figure 6.8. The momentum balance equation is time differentiated and it is assumed that there is no change over time in the traction forces on the modelled storage unit due to overburden/confining stresses. There is however an induced initial stress/deformation state, due to this overburden, which is determined from separate simulation. Note therefore that the overburden/sealing unit is not modelled explicitly as part of the spatial domain with parameterised physical properties loading the system by self-weight, but simply as having induced an initial stress state within the storage unit. System loading is due to the mass flux of CO_2 at the inner boundary as indicated for the nonwetting mass balance equation, which is expected to reduce the in situ effective stress state causing expansion and uplift within the pre-compressed solid porous layer. The conditions $u_x|\Gamma_{\mathrm{in}} = 0$ and $u_y|\Gamma_{\mathrm{lower}} = 0$ are idealised assumptions for this benchmark case (particularly, the wellbore which is restrained radially while able to elongate axially). With respect to the wellbore, more accurate boundary conditions capturing the coupled induced well interface fluid pressures and tractions, which may lead to its expansion ($u_x|\Gamma_{\mathrm{in}} \neq 0$) and material failure is a point for further study, especially if fracturing is of concern [15, 91, 107]

The additionally required mechanical parameter values are given in Table 6.1. The analytical solution for the averaged fluid pressures accounts for a porous solid (formation rock) compressibility, $c_{n\mathrm{p}}$, in the simple form introduced in (3.27). In (3.27), $c_{n\mathrm{p}}$ was also equated to the numerical model parameters which further characterise the mechanical behaviour of the formation rock, namely E, ν, b, and n. Given the valuations for these parameters in Table 6.1, a corresponding value for $c_{n\mathrm{p}}$ is given at 5.0×10^{-10} Pa^{-1}. This is used to initially parametrise the analytical model. The numerical and analytical pressure solutions are compared for verification. The initial results are given in Figures 6.9 and 6.10 for the numerical model (solid lines) with corresponding results from the analytical model (solid circular markers) for the four extreme base case scenarios.

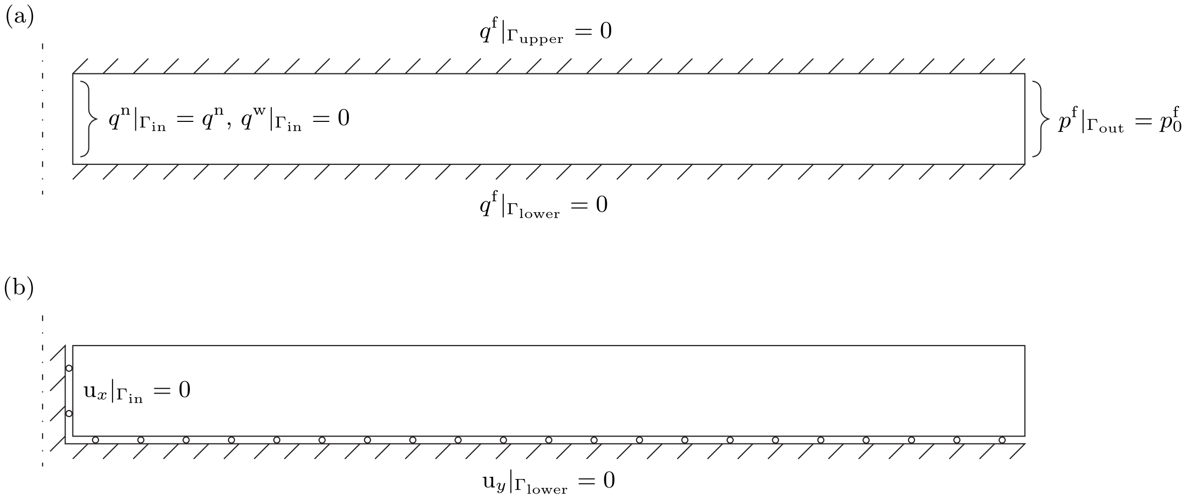

Figure 6.8: Model boundary condition schematic for hydro-mechanical behaviour of (a) fluid pressure and flux (mass balance) boundary conditions and (b) solid displacement (momentum balance) boundary conditions. Superscript f denotes both fluid phases ($\mathrm{f} = \mathrm{w}, \mathrm{n}.$).

To illustrate the validity of the coupled model components, the realistic base case elasticity of the formation, E (Table 6.1), is doubled, which subsequently halves $c_{n\mathrm{p}}$. The numerical and analytical results which indicate the effect on the system response for comparison, are plotted in Figures 6.9 and 6.10 (dashed lines and circular markers). The non-deformable cases as presented previously in Section 6.7.2 are also replotted for comparison (dotted lines and circular markers), which are also reproduced in the deformable model by taking $E \to \infty$.

The numerical model is additionally able to compute the corresponding displacements/stress states over the reservoir domain. The deformed profile of the corresponding upper sealing (caprock) boundary is also given in Figures 6.9 and 6.10. The change in the deformation profile over a 400 day period with time-steps of $(4\mathrm{n})^2$ days, where $\mathrm{n} = 1 \to 5$, are presented for the three $E/c_{n\mathrm{p}}$ cases.

By coupling the solid host rock deformation and on reducing the Young's modulus, the averaged excess fluid pressures are seen to reduce. This is because the porous medium is able to displace/expand and thereby accommodate the prescribed fluid flux at lower excess fluid pressures. In Figures 6.9 and 6.10 the impermeable boundary layer, which represents a flexible sealing caprock layer, is therefore seen to uplift. The trajectory of material points at 100 m intervals are shown by the grey lines and intersecting dots, which displace outward radially and upward axially/vertically. This displaced profile is magnified to scale by 5×10^4 for detailed illustration. Initially the radial expansion occurs at a greater rate relative to the vertical, an effect which decreases as the pressure wave extends causing the points to gradually increase their rate of

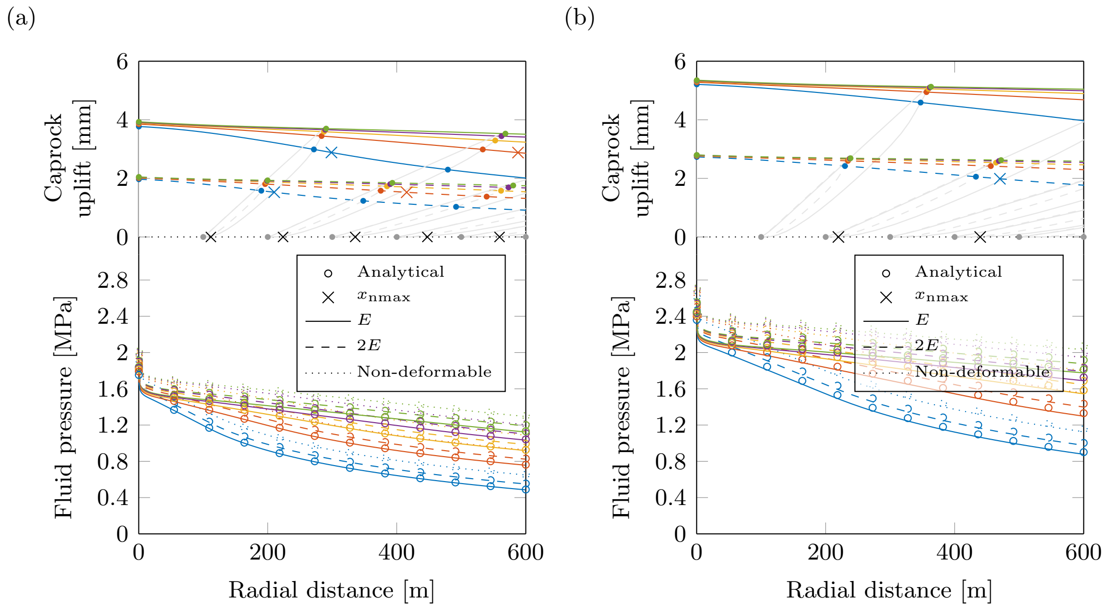

Figure 6.9: Shallow depth (a) cool and (b) warm formation corresponding average fluid pressure distributions and caprock uplifts for rock elasticity cases E (solid lines), $2E$ (dashed lines), and non-deformable (dotted lines). The time steps are plotted at intervals of $(4n)^2$ days, where $n = 1$ (blue) → 5 (green). The grey lines indicate the trajectory of the caprock surface material points at 100 m intervals, magnified to scale by 5×10^4, with the intersection dots marking the trajectory at the time intervals and the crosses marking the corresponding magnified extent of the fluid interface along/under the deformed caprock.

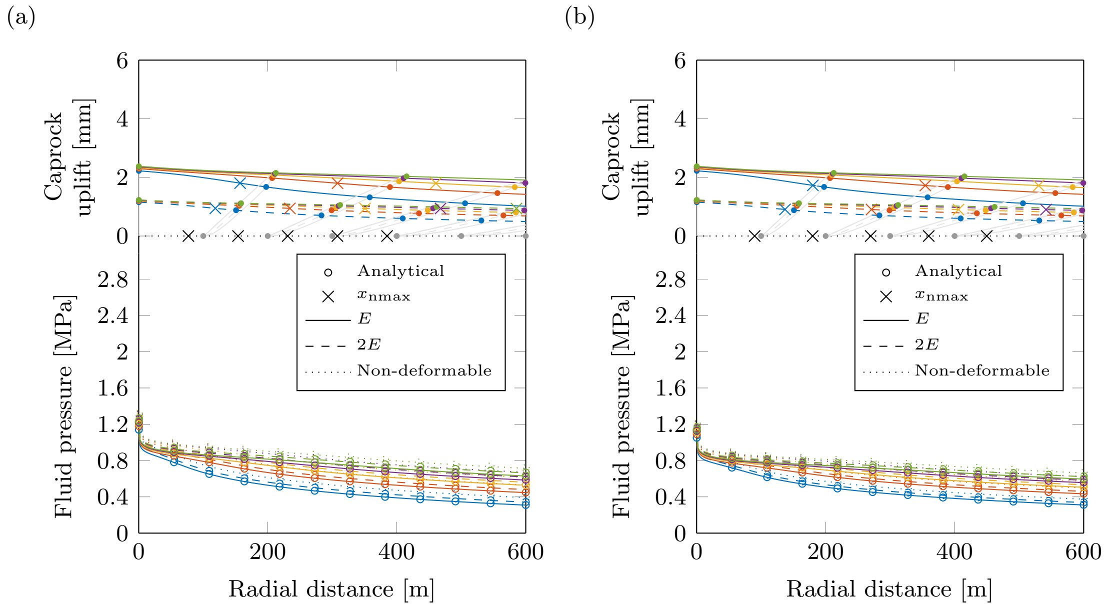

Figure 6.10: Deep depth (a) cool and (b) warm formation corresponding average fluid pressure distributions and caprock uplifts for rock elasticity cases E (solid lines), $2E$ (dashed lines), and non-deformable (dotted lines). The time steps are plotted at intervals of $(4n)^2$ days, where $n = 1$ (blue) → 5 (green). The grey lines indicate the trajectory of the caprock surface material points at 100 m intervals, magnified to scale by 5×10^4, with the intersection dots marking the trajectory at the time intervals and the crosses marking the corresponding magnified extent of the fluid interface along/under the deformed caprock.

vertical displacement. As the radial extent of the fluid interface (denoted by cross marks on the corresponding profile) passes a given material point, the point undergoes a final and more sudden shift to dominance in vertical displacement. At 400 days, injection is ceased and the displaced material points eventually return to their initial state, these returning trajectories are demonstrated to occur linearly as the induced excess pore pressures dissipate over time.

The uplift of the caprock and overburden is a key engineering aspect for monitoring and assessing a GCS reservoir, where research on measuring uplift via GPS, tilt-meters and satellite (InSAR, Table 2.8) is ongoing [29, 163]. Coupled models are therefore important in order to interpret the measured data (via inverse techniques [195]) in order to infer the flow and positioning of the CO_2 body, and the performance, particularly the stress state, of the storage system. Current field measurements on CO_2 storage projects indicate surface uplifts in the order of a few mm/year which are in line with the results determined here independently.

It is important to understand and anticipate the build-up of pressures within the well and storage formation, as it may be required that the hydraulic fracture pressures be avoided within the reservoir and particularly in the sealing caprock. Typical fracture gradients, increasing with depth, present fracture pressures in the region of that necessary in order to take the rock or a fracture surface out of compression (where the fluid pressure overcomes the minimum compressive effective principal stress, the direction of which controlling the orientation of the fracture). For instance, the Hubbert-Willis model [91] assumes the simple relationship for fracture pressure at a point as, $p_{\text{frac}} = \sigma_{\text{min}} + p = p + \Delta p$ (assuming both solid and fluid positive in compression), where σ_{min} and p are the minimum effective stress and initial formation pore pressure respectively.

Although the average excess fluid pressures change appreciably with changes in the compressibility/deformability of the rock, the pressure gradient profiles of which, responsible for the fluid movement, remain relatively uniform. As a result there is only a slight change in the fluid saturation/interface profile. This was explored with the finite difference solution trialled during the development of the system of equations in Section 3.2.6. It was observed that the fluid interface/front slowed slightly on increasing the compressibility significantly, due to the related increase in storage capacity. However, this is for the simple 1D case with no capillary or gravity effects, incorporating further the relation of stress state on the saturation properties of the system is a point for further study.

Localised changes in effective stress undergone by the porous medium go from the initial *in situ* state along a stress path presenting a general reduction in the deviatoric and mean effective stresses. This is typical for an injection scenario, the opposite of which being typical for an extraction scenario. If uncontrolled, rock material failure envelops could be approached, the implications of which is potential seismicity and leakage. Regardless of failure however, the coupled mechanical deformation still affects fluid pressures, fluid flow and the extent of CO_2 saturation. Now benchmarked, further study should include modelling the caprock body within the computed domain, in order to assess the actual extent of the CO_2 migration as effected by the coupled processes. The caprock will also have different mechanical properties than the storage rock, and if stiffer would cause stress arching effects, thereby transferring stress to the outer regions of the storage site/reservoir [94, 163].

6.7.4 Two phase double-porosity (fractured) Hydro-Mechancial behaviour: (4H)M

The two phase fluid behaviour as modelled independently for both of the double-porosity sub-domains (matrix and fracture) was benchmarked in Section 6.7.2, and in Section 6.7.3 the porous solid deformation behaviour was coupled to the matrix two phase fluid sub-domain for further assessment. In this section the simultaneous behaviour of the two fluid phases flowing through both sub-domains, with the matrix sub-domain coupled to the deformation of the porous solid is assessed. As formulated in Chapter 3, the simultaneous fluid flow within the sub-domains is coupled via the double-porosity leakage/transfer terms listed in (4.32). For each fluid phase these transfer terms are a function of the conductivity of the porous matrix (which is a function of the matrix permeability and the fluid phase viscosity), and the double-porosity shape factor, $\bar{\alpha}$. The shape factor characterises the geometry of the idealised fracture network and is parametrised given the number of fracture sets and the fracture spacings (Section 2.10).

The scenario modelled is one where the prescribed fluid flux is at the inner boundary of the secondary sub-domain (fracture porosity/sub-domain), that is, a pervading fracture network of higher permeability, through which the injected fluid enters the domain from the central well. Fluid flow in and out the primary sub-domain (matrix porosity/sub-domain) is then controlled by the transfer terms and the pressures difference across the sub-domains within each fluid phase. The cool shallow reservoir base parameter set (Table 6.1) is used in this section. The initial conditions for the mass and momentum balance are as Section 6.7.3, with the sub-domains having the same initial pressure conditions. The new boundary conditions as described are detailed in Figure 6.11.

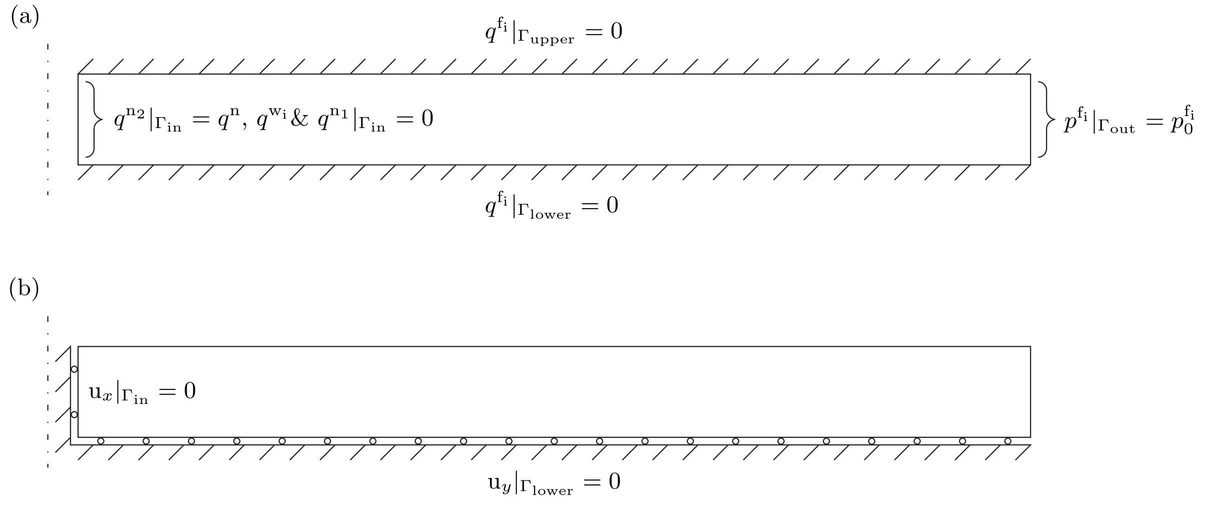

Figure 6.11: Model boundary condition schematic for double-porosity hydro-mechanical behaviour of (a) fluid pressure and flux (mass balance) boundary conditions and (b) solid displacement (momentum balance) boundary conditions. Superscript f denotes both fluid phases ($\mathrm{f} = \mathrm{w}, \mathrm{n}.$).

The system is trialled for a series of permeabilities and leakage/transfer parametrisations. Referring to Figure 6.12(a) the analytical solution for flow in a single sub-domain (here the fracture network) governed by Darcy flow with no transfer to/from the sub-domain, is given (circular marks). For comparison, the same scenario is benchmarked by the numerical model with the shape factor, $\bar{\alpha} = 0$ (dotted lines). That is, no mass transfer between the fracture and matrix sub-domain takes place as the off-diagonal $\mathbf{L}$ coupling terms of (4.32) have become zero as a result, and flow only occurs through the fracture sub-domain. The numerical model is now parametrised with the more realistic capillary pressure-saturation behaviour from Table 6.1, for both sub-domains. This is seen to cause a slight discrepancy in the numerical CO_2 saturation profiles with respect to the analytical solutions, due to the numerical solution exhibiting a greater degree of dispersion.

On increasing $\bar{\alpha}$ to a value of 0.6 m^{-2}, which corresponds to a matrix block fracture spacing of $\bar{l} =$ 10 m (2.10), transfer between the sub-domains takes place and the solution is altered (solid lines). At earlier time-steps, the CO_2 phase is seen to advance ahead through the fracture network, similarly to the no-transfer case, however where the fluid pressures have become elevated closer to the injection well transfer from the fracture sub-domain has begun to occur where CO_2 mass is seen to have displaced from the fracture to the matrix saturation profile. This effect is seen to develop over time as the pressures and CO_2 phase moves outward. Note that the matrix has a higher porosity than the fracture network so the utilisation of space becomes improved for the transferred mass.

The corresponding pressure profiles for the averaged fluid pressures in the sub-domains falls as a result of the transfer term increasing the overall permeability of the system. This is seen on inspecting the discretised governing system (4.32) at steady-state for a single fluid phase. Multiplying out the conductivity matrix $\boldsymbol{\mathcal{K}}$ and primary variables for the porous matrix sub-domain, with no induced flux, gives $(\mathbf{H}_1 + \mathbf{L})\mathbf{p}_1 - \mathbf{L}\mathbf{p}_2 = \mathbf{0}$, and for the fracture sub-domain, with an induced flux, gives $-\mathbf{L}\mathbf{p}_1 + (\mathbf{H}_2 + \mathbf{L})\mathbf{p}_2 = \mathbf{f}_2$ (where $\mathbf{H}_\mathrm{i}$ are the conductivities of the domains and $\mathbf{L}$ is their mutual transfer). On $\mathbf{L} = \mathbf{0}$, $\mathbf{H}_1\mathbf{p}_1 = \mathbf{0}$ and $\mathbf{H}_2\mathbf{p}_2 = \mathbf{f}_2$. That is, a pressure gradient and subsequent flow occurs only in the fracture network sub-domain. However, after substitution, when $\mathbf{L}$ becomes large, $(\mathbf{H}_1 + \mathbf{H}_2)\mathbf{p}_2 \gtrapprox (\mathbf{H}_1 + \mathbf{H}_2)\mathbf{p}_1 \approx \mathbf{f}_2$, meaning that the pressure in the fracture sub-domain is higher and that both pressures are controlled predominantly by the higher conductivity, here that of the fracture sub-domain, $\mathbf{H}_2$. Hence, on increasing $\mathbf{L}(\bar{\alpha})$ from zero, the average numerical pressure solution profile in the fracture sub-domain (solid lines) falls, and that of the matrix rises, though to a marginally lesser pressure value than in the fracture, depending on the magnitude of the transfer term.

The $\bar{\alpha}$ parameter is increased further to a value of 60 m^{-2}, corresponding to a smaller matrix block fracture spacing of $\bar{l} = 1$ m with the same permeabilities. As a result, more mass transfer between the fracture and matrix sub-domain takes place at the early stages. This is seen by the effect on the saturation profiles (dashed lines), where the CO_2 more readily displace to the matrix sub-domain.

For Figure 6.12(b) the matrix permeability alone is decreased by an order of magnitude, in turn reducing $\mathbf{H}_1(\mathbf{k}_1)$ and $\mathbf{L}(\mathbf{k}_1)$, for the same set of trials. The analytical solution therefore remains the same because it only considers flow in the no-transfer fracture network case which is unaffected by the matrix permeability. For the cases where transfer occurs, the effect of reducing $\mathbf{k}_1$ is seen to marginally increase the averaged fluid pressures and thus the uplift of the sealing (caprock) boundary. The marginal effect is because $\mathbf{H}_2(\mathbf{k}_2)$ is the dominant factor, given

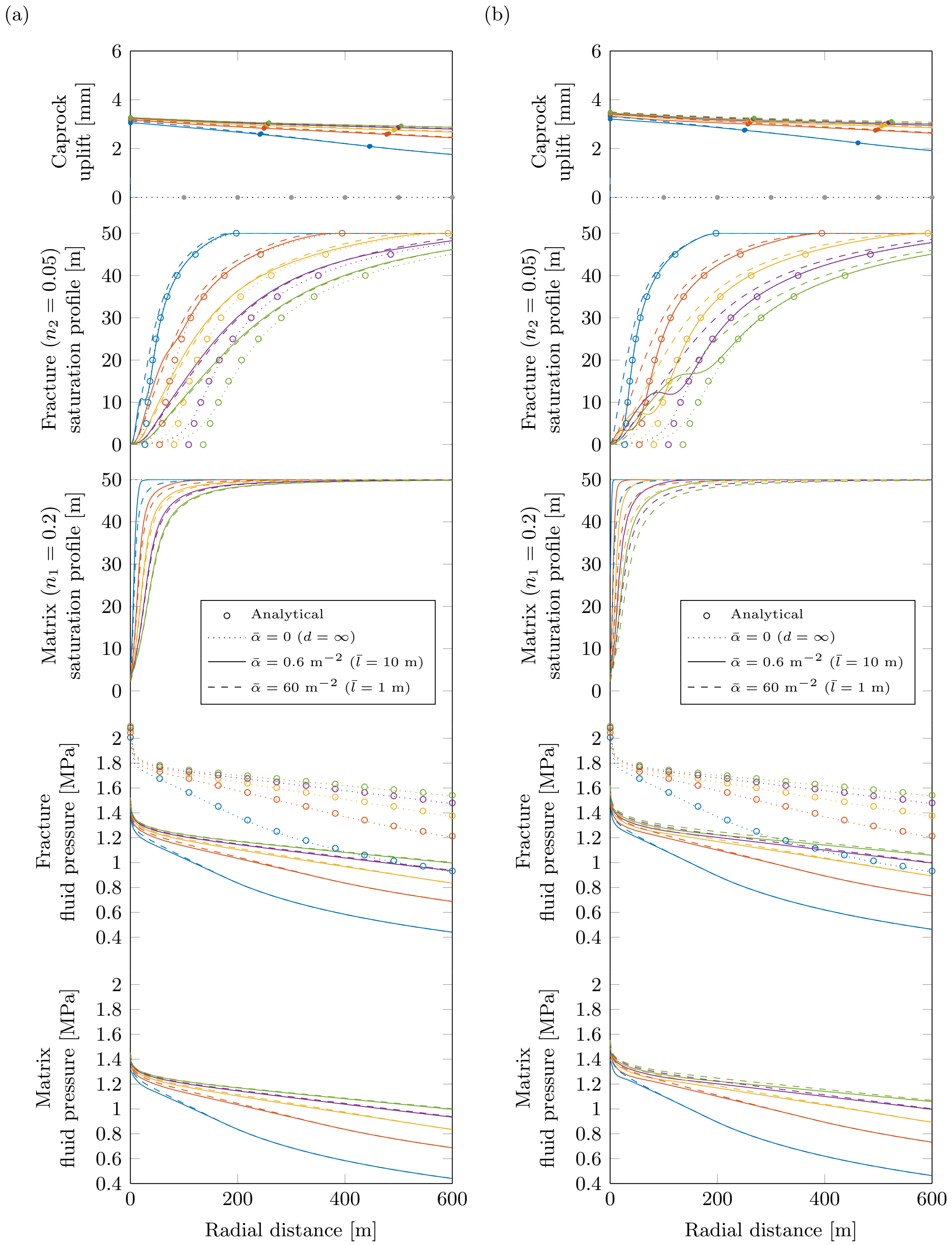

Figure 6.12: Shallow depth cool fractured (double-porosity) formation corresponding saturations, averaged fluid pressure distributions and caprock uplift. The system fracture permeability is $\mathbf{k}_2 = 1.875 \times 10^{13}$ m. For (a) the matrix permeability is $\mathbf{k}_1 = 1.875 \times 10^{14}$ m. For (b) the matrix permeability is $\mathbf{k}_1 = 1.875 \times 10^{15}$ m. The time steps are plotted at intervals of $(4n)^2$ days where $n = 1$ (blue) → 5 (green).

$\mathbf{H}_2(\mathbf{k}_2) \gg \mathbf{H}_1(\mathbf{k}_1)$. The effect on the saturation profiles for the lower $\bar{\alpha}$ values (solid lines), that of a higher fracture spacing, is to markedly retard the displacement of CO_2 from the fracture to the matrix sub-domain. This physical parametrisation, for instance, is essentially seen to be a poorer use of the available reservoir storage space, that is the CO_2 in the fracture network extends out further and less of the available void space within the porous matrix is utilised for storage, as indicated by the regions under the saturation curves.

A more elaborate (4H)M scenario is now modelled, where the gravitational terms are parametrised, and thus the upwards buoyancy force driven movement of CO_2 is computed directly. Included is also the more realistic saturation-capillary pressure behaviour. The parameters used are given as of the cool and shallow scenario in Table 6.1, with permeabilities at 1.875×10^{-14} m^2 and 1.875×10^{-13} m^2 for the matrix and fracture sub-domains respectively, with a fracture spacing of 0.1 m. Additionally, the relative permeability exponents are increased from simple linear base case behaviour to valuations of $m_{\mathrm{k}} = n_{\mathrm{k}} = 1.5$. The fluid pressure initial conditions and far-field outer boundary conditions of Figure 6.11 are considered to have a hydrostatic distribution. The initial distribution of stress due to the lithostatic body forces within the host rock is similarly augmented. Additionally, the reference pressure used in order to parametrise the fluid properties is at the centreline of the hydrostatic distribution.

To highlight the gravity driven flow a scenario motivated by [136] is simulated. The same domain as previously computed is used, however the CO_2 is injected only in through the bottom 5 m of the 50 m domain. Accordingly the mass injection rate is reduced by $M_{\mathrm{n}}/10$, such that the same rate of injection per unit well height is prescribed, that of 0.4 $\mathrm{kg/s/m_{well}}$. As there is no low permeability or impermeable boundary directly above the 5 m injection well zone, the fluid phases are free to migrate upwards from the injection point. There is however an impermeable boundary (sealing layer) 45 m above the central injection zone. This scenario may be viewed as one with a fracture network pervading through the layer (caprock or otherwise) directly above the injection point until meeting an upper intact (non-fractured) impermeable sealing layer as modelled by the upper no flux prescribed boundary condition.

Results for saturation within both sub-domains are computed at 4 and 16 days, and are rendered in quarter symmetry for clearer visualisation in Figure 6.13. In this less confined scenario, gravity driven flow is seen to override the movement of CO_2. This upwards movement occurs predominantly through the more conductive path of the fracture sub-domain, until being trapped by the impermeable layer. During this movement, only a small degree of transfer to the porous matrix takes place, other than around the high pressure zone of the injection well. On reaching the impermeable boundary the CO_2 begins to collect, increasing the local nonwetting relative permeability. As a result, this region becomes move conductive for the in flux of CO_2. This prompts further upwards migration, and the original CO_2 plume volume starts to experience a re-imbibition of brine lower in the reservoir once the CO_2 moves more readily upwards and along the impermeable layer. Also, indicated is the utilisation of pore storage space when injecting through a fracture network in a storage system of this type.

6.7.4.1 Double-porosity effects on trapping mechanisms

The free-phase CO_2 within a double-porosity formation during injection extends over much greater distances than it would injected into an equivalent single-porosity system. This is because the CO_2 enters through the secondary fracture network volume of lower porosity and higher

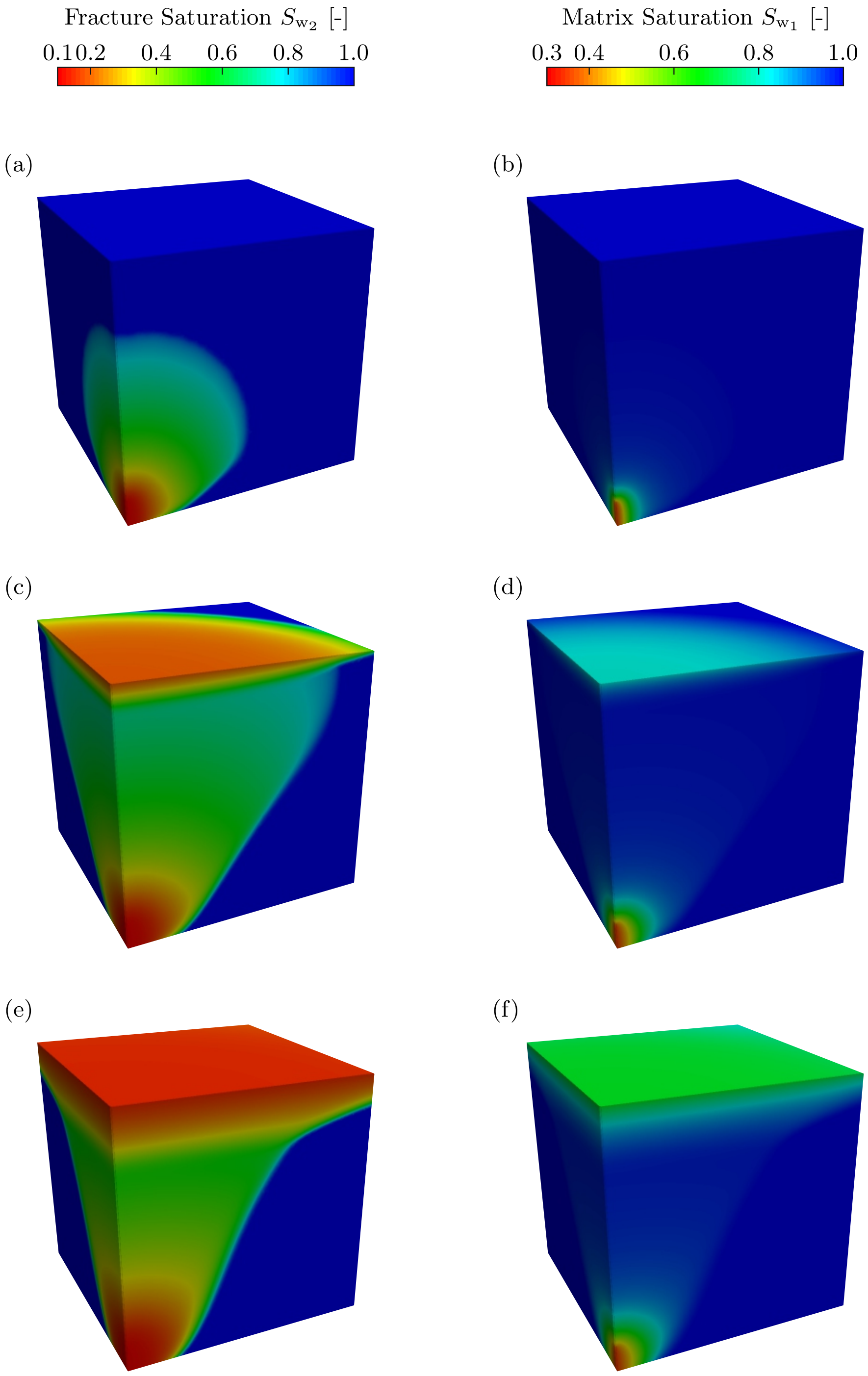

Figure 6.13: Fluid saturation profiles within a double-porosity storage system at 4 days (a & b), 16 days (c & d), 36 days (e & f). Saturations within the fracture network sub-domain are given in (a, c & e), and saturations within the porous matrix sub-domain are given in (b, d & f). Note that the minimum saturations within the sub-domains as scaled is due to the wetting phase residual saturations (S_{rw_i}) which are 0.1 and 0.3 for the fracture and matrix sub-domains respectively. Note that the images are quarter symmetric sections rendered from the computed axisymmetric domain for ease of illustration.

permeability, where the CO_2 therefore migrates at greater velocities, generally bypassing the much less permeable matrix pore space. Thus a larger total formation volume space is required with which to accommodate and encapsulate the injected CO_2.

This effect poses a greater risk for structural (or stratigraphic) trapping because in a double-porosity formation the mass of stored CO_2 will occupy a larger area with a greater likelihood of intercepting leakage pathways and spilling out from under designated trapping interfaces. This is compounded with the issue of having the CO_2 migrating in a fissure/fracture network which may also pervade an intended sealing caprock.

However, in a double-porosity system the longer term dissolution trapping mechanisms are significantly enhance given that the free-phase CO_2 is in contact with greater interface areas of the brine which is housed in the matrix pore space surrounding the CO_2 in the fractures. In a single-porosity formation dissolution (and reaction) occurs principally at the outer interface boundaries of the CO_2 free-phase region where it is within contact with the brine that it is displacing. Behind this interface the CO_2 has largely dried out the host brine and beyond this interface there is no CO_2 yet present for dissolution trapping to occur. Therefore, within a single-porosity formation dissolution trapping, particularly in the short term, is generally limited to the movement of the outer fluid interface. Alternatively, in a double-porosity formation it is the fracture network that will dry out while the surrounding matrix pore space remains predominantly saturated with the host brine. This is caused by the low permeability and CO_2 relative permeability in the porous matrix which restricts CO_2 free-phase movement through it, wherein the host brine is not significantly displaced behind the CO_2 front out in the fractures. Although there is little fracture/matrix phase transfer, there is enhanced dissolution and diffusive transfer across the fracture/matrix interface due to the high imposed concentration gradient between the free-phases separated by this interface. This dissolution processes is a more definitive trapping mechanism than free-phase storage within the matrix.

The enhanced dissolution trapping also enhances the contact area and time between dissolved CO_2 and the rock minerals within the porous matrix environment, which is also advantageous for mineralisation trapping mechanisms to occur. An appropriately simplified study on these interesting effects in the context of GCS is given in [38]. This is for an isothermal non-deformable case with no/simplified free-phase CO_2 movement in the pore matrix space, and thereby concentrates principally on the dissolution and diffusive processes. In the present study the lag between the free-phase movements within the matrix and fracture space are addressed in detail in conjunction with the coupled effects of pressure evolution and site deformation. Additionally coupling phase miscibility is however a key point for further research. Due to the enhance dissolution into the pore matrix space in double-porosity systems, long term storage simulations particularly after the injection stage will become inaccurate if they do not model these dissolution effects. This is because they will not account for the CO_2 mass stored by dissolution in the matrix pore space and over predict CO_2 mass within the fracture network space. Finally, a key design aspect when considering a double-porosity storage system is in balancing the advantages promoting the rate and extent of CO_2 dissolution trapping and the disadvantages limiting structural/stratigraphic trapping.

6.7.5 Two phase Hydro-Thermal behaviour: (2H)T

In this section the coupled thermal behaviour is assessed. As discussed in Section 2.6.8.3, a key issue potentially affecting reservoir storage performance, is Joule-Thomson cooling (JTC). This is caused by the non-idealised thermodynamic behaviour of CO_2 which is shown to be prevalent in low pressured (depleted) reservoirs. The base case scenarios of Table 6.1 are parametrised according to a range of brine aquifers of normal pressure and temperature gradients at acceptable depths where the pressures and temperatures are such that any cooling due to JTC is negligible. However depleted/disused reservoirs, which are useful given the geological knowledge and infrastructure available due to past exploitation, form another subset of potential storage systems with different engineering challenges, characterised by low/under pressured host fluid systems.

To assess the effects of JTC in a low pressured reservoir and thus assess the developed numerical system in this context, a lower pressure reservoir parameter set is given in Table 6.6. The essential change from the previous scenarios is that due to the significant initial/reference pressure change, the CO_2 phase now exhibits a particularly low density, viscosity and heat capacity with high compressibility and expansivity. This has the effect of increasing the Joule-Thomson coefficient (related via 6.15) thereby increasing its significance in the system of equations.

For verification, comparison is made with an analytical solution for JTC [125], which is a special case of the numerical model. Firstly, from the main discretised system of governing equations (4.32), the coupled mass and energy balance components for the solid and the two fluid phases in the primary sub-domain (sub-matrix rows/columns 2–3 & 6) are isolated with no/zeroed transfer terms.

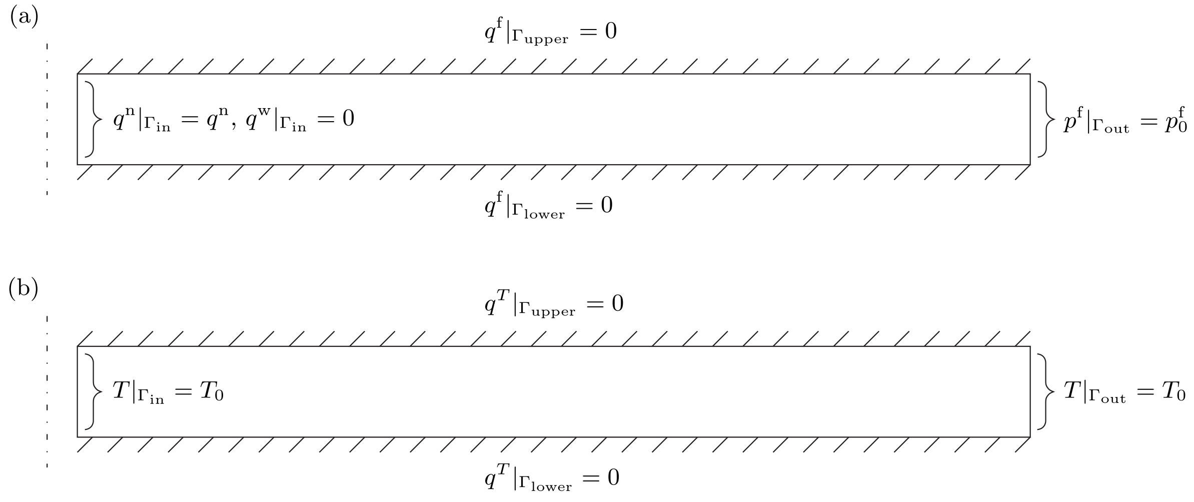

Figure 6.14: Model boundary condition schematic for hydro-thermal behaviour of (a) fluid pressure and flux (mass balance) boundary conditions and (b) thermal (energy balance) boundary conditions. Superscript f denotes both fluid phases ($\mathrm{f} = \mathrm{w}, \mathrm{n}.$).

The scenario to be modelled is illustrated in Figure 6.14. The low initial pressure and temperature conditions are given in Table 6.6, and are assumed uniform. The thermal boundary conditions represent a scenario where CO_2 is injected at a constant temperature which is the same as the initial state of the reservoir.

Table 6.6: Lower pressure (depleted) reservoir parameter set for Joule-Thomson cooling scenarios.

Storage system parameters

Porous region		Matrix$_1$	Fract.$_2$	Fluids	
Physical Parameters	Sym.				Units
Reservoir depth	D			1.0	km
Reference fluid pressure	p_{ref}			5.0	MPa
Reference temperature	T_{ref}			45.0	°C
Reference vertical effective stress	σ'_{v}			13.0	13.0
Brine density	ρ^{w}			1062	kg/m^3
Brine viscosity	μ^{w}			728.1	µPa s
Brine bulk modulus	K_{w}			2.618	GPa
Brine thermal expansion coef.	β^{w}			0.460	$\times10^{-3}$/K
Brine specific isobaric heat cap.	c_p^{w}			3824	J/kg·K
Brine thermal conductivity	χ^{w}			0.626	W/m·K
CO$_2$ density	ρ^{n}			108.7	kg/m^3
CO$_2$ viscosity	μ^{n}			17.18	µPa s
CO$_2$ bulk modulus	K_{n}			0.00364	GPa
CO$_2$ thermal expansion coef.	β^{n}			7.51	$\times10^{-3}$/K
CO$_2$ specific isobaric heat cap.	c_p^{n}			1400	J/kg·K
CO$_2$ thermal conductivity	χ^{n}			0.0231	W/m·K
Intrinsic rock density	ρ^{s}	2600		~	kg/m^3
Young's modulus	E	14.4		~	GPa
Poisson's ratio	ν	0.2		~	-
Biot's parameter	b	1.0		~	-
Thermal expansion coef.	β^{s}	0.035		~	$\times10^{-3}$/K
Specific isobaric heat cap.	c_p^{s}	1000		~	J/kg·K
Thermal conductivity	χ^{s}	2.51		~	W/m·K
Porosity	n	0.3	0.1	~	-
Brine residual saturation	S_{rw}	0.1	0.1	~	-
CO$_2$ residual saturation	S_{rn}	0.0	0.0	~	-
Intrinsic permeability	$\mathbf{k}$	0.5	1.0	~	$\times10^{-13}$ m^2
Brine end-point relative perm.	k_{rw0}	1.0	1.0	~	-
CO$_2$ end-point relative perm.	k_{rn0}	0.5	0.5	~	-
Brine relative perm. exponent	m_{k}	1.0	1.0	~	-
CO$_2$ relative perm. exponent	n_{k}	1.0	1.0	~	-
van Genuchten parameter	m_{v}	0.5	0.6	~	-
van Genuchten parameter	p_{v}	10.0	2.0	~	kPa
Fracture spacing	$\bar{l}$	-	1.0	~	m
Well height/reservoir thickness	H	50		~	m
Well radius	r	0.2		~	m
CO$_2$ Mass injection rate	M_{n}	3		~	kg/s

The parameter valuations of Table 6.6 and the modelled scenario are guided by the scenarios studied in [125, 129, 141], with the thermodynamic properties parametrised accurately as discussed in Section 6.1. Again, the extensive thermophysical fluid properties are simply a function of the reference pressure and temperature data, and are tabulated for inspection. Therefore, the reference pressure and temperature need only be specified in the model such that all the thermodynamic properties consistently correspond to the same reference p-T data.

The analytical solution solves a special 1D limit case of the general energy balance (3.67) as was derived. That is,

$$(\rho c_p)^{\mathrm{ep}}_{\mathrm{eff}} \frac{\partial T}{\partial t} = -\mathrm{q}^{\mathrm{n}} \rho^{\mathrm{n}} c_p^{\mathrm{n}} \left[\frac{\partial T}{\partial x} - \mu^{\mathrm{n}}_{\mathrm{JT}} \frac{\partial P}{\partial x} \right], \tag{6.14}$$

where on the l.h.s. is the effective overall system heat capacity term which is considered at the end-point state where $S_{\mathrm{w}} = S_{\mathrm{rw}}$, see (3.67). The r.h.s. considers only the nonwetting $\mathrm{CO_2}$ phase thermodynamic behaviour, where $\mu^{\mathrm{n}}_{\mathrm{JT}}$ is the Joule-Thomson coefficient as introduced in Section 2.6.8.3. The Joule-Thomson behaviour is implicit in the full general energy balance equation (3.67) and may be related following the thermodynamic relation (3.59), which gives

$$\mu^{\mathrm{n}}_{\mathrm{JT}} = \frac{\beta^{\mathrm{n}} T - 1}{\rho^{\mathrm{n}} c_p^{\mathrm{n}}} \tag{6.15}$$

which, along with the effective system heat capacity, is updated in the numerical formulation during computation. However, the JTC parameter $\mu^{\mathrm{n}}_{\mathrm{JT}}$ is known to remain reasonably steady in value such that it may be considered constant at the pressures and temperatures of interest [125]. Equation (6.14) assumes a single phase steady-state pressure/flow field, and negligible thermal conductivity. Given that the heat capacities of the rock and brine ahead of the advection front retard temperature change, the formulation of (6.14) considers that the thermal action occurs in the $\mathrm{CO_2}$ dominant region behind the fluid interface. The reduced form (6.14) also considers the fluid pressure to be at steady-state with the system temperature transient. The steady-state pressure is introduced into (6.14) given (6.12) (hence the analytical well pressure is undefined), and the extent of the $\mathrm{CO_2}$ phase by (3.38) while assuming no mobility contrast such that the $\mathrm{CO_2}$ body is an advancing cylinder of fluid within the pore space. The analytical system is then solved via Laplace transformation.

In Figure 6.15, the analytical solutions indicating the reduction in system temperature over time for the parameter set up of Table 6.6 are illustrated (dashed lines). The numerical solution is plotted for comparison (solid lines), which demonstrates the expected degree of agreement. The numerical model accounts for the realistic movement and dispersion of the $\mathrm{CO_2}$ phase, and the conductivity of the system. Thus, the numerically described thermal effects are generally spread about the sharper analytical solution. Contributing also to the discrepancy in temperature between model solutions is the transient increases in pressure captured by the numerical system, which would have a heating effect, and the compressibility of the fluids, which would reduce the pressure gradients in space.

From Figure 6.15(a) to Figure 6.15(b) the intrinsic permeability is doubled, which is seen to reduce the spatial pressure gradient thus reducing the degree of cooling within the system. Note that significant reductions in reservoir in temperature could lead to a reduction in reservoir performance due to increased $\mathrm{CO_2}$-hydrate formation and significant cooling of the (residual) brine which would adversely affect its thermal-physical properties, ultimately restricting flow.

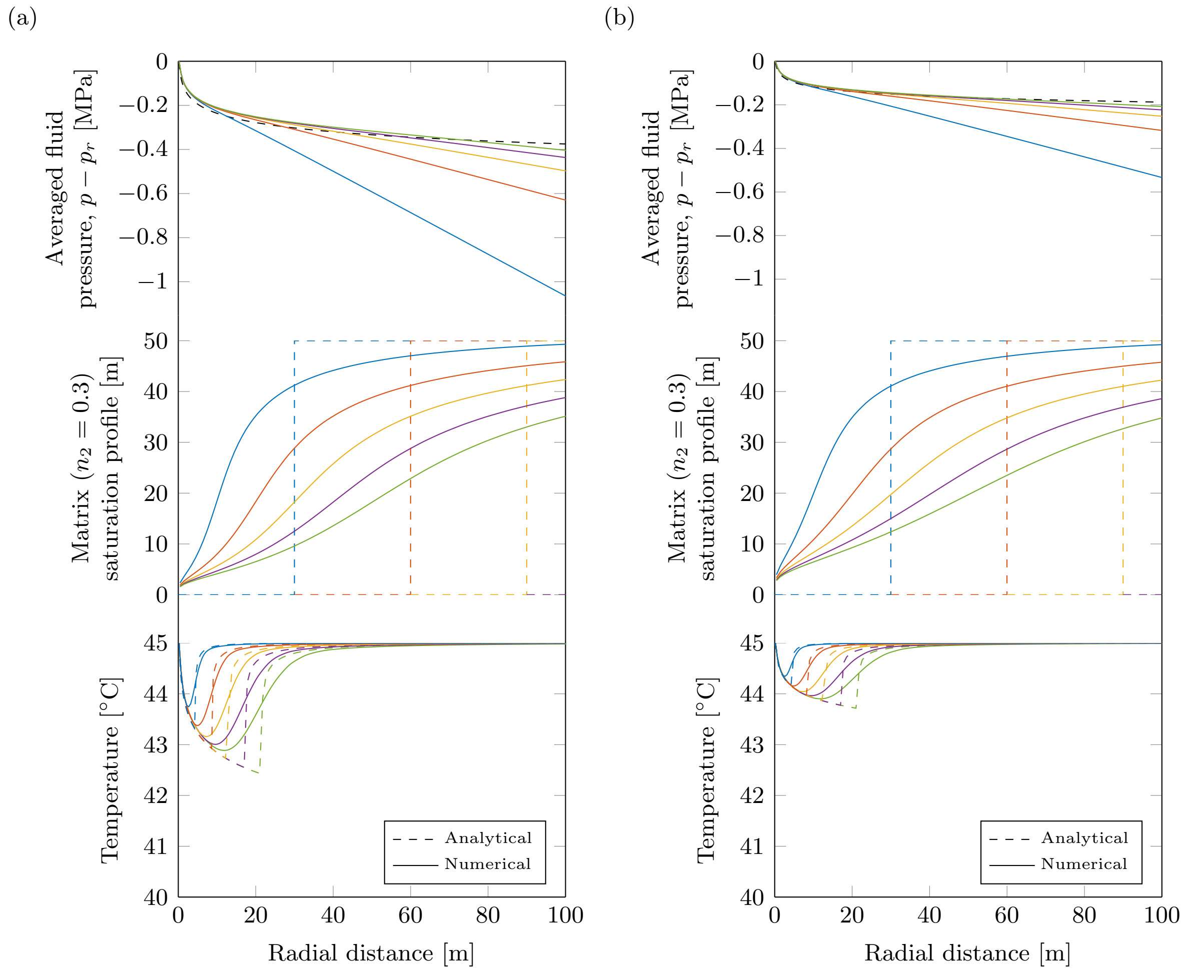

Figure 6.15: Low pressure (depleted) reservoir scenario highlighting Joule-Thomson cooling with the corresponding normalised averaged fluid pressures and saturations. The reservoir parameters are given in Table 6.6, where in (a) the intrinsic permeability is $\mathbf{k}_1 = 0.5 \times 10^{-13}$ m and in (b) the intrinsic permeability is $\mathbf{k}_1 = 1 \times 10^{-13}$ m. The time steps are plotted at intervals of $(4n)^2$ days where $n = 1$ (blue) → 5 (green).

6.7.6 Two phase single and double-porosity Hydro-Thermo-Mechanical behaviour: (2/4H)TM

This section extends on the previous by introducing the coupled mechanical behaviour and the fracture network sub-domain in succession. From the discretised system of governing equations (4.32), that is the coupled momentum, mass and energy balance equations for the solid and the two fluid phases in the primary sub-domain (sub-matrix rows/columns 1–3 & 6) isolated with no/zeroed transfer terms are followed by computation with the whole system of governing equation thus incorporating both sub-domains. The initial and boundary conditions are adopted from Sections 6.7.3, 6.7.4 and 6.7.5, illustrated together in Figure 6.16.

From Table 6.6 the single porosity hydro-thermo-mechanical scenario is modelled and presented in Figure 6.17(a) (solid lines), with the single porosity hydro-mechanical isothermal case computation plotted for comparison (dashed lines). The effect of coupling the thermal effects has had little effect on the saturation and pressure profiles, though further potential to couple these phenomena with respect to temperature was neglected on the formulation steps leading to (3.14–3.15) and (3.19–3.20). See also (2.55) and (3.3). However, the localised reduction in temperature due to JTC has caused the host rock to contract slightly, relative to the isothermal case, in a similarly localised manner. This coupled effect with the momentum balance equation, due to the degree of solid phase thermal expansion, is seen to partially offset the ensuing uplift due to the induced rise in fluid pressure. Note that the rise in pressure is also causing the spatial pressure gradient that results in the coupled expansive cooling of the CO_2 dominant region of the system. The solid displacements are magnified to scale by 5×10^4, with the dot markers on the profile signifying the deformed material point at the 100 m interval.

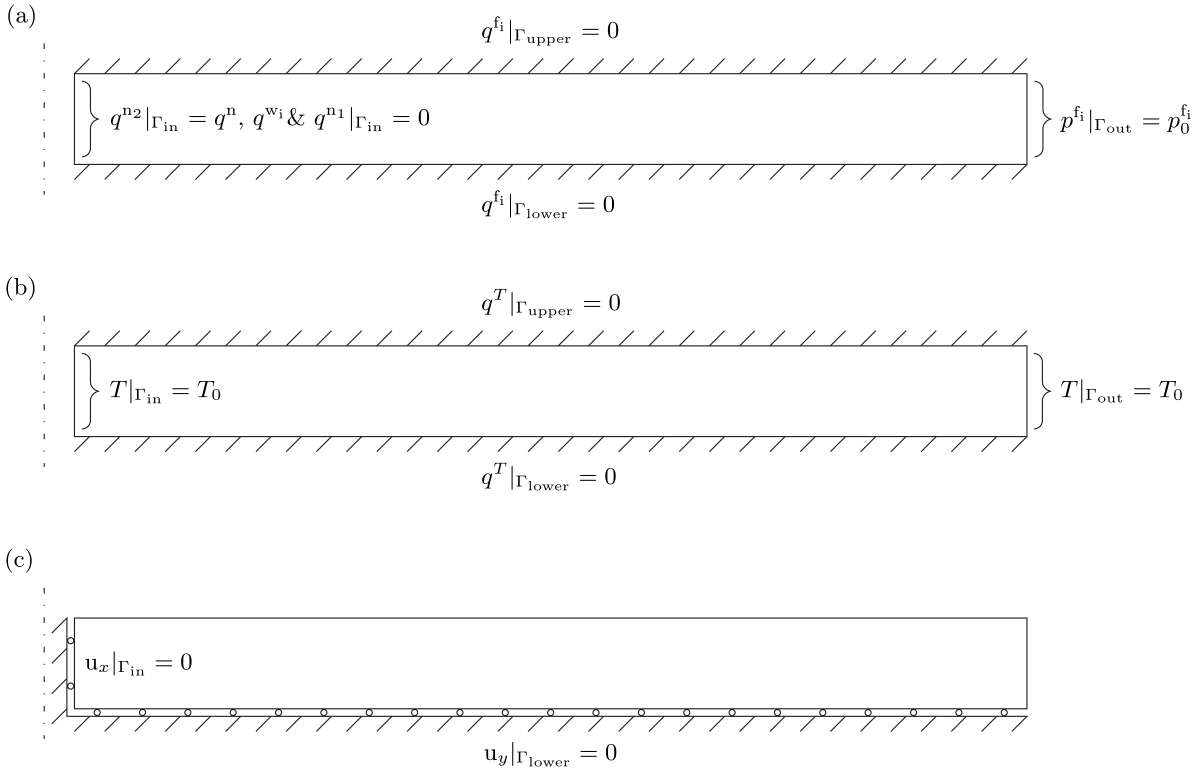

Figure 6.16: Model boundary condition schematic for the (fractured) hydro-thermo-mechanical behaviour of (a) fluid pressure and flux (mass balance), (b) thermal (energy balance), and (c) solid displacement (momentum balance) boundary conditions. Superscript f denotes both fluid phases ($\mathrm{f} = \mathrm{w}, \mathrm{n}.$).

From Table 6.6, the double-porosity (fractured) hydro-thermo-mechanical scenario is now modelled and presented in Figure 6.17(b) (solid lines), with the double-porosity (fractured) hydro-mechanical isothermal case computation plotted for comparison (dashed lines). The system is now fractured, in that compared to the previous scenario, a pervading fracture network is introduced. The flux of CO_2 is now also prescribed on the secondary fracture sub-domain. As the fracture sub-domain has a higher permeability than the original matrix sub-domain, which was previously injected into, the average system pressures and pressure gradients have reduced significantly. The system temperature reduction due to JT expansion and cooling has therefore also reduced. Accordingly, the upper surface uplift is reduced along with the offset in uplift reduction due to the corresponding decrease in system cooling.

This change in uplift due to the thermal effects suggests potential for the detection of system cooling form surface movement, if the system parametrisation permits. Additionally, introducing

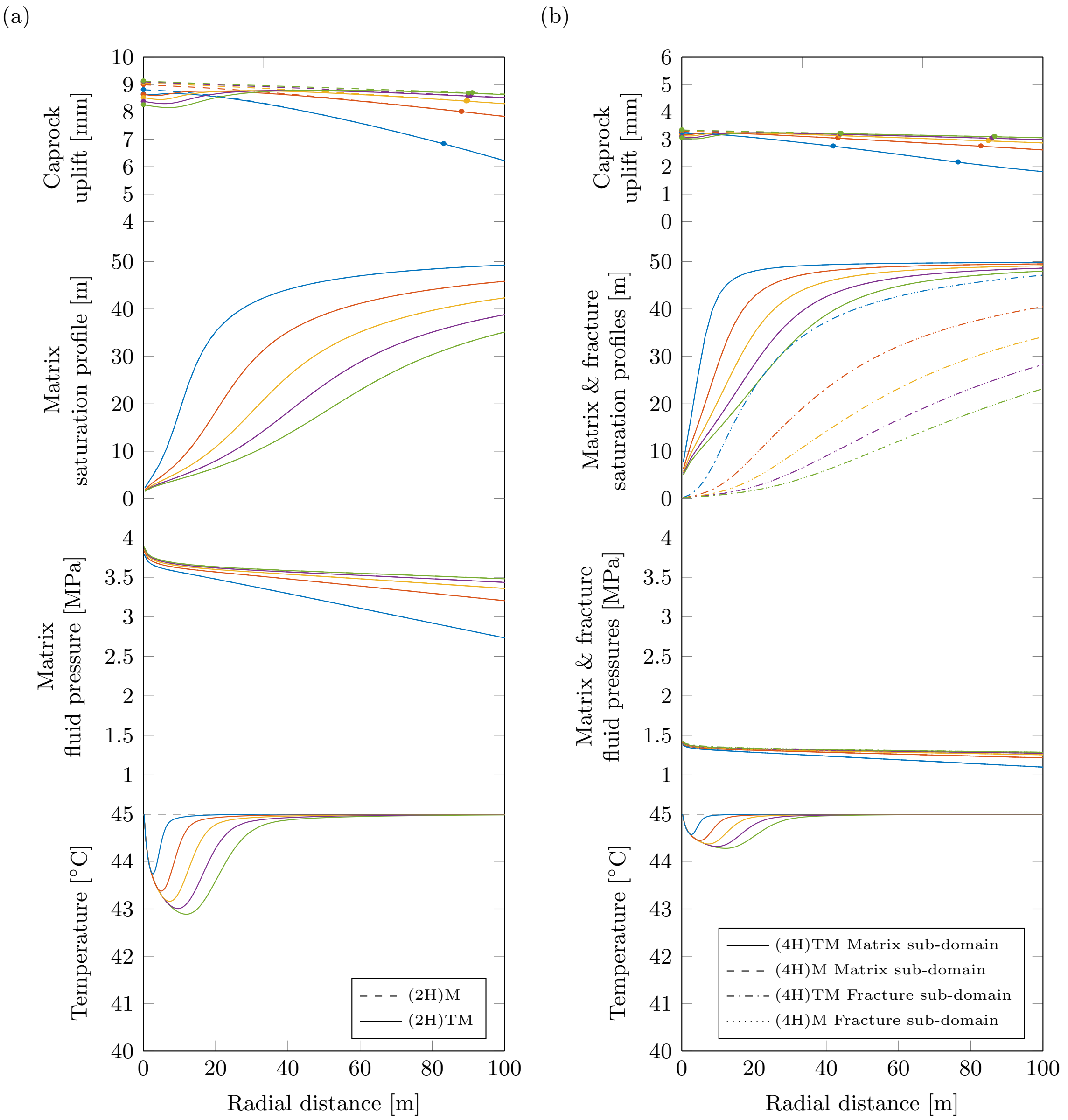

Figure 6.17: Low pressure (depleted) reservoir scenario highlighting Joule-Thomson cooling with coupled mechanical behaviour. Presented are the corresponding mechanical deformation, saturation, averaged fluid pressure and temperature profiles. The reservoir parameters are given in Table 6.6. (a) is the single porosity scenario and (b) is the double-porosity scenario. The time steps are plotted at intervals of $(4n)^2$ days where $n = 1$ (blue) $\rightarrow 5$ (green).

fractures into the system would alleviate the effect of cooling if it was to become problematic, as the initial permeability causing higher pressures would have less of an influence on inducing higher system pressures. Note also the corresponding change in the storage location of the CO_2 in the two sub-domains between scenarios.

This section has considered a CO_2-brine fluid system. Additionally, a depleted system may also contain residual methane and/or other hydrocarbons, the inclusion of other phases is within scope of the current formulation for potential further study in this context.

6.8 Algorithm performance

Figure 6.18(a) illustrates the numerical improvements gained when running the algorithm in different modes for the same model scenario. For comparison the cumulative number of calls to the linear solver (and to form the nonlinear coefficient matrices) is used as a metric, as it is the most expensive computational process (indicative of the computational time spent), particularly for large coupled arrays. Computed is the solution at 400 days for the (2H)M cool shallow reservoir model scenario as discussed in Section 6.7.3. The application of control theory is used in all modes, whereby the local truncation error and the algorithm ability to bring about convergence has controlled the time-stepping. Noting that it is inherent in the algorithm that nonlinear convergence is made possible by careful selection of the time-step size given that no Jacobian information for convergence is available prior to computation over the time-step. As such, no comparison is made with any heuristic time stepping. It is however a point for further research to potentially process information from the previously converged steps for further improved convergence rates.

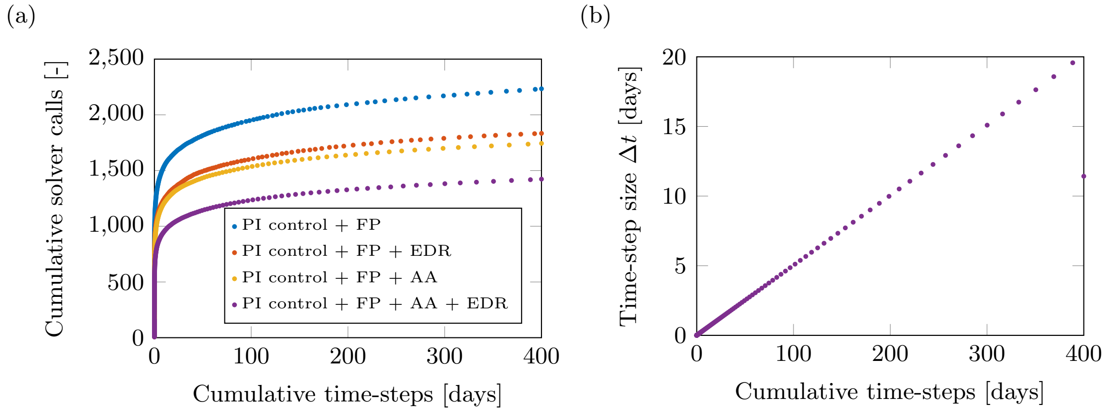

Figure 6.18: (a) Cumulative number of calls to the linear solver required to model the first 100 hours by a standard fixed-point (FP) procedure with PI control, compared with modified methods integrating embedded date recovery (EDR) and Anderson acceleration mixing (AA), displayed in a series of combinations as labelled in the chart. The numerical parameters are listed for the control components in Table 6.2 and for the acceleration components in Table 6.3. (b) Adapted time-step sizes to reach a solution at 400 days as controlled by the gain factors in Table 6.3.

Using the base parametrisations of Tables 6.2 and 6.3, the standard fixed-point (FP) procedure is employed without acceleration ($m_{\max} = 0$) and without enhanced data recovery (EDR) in order to compute the solution at 400 days with a benchmark performance. Computing the solution again with the recovered enhanced data inherent in the dual solution (embedded pair) control procedure (5.54) an improvement in convergence/performance is observed due to the availability of an improved initial solution estimate for each nonlinear time-step. This trial is carried out again with acceleration (AA), for $m_{\max} = 5$. For this model scenario, from the first benchmark an improvement in the number of solver calls per unit time-step of approximately 36% is gained by mixing the vector sequence of iterations initiated with the enhanced data recovery.

This general trend in improvement is seen throughout all coupled scenarios and over practical ranges of numerical parametrisation to various extents. Further improvements are seen when the controller selects relatively larger time-steps and/or when tighter convergence tolerances are specified, that is, when placing more burden on the nonlinear solver such that fewer time-step cycles are required over a given time domain. For such a scenario, the Anderson mixing has a greater scope for processing information from the early iterations, of what would otherwise have been a lengthy iteration processes. If conversely very small time-steps are selected, due to the specification of low truncation tolerances with high or low residual tolerances, smaller time-step sizes will be required. Thus the burden is taken off the nonlinear solver, whereby the number of iterations required for convergence declines and the improvement in employing the acceleration procedure is reduced. However, the number of time-steps required would increase over the same time domain. Optimisation of the numerical parameters for a given scenario in terms of achieving an optimal number of solution calls per unit time-step is therefore a point for further study. In particular, PI control parameters are themselves sensitive to altering the computational effort per unit time modelled, and would require further investigation, certain approaches for such an analysis are presented in [77].

In Figure 6.18(b) the controlled growth in time-step size over the cumulative sequence of time-steps is given for the 'PI control + FP + AA + EDR' case. Indicated is a steady growth factor of approximately 1.05, which controls the local truncation error throughout computation, depending on the numerical parametrisation. Note that the controller was tasked to reach a solution at 400 days constrained by the truncation error tolerance. Therefore, the final time-step size at 400 days is smaller since it is assessed in the current time-step whether it is within tolerance to compute a solution at the desired time interval. Thus rather than stepping over the solution of a desired time interval, the growth factor is accordingly reduced. If many specific time interval solutions are required, optimally adjusting the growth factor ahead of time thereby preventing any inefficient time-stepping would be an additional improvement.

Chapter 7

Muographic Modelling Applications

How to efficiently/cost-effectively monitor a GCS site in a passive and continuous manner is an existing problem. The model formulation, numerical implementation and coding of this work are also developed for the purpose of assessing and developing muon radiography as a novel and unconventional solution to this problem. As outlined in Chapters 1 and 2, this work has been carried out as part of a collaborative project on the interrelated demand for the effective governance, monitoring and modelling of GCS. A key vision of this project is the notion of employing cosmic-ray muon imaging as a passive and continuous monitoring aid for GCS [114].

Cosmic-ray muon tomography and transmission imaging (Section 2.11.2) have been proven to be feasible for imaging stationary and dynamic large scale objects [10, 188]. The first studies on applying this technique for imaging a realistic geo-stored CO_2 body are presented in the following two sections.

Firstly, Section 7.1 presents and implements a workflow for embedding the numerical code with a particle transport simulation code in order to model and assess the conceptual viability of using muon radiography as a means to monitor geo-stored CO_2. This is carried out for a realistic though idealised site for study purposes. The full extensive account of this study is given in the co-authored work of [108]. Due to the various specialisations involved, which are beyond the scope of this thesis, complementary details are primarily given in this section with respect to the multi-physics modelling strategy and code integration which made the multifaceted simulation possible.

Secondly, in Section 7.2, an alternative method for modelling muon radiography is adopted based on the co-authored work of [23]. This method is based on muon survival statistics rather than explicit muon-by-muon simulations through the subsurface. The muon physics is therefore implemented in a highly simplified manner, however the method is significantly more computationally efficient in comparison. This approach is demonstrated to be ideal for screening and optimising storage scenarios. To this effect, a realistic, non-idealised and challenging real-world CO_2 storage scenario is assessed using this approach and is discussed.

7.1 Modelling muon radiography for monitoring a GCS site

The site selected for the study is situated offshore above Boulby Mine, Cleveland, UK. Though no CO_2 will be stored there, the site is selected because the mine below is accessible and has research facilities for prototyping and testing muon detectors. Additionally, the geological data above the mine is available to the research team and is well understood for the purpose of processing for simulation.

7.1.1 Modelling methodology

The object-orientated programming framework Geant4 [1] (Section 2.11.2.3) is used to host the present simulation. A virtual environment is constructed of a ∼40 km^2 geological area extending from the sea surface to a subsurface muon detector; it represents the medium through which the muons will travel, interact and decay. This geological body is populated with the known Boulby geological data. The detector is conceptualised of plastic scintillator and photo-sensor technology with an effective detection surface area corresponding to 1000 m^2, and is located at a trial depth within the mine of 776 m below the seabed. This depth is selected as it is the depth for a test site within the mine for muon detector prototyping to take place. The results of this simulation are therefore to aid muon detector design for GCS applications, which is also ongoing research.

The energy spectrum of cosmic-ray muons arriving through the sea surface is described by the Gaisser parametrisation [66] (Section 2.11.2), which accounts for the correlations between muon energy and trajectory (zenith angle). Monte Carlo methods are used to sample according to the parametrisation in order to generate muons. The Geant4.9.6 'shielding' physics list [1] is used to simulate the loss of muon energy through the subsurface due to interaction with the matter of the modelled subsurface. To assess the sufficiency of this modelling approach the reader is referred to [1, 108, 113].

The muon energy loss is principally related to the density and composition (mean atomic number and weight) of the bulk medium through which they travel and interact (Section 2.11.2). If the muon energy becomes low enough the muon will stop or decay and be absorbed. By altering the bulk density and composition of the bulk medium the observable muon flux through it will therefore change. As a result, it is possible to map the bulk density and composition by observing changes in the muon flux emerging form the medium of interest, if indeed a known or steady flux is entering the medium.

The simulation is initially carried out over the geological body of interest in order to establish a statistically independent expectation count of muon events over time through the detector without CO_2 in place. The muon flux reaching the simulated detector is determined to be approximately 2.3×10^{-7} cm^{-2} s^{-1} (200 m^{-2} day^{-1}). Subsurface muon flux distributions are tabulated and discussed further in [113].

7.1.1.1 Boulby GCS test model

It is the change in the bulk properties (primarily the bulk density) of this subsurface environment that affects the measured flux of muons. To assess this effect through a geological body undergoing CO_2 storage, a supposed vertical injection well is centred horizontally directly in line above the detector. The region about the injection well is to undergo changes in bulk density and composition by modelling the injection of CO_2. The evolving CO_2 body, with an injection height of 170 m, is centred vertically at a trial depth of 570 ± 85 m below the seabed, located 121 m directly above the detector. This is geologically consistent with the strata at the Boulby site, as it places the CO_2 body within a permeable sandstone formation which is overlay by mudstone at a depth which coincides with the top of the injection well.

Table 7.1: Boulby test site storage formation parameter set.

Storage system parameters			
Physical Parameters	Sym.		Units
Brine density	ρ^{w}	1100	kg/m^3
Brine viscosity	μ^{w}	900	µPa s
Brine bulk modulus	K_{w}	2.90	GPa
CO_2 density	ρ^{n}	720	kg/m^3
CO_2 viscosity	μ^{n}	60.0	µPa s
CO_2 bulk modulus	K_{n}	0.025	GPa
Intrinsic rock density	ρ^{s}	2670	kg/m^3
Porosity	n	0.15	-
Brine residual saturation	S_{rw}	0.4438	-
CO_2 residual saturation	S_{rn}	0.0	-
Intrinsic permeability	$\mathbf{k}$	1.875×10^{-13}	m^2
Brine end-point relative perm.	k_{rw0}	1.0	-
CO_2 end-point relative perm.	k_{rn0}	0.3948	-
Brine relative perm. exponent	m_{k}	3.2	-
CO_2 relative perm. exponent	n_{k}	2.6	-
van Genuchten parameter	$\mathrm{m_v}$	0.46	-
van Genuchten parameter	p_{v}	19.6	kPa
Well/Storage height	H	170	m
Well radius	r	0.2	m
CO_2 mass injection rate	M_{n}	20	kg/s

The change in the subsurface bulk density and composition due to the injection of a mass of CO_2 is determined by the numerical model (4.32) which is parametrised as of Table 7.1, based on the geological data determined from site and the system parameter studies of [99, 128]. For this first investigation, the bulk density and composition changes are assumed to be due principally to the multiphase displacing (drainage) phenomena within the storage system, which is considered to occur with a stable fluid interface. The model is thus parametrised to account accurately for multiphase saturation behaviour, whilst ignoring the solid deformation, miscibility, and thermal behaviour. This does however present a realistic, though idealised, axisymmetric fluid interface with a density/composition contrast through which the effect on the muon flux can be computed in order to assess the feasibility of using muon radiography to detect a moving CO_2 body/brine-CO_2 interface. The idealised model is meaningful for this first conceptual study because it gives a realistic though basic bulk density/composition contrast, which allows for ease of interpreting the results and practically assessing the changes in muon flux through the geological body.

The mudstone above the storage region is assumed to be impermeable, and given the relatively low mass injection rate per unit well height, the CO_2 body modelled during injection demonstrates significant buoyancy effects collecting as a relatively thin layer away from the injection well under the sandstone/mudstone interface whilst migrating radially (7.2(a)).

The numerical model outputs are used to give a bulk composition and to compute a macroscopic bulk density by summation of the product of the intrinsic phase densities and their corresponding volume fractions, after the review of Section 2.1.2 and as used for the bulk density in the momentum balance formulation (3.44),

$$\rho = (1-n)\rho^{\mathrm{s}} + nS_{\mathrm{n}}\rho^{\mathrm{n}} + nS_{\mathrm{w}}\rho^{\mathrm{w}}. \tag{7.1}$$

The current simulation framework is constrained to simulate muon interactions through one static geological scenario at a time. The information provided by the numerical model is therefore produced for a sequence of 10 sequential time intervals which correspond to $(2n)^2$ days, where $n = 1 \to 10$, from the start of CO_2 injection. This stepping was chosen given the relationship of the radial fluid interface extent with time ($x_{\mathrm{nmax}} \propto \sqrt{t}$), such that the CO_2 body to be tracked is extending over a uniform distance for each interval. Given the parametrisation of Table 7.1, that is an approximate radial extent increase of 36 m per time interval until an approximate distance of 360 m from the well is reached at 400 days (this may also be verified by (3.38)). Therefore, the storage formation state at time interval n, as computed, represents an average storage system state between the period $(2n-1)^2$ to $(2n+1)^2$ days.

7.1.1.2 Model integration

The numerically computed bulk density and composition states of the storage formation are embedded in the Geant4 framework by exploiting its object-orientated architecture by making use of the voxel (volumetric pixel) processing capabilities within its libraries. The voxelisation capabilities are typically utilised for constructing medical phantoms to undergo simulation with radiography. This code integration may be visualised in Figure 7.1, which outlines a workflow for embedding the numerical model nodal solutions with the existing object-orientated architecture. Essentially, the GeometryConstruction class handles the modelled physical objects of matter (geological body and detector) with which particles are to interact. This is informed of the local voxelised changes in bulk density and composition from the numerical model nodal solutions via the PhantomConfiguration and VoxelParametrisation classes.

For example, Figure 7.2(a) illustrates the bulk density as computed by the numerical model at $n = 4$ (64 days). Figure 7.2(b) illustrates the corresponding voxelisated form which is embedded

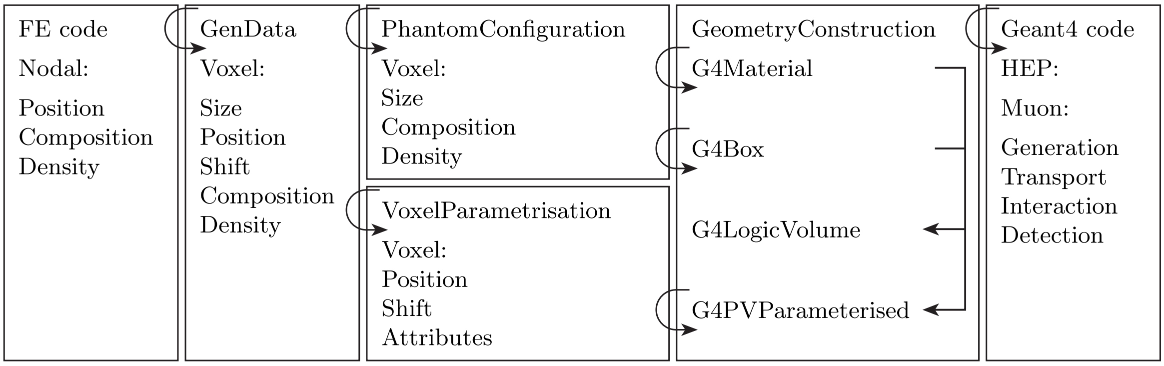

Figure 7.1: Schematic of classes developed to embed the numerical code with the Geant4 framework.

computationally in the framework, allowing for the passage and interaction of muons to be simulated through the local numerically modelled storage system properties. The voxelisation is achieved by interpolating the desired properties at the centroid of the voxels from an overlay of the finite element mesh. This means that the design requirements of the finite element mesh and of the voxelised mesh are free from one another. The properties of each voxel are constrained by the system architecture to be uniform, and the resolution/size of the voxels is computed at 10 m × 10 m × 10 m. Beyond the extent of the rendered voxels the formation property as illustrated is unchanged by CO_2 injection at that time interval.

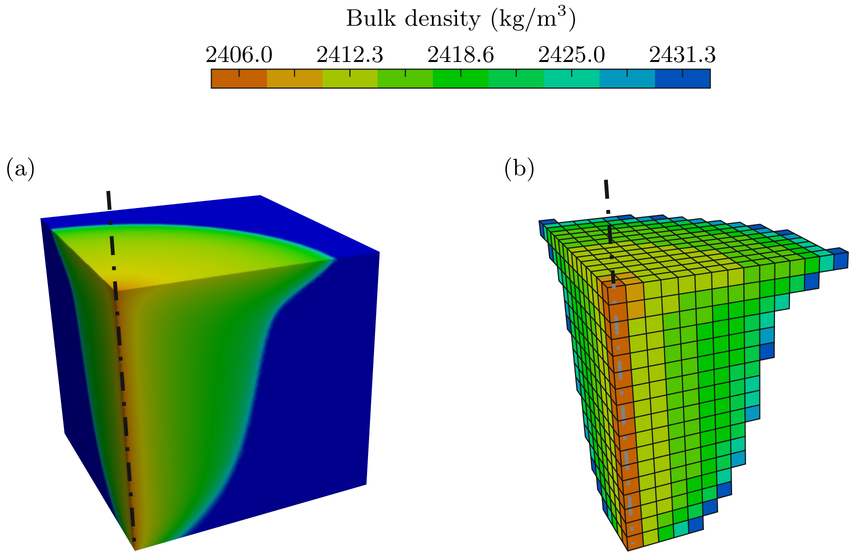

Figure 7.2: Quarter symmetric illustration of the bulk density of the storage system (a) before and (b) after voxelisation.

7.1.2 Simulation results and discussion

The simulation takes place over each of the increasingly large sequential time intervals n, through which the radial extent of the voxelised plume steps outwards uniformly. For each time interval the following simple significance statistic is taken in order to assess the effect on the muon count in the detector due to the presence of the modelled evolving CO_2 body,

$$S = \frac{N - N_0}{\sqrt{N + N_0}}, \tag{7.2}$$

where N is the number of muons which interact with the detector over the time period corresponding to the nth time interval during CO_2 injection, and N_0 is the independently sampled number of muon interactions before injection for the same length of time.

In order to highlight the validity of the numerical results in the vein of Section 6.7, with which to assess the model application with the simulation of muon radiography, the column mass density is introduced,

$$\sigma = \int \rho(z)\,\mathrm{d}z, \tag{7.3}$$

where $\rho(z)$ is the bulk mass density as a function of the column path position z. Previously, the storage system variations were presented over the radial extent of the storage system. However, the muon detector observes over discrete zenith and azimuth angular bins, which are considered in this study to be at a cellular resolution of 7° × 36° [108]. It is the change in column density along the muon paths to the detector that primarily affects the muon count within the detector. Thus, the change in the column density (7.3) over zenith paths to the detector is computed numerically from the model nodal bulk density which is first determined as of (7.1). Note that in this study the modelled change in bulk density of the storage system is due only to the displacing fluid saturation behaviour between the fluid phases given that the intrinsic fluid properties are considered constant. This bulk density change was initially indicated in the vertically averaged density profiles presented in Figures 3.3 after (3.39).

Presented in Figure 7.3(a) are the axisymmetric changes over time in the column density through the storage system over the ten 7° zenith bin paths to the detector, as given by integrating through their midpoint over the spatial domain of the numerical model at the respective time intervals. The first five n time intervals corresponding to the initial stages of injection, which exhibit the smallest changes in column density, are highlighted here for clarity. For each time interval, the outer extent of the fluid interface, as observed through the angular zenith bins, may be inferred where the plots begin to deviate from the zero density change baseline. In Figure 7.3(b), plotted for the same range of time intervals, is the corresponding significance (7.2) at the ten 7° zenith bins for a single 36° azimuth angular region, which exemplifies the resolution of the simulated muon detector. The distribution of S is seen to develop along with the movement of the CO_2 body. Note that the sensitivity of the results is also affected by the differences in length and area covered by the muon path cellular regions over which the distributed statistics are observed, which requires further study in this context.

In Figures 7.4(a & c), the distributed significance statistic S is now presented in angular bins including all the azimuth regions, this is done for the latter two time intervals considered in Figures 7.3(a & b). Therein, the results of Figure 7.3(b) are seen over the 0°–36° azimuth angular region. The distribution corresponds to the form of the inaccessible CO_2 body through which the geo-storage system bulk density has changed, indicative of the extent of CO_2 placement. Figures 7.4(a) is at $n = 4$ (49–81 days). The white circle represents the actual radial extent of

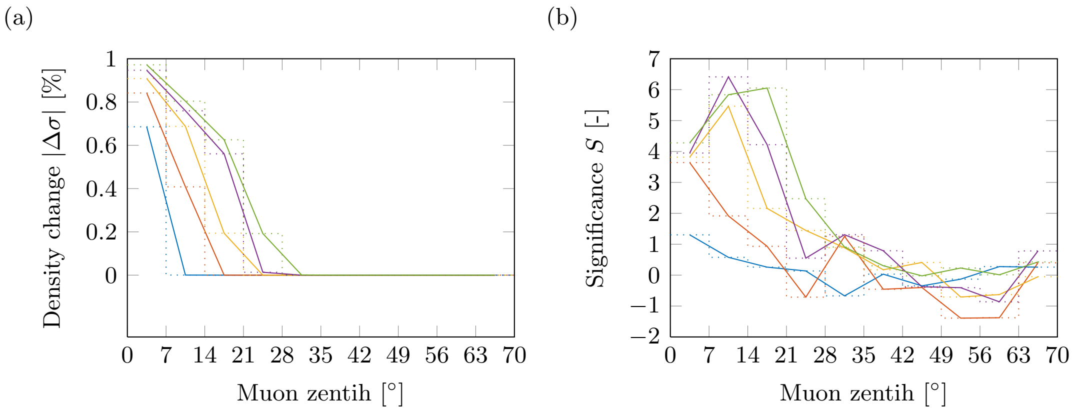

Figure 7.3: Change in the numerical model column bulk mass density (a) with the corresponding significance (b) over muon zenith and time form first injection. The time intervals are at $(2n)^2$ days, where $n = 1 \rightarrow 5$. Results are plotted at 7° zenith bin intervals (dotted lines) which are connected linearly for interpretation (solid lines).

the bulk density change (fluid interface) as calculated by the numerical model and voxelised at the corresponding 64 day radial extent midpoint, representative for the time period. The thicker transparent circle indicates what would be the region covered by the fluid interface extent as it moves over the 49–81 day period. The effect of the resolution of the voxelised model both in time and space, is a point for further study. Figure 7.4(c) illustrates the progression in the statistical significance at the next, $n = 5$ (81–121 days) time interval. The development in S between Figures 7.4(a & c) illustrates the potential to track the movement of the CO_2 body/interface using muon radiography. In Figures 7.4(b & d), the same results are presented after linear interpolation along the coordinate axes from the mid-points of the discrete angular bins.

It is demonstrated that the modelling strategy is effective and that there is a significant change in the computed muon flux which corresponds with the movement of the injected CO_2 mass. Indicating that the placed CO_2 reduces the local bulk density of the storage system such that it significantly affects the muon flux at the scales of interest. Further details and results, as well as detailed discussions on the design of the detector and the potential relative costing involved in deploying and implementing the technology in the field are given in [108].

Note that a particularly shallow formation and detector depth with respect to practical GCS scenarios is trialled in this study. This is due to the constraint of the Boulby geology and test site depth proposed for detector prototyping. A key interpretation from the results is therefore the design/redesign and performance of the detector as simulated in this model given its location and desired resolution. By carrying out this simulation, data is also available for corroborating the actual muon flux determined from a test site detector. Thus, in addition to proving the concept, the work carried out at this stage is primarily on developing and proving a modelling strategy/workflow in order to carry out an analysis of this type, envisaged with more accurate model settings in the future.

Due to the inherent unpredictability of geological storage sites, the workflow proposed is an integral component of the future use and development of this technology. This is because it will be essential to have a detailed simulation of anticipated muon flux from a (planned) model from

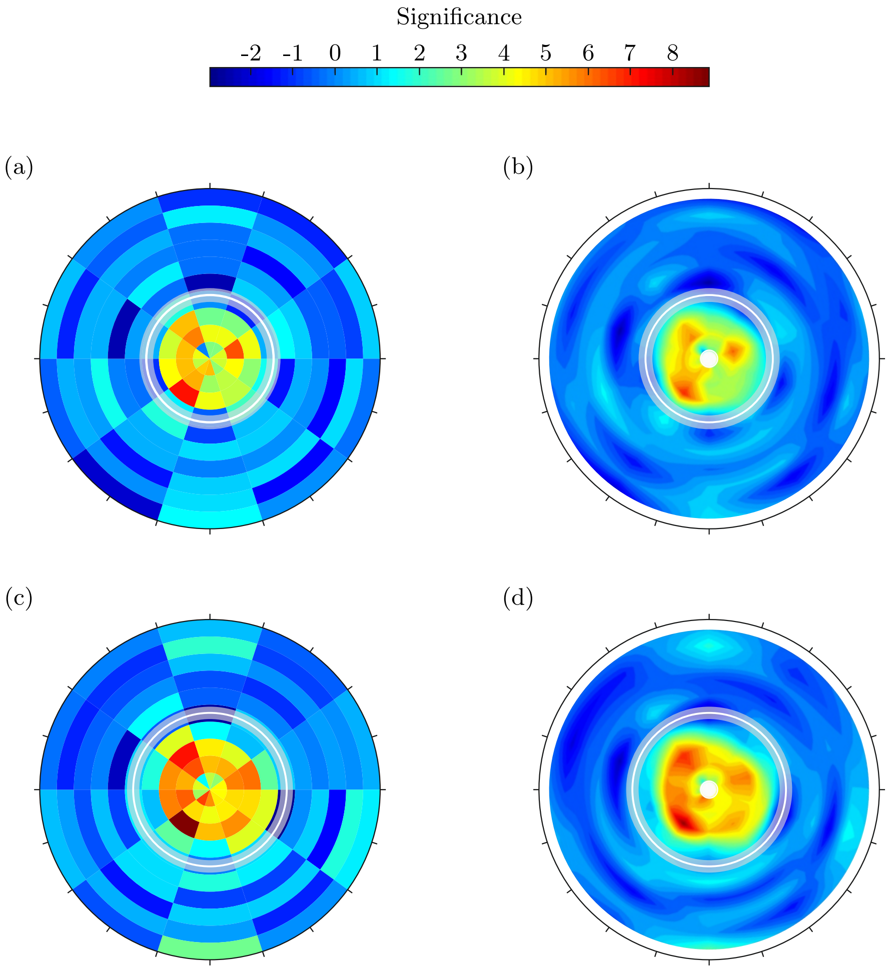

Figure 7.4: Local significance of the change in muon flux through the simulated detector, displayed both in angular bins (a) & (c), and interpolated linearly along the angular coordinates (b) & (d). The results of (a) & (b) correspond to the 49–81 days time-step, and (c) & (d) corresponds to the 81-121 days time step. The actual location of the moving radial extent of the modelled bulk density change (fluid interface) over each time step is indicated by the thick transparent circles and the solid white circle indicates the representative location during simulation of the time step. The angular bins are 7° zenith and 36° azimuth

.

which actual measured/detected results can be acted upon. This is particularly in view of any discrepancies from the modelled results, which for instance, could potentially signify adverse behaviour such as leakage through prior non-existing or undetected fractures and/or faults. As this potential complementary technology is passive and continuous, any discrepancies could be acted upon and corroborated with more intensive and detailed periodic monitoring, for instance via seismic survey, as part of a global monitoring strategy.

For a fixed effective area of muon detector, the available muon statistics decrease with depth and increase with time. The simulated depths are therefore non-conservative in this study as they are relatively shallow for the purposes of GCS. However, the mass rate of CO_2 injection and the scale of time (and correspondingly the scale of the CO_2 body) studied are conservative as they are on the relatively small end of the spectrum for what would be encountered in practice. Additionally, encouraging significance estimates for detecting at greater depths are however also possible in view of this study. Nevertheless, initial results indicate that although monitoring GCS is a demanding application for muon radiography, it is feasible for relatively shallow GCS scenarios with relatively high injected masses with the current feasible design of detector and statistical processing. Otherwise, the effective receiving area of the detector would have to increase impractically in order to provide the necessary statistics.

This muon radiography simulation process is very computationally demanding given that the muon-by-muon interactions are explicitly modelled using Monte Carlo techniques over large 3D domains. Given it also follows from discussion that a screening method for GCS sites with potential for muon radiography is desirable, a faster complementary method for assessing this technology is sought. The first study of this type is given in the co-authored work of [23]. This Research involves a simplified muon propagation model based on the underlying probabilities within the system for determining the muon flux for a given geological setting. To this end, methods on optimally interpreting the low-contrast muon data are also developed.

7.2 Site screening of muon radiography for a real-world scenario

Site screening metrics for potential responses in the muon flux through a site are desirable given the considerable number of potential storage sites and the demands on time and computation in generating high-resolution models of the geology, fluid flow processes, and muon transport/interaction. In this section a simplified thought efficient method of computing subsurface muon statistics is adopted and applied to a real-world CCS storage scenario.

After [23], the following expression is stated giving an approximated muon flux arriving from a given direction (or ray-path) m of the subsurface to a detector region,

$$J_m = G_\mu(\theta_m)\ \Xi(z_m, \theta_m), \tag{7.4}$$

where $G_\mu(\theta_m)$ is the surface flux determined via integration over the muon energy spectrum of the differential muon intensity at surface level as given by the Gaisser parametrisation for high-energy muons [66] (Section 2.11.2 and (2.66)), and is therefore the surface level mean muon count rate per unit area per unit solid angle, as a function of the muon arrival zenith angle θ_m. The function $\Xi(z_m, \theta_m)$ is the survival probability of a random muon reaching the distance z_m through the subsurface at θ_m. The survival function within expression (7.4) thus modifies the theoretical flux from that at the surface to that at a subsurface (detector) region, at a given distance z_m through the zenith θ_m. The survival probability function is determined statistically in advance representative of a standardised rock material with a bulk density ρ_0 of 2650 kg/m^3 [23, 113]. The function presents a quasi-exponentially decreasing relationship of survival probability with increasing penetration depth at each zenith for a randomly selected cosmic-ray muon. The functions G_μ and Ξ are determined from the same muon energy distribution, where the statistics ignore low energy muons (<100 GeV), as a results the functions are only valid for depths greater than a few hundred metres. Note that in Section 7.1.1 the extent of the muon survival and penetration due to interaction within the subsurface was modelled explicitly on a muon-by-muon basis.

A change in muon survival probability is assumed to be due principally to a change in the amount of bulk material encountered. Material elemental composition is also a secondary factor which is ignored here, this simplification is considered appropriate for the proposes of site screening. Based on this assumption the key approximation is made whereby an effective distance $\tilde{z}$ is computed by integrating along a muon ray-path; the density encountered relative to the reference density ρ_0 for which the survival probabilities are predetermined,

$$\tilde{z}_m = \int_{z_{\mathrm{suf}}}^{z_{\mathrm{det}}} \frac{\rho(z_m)}{\rho_0} \, \mathrm{d}z. \tag{7.5}$$

A change in effective distance along a ray-path due to changes in bulk density along that path thus updates the survival probability, whereby a reduction in the ray-path bulk column density reduces the integrated effective distance and hence increases the survival probability of the muons. This ray-tracing procedure [23] is carried out rapidly for a given spatially discretised domain of evolving bulk density in order to produce $\tilde{z}_m$ over time for a region of paths to a detector for computation in (7.4).

7.2.1 Real-world CO_2 geo-storage model

The modelling approach based on the underlying muon survival statistics is applied to a real ongoing GCS scenario, this is done for examination as well as for potential screening ahead of more computationally expensive explicit muon-by-muon simulations in view of accurately predicting potential CO_2 storage/detector behaviour for detector design and instrumentation.

The site selected is the Norwegian North Sea CCS Sleipner project where storage takes place in the Utsira marine brine/sandstone dominated formation. The formation is overlay by Nordland shale which acts as a seal aiding CO_2 storage. This is the first commercial scale project beginning injection in 1996 storing approximately 1 Mtpa of CO_2. This has been a successful research and development project prompting scientific information on site performance and the availability of corresponding (real-world) model data. It is therefore a natural selection for further study on the application of muon radiography.

The local geological structure of the central region where CO_2 is being stored within the sandstone formation is plotted in Figure 7.5, after the geo-cellular data of [175]. This highlights the depth, location and extent of the region. The depth axis is scaled by a factor of 20 relative to the horizontal axes in order to visually amplify the structure of the geological body which is important for understanding the main flow/storage behaviour within the region. The geo-cellular data is particularly accurate at a resolution of 50 m × 50 m × 1 m. The layer is overlay by a low permeability shale such that the top surface is considered impermeable. The spatial model data available is that of the uppermost layer of the Utsira formation where the CO_2, due to its buoyancy, collects and spills under the shale/sandstone interface. CO_2 injection occurs along a 38 m deviated well interval at a depth of 1012 m, which is at the base of the Utsira formation, the CO_2 enters the modelled region (Figure 7.5) from below in the centre.

The rock parametrisations are discussed and listed in [175]. In particular, the measured sandstone porosity varies in the range of 0.35 to 0.36 with a residual brine saturation of 0.11, and

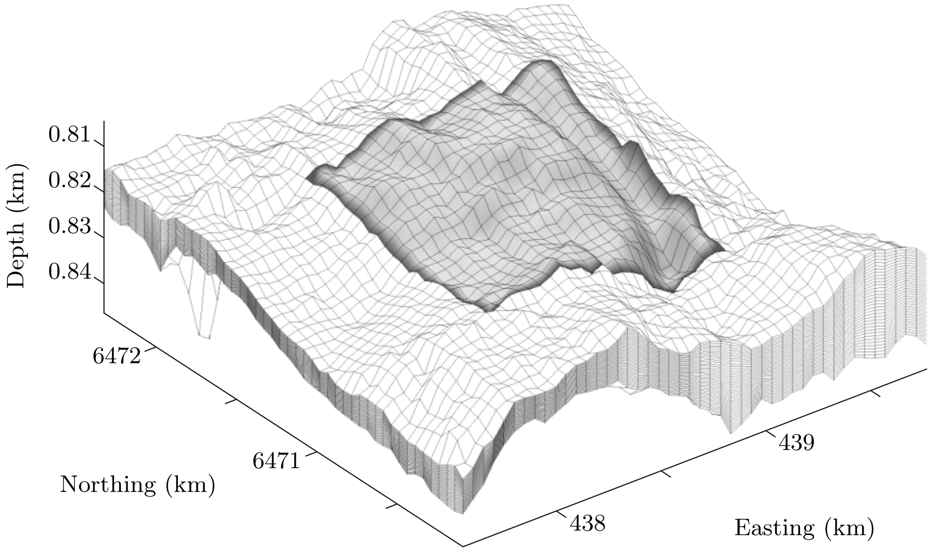

Figure 7.5: Local geological model of the Utsira formation top layer involved in the Sleipner project. Muon ray-trace modelling takes place through the central shaded region. The vertical dimension is scaled by a factor of 20 to highlight the topography of the shale/sandstone interface.

the permeability in the [x, y, z] orthogonal directions is respectively in the range of [1.7, 1.7, 0.48]$\times 10^{-12}$ m^2 to [2.0, 2.0, 0.57]$\times 10^{-12}$ m^2. In order to compute the bulk density variation over the entire geological site, from a potential detector location to sea level, the rock grain density is taken as 2670 kg/m^2 with the seabed at 110 m uniformly below sea level.

Taking a reference depth of 820 m with a hydrostatic gradient of 10.5 MPa/km and a thermal gradient of 35.6°C/km with 7°C at the seabed, gives a brine to CO_2 density contrast of 1110 kg/m^3 to 693 kg/m^3 and a contrast in viscosity of 1040 µPa·s to 55 µPa·s respectively, determined as of Section 6.1. Assuming the fluid properties remain constant, the CO_2 on displacing the brine to residual saturation within this region of relatively high porosity gives a favourable bulk density change in the order of 6%. However, the upper layer region of the Utsira site modelled in isolation is particularly challenging for the application of muon radiography given that the CO_2, on entering the modelled region, spills as a relatively thin layer at several metres of thickness along the shale/sandstone interface. Thus the change in column density, which is required for detection by way altering the muon statistics, occurs over only several metres in this case.

To model injected CO_2 migration and brine displacement, and the corresponding changes in system bulk density, the usual governing equations are employed in their simplest necessary form due to the complexity of the geological model. This form is that of a two phase immiscible incompressible isothermal flow problem. To achieve this, open-source routines developed by [112], promoting existing benchmark models of the Utsira storage formation, are employed in order to capture and process the 3D geo-cellular data in particular. In co-action with the developments of this work it presents a modelling environment for prototyping bespoke subsurface flow modelling of this sort where real geological data is of concern. In solving the system of governing equations, realistic injection rates are prescribed with the assumption of far-field hydrostatic boundary conditions.

7.2.2 Model screening results and discussion

In Figure 7.6 the modelled migration of CO_2 along the shale/sandstone interface within the geological region is depicted at yearly intervals for the first 4 years of injection. The injection rate is relatively low given the geological extents of the entire formation, and once the injected CO_2 reaches the modelled region from the centre, its movement is primarily gravity-driven demonstrating strong phase segregation, and thus its movement is highly sensitive to the interface topology. This is indicated by the extent and shape of the CO_2 plume with respect to the contour lines plotted in grey. Figure 7.5 observes the geological model from the south-west, where the topology of the upper impermeable shale/sandstone interface is seen to elevate northwards out into distinct channels. This explains the dominant northwards migration and forking of the buoyant CO_2 plume giving the isolated flow paths as it rises through the brine while in contact with the interface. Hence the geological structure (or contours) encompass the CO_2 plume/body where it has become trapped, which is a key occurrence for long-term managed storage. Note that long-term migration modelling of the Sleipner project indicates that a large structural trap is encountered further northwards. The plume behaviour, as modelled, is also substantiated by seismic monitoring data [175] which similarly outlines the plume positioning as is illustrated and described.

At each yearly point the muon flux is calculated at a theoretical detector, which is located at a trial vertical depth of 1020 m centred horizontally in line with the modelled domain. To do so, ray-paths from the detector are back-projected to sea level within a 70° zenith scope along the orthogonal directions, such that a trialled 20×20 m-pixelated horizontal surface is generated through which muon flux calculations are performed. This surface back-projects through the shaded region of Figure 7.5 and the region within the red squares of Figure 7.6. The area A_m of each pixel may be used to determine a subtended solid angle $\Omega_m = \cos(\theta_m) A_m / z_m^2$, from which a muon count rate per unit area of detector through each pixel can be calculated, thus

$$\Phi_m = J_m \Omega_m = G_\mu(\theta_m)\ \Xi(\tilde{z}_m, \theta_m)\ \Omega(z_m, \theta_m), \tag{7.6}$$

where the survival probability is now a function of the effective distance $\tilde{z}_m$. This operation is performed at all projected pixels through their ray-path to the detector at the 4 yearly points in time over which the effective distances, after (7.5), evolve due to the movement of CO_2 and brine. The relative change in muon flux from the flux post-injection at the 4 yearly time points are shown in Figure 7.6 alongside the corresponding modelled fluid migration. Note how the predicted muon flux responds to the migration and extent of the injected CO_2 plume, along the ray-paths.

In order to assess the detectability of the changes in muon flux, a time duration to achieve a statistically significant change in muon count is given by rearranging (7.2) to give

$$t = \left[\frac{S \cdot \sqrt{\Phi + \Phi_0}}{\sqrt{a} \cdot (\Phi - \Phi_0)} \right]^2, \tag{7.7}$$

where S are the statistical standard deviations and a is the area of the detector, note that the

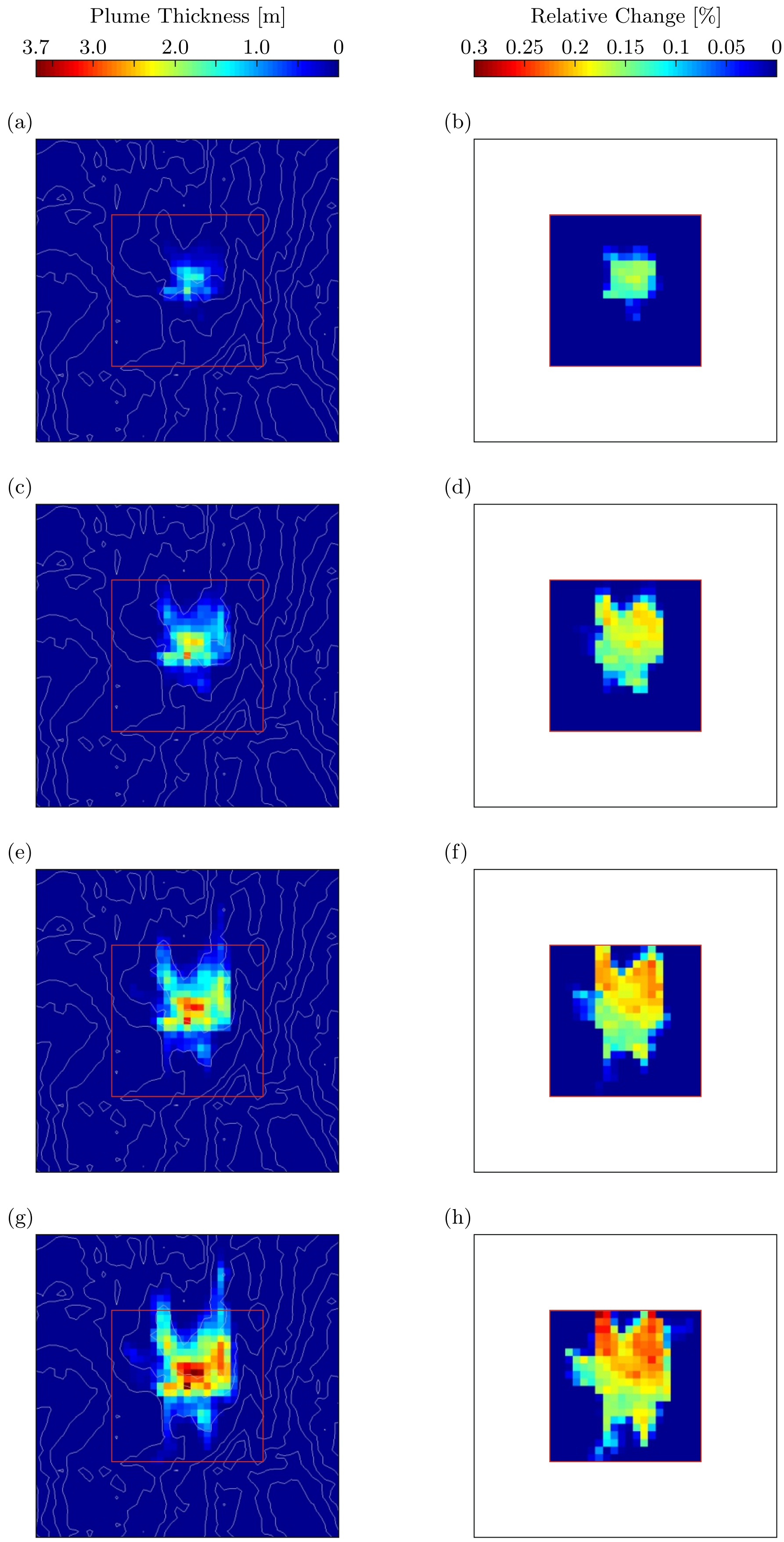

Figure 7.6: (a), (c), (e) & (g) depict the computed vertical thickness and extent of the CO_2 at yearly intervals since the start of injection. (b), (d), (f) & (h) depict the corresponding relative changes in muon flux at that time from the flux pre-injection.

number of muon events is $N = \Phi \cdot a \cdot t$. Considering a statistically reliable significance of $S = 3$ and a detector area of 1000 m^2 [108, 114], the results of Table 7.2 are produced based on the total muon flux to the detector for the studied site.

Table 7.2: Changes in total muon flux during CO_2 injection.

Time of injection T [year]	Total Muon Flux Φ [$\text{m}^{-2}\text{days}^{-1}$]	Time for statistical significance t [days]
0	145.068	-
1	145.198	155
2	145.270	64
3	145.292	52
4	145.314	43

The predicted time values of Table 7.2 required for detecting the changes in total flux for this scenario are reasonable after the first year with respect to the rate at which the plume evolves globally on a yearly basis. However by assessing the total flux any localised plume features are ignored. That is, the statistics will become overly challenging when resolving over distinct detector angular/pixelated observation regions. This is both in terms of the relatively low changes in muon flux over time for this site/scenario and more generally in terms of achieving useful angular resolutions in practice, which is ongoing research in muon borehole detector design [108, 114]. Nevertheless, the outlined workflow presents a useful method for potential site screening and optimally locating and configuring (multiple) potential muon detectors. Additionally, simple methods have been employed in this study for data analysis, utilising information theory based methods would improve the analysis of the available data [23].

For thin horizontal CO_2 plume regions in particular, the periods of time required to acquire the necessary statistics in order to reliably determine plume positioning are likely to be too great if the plume is particularly mobile. However, once such a plume has become immobile within a large structural geological trap, by design it is to remain there for geological periods, which will present enough time for the relevant statistics to be gathered to monitor and ensure that long-term structural trapping is occurring. This prompts muon radiography as a potential long-term passive monitoring strategy component to indicate if and how structural traps post-injection phase are retaining even potentially thin CO_2 plumes once they have become immobile.

7.3 Evaluation

A landmark is made in the development of muon radiography for monitoring GCS, in that a modelling framework is developed which allows for the complete multifaceted simulation of the proposed technology as it would operate in the field. From this framework the first detailed simulations of muon radiography for monitoring geo-stored CO_2 is carried out and assessed for realistic scenarios. The results indicate that muon radiography is sensitive to subsurface CO_2 injection and movement on the scales of interest, demonstrating the conceptual viability of the technology for GCS. In this thesis it is the fluid flow modelling in view of this application and key components to the multifaceted modelling strategy which are developed, as is discussed. The simulations involve realistic calibration in terms of geological data, CO_2-brine fluid flow behaviour, muon radiography and muon detector configuration, though as is discussed various idealisations are assumed for the purposes of study and development at this stage.

The technology is demonstrated to be conceptually viable, however GCS is a demanding application for muon radiography. Initial study indicates that only shallow storage systems at depths of approximately 1 km with deep injection layers are feasible for this technology given the otherwise adverse muon statistics with increased depth and reduced plume height. As such, this technology may be envisaged as a low-resolution passive-continuous monitoring aid as part of a monitoring strategy with other techniques. The potential use of this technology will also depend largely on the practicality/relative cost of deploying and instrumenting a muon detector subsurface in the field. Initial estimates indicate that the use of modified existing wells and multilateral sidetrack drilling technology is feasible and the costs involved are potentially favourable in comparison with established alternative monitoring technologies.

The angular scope of a muon detector is demonstrated to cover a region of approximately a square kilometre. Given the significant long-term lateral extent of realistic CO_2 plumes which may be over several square kilometres, multiple detectors may be required as part of a monitoring strategy in order to capture the entire movement of the plume. Furthermore, multiple detectors which collect information from overlapping subsurface regions would allow for the additional re-construction of a 3D tomographic images of the bulk density variations via triangulation of the muon statistics.

Further study may also consider other monitoring applications for muon radiography, which are of particular concern for reasons of safety, understanding and/or effectiveness. Speculatively, application such as monitoring the extent of hydraulic fracturing and the ensuing enhanced hydrocarbon recovery, the monitoring of inaccessible glacial/ice shelf melting, the movement of large contaminated regions of groundwater including leachate, as well as monitoring for the purposes of mining and subsurface tunnelling and/or excavation works.

Furthermore, it is envisaged from this work that various monitoring technologies could be simulated within the same framework (coupled and/or uncoupled with the storage system model) including for instance muon radiography, electrokinetics, and seismology. From this a series of detection resolutions and attributes could be ascertained in order to compare, contrast and combine in order to determine an optimal monitoring strategy for a given storage scenario. As such, this may operate as part of a larger framework in order that a holistic approach is taken in terms of the engineered storage and monitoring design, in that it may be optimised in terms of the complete enviro-socio-economic cost-benefits involved.

Chapter 8

Conclusions & Further Work

8.1 Conclusions

In this work, an in-house research-code framework is developed for modelling fully coupled geological scale HTM multiphase processes in deformable fractured porous media with the additional modelling of muon radiography. This is carried out as part of a multi-disciplinary project on the governance, monitoring and modelling of geological carbon storage in view of recent CCS initiatives.

The framework developed essentially operates as a toolkit, offering computational reach for the study and development of both the physical and numerical aspects of the coupled system modelled, in addition to its application. As such, aspects of the framework, its formulations and methodologies may be incorporated with other research and/or numerical codes. As well as offering alternative numerical methods, the findings of this thesis are also in essence to highlight the coupled nature of GCS systems. This is particularly for developing GCS monitoring techniques, and to help indicate when the effect of storage system couplings are important during engineering decision making processes.

The following key observations are made which have further engineering implications, which also corroborate and expand up on existing studies.

- The fully coupled HTM double-porosity model formulation and its implementation performed well in the verification and validation studies. The numerical solutions match the analytical versions as expected for all the benchmark hydraulic, thermal and mechanical scenarios. To achieve this the numerical model is appropriately simplified/parametrised, as is discussed in detail, in order to enact the simplified analytical solutions. On enabling/parametrising the further sophistications of the numerical model, the solutions followed expected trends in respect of the additional phenomena being accounted for. As such, the enacted analytical model solutions may be viewed as special or uncoupled cases. This also demonstrates the physical relaxations made when using simplified models and their appropriateness in comparison with fully coupled models. Particularly sensitive relaxations which should be considered when employing simplified/analytical models are potential coupled double-porosity effects, deformation effects in relatively high pressured and compressible formations, thermal effects in low pressured (depleted) formations, and any fluid phase saturation behaviour if a high resolution model is required.

- This work demonstrates the effectiveness of a fully coupled non-isothermal multiphase Biot-type double-porosity modelling formulation implemented with the finite element method and with a specifically devised adaptive control theoretical accelerated nonlinear solver. These discretisation methods are advocated given the complexity of the full system of equations and the need to refine and/or adapt the spatial and temporal discretisations as a result of this complexity.

- The performance of the additionally coupled aspects have a significant effect on the response of the storage system, however they are in general very site specific. Therefore when implementing similar models it is important to be clear on what phenomena and outcome it is necessary to assess given the site to be modelled. Especially given the additional complexities and computational expense in solving fully coupled formulations.

- Coupling the mechanical behaviour demonstrates that there is appreciable storage formation deformation in the order of several millimetres with which the coupled pore fluid pressures are particularly sensitive. Indicating potential for seismicity, fracturing and fault/fracture reactivation. A progressive reduction in the stiffness of the formation progressively reduces the necessary pore fluid pressures, along with additional site deformation. The manner in which the formation deforms is also indicative of the pressure and fluid phase distributions. These effects are most prominent for shallow and warm formations, where reductions in pressure due to coupled solid deformation are in the order of 5–10%.

- Incorporating a pervading fissure/fracture network as an additionally coupled hydraulic sub-domain within the porous system alters and limits key HTM storage system behaviour considerably. In particular, this significantly alters the pore pressure and fluid phase distributions and hence the deformation of the formation. During injection the low porosity high permeabiltiy fracture network is demonstrated to become readily occupied by the CO_2 and globally controls fluid migration within the system. This amplifies the radial outreach and buoyancy migration of the free-phase CO_2, compared to an equivalent single-porosity system. Relatedly, free-phase CO_2 movement in the more abundant surrounding matrix pore space for efficient and more manageable structural storage becomes more restricted. This is particularly important when considering the potential extent and integrity of site specific structural trapping mechanisms. As it could mean that the injected volume extends out uncontrolled primarily in the low volume fracture space in a manner without transferring to the porous matrix space, which is difficult to predict and monitor. This restriction and the general system performance is particularly sensitive to the fracture geometry and permeability parametrisations.

- The double-porosity system however potentially enhances dissolution and mineral trapping due to the increased contact area between the free-phases at the fracture/matrix interface.

This interface will present a high concentration gradient where CO_2 diffusion will take place promoting more definitive dissolution and mineral trapping within the matrix pore space blocks. This advantage should however be balanced with the previous point on the potential reduced structural trapping performance. Implementing double-porosity models simulating long-term storage will become inaccurate if they ignore this dissolution process, thereby overestimating the mass of CO_2 present in the fracture network space and underestimating the entire long-term storage performance of the site. Modelled and managed correctly double-porosity systems are a potential asset of particular importance for CO_2 storage.

- In this work the lag between free-phase movements between the fracture/matrix subdomains is addressed in conjunction with the coupled pore pressure evolution and site deformation. The extent of the CO_2 free-phase interface in the matrix pore space is demonstrated to lag at approximately 25% of the extent within the fracture network space. This result is decreased further on lowering the matrix permeability and the degree of fracturing. In a double-porosity system the porous matrix regions which are demonstrated to become more readily occupied by the injected CO_2 are those within the vicinity of the injection well and along impermeable boundaries. In between, the free-phase CO_2 passes readily through the fracture network with little transfer to the porous matrix space, given realist parameterisation.

- Coupling the thermal behaviour is particularly important for low pressured storage formations with high pressure gradients. This is given the significant reduction in temperature which can occur along these gradients due to the expansive cooling of the injected CO_2. Additionally coupling the mechanical response demonstrates that the deformation of the formation is responsive to reductions in temperature due to this cooling effect, where the uplift of the formation due to the pressure evolution is partially offset by the coupled thermal evolution. This could have engineering implications for monitoring purposes and for controlling solid stress states. The offset in uplift due to cooling is however demonstrated to be almost an order of magnitude less than the overall deformation. Although large deformation offsets could be indicative of excessive formation cooling. On pervading the formation with a fracture network, thereby creating a double-porosity system, the temperature reduction, deformation and offset effects are significantly diminished. This is due particularly to the reduced pressure gradient which is controlled by the higher permeability of the fracture network.

- It is demonstrated that the extent of appropriateness in employing various system couplings depends on the storage scenario under consideration and on the information desired.

- In this thesis a fully coupled numerical model is applied in increasing complexity where various numerical terms are explicitly coupled and uncoupled in order to highlight various phenomena. This may be heeded by engineers implementing GCS models so they may be aware of the exact physical and numerical inclusions and omissions being made. This is typically obscured within the literature when applying existing numerical models to new scientific scenarios.

- Extending the usual Euler backward implicit time-stepping scheme with control theory by computing an additionally embedded solution of adjacent order to efficiently adapt the time-stepping is effective for modelling coupled GCS scenarios. This approach also indicates to the modeller the local truncation errors involved during time-stepping which may be of importance given the low order of the discretisation scheme. By controlling the time-stepping it also pre-emptively aids the nonlinear solver, as it is constrained from attempting computation over excessively large time-steps.

- As an alternative to employing a Newton-type method for solving the complex coupled nonlinear systems, an accelerated fixed-point-type procedure is employed. This improves convergence over a standard fixed-point procedure by processing optimised linear combinations of previous iteration vector sequences. This scheme is demonstrated to be effective for modelling coupled multi-physics multiphase GCS/injection scenarios. Embedded control theoretical data may also be used to enhance the convergence of this acceleration method. The control/acceleration algorithm developed in this thesis demonstrated an overall improvement in computational efficiency of over 30% in terms of reduced number of required calls to the linear solver, compared to un-accelerated cases for the types of systems modelled in this thesis. The extent of this improvement is dependent on the coupled system employed and the balance of the selected numerical tolerances and control parameters. The approach developed is most applicable for large complex nonlinear system arrays which are difficult/expensive to linearise via Newton-type methods.

- In the literature extensive studies have been carried out on the interrelation between various modelling and monitoring processes for GCS. This thesis studies novel interrelationships for the muographic monitoring of GCS. The workflow developed to achieve this has the advantaged that it allows for any other models, results or measurements of subsurface processes to be implemented. This is essentially because the muon radiographic processes and the subsurface modelling processes are uncoupled on the scales of interest, such that they may be modelled sequentially.

- The Boulby CO_2 storage test model presents a scenario with a feasible but relatively low mass injection rate per unit height of well. This is a vertical well, located within a region assumed axially symmetric directly beneath an impermeable flat mudstone/sandstone horizontal layer. The characteristics of the CO_2 plume in this site are ones of significant buoyancy with horizontal migration along an impermeable seal. One year of constant CO_2 injection at 20 kg/s CO_2, stores approximately 0.63 Mt of CO_2 within a radial extent of 360 m form the injection well which has a height of 170 m. During this injection period the column density changes through the storage system to the detector, located at a depth of 776 m, are in the order of $\lesssim 1\%$. These changes are seen to be resolved statistically at a feasible angular resolution in under approximately 50 days of injection/monitoring. This is however only achieved over the angular regions to the detector which correspond to the core location of CO_2 plume, where the thinner outer interface regions appear largely undetected. This highlights the current feasible resolution conceivable with this technology and what it quantitatively can achieve during the initial injection stages of GCS.

- The top layer of the Sleipner CO_2 storage test model presents a challenging scenario where an especially thin layer of $CO_2 \lesssim 4$ m migrates under an assumed impermeable shale/sandstone layer with a complex topography consisting of various flow channels. This presents a challenge for the application of muon radiography for monitoring purposes. A screening procedure is adopted in order to asses the relative changes in muon flux though designated back projected pixel regions. This gives indication of where relative flux changes will occur for this site, in practice the time required for a feasible sized borehole detector to resolve these changes with statistical significance demonstrates the application to be overly demanding. However when assessing the total muon flux it is resolvable in approximately 50 days after two years of injection once the plume has reached a more substantial size.
- Monitoring GCS is a challenging application for muon radiography. This study demonstrates feasibility for relatively shallow storage formations at depths of approximately 1 km with relatively deep injection layers. This is due to the significant reduction in the muon statistics over time with detector depth and small contrasts in column bulk density. However, immobile plume regions, potentially within structural traps, will remain in place by design for geological periods which will present enough time for the relevant muon statistics to be gathered to ensure that immobile structural trapping is occurring. Given the extent of realistic CO_2 plumes, multiple detectors may also be required in order to cover the long-term lateral extents of CO_2 migration.

8.2 Further work

The conclusions drawn are evidence for the importance in considering coupled hydro-thermo-mechanical behaviour when modelling GCS systems. The numerical methods and modelling methodologies developed may also be adopted and extended extensively for further research studies.

Further work would extend naturally in the way of 3D spatial discretisation encompassing all coupled phenomena which would allow for the modelling of real-world storage scenarios. This is an interesting prospect given that spatially accurate GCS system data is becoming widely available for the interests of scientific research. Parallel areas of research on the miscible/chemical behaviour of the phases may also be incorporated by allowing for the extra degrees of freedom accounting for species component mass fractions within the phases at the formulation stage, this is discussed as being of particular importance for double-porosity systems. The aspect of phase miscibility and component reactivity is further facilitated by the existing hydro-thermal framework bases. Additionally, the variability of the system parameters could be studied further in response to the HTM processes, particularly the thermophysical fluid properties, as well as variability in porosity, permeability, and residual saturation.

Further to modelling an exiting pervading fissure/fracture network within a partially saturated porous medium, is addressing coupled fracture initiation, propagation and dynamics due to combined mechanical hydraulic and thermal effects and loads. This would generally have application outside of GCS, with particular application to hydraulic fracturing (for the release of hydrocarbons) and the dynamics of fractures and faults. In order to capture this phenomena explicitly, advanced adaptive discretisation techniques would be required in view potentially of interface element, partition-of-unity, and spline/isogeometric techniques.

Further development for the control/acceleration algorithm should be on the interrelatedness of the spatial discretisation, further optimisation via convergence rate control, and the importance of the individual coupled sub-vector sequences, as well as harnessing information from previous time-step iteration sequences. Additionally, there is also scope to partition the full discretised system of equations and stagger the temporal integration. This would follow further investigation on the strength of coupling between all the HTM processes. Comparative studies may also be conducted to assess the cost-benefit of this numerical approach with numerical differentiation and algorithmic/automatic differentiation techniques. This would be to understand how they may be incorporated, and for which scenarios each may be optimally employed.

Given the large number of numerical and physical parameters inherent in the model, further parametric studies and sensitivity analyses would be beneficial in order to understand their relative importance. This should be carried out with further verification and validation scenarios, moving towards more realistic GCS site selection in particular.

With a valid modelling/monitoring methodology and framework in place, a natural extension for further work is on more representative physical modelling of GCS systems with which to further assess the effect on subsurface muon flux. As such, spatially complex 3D storage models may be employed further within the framework, potentially involving observed and/or computed real-world CO_2 geo-storage data. From such studies, the extent to which localised storage features can be interpreted or inferred, such as faults, fractures, channels and traps, may also be assessed. It is also of interest to account for the effect of density and compositional changes on muon flux due to excessive sub-critical compression/expansion of the fluids and the miscibility and chemical reactivity of the phases. This is particularly with respect to the long-term storage and monitoring of the plume once it has become idle after injection, where the acquisition of more muon data will also be achievable. Additionally, in line with the ethos of the efficient simplified muon flux screening approach, multiple speculative GCS scenarios could be assessed in batch via simplified (semi-)analytical models in order to understand the global possibilities and impact of muographic monitoring.

In this work a single detector array is considered for monitoring purposes, whereby changes in the line-of-sight muon flux over an angular distribution are used to interpret the movement of the CO_2 body. Future studies would include also the simulation of multiple muon detector arrays located at various points beneath the GCS system. This would allow for the additional re-construction of a 3D tomographic image of the density and composition variations via triangulation of the muon statistics. The study of multiple detector arrays is also necessitated for this technology given that long-term storage scenarios would need to be monitored over greater lateral extents than is achievable with a single detector array.

References

[1] S. Agostinelli and Others. GEANT4—a simulation toolkit. *Nuclear Instruments and Methods in Physics Research Section A: Accelerators, Spectrometers, Detectors and Associated Equipment*, 506:250–303, 2003.

[2] J. Ahrens, B. Geveci, and C. Law. *ParaView: An End-User Tool for Large Data Visualization.* Elsevier, 2005.

[3] E.C. Aifantis. Introducing a multi-porous medium. *Developments in Mechanics*, 8:209–211, 1977.

[4] A.K. Al-Hadhrami, L. Elliott, and D.B. Ingham. A New Model for Viscous Dissipation in Porous Media Across a Range of Permeability Values. *Transport in Porous Media*, 53: 117–122, 2003.

[5] R. Al-Khoury and L.J. Sluys. A computational model for fracturing porous media. *International Journal for Numerical Methods in Engineering*, 70:423–444, 2007.

[6] J. Alberty, C. Carstensen, and S.A. Funken. Remarks around 50 lines of Matlab: short finite element implementation. *Numerical Algorithms*, 20:117–137, 1999.

[7] A.A. Aleksandrov, E.V. Dzhuraeva, and V.F. Utenkov. Viscosity of Aqueous Solutions of Sodium Chloride. *High Temperature*, 50:354–358, 2012.

[8] A.A. Aleksandrov, E.V. Dzhuraeva, and V.F. Utenkov. Thermal Conductivity of Sodium Chloride Aqueous Solutions. *Thermal Engineering*, 60:190–194, 2013.

[9] J. Allison and Others. GEANT4 Developments and Applications. *IEEE Transaction on Nuclear Science*, 53:270–278, 2006.

[10] L.W. Alvarez, J.A. Anderson, F. El-Bedwei, J. Burkhard, A. Fakhry, A. Girgis, A. Goneid, F. Hassan, D. Iverson, G. Lynch, Z. Miligy, A.H. Moussa, M. Sharkawi, and L. Yazolino. Search for Hidden Chambers in the Pyramids. *Science*, 167:832–839, 1970.

[11] D.G. Anderson. Iterative Procedures for Nonlinear Integral Equations. *Journal of the Association for Computing Machinery*, 12:547–560, 1965.

[12] H. Askes. *Advanced spatial discretisation strategies for localised failure: Mesh adaptivity and meshless methods.* PhD thesis, Delft University of Technology, 2000.

[13] U. Ayachit. *The ParaView Guide: A Parallel Visualization Application.* Kitware, 2015.

[14] S. Bachu, W.D. Gunter, and E.H. Perkins. Aquifer Disposal of CO_2: Hydrodynamic and Mineral Trapping. *Energy Conversion and Management*, 35:269–279, 1994.

[15] O.R. Barani, A.R. Khoei, and M. Mofid. Modeling of cohesive crack growth in partially saturated porous media; a study on the permeability of cohesive fracture. *International Journal of Fracture*, 167:15–31, 2011.

[16] G.I. Barenblatt. The mathematical theory of equilibrium cracks in brittle fracture. *Advances in Applied Mechanics*, 7:55–129, 1962.

[17] G.I. Barenblatt, I.P. Zheltov, and I.N. Kochina. Basic Concepts in the Theory of Seepage of Homogeneous Liguids in Fissured Rocks (Strata). *Journal of Applied Mathematics and Mechanics, USSR*, 24:1286–1303, 1960.

[18] K.-J. Bathe. *Finite Element Procedures.* Prentice Hall, 1995.

[19] D. Baù, B.M. Cody, and A. González-Nicolás. An iterative global pressure solution for the semi-analytical simulation of geological carbon sequestration. *Computational Geosciences*, 19:781–789, 2015.

[20] I.H. Bell, J. Wronski, S. Quoilin, and V. Lemort. Pure and Pseudo-pure Fluid Thermophysical Property Evaluation and the Open-Source Thermophysical Property Library CoolProp. *Industrial & Engineering Chemistry Research*, 53:2498–2508, 2014.

[21] S.M. Benson and D.R. Cole. CO_2 Sequestration in Deep Sedimentary Formations. *Elements*, 4:325–331, 2008.

[22] S.M. Benson and P. Cook. Underground geological storage. In *IPCC Special Report on Carbon dioxide Capture and Storage*, chapter 5, pages 195–276. 2005.

[23] C.J. Benton, C.N. Mitchell, M. Coleman, S.M. Paling, D.L. Lincoln, L. Thompson, J. Klinger, S.J. Telfer, S.J. Clark, and J.G. Gluyas. Optimizing geophysical muon radiography using information theory. *Geophysical Journal International*, (in preparation).

[24] S. Berg and H. Ott. Stability of CO_2-brine immiscible displacement. *International Journal of Greenhouse Gas Control*, 11:188–203, 2012.

[25] S. Berg, S. Oedai, and H. Ott. Displacement and mass transfer between saturated and unsaturated CO_2-brine systems in sandstone. *International Journal of Greenhouse Gas Control*, 2011.

[26] M.A. Biot. General Theory of Three-Dimensional Consolidation. *Journal of Applied Physics*, 12:155–164, 1941.

[27] M.A. Biot and D.G. Willis. The Elastic Coefficients of the Theory of Consolidation. *Journal of Applied Mechanics*, pages 594–601, 1957.

[28] R.B. Bird, W.E. Stewart, and E.N. Lightfoot. *Transport Phenomena.* John Wiley & Sons, 2nd edition, 2002.

[29] R.C. Bissell, D.W. Vasco, M Atbi, M Hamdani, M Okwelegbe, and M.H. Goldwater. A Full Field Simulation of the In Salah Gas Production and CO_2 Storage Project Using a Coupled Geo-mechanical and Thermal Fluid Flow Simulator. *Energy Procedia*, 4:3290–3297, 2011.

[30] T.A. Boden, G. Marland, and R.J. Andres. *Global, Regional, and National Fossil-Fuel CO_2 Emissions.* Carbon Dioxide Information Analysis Center, Oak Ridge National Laboratory, U.S. Department of Energy, Oak Ridge, Tenn., U.S.A, 2015.

[31] J.R. Booker. The Consolidation of a Finite Layer Subject to Surface Loading. *International Journal of Solids and Structures*, 10:1053–1065, 1974.

[32] R.M. Bowen. Incompressibe Porous Media Models by Use of The Theory of Mixtures. *International Journal of Engineering Science*, 18:1129–1148, 1980.

[33] R.M. Bowen. Compressible Porous Media Models by Use of The Theory of Mixtures. *International Journal of Engineering Science*, 20:697–735, 1982.

[34] R.H. Brooks and A.T. Corey. Hydraulic Properties of Porous Media. *Hydrology Papers Colorado State University*, 1964.

[35] R.N. Brooks and A.T. Corey. Properties of Porous Media Affecting Fluid Flow. *Journal of the Irrigation and Drainage Division*, pages 61–88, 1966.

[36] E.V. Bugaev, A. Misaki, V.A. Naumov, T.S. Sinegovskaya, S.I. Sinegovsky, and N. Takahashi. Atmospheric muon flux at sea level, underground, and underwater. *Physical Review D*, 58:054001, 1998.

[37] N.T. Burdine. Relative Permeability Calculations from Pore-size Distribution Data. *Petr. Trans., Am. Inst. Mining Metall. Eng.*, 1953.

[38] J.F. Carneiro. Numerical simulations on the influence of matrix diffusion to carbon sequestration in double porosity fissured aquifers. *International Journal of Greenhouse Gas Control*, 3:431–443, 2009.

[39] Y.A. Çengel and M.A. Boles. *Thermodynamics: An Engineering Approach*. McGraw-Hill, 5th edition, 2006.

[40] Y. Chen, L.J. Durlofsky, M. Gerritsen, and X.H. Wen. A coupled local-global upscaling approach for simulating flow in highly heterogeneous formations. *Advances in Water Resources*, 26:1041–1060, 2003.

[41] H. Class, R. Helmig, and P. Bastian. Numerical simulation of non-isothermal multiphase multicomponent processes in porous media. 1. An efficient solution technique. *Advances in Water Resources*, 25:533–550, 2002.

[42] H. Class, A. Ebigbo, R. Helmig, H.K. Dahle, J.M. Nordbotten, M. A. Celia, P. Audigane, M. Darcis, J. Ennis-King, Y. Fan, B. Flemisch, S.E. Gasda, M. Jin, S. Krug, D. Labregere, A. Naderi Beni, Rajesh J. Pawar, A. Sbai, S.G. Thomas, L. Trenty, and L. Wei. A benchmark study on problems related to CO_2 storage in geologic formations. *Computational Geosciences*, 13:409–434, 2009.

[43] J.D. Clayton and J.J. Rencis. Numerical integration in the axisymmetric finite element formulation. *Advances in Engineering Software*, 31:137–141, 2000.

[44] B.M. Cody, D. Baù, and A. González-Nicolás. Stochastic injection-strategy optimization for the preliminary assessment of candidate geological storage sites. *Hydrogeology Journal*, 23:1229–1245, 2015.

[45] B.D. Coleman and W. Noll. The Thermodynamics of Elastic Materials with Heat Conduction and Viscosity. *Archive for Rational Mechanics and Analysis*, 13:167–178, 1963.

[46] R.D. Cook, D.S. Malkus, M.E. Plesha, and R.J. Witt. *Concepts and Applications of Finite Element Analysis*. John Wiley & Sons, 4th edition, 2002.

[47] O. Coussy. *Poromechanics*. John Wiley & Sons, 2004.

[48] O. Coussy. *Mechanics and Physics of Porous Solids*. John Wiley & Sons, 2010.

[49] A.K. Dahaghi. Numerical Simulation and Modeling of Enhanced Gas Recovery and CO_2 Sequestration in Shale Gas Reservoirs: A Feasibility Study. *SPE International Conference on* CO_2 *Capture, Storage, and Utilization*, 2010.

[50] L.P. Dake. *Fundamentals of reservoir engineering*. Elsevier Science, 1998.

[51] T.A. Davis. *Direct Methods for Sparse Linear Systems*. SIAM, 2006.

[52] T.A. Davis and I.S. Duff. An Unsymmetric-pattern Multifrontal Method for Sparse LU Factorization. *SIAM Journal on Matrix Analysis and Applications*, 18:140–158, 1997.

[53] R. de Boer. Development of Porous Media Theories – A Brief Historical Review. *Transport in Porous Media*, 9:155–164, 1992.

[54] R. de Boer. Theoretical poroelasticity—a new approach. *Chaos, Solitons & Fractals*, 25: 861–878, 2005.

[55] R. de Boer and W. Ehlers. Uplift, Friction and Capilliarity: Three Fundamental Effects for Liquid-saturated Porous Solids. *International Journal of Solids and Structures*, 26: 43–57, 1990.

[56] J.J. de la Porte, C.A. Kossack, and R.W. Zimmerman. The Effect of Fracture Relative Permeabilities and Capillary Pressures on the Numerical Simulation of Naturally Fractured Reservoirs. *Society of Petroleum Engineers*, 2005.

[57] R.H. Dean, X. Gai, C.M. Stone, and S.E. Minkoff. A Comparison of Techniques for Coupling Porous Flow and Geomechanics. *Society of Petroleum Engineers*, pages 132–140, 2006.

[58] T. Driesner. The system H_2O-NaCl. Part II: Correlations for molar volume, enthalpy, and isobaric heat capacity from 0 to 1000 °C, 1 to 5000 bar, and 0 to 1 X_{NaCl}. *Geochimica et Cosmochimica Acta*, 71:4902–4919, 2007.

[59] L.J. Durlofsky. Upscaling of Geocellular Models for Reservoir Flow Simulation: A Review of Recent Progress. *7th International Forum on Reservoir Simulation*, 2003.

[60] A. El-Hamalawi and M.D. Bolton. A posteriori error estimation in axisymmetric geotechnical analyses. *Computers and Geotechnics*, 29:587–607, 2002.

[61] A. Estublier and A.S. Lackner. Long-term simulation of the Snøhvit CO_2 storage. *Energy Procedia*, 1:3221–3228, 2009.

[62] V. Eyert. A Comparative Study on Methods for Convergence Acceleration of Iterative Vector Sequences. *Journal of Computational Physics*, 124:271–285, 1996.

[63] C.L. Farmer. Upscaling: A review. *International Journal for Numerical Methods in Fluids*, 40:63–78, 2002.

[64] A. Fenghour, W.A. Wakeman, and V. Vesovic. The Viscosity of Carbon Dioxide. *Journal of Physical and Chemical Reference Data*, 27:31–44, 1998.

[65] M. Ferronato, G. Gambolati, and P. Teatini. Ill-conditioning of finite element poroelasticity equations. *International Journal of Solids and Structures*, 38:5995–6014, 2001.

[66] T.K. Gaisser. *Cosmic Rays and Particle Physics.* Cambridge University Press, 1990.

[67] G. Gambolati, G. Pini, and M. Ferronato. Direct, partitioned and projected solution to finite element consolidation models. *International Journal for Numerical and Analytical Methods in Geomechanics*, 26:1371–1383, 2002.

[68] V. Ganine, N.J. Hills, and B.L. Lapworth. Nonlinear acceleration of coupled fluid-structure transient thermal problems by Anderson mixing. *International Journal for Numerical and Analytical Methods in Fluids*, 71:939–959, 2013.

[69] D. Gawin, B. A. Schrefler, and M. Galindo. Thermo-hydro-mechanical analysis of partially saturated porous materials. *Engineering Computations*, 13:113–143, 1996.

[70] H.R. Ghafouri and R.W. Lewis. A Finite Element Double Porosity Model for Heterogeneous Deformable Porous Media. *International Journal for Numerical and Analytical Methods in Geomechanics*, 20:831–844, 1996.

[71] D.K. Gledhill and J.W. Morse. Calcite dissolution kinetics in Na-Ca-Mg-Cl brines. *Geochimica et Cosmochimica Acta*, 70:5802–5813, 2006.

[72] J. Gluyas and S.A. Mathias. *Geological Storage of Carbon Dioxide (CO_2): Geoscience, Technologies, Environmental Aspects and Legal Frameworks.* Woodhead Publishing Series in Energy, 2014.

[73] B. Gong, M. Karimi-Fard, and L.J. Durlofsky. Upscaling Discrete Fracture Characterizations to Dual-Porosity, Dual-Permeability Models for Efficient Simulation of Flow With Strong Gravitational Effects. *Society of Petroleum Engineers Journal*, 13, 2008.

[74] A. González-Nicolás, D. Baù, B.M. Cody, and A. Alzraiee. Stochastic and global sensitivity analyses of uncertain parameters affecting the safety of geological carbon storage in saline aquifers of the Michigan Basin. *International Journal of Greenhouse Gas Control*, 37: 99–114, 2015.

[75] K. Gustafsson and G. Söderlind. Control Stratergies for the Iterative Solution of Nonlinear Equations in ODE Solvers. *SIAM J. Sci. Comput.*, 18:23–40, 1997.

[76] K. Gustafsson, M. Lundh, and G. Söderlind. A PI Stepsize Control For The Numerical Solution of Ordinary Differential Equations. *BIT*, 28:270–287, 1988.

[77] E. Hairer and G. Wanner. *Solving Ordinary Differential Equations II: Stiff and Differential-Algebraic Problems.* Springer, 2nd edition, 1996.

[78] E. Hairer, S.P Nørsett, and G. Wanner. *Solving Ordinary Differential Equations I: Nonstiff Problems.* Springer, 1987.

[79] G. E. Hammond, P. C. Lichtner, and R. T. Mills. Evaluating the performance of parallel subsurface simulators: An illustrative example with PFLOTRAN. *Water Resources Research*, 50:208–228, 2014.

[80] M. Hassanizadeh and W.G. Gray. General conservation equations for multi-phase systems: 1. Averaging procedure. *Advances in Water Resources*, 2:131–144, 1979.

[81] M. Hassanizadeh and W.G. Gray. General conservation equations for multi-phase systems: 2. Mass momenta, energy, and entropy equations. *Advances in Water Resources*, 2: 191–203, 1979.

[82] M. Hassanizadeh and W.G. Gray. General conservation equations for multi-phase systems: 3. Constitutive theory for porous media flow. *Advances in Water Resources*, 3:25–40, 1980.

[83] S.M. Hassanizadeh. Derivation of basic equations of mass transport in porous media, Part 2. Generalized Darcy's and Fick's laws. *Advances in Water Resources*, 9:207–222, 1986.

[84] S.M. Hassanizadeh. Derivation of basic equations of mass transport in porous media, Part 1. Macroscopic balance laws. *Advances in Water Resources*, 9:196–206, 1986.

[85] S.M. Hassanizadeh. Mechanics and thermodynamics of multiphase flow in porous media including interphase boundaries. *Advances in Water Resources*, 13:169–186, 1990.

[86] S.M Hassanizadeh and W.G. Gray. Mechanics and thermodynamics of multiphase flow in porous media including interphase boundaries. *Advances in Water Resources*, 13:169–186, 1990.

[87] H. Hassanzadeh, M. Pooladi-Darvish, A.M. Elsharkawy, D.W. Keith, and Y. Leonenko. Predicting PVT data for CO_2-brine mixtures for black-oil simulation of CO_2 geological storage. *International Journal of Greenhouse Gas Control*, 2:65–77, 2008.

[88] C. He and L.J. Durlofsky. Structured flow-based gridding and upscaling for modeling subsurface flow. *Advances in Water Resources*, 29:1876–1892, 2006.

[89] W. He, C. Beyer, J.H. Fleckenstein, E. Jang, O. Kolditz, D. Naumov, and T. Kalbacher. A parallelization scheme to simulate reactive transport in the subsurface environment with OGS#IPhreeqc 5.5.7-3.1.2. *Geoscientific Model Development*, 8:3333–3348, 2015.

[90] E. Heidaryan, T. Hatami, M. Rahimi, and J. Moghadasi. Viscosity of pure carbon dioxide at supercritical region: Measurement and correlation approach. *The Journal of Supercritical Fluids*, 56:144–151, 2011.

[91] M.K Hubbert and D.G Willis. Mechanics of Hydraulic Fracturing. *Society of Petroleum Engineers of AIME*, 1972.

[92] J.A. Hudson and J.P. Harrison. *Engineering Rock Mechanics.* Elsevier Ltd, 1997.

[93] International Energy Agency (IEA). World Energy Outlook Special Report 2015: Energy and Climate Change. 2015.

[94] IEAGHC. Caprock Systems for CO_2 Geological storage. 2011.

[95] D.B. Ingham, A. Bejan, E. Mamut, and I. Pop. *Emerging Technologies and Techniques in Porous Media.* Springer, 2004.

[96] IPCC. Summary for Policymakers. In *IPCC Special Report Carbon Dioxide Capture and Storage.* 2005.

[97] IPCC. Climate Change 2014: Synthesis Report. Contribution of Working Groups I, II and III to the Fifth Assessment Report of the Internation Panel on Climate Change, 2014.

[98] B.M. Irons. A frontal solution scheme for finite element analysis. *International Journal for Numerical Methods in Engineering*, 2:5–32, 1970.

[99] J.C. Jaeger, N.G.W. Cook, and R.W. Zimmerman. *Fundamentals of Rock Mechancis.* Blackwell Publishing, 4th edition, 2007.

[100] K. Jihoon, E.L. Sonnenthal, and J. Rutqvist. Formulation and sequential numerical algorithms of coupled fluid/heat flow and geomechanics for multiple porosity materials. *International Journal for Numerical Methods in Engineering*, 92:425–456, 2012.

[101] G. Kaufmann and W. Dreybrodt. Calcite dissolution kinetics in the system $CaCO_3$-H_2O-CO_2 at high undersaturation. *Geochimica et Cosmochimica Acta*, 71: 1398–1410, 2007.

[102] D. Kavetski, P. Binning, and S.W. Sloan. Adaptive time stepping and error control in a mass conservative numerical solution of the mixed form of Richards equation. *Advances in Water Resources*, 24:595–605, 2001.

[103] D. Kavetski, P. Binning, and S.W. Sloan. Adaptive backward Euler time stepping with truncation error control for numerical modelling of unsaturated fluid flow. *International Journal for Numerical Methods in Engineering*, 53:1301–1322, 2002.

[104] D. Kavetski, P. Binning, and S.W. Sloan. Truncation error and stability analysis of iterative and non-iterative ThomasGladwell methods for first-order non-linear differential equations. *International Journal for Numerical Methods in Engineering*, 60:2031–2043, 2004.

[105] J. Kestin, M. Sokolov, and W.A. Wakeham. Viscosity of Liquid Water in the Range −8°C to 150°C. *Journal of Physical and Chemical Reference Data*, 7:941–948, 1978.

[106] J. Kestin, H.E. Khalifa, and R.J. Correia. Tables of the Dynamic and Kinematic Viscosity of Aqueous NaCl Solutions in the Temperature Range 20–150 °C and the Pressure Range 0.1–35 MPa. *Journal of Physical and Chemical Reference Data*, 10:71–87, 1981.

[107] A.R. Khoei, S. Moallemi, and E. Haghighat. Thermo-hydro-mechanical modeling of impermeable discontinuity in saturated porous media with X-FEM technique. *Engineering Fracture Mechanics*, 96:701–723, 2012.

[108] J. Klinger, S.J. Clark, M. Coleman, J.G. Gluyas, V.A. Kudryavtsev, D.L. Lincoln, S. Pal, S.M. Paling, N.J.C. Spooner, S. Telfer, L.F. Thompson, and D. Woodward. Simulation of muon radiography for monitoring CO_2 stored in a geological reservoir. *International Journal of Greenhouse Gas Control*, 42:644–654, 2015.

[109] K.G. Knauss, J.W. Johnson, and C.I. Steefel. Evaluation of the impact of CO_2, co-contaminant gas, aqueous fluid and reservoir rock interactions on the geologic sequestration of CO_2. *Chemical Geology*, 217:339–350, 2005.

[110] O. Kolditz, S. Bauer, N. Böttcher, D. Elsworth, U.-J. Görke, C.-I. McDermott, C.-H. Park, A.K. Singh, J. Taron, and W. Wang. Numerical simulation of two-phase flow in deformable porous media: Application to carbon dioxide storage in the subsurface. *Mathematics and Computers in Simulation*, 82:1919–1935, 2012.

[111] O. Kolditz, U.-J. Görke, H. Shao, and W. Wang, editors. *Thermo-Hydro-Mechanical-Chemical Processes in Fractured Porous Media: Benchmarks and Examples.* Springer, 2012.

[112] S. Krogstad, K.-A. Lie, O. Møyner, H.M. Nilsen, X. Raynaud, and B. Skaflestad. MRST-AD – An Open-Source Framework for Rapid Prototyping and Evaluation of Reservoir Simulation Problems. *Society of Petroleum Engineers*, 2015.

[113] V.A. Kudryavtsev. Muon simulation codes MUSIC and MUSUN for underground physics. *Computer Physics Communications*, 180:339–346, 2009.

[114] V.A. Kudryavtsev, N.J.C. Spooner, J.G. Gluyas, C. Fung, and M. Coleman. Monitoring subsurface CO_2 emplacement and security of storage using muon tomography. *International Journal of Greenhouse Gas Control*, 11:21–24, 2012.

[115] S.H. Lee, M.F. Lough, and C.L. Jensen. Hierarchical modeling of flow in naturally fractured formations with multiple length scales. *Water Resources Research*, 37:443–455, 2001.

[116] P. Lemonnier and B. Bourbiaux. Simulation of Naturally Fractured Reservoirs. State of the Art. *Oil & Gas Science and Technology – Revue de l'Institut Français du Pétrole*, 65: 263–286, 2010.

[117] R.J. Lenhard, J.C. Parker, and S. Mishra. On the Correspondence Between Brooks-Corey and van Genuchten Models. *Journal of Irrigation and Drainage Engineering*, 115:744–751, 1989.

[118] R.W Lewis and H.R Ghafouri. A Novel Finite Element Double Porosity Model for Multiphase Flow through Deformable Fractrured Porous Media. *International Journal for Numerical and Analytical Methods in Geomechanics*, 21:789–816, 1997.

[119] R.W. Lewis and W.K.S. Pao. Numerical Simulation of Three-Phase Flow in Deforming Fractured Reservoirs. *Oil and Gas Science and Technology*, 57:499–514, 2002.

[120] R.W. Lewis and B.A. Schrefler. *The Finite Element Method in the Static and Dynamic Deformation and Consolidation of Porous Media.* John Wiley & Sons, 2nd edition, 1998.

[121] D. Li, S. Bauer, K. Benisch, B. Graupner, and C. Beyer. OpenGeoSys-ChemApp: A coupled simulator for reactive transport in multiphase systems and application to CO_2 storage formation in Northern Germany. *Acta Geotechnica*, 9:67–79, 2014.

[122] J. Liu, Y. Sano, and A. Nakayama. A simple mathematical model for determining the equivalent permeability of fractured porous media. *International Communications in Heat and Mass Transfer*, 36:220–224, 2009.

[123] I. Masters, W.K.S. Pao, and R.W. Lewis. Coupling Temperature to a Double-Porosity Model of Deformable Porous Media. *International Journal for Numerical Methods in Engineering*, 49:421–438, 2000.

[124] S.A. Mathias, P.E. Hardisty, M.R. Trudell, and R.W. Zimmerman. Approximate Solutions for Pressure Buildup During CO2 Injection in Brine Aquifers. *Transport in Porous Media*, 79:265–284, 2009.

[125] S.A. Mathias, J.G. Gluyas, C.M. Oldenburg, and C. Tsang. Analytical solution for Joule-Thomson cooling during CO_2 geo-sequestration in depleted oil and gas reservoirs. *International Journal of Greenhouse Gas Control*, 4:806–810, 2010.

[126] S.A. Mathias, J.G. Gluyas, G.J. González Martínez de Miguel, and S.A. Hosseini. Role of partial miscibility on pressure buildup due to constant rate injection of CO_2 into closed and open brine aquifers. *Water Resources Research*, 47, 2011.

[127] S.A. Mathias, G.J. González Martínez de Miguel, K.E. Thatcher, and R.W. Zimmerman. Pressure Buildup During CO2 Injection into a Closed Brine Aquifer. *Transport in Porous Media*, 89:383–397, 2011.

[128] S.A. Mathias, J.G. Gluyas, G.J. González Martínez de Miguel, S.L. Bryant, and D. Wilson. On relative permeability data uncertainty and CO_2 injectivity estimation for brine aquifers. *International Journal of Greenhouse Gas Control*, 12:200–212, 2013.

[129] S.A. Mathias, J.N. McElwaine, and J.G. Gluyas. Heat transport and pressure buildup during carbon dioxide injection into depleted gas reservoirs. *Journal of Fluid Mechanics*, 756:89–109, 2014.

[130] M. Melenk and I. Babuskab. The partition of unity finite element method: Basic theory and applications. *Computational Methods Applied Mechanical Engineering*, 139:289–314, 1996.

[131] P. Moonen. *Continuous-discontinuous modelling of hygrothermal damage processes in porous media.* PhD thesis, Delft University of Technology, 2009.

[132] H.J. Morel-Seytoux, P.D. Meyer, M. Nachabe, J. Tourna, M.T. van Genuchten, and R.J. Lenhard. Parameter Equivalence for the Brooks-Corey and van Genuchten soil characteristics: Preserving the effective capillary drive. *Water Resources Research*, 32:1251–1258, 1996.

[133] Y. Mualem. A New Model for Predicting the Hydraulic Conductivity of Unsaturated Porous Media. *Water Resources Research*, 12:513–522, 1976.

[134] United Nations. Transforming our world: the 2030 Agenda for Sustainable Development, 2015.

[135] R. D. Neidinger. Introduction to Automatic Differentiation and MATLAB Object-Oriented Programming. *SIAM Review*, 52:545–563, 2010.

[136] R. Neumann, P. Bastian, and O. Ippisch. Modeling and simulation of two-phase two-component flow with disappearing nonwetting phase. *Computational Geosciences*, 17: 139–149, 2013.

[137] D.A. Nield and A. Bejan. *Convection in Porous Media.* Springer, 4th edition, 2012.

[138] J.M. Nordbotten and M.A. Celia. Similarity solutions for fluid injection into confined aquifers. *Journal of Fluid Mechanics*, 561:307–327, 2006.

[139] J.M. Nordbotten, M.A. Celia, and S. Bachu. Injection and Storage of CO_2 in Deep Saline Aquifers: Analytical Solution for CO_2 Plume Evolution During Injection. *Transport in Porous Media*, 58:339–360, 2005.

[140] D.M. O'Carroll, K.G. Mumford, L.M. Abriola, and J.I. Gerhard. Influence of wettability variations on dynamic effects in capillary pressure. *Water Resources Research*, 46:1–13, 2010.

[141] C.M. Oldenburg. Joule-Thomson cooling due to CO_2 injection into natural gas reservoirs. *Energy Conversion and Management*, 48:1808–1815, 2007.

[142] J. Oliver. Modelling Strong Discontinuites in Solid Mechanics via Strain Softening Constitutive equations. Part 2: Numerical Simulation. *International Journal for Numerical Methods in Engineering*, 39:3601–3623, 1996.

[143] J. Oliver. On the discrete constitutive models induced by strong discontinuity kinematics and continuum constitutive equations. *International Journal of Solids and Structures*, 37: 7207–7229, 2000.

[144] J. Oliver, A.E. Huespe, M.D.G. Pulido, and E. Chaves. From continuum mechanics to fracture mechanics: the strong discontinuity approach. *Engineering Fracture Mechanics*, 69:113–136, 2002.

[145] J.M. Ortega and W.C. Rheinboldt. *Iterative Solutions of Nonlinear Equations in Several Variables.* Academic Press, 1970.

[146] W.K.S. Pao and R.W. Lewis. Three-dimensional finite element simulation of three-phase flow in a deforming fissured reservoir. *Computer Methods in Applied Mechanics and Engineering*, 191:2631–2659, 2002.

[147] D.J. Payen and K.-J. Bathe. The use of nodal point forces to improve element stresses. *Computers & Structures*, 89:485–495, 2011.

[148] A. Pérez-Foguet, A. Rodríguez-Ferran, and A. Huerta. Numerical differentiation for non-trivial consistent tangent matrices: an application to the MRS-Lade model. *International Journal for Numerical Methods in Engineering*, 48:159–184, 2000.

[149] A. Pérez-Foguet, A. Rodríguez-Ferran, and A. Huerta. Numerical differentiation for local and global tangent operators in computational plasticity. *Computer Methods in Applied Mechanics and Engineering*, 189:277–296, 2000.

[150] S. Pesente, S. Vanini, M. Benettoni, G. Bonomi, P. Calvini, P. Checchia, E. Conti, F. Gonella, G. Nebbia, S. Squarcia, G. Viesti, A. Zenoni, and G. Zumerle. First results on material identification and imaging with a large-volume muon tomography prototype. *Nuclear Instruments and Methods in Physics Research Section A: Accelerators, Spectrometers, Detectors and Associated Equipment*, 604:738–746, 2009.

[151] K.S. Pitzer, C.J. Peiper, and H.R. Busey. Thermodynamic Properties of Aqueous Sodium Chloride Solutions. *Journal of Physical and Chemical Reference Data*, 13:1–102, 1984.

[152] W. Powrie. *Soil Mechanics: Concepts and Applications*. Spon Press, 2nd edition, 2004.

[153] J.M. Prausnitz, R.N. Lichtenthaler, and E. Gomes de Azevedo. *Molecular Thermodynamics of Fluid-Phase Equilibria*. Prentice Hall, 2nd edition, 1986.

[154] W.C. Priedhorsky, K.N. Borozdin, G.E. Hogan, C. Morris, A. Saunders, L.J. Schultz, and M.E. Teasdale. Detection of high-Z objects using multiple scattering of cosmic ray muons. *Review of Scientific Instruments*, 74:4294–4279, 2003.

[155] T. Rahmam and J. Valdman. Fast MATLAB assembly of FEM matrices in 2D and 3D: nodal elements, 2010.

[156] J.-F. Remacle, J. Lambrechts, B. Seny, E. Marchandise, A. Johnen, and C. Geuzaine. Blossom-Quad: a non-uniform quadrilateral mesh generator using a minimum cost perfect matching algorithm. *International Journal for Numerical Methods in Engineering*, 89: 1102–1119, 2012.

[157] Ph. Renard and G. de Marsily. Calculating equivalent permeability: a review. *Advances in Water Resources*, 20:253–278, 1997.

[158] L. A. Richards. Capillary conduction of liquids through porous mediums. *Journal of Applied Physics*, 1:318–333, 1931.

[159] B.A. Robinson, H.S. Viswanathan, and A.J. Valocchi. Efficient numerical techniques for modeling multicomponent ground-water transport based upon simultaneous solution of

strongly coupled subsets of chemical components. *Advances in Water Resources*, 23: 307–324, 2000.

[160] P.S.Z. Rogers and K.S. Pitzer. Volumetric Properties of Aqueous Sodium Chloride Solutions. *Journal of Physical and Chemical Reference Data*, 11:15–81, 1982.

[161] A.M. Rowe and J.C.S. Chou. Pressure-Volume-Temperature-Concentration Relation of Aqueous NaCl Solutions. *Journal of Chemical and Engineering Data*, 15:61–66, 1970.

[162] J. Rutqvist. Status of the TOUGH-FLAC simulator and recent applications related to coupled fluid flow and crustal deformations. *Computers & Geosciences*, 37:739–750, 2011.

[163] J. Rutqvist. The Geomechanics of CO_2 Storage in Deep Sedimentary Formations. *Geotechnical and Geological Engineering*, 30:525–551, 2012.

[164] J.E. Santos, J. Germán Rubino, and C.L. Ravazzoli. A numerical upscaling procedure to estimate effective plane wave and shear moduli in heterogeneous fluid-saturated poroelastic media. *Computer Methods in Applied Mechanics and Engineering*, 198:2067–2077, 2009.

[165] J.H. Saunders, M.D. Jackson, and C.C. Pain. Fluid flow monitoring in oil fields using downhole measurements of electrokinetic potential. *Geophysics*, 73:E165–E180, 2008.

[166] G. Scalabrin, P. Marchi, F. Finezzo, and R. Span. A Reference Multiparameter Thermal Conductivity Equation for Carbon Dioxide with an Optimized Functional Form. *Journal of Physical and Chemical Reference Data*, 35:1549–1575, 2006.

[167] B.A. Schrefler and L. Simoni. Comparison between different finite element solutions for immiscible two phase flow in deforming porous media. *Computer Methods and Advances in Geomechanics*, 1991.

[168] B.A. Schrefler and Z. Xiaoyong. A Fully Coupled Model for Water Flow and Airflow in Deformable Porous Media. *Water Resources Research*, 29:155–167, 1993.

[169] W. Schroeder, K. Martin, and B. Lorensen. *The Visualization Toolkit*. Kitware, 4th edition, 2006.

[170] L.J. Schultz, K.N. Borozdin, J.J. Gomez, G.E. Hogan, J.A. McGill, C.L. Morris, W.C. Priedhorsky, A. Saunders, and M.E. Teasdale. Image reconstruction and material Z discrimination via cosmic ray muon radiography. *Nuclear Instruments and Methods in Physics Research Section A: Accelerators, Spectrometers, Detectors and Associated Equipment*, 519:687–694, 2004.

[171] L.J. Schultz, G.S. Blanpied, K.N. Borozdin, A.M. Fraser, N.W. Hengartner, A.V. Klimenko, C.L. Morris, C. Orum, and M.J. Sossong. Statistical Reconstruction for Cosmic Ray Muon Tomography. *IEEE Transactions on Image Processing*, 16:1985–1993, 2007.

[172] A. Settari and F.M. Mourits. A Coupled Reservoir and Geomechanical Simulation System. *Society of Petroleum Engineers*, 3:219–226, 1998.

[173] L.F. Shampine. Local Error Estimate by Doubling. *Computing*, 34:179–190, 1985.

[174] H.Y. She and B.E. Sleep. The effect of temperature on capillary pressure-saturation relationships for air-water and perchloroethylene-water systems. *Water Resources Research*, 34:2587–2597, 1998.

[175] V. Singh, A. Cavanagh, H. Hansen, B. Nazarian, M. Iding, and P. Ringrose. Reservoir Modeling of CO_2 Plume Behavior Calibrated Against Monitoring Data From Sleipner, Norway. *SPE Annual Technical Conference & Exhibition*, 2010.

[176] S.W. Sloan and A.J. Abbo. Biot Consolidation Analysis with Automatic Time Stepping and Error Control Part 1: Theory and Implementation. *International Journal for Numerical and Analytical Methods in Geomechanics*, 23:467–492, 1999.

[177] S.W. Sloan and A.J. Abbo. Biot Consolidation Analysis with Automatic Time Stepping and Error Control Part 2: Applications. *International Journal for Numerical and Analytical Methods in Geomechanics*, 23:493–529, 1999.

[178] G. Söderlind. Automatic control and adaptive time-stepping. *Numerical Algorithms*, 31: 281–310, 2002.

[179] G. Söderlind. Time-step selection algorithms: Adaptivity, control, and signal processing. *Applied Numerical Mathematics*, 56:488–502, 2006.

[180] G. Söderlind and L. Wang. Evaluating numerical ODE/DAE methods, algorithms and software. *Journal of Computational and Applied Mathematics*, 185:244–260, 2006.

[181] R. Span and W. Wagner. A New Equation of State for Carbon Dioxide Covering the Fluid Region from the Triple-Point Temperature to 1100 K at Pressures up to 800 MPa. *Journal of Physical and Chemical Reference Data*, 25:1509–1596, 1996.

[182] R. Span and W. Wagner. Equations of State for Technical Applications. I. Simultaneously Optimized Functional Forms for Nonpolar and Polar Fluids. *International Journal of Thermophysics*, 24:1–39, 2003.

[183] N. Spycher and K. Pruess. CO_2-H_2O mixtures in the geological sequestration of CO_2. II. Partitioning in chloride brines at 12–100°C and up to 600 bar. *Geochimica et Cosmochimica Acta*, 69:3309–3320, 2005.

[184] N. Spycher, K. Pruess, and J. Ennis-King. CO_2-H_2O mixtures in the geological sequestration of CO_2. I. Assessment and calculation of mutual solubilities from 12 to 100°C and up to 600 bar. *Geochimica et Cosmochimica Acta*, 67:3015–3031, 2003.

[185] M. Stephenson. *Returning Carbon to Nature: Coal, Carbon Capture, and Storage*. Elsevier, 2013.

[186] M. Talebian, R. Al-Khoury, and L.J. Sluys. A Computational Model for Coupled Multiphysics Processes of CO_2 Sequestration in Fractured Porous Media. *Advances in Water Resources*, 59:238–255, 2013.

[187] M. Talebian, R. Al-Khoury, and L.J. Sluys. Coupled Electrokinetic-Hydromechanic Model for CO_2 Sequestration in Porous Media. *Transport in Porous Media*, 98:287–321, 2013.

[188] H.K.M. Tanaka, T. Kusagaya, and H. Shinohara. Radiographic visualization of magma dynamics in an erupting volcano. *Nature Communications*, 5:1–9, 2014.

[189] K. Terzaghi. *Erdbaumechanik auf bodenphysikalischer Grundlage.* 1925.

[190] R.M. Thomas and I. Gladwell. Variable-order variable-step algorithms for second-order systems. Part 1: The methods. *International Journal for Numerical Methods in Engineering*, 26:39–53, 1988.

[191] T.K. Tokunaga. DLVO-Based Estimates of Adsorbed Water Film Thicknesses in Geologic CO_2 Reservoirs. *American Chemical Society*, 28:8,001–8,009, 2012.

[192] F.L. Toth, editor. *Geological Disposal of Carbon Dioxide and Radioactive Waste: A Comparative Assessment*, volume 44 of *Advances in Global Change Research Series.* Springer, 2011.

[193] United Nations. Adoption of the Paris Agreement. *Framework Convention on Climate Change*, 2015.

[194] M.Th. van Genuchten. A Closed-form Equation for Predicting the Hydraulic Conductivity of Unsaturated Soils. *Soil Science Society of America Journal*, 44:892–898, 1980.

[195] D.W. Vasco, A. Rucci, A. Ferretti, F. Novali, R.C. Bissell, P.S. Ringrose, A.S. Mathieson, and I.W. Wright. Satellite-based measurements of surface deformation reveal fluid flow associated with the geological storage of carbon dioxide. *Geophysical Research Letters*, 37: 1–5, 2010.

[196] V. Vilarrasa, D. Bolster, M. Dentz, S. Olivella, and J. Carrera. Effects of CO_2 Compressibility on CO_2 Storage in Deep Saline Aquifers. *Transport in Porous Media*, 85:619–639, 2010.

[197] V. Vilarrasa, D. Bolster, S. Olivella, and J. Carrera. Coupled hydromechanical modeling of CO_2 sequestration in deep saline aquifers. *International Journal of Greenhouse Gas Control*, 4:910–919, 2010.

[198] H.F. Walker and P. Ni. Anderson Acceleration for Fixed-Point Iterations. *SIAM Journal on Numerical Analysis*, 49(4):1715–1735, jan 2011.

[199] H.F. Walker, C.S. Woodward, and U.M. Yang. An Accelerated Fixed-Point Iteration For Solution of Variably Saturated Flow. *International Conference on Water Resources*, 2010.

[200] W. Wang, T. Schnicke, and O. Kolditz. Parallel Finite Element Method and Time Stepping Control for Non-Isothermal Poro-Elastic Problems. *Tech Science Press*, 21:217–235, 2011.

[201] J.E. Warren and P.J. Root. The Behavior of Naturally Fractured Reservoirs. *Society of Petroleum Engineers Journal*, pages 245–255, 1963.

[202] G.N. Wells and L.J. Sluys. A new method for modelling cohesive cracks using fnite elements. *International Journal for Numerical Methods in Engineering*, 50:2667–2682, 2001.

[203] X.H. Wen and J.J. Gómez-Hernández. Upscaling hydraulic conductivities in heterogeneous media: An overview. *Journal of Hydrology*, 183:ix–xxxii, 1996.

[204] M.D. White and M. Oostrom. *Subsurface Transport Over Multiple Phases.* 2003.

[205] T. Xu, E. Sonnenthal, N. Spycher, and K. Pruess. TOUGHREACT—A simulation program for non-isothermal multiphase reactive geochemical transport in variably saturated geologic media: Applications to geothermal injectivity and CO_2 geological sequestration. *Computers & Geosciences*, 32:145–165, 2006.

[206] Z. Ziabakhsh-Ganji and H. Kooi. An Equation of State for thermodynamic equilibrium of gas mixtures and brines to allow simulation of the effects of impurities in subsurface CO_2 storage. *International Journal of Greenhouse Gas Control*, 11:S21–S34, 2012.

[207] O.C. Zienkiewicz, R.L. Taylor, and J.Z. Zhu. *The Finite Element Method: Its Basis and Fundamentals.* Elsevier Butterworth-Heinemann, 6th edition, 2005.

[208] R.W. Zimmerman. Thermal Conductivity of Fluid-Saturated Rocks. *Journal of Petroleum Science and Engineering*, 3:219–227, 1989.

[209] R.W. Zimmerman, W.H. Somerton, and M.S. King. Compressibility of Porous Rocks. *Journal of Geophysical Research*, 91:12,765–12,777, 1986.